The interplay between cosmology and galaxy formation

Jaime Salcido Negrete

Abstract

The standard ΛCDM model of cosmology has been very successful in matching a large set of observational constraints and describes accurately the evolution of our Universe. Within this framework, the gravitational collapse of cold dark matter structures depends solely on the cosmological background. The formation of galaxies inside these haloes is thought to be determined by complex baryonic process and we rely on numerical techniques to model their effects.

Here, we investigate the impact of the cosmological background on galaxy formation. We take the advantage of state of the art cosmological hydrodynamical simulations from the EAGLE suite to vary the cosmological parameters, in particular, the cosmological constant, to test its effect on the efficiency of star formation. We use this set of new simulations to calculate the likelihood of the observed value of the cosmological constant, given a measure of the multiverse. We discuss the implication of our results in the context of the anthropic principle.

We use this framework to develop a fully analytic model of galaxy formation that connects the growth of dark matter haloes in a cosmological background, with the build-up of stellar mass within these haloes. The model identifies the physical processes that drive the Galaxy-Halo co-evolution through cosmic time. Despite the complexity of the baryonic processes involved, galaxy formation is revealed as a remarkably simple process, where the instantaneous star formation efficiency within halos is only a function of their virial temperature and can be described with a 'single' differential equation. We find that the model reproduces self-consistently the shape and evolution of the cosmic star formation rate density, the specific star formation rate of galaxies, and the galaxy stellar mass function, both at the present time and at high redshift.

Finally, we use the merger rate of supermassive black holes in the EAGLE simulations to estimate the expected event rate of gravitational wave signals that could be resolved by future space-based gravitational wave detectors. We discuss the power of these detections to provide information about the origin of supermassive black holes and the initial mass distribution of black hole seeds.

The interplay between cosmology and galaxy formation

Jaime Salcido Negrete

A thesis submitted to the University of Durham
in accordance with the regulations
for admittance to the Degree of
Doctor of Philosophy

Institue for Computational Cosmology
Department of Physics
University of Durham
England

September 2018

Dedicated to

Daniel and Anne

without whose infinite energy, this thesis would have been finished in half the time, but without all the happiness and love.

Our love for you has taught us the immensity of the Universe. Your mom and I would love you both in any possible Universe.

Declaration

The work described in this thesis was undertaken between October 2014 and September 2018 while the author was a research student under the supervision of Prof. Richard Bower and Prof. Tom Theuns in the Department of Physics at the University of Durham. This work has not been submitted for any other degree at the University of Durham or any other University.

Chapters 3, 4 and 6 have all been published as papers in Monthly Notices of the Royal Astronomical Society (MNRAS):

- *The impact of Dark Energy on Galaxy Formation. What does the future of our Universe hold?*
  Salcido J., Bower, R. G., Barnes, L. A., Lewis, G. F., Elahi, P. J., Theuns, T., Schaller, M., Crain, R. A., Schaye, J., MNRAS 2018, Volume 477, Issue 3, Pages 3744-3759

- *Galaxy formation efficiency and the multiverse explanation of the cosmological constant with EAGLE simulations*
  Barnes, L., Elahi, P. J, **Salcido J.**, Bower R. G., Lewis, G. F., Theuns, T., Schaller, M., Crain, R. A., Schaye, J., MNRAS 2018, Volume 477, Issue 3, Pages 3727-3743

- *Music from the heavens - gravitational waves from supermassive black hole mergers in the EAGLE simulations*
  Salcido J., Bower R. G., Theuns T., McAlpine S., Schaller M., Crain R. A., Schaye J., Regan J., MNRAS 2016, Volume 463, Issue 1, Pages 870-885

Chapter 5 is work currently in progress and will be submitted soon in the form of a paper to MNRAS.

All text and figures contained in this thesis have been produced by the author (except where explicitly stated otherwise). The simulations and data analysis described in Chapter 4 are the direct work of the author, in collaboration with the supervisors named above, along with other researchers at the University of Sydney, Western Sydney University and the University of Western Australia.

Acknowledgements

I am thankful to my mentors, Prof. Richard Bower and Prof. Tom Theuns, for their guidance during my PhD. Their passion and deep understanding of physics were truly inspirational. Thank you, Richard, for your endless enthusiasm, and for your enduring support and patience when transforming an engineer into a cosmologist seemed like an impossible task. Thank you, Tom, for spending endless hours with me in front of a blackboard, until I was finally able to grasp what you were trying to teach me. I deeply appreciate both of you and value everything that I have learned from you.

To my wife, without whose endless support and patience, I would never have done this. Diana, life is much better with you by my side. Thank you for all that you do for our family. This goal is also yours. I love you!

To my Dad, for your trust in me and for your endless support. You taught me to fly high, and marvel at the havens. Mom, thank you for your tenderness to me. Your love supported me in the hard times of this process. To Javi, who is my best friend and makes me both laugh and cry. Thank you for inspiring me to embark on this adventure. And to Danny, my dear sister, who is the treasure of our family. You will always be my sweet little sister.

There is a very long list of friends I have accumulated at Durham during all these years. There is far too many to name individually, but in particular, I would like to thank the 'Schwartz-Cruz', who became our closest friends in Durham. We have shared projects, houses, laughter and tears. We have become one big Mexican family, and we will always be friends. Thank you, Ary, Ernesto and Camila.

Thank you also to my colleagues. Again, far too many to name individually, but in particular, I have had the privilege to share an office with incredibly talented people.

Stuart, Ruari, Ben, Paddy, Dave, Sownak, Piotr, and Josh, you made the office a truly enjoyable place to be.

I am also privileged to have lived in such a beautiful place like Durham for the last five years. But what made this time truly special, is that I found a home, a family at St Nic's Church. To my family of St Nic's, thank you for your boundless care and love.

I am also grateful to the Mexican Council for Science and Technology (CONACyT) for funding this research.

Finally, to my God, who knitted me together before the formation of the Universe. Who knows all the stars, and still knows me by name. All things are for you and through you. Your love reaches to the havens, and I am your son. Thank you!

Contents

List of Figures

List of Tables

In the beginning...

1 Introduction

> *Scientific progress is the discovery of a more and more comprehensive simplicity... The previous successes give us confidence in the future of science: we become more and more conscious of the fact that the universe is cognizable*
>
> **— Georges Lemaître**

The mysteries of the heavens have captivated human imagination since ancient times. The nature of the cosmos and our place within it has both inspired and intrigued scientists, philosophers, theologians, artists and science fiction writers alike. From the scientific point of view, the study of our Universe has been filled with surprising observational discoveries and revolutionary ideas that trace back to the scientific revolution during the Renaissance, and the Enlightenment.

In the mid-18th century, Thomas Wright of Durham (not far away from where this work has been written) first proposed that 'faint nebulae' were beyond our own galaxy. He proposed that the Milky Way was one tiny galaxy in a sea of island worlds, 'external creation, bordering upon the known one, too remote for even our telescopes to reach' (Wright, 1750). This idea gave rise to a debate that lasted for centuries, whether 'spiral nebulae' were part of our galaxy, or were more distant objects (Shapley & Curtis, 1921).

It was not until 1925, when Edwin Hubble estimated the distance to faint nebulae using Cepheid variables, that it was demonstrated they were 'remote stellar systems' (Hubble, 1925). He confirmed that spiral nebulae were galaxies, comparable in size, but laying outside, our own Milky Way. This marked the birth of extragalactic astronomy. Only four years later, Hubble showed that all distant galaxies are moving away from us, with velocities that are, on average, proportional to their distance (Hubble, 1929). Hubble made one of the most important discoveries in the history of cosmology, he discovered the expansion of the universe.

However, the idea of a 'Big Bang' cosmology precedes the observational evidence of an expanding universe. In the early 13th century, in his treatise on light, the English scientist and clergyman Robert Grosseteste was the first to propose a cosmological model in which the Universe was created in a Big-Bang-like explosion (Bower et al., 2014). Almost 700 years later, in 1916, Albert Einstein published his groundbreaking theory of General Relativity, which allowed us, for the first time, to construct self-consistent models of the Universe as a whole (Einstein, 1916). Alexander Friedmann in 1922 and Georges Lemaître in 1927 independently discovered a family of solutions to Einstein field equations of gravitation that describe an expanding universe (Friedmann, 1922; Lemaître, 1927). Since then, the 'Hot Big Bang' gradually became the most popular hypothesis of cosmology.

Another important turn of events in our understanding of our universe arrived in the 1930s, when Jan Oort and Fritz Zwicky, while studying the velocities of stars in the Milky Way, and galaxies within the Coma Cluster respectively, inferred the existence of an apparently invisible form of matter, to fully account for their gravitational dynamics (Oort, 1932; Zwicky, 1933). This mysterious 'dark matter' has been a topic of increasing interest in cosmology since then.

At the end of 20th century, observations of distant supernovae revealed an even more unexpected phenomenon, the universe is not only expanding, but it is doing so, at an accelerated rate (Riess et al., 1998; Perlmutter et al., 1999). This discovery provided the first suggestion of the existence of a bizarre form of 'dark energy' that competes against gravitational forces on large scales.

Many more careful observations, combined with theoretical breakthroughs, and technological advances during the last century, have led to the emergence of a comprehensive model of the evolution of our Universe. The present best-fit cosmological model, known as the concordance model, or ΛCDM, includes both, a treatment of dark energy as a cosmological constant, Λ, and Cold (i.e. non-relativistic) Dark Matter. This model has been very successful in matching observational data, and describes accurately the evolution of our Universe. Despite its success, the nature of its two major components, the cosmological constant and the cold dark matter, are still unknown. Shedding light on the nature of these two components, is one of the major challenges of modern cosmology and particle physics.

This chapter reviews the standard model of cosmology and discusses the role of simulations in understanding galaxy formation.

1.1 Cosmology

The understanding of the physical laws that govern the origin, evolution, and eventual fate of the Universe is a branch of science known as physical cosmology. The theoretical framework within which we study cosmology rests upon two key assumptions. First, the cosmological principle: that, on large scales, the Universe is spatially homogeneous and isotropic, i.e. observers at different locations in space will observe, more or less, the same thing in all directions. Second, that Einstein's General Theory of Relativity (GR) is the correct description of gravity. In GR, the space-time structure of the Universe is determined by the matter distribution within it via the Einstein Field equations,

$$R_{\mu\nu} - \frac{1}{2}g_{\mu\nu}R + \Lambda g_{\mu\nu} = \frac{8\pi G}{c^4}T_{\mu\nu}, \tag{1.1}$$

where $R_{\mu\nu}$ is the Ricci curvature tensor, R is the scalar curvature, $g_{\mu\nu}$ is the metric tensor, which captures all the geometric and causal structure of spacetime, Λ is a cosmological constant, G is Newton's gravitational constant, c is the speed of light in vacuum, and $T_{\mu\nu}$ is the stress-energy tensor. The cosmological principle implies that space is invariant under rotations and translations, i.e. it is maximally symmetric. The family of solutions of the Einstein field equations that describe these maximally-symmetric hyper-surfaces evolving in time are described by the Friedmann-Lemaître-Robertson-Walker (FLRW) metric,

$$\mathrm{d}s^2 = -c\mathrm{d}t^2 + a(t)^2\left[\frac{\mathrm{d}r^2}{1-\kappa r^2} + r^2(\mathrm{d}\theta^2 + \sin^2\theta\mathrm{d}\phi^2)\right], \tag{1.2}$$

where r, θ and ϕ are spherical polar comoving coordinates, $a(t)$ is the dimensionless time dependent scale factor of the Universe, normalised such that it has a value of $a(0) = 1$ at the present time, and κ is the spatial curvature.

Using the FLRW metric into Eq. (1.1), and modelling matter and energy by a perfect fluid, yields the well know Friedmann equations,

$$\left(\frac{\dot{a}}{a}\right)^2 = H^2(t) = \frac{8\pi G}{3}\rho - \frac{\kappa c^2}{a^2} + \frac{\Lambda c^2}{3}, \tag{1.3}$$

and

$$\frac{\ddot{a}}{a} = \frac{4\pi G}{3}\left(\rho + 3\frac{P}{c^2}\right) + \frac{\Lambda c^2}{3}, \tag{1.4}$$

where dotted variables denote time derivatives, the Hubble parameter $H(t)$ is the rate of change of the size of the Universe with respect to its size, ρ and P are the density and pressure of the different components of the Universe.

Taking the time derivative of Eq. (1.3) and substituting in Eq. (1.4) yields the conservation, or fluid equation,

$$\dot{\rho} + 3\frac{\dot{a}}{a}\left(\rho + \frac{P}{c^2}\right) = 0. \tag{1.5}$$

Perfect fluids relevant to cosmology obey a simple equation of state, of the form,

$$P = w\rho c^2. \tag{1.6}$$

If the parameter w is time-independent, then substituting Eq. (1.6) into Eq. (1.5) yields,

$$\rho \propto a^{-3(1+w)}, \tag{1.7}$$

which describes the evolution of the density as a function of the scale factor a. This is particularly useful, because it allows us to use Eq. (1.3) solely to determine the evolution of the scale factor $a(t)$, given a specification of the amounts of energy density, ρ, in all the different species (matter and radiation), along with their equations of state, the amount of spatial curvature κ, and the cosmological constant Λ. It is common practice to further simplify Eq. (1.3) by considering the cosmological constant as an energy component with density $\rho_\Lambda = \Lambda c^2/8\pi G$, with an equation of state with $w = -1$, and treating the contribution of spatial curvature as a fictitious energy density as $\rho_\kappa = -3\kappa/8\pi G a^2$, with an equation of state with $w = -1/3$. The behaviour of all the different components of the energy density, plus curvature, are then summarised in Table 1.1.

Table 1.1.: Behaviour of the different species of energy density and curvature in a homogeneous and isotropic universe, described by Eq. (1.7).

Component	w	$\rho \propto$
Matter	0	a^{-3}
Radiation	1/3	a^{-4}
Curvature	-1/3	a^{-2}
Vaccum	-1	a^{0}

Using the energy densities of all the different components at the present time, we can then write Eq. (1.3) as

$$H^2(t) = \frac{8\pi G}{3}\left[\rho_{r,0}\left(\frac{a_0}{a}\right)^4 + \rho_{m,0}\left(\frac{a_0}{a}\right)^3 + \rho_{k,0}\left(\frac{a_0}{a}\right)^2 + \rho_{\Lambda,0}\right], \tag{1.8}$$

where the subscript '0' denotes values at the present time, ρ_r, ρ_m and ρ_Λ, are the energy densities of the radiation, non-relativistic matter, and the cosmological constant components respectively, and ρ_k is the fictitious energy density of the spatial curvature.

The universe at a particular epoch tends to be dominated by one component on the right hand side of Eq. (1.8). In that case, the Friedmann equation can be summarised as,

$$\left(\frac{\dot{a}}{a}\right)^2 \propto a^{-3(1+w)}, \tag{1.9}$$

which can be easily solved for each component in Table 1.1,

$$a \propto \begin{cases} e^{\rho_{\Lambda,0}t} = e^{\sqrt{\frac{\Lambda c^2}{8\pi G}}t} & \text{for } \Lambda\text{-dominated,} \\ t & \text{for curvature-dominated,} \\ t^{2/3} & \text{for matter-dominated,} \\ t^{1/2} & \text{for radiation-dominated.} \end{cases} \tag{1.10}$$

It is immediately evident that for all solutions, except for $w = -1$ (i.e. a Λ-dominated model), $a(t) \to 0$ at some finite time, which we define as $t = 0$. That is a remarkable result, because any universe containing just radiation or matter predicts a Hot Big Bang where $\rho(t) \to \infty$ at $t = 0$. Of course, our Universe contains a combination of all the different energy density species. It is a common practice to define a special value of the density that would be required to produce a flat universe, i.e. $\kappa = 0$, and hence $\rho_\kappa = 0$. This is known as the critical density,

$$\rho_{\text{crit}} = \frac{3H^2(t)}{8\pi G}. \tag{1.11}$$

Then, Eq. (1.8) can be written as,

$$\left(\frac{\dot{a}}{a}\right)^2 = H_0\left[\Omega_{r,0}a^{-4} + \Omega_{m,0}a^{-3} + \Omega_{k,0}a^{-2} + \Omega_{\Lambda,0}\right], \tag{1.12}$$

where we have introduced the density parameter $\Omega_{i,0} = \rho_{i,0}/\rho_{\mathrm{crit},0}$. A large amount of current work in cosmology is focussed upon determining these values. Once the contribution of all the different components of the universe are known, it allows for a full description of is evolution.

1.2 The ΛCDM universe

In a Hot Big Bang cosmology, the Universe was smaller, much denser, and hotter in the past. Under these conditions, the mean free path of photons would have been short enough to ensure thermal equilibrium, radiation would immediately ionise any hydrogen atoms that formed from free protons and electrons. The Universe was then filled with a plasma of protons, electrons and photons. As the Universe expanded it cooled down; photons lost enough energy to allow electrons and protons to bind together for the first time and form hydrogen atoms. This epoch, known as recombination, occurred about 380,000 years after the Big Bang. The Universe became transparent, letting the photons from this decoupling of radiation from baryonic matter to travel freely through space, transporting the imprints of this primordial state. This 'afterglow of the Big Bang' propagated freely since then, shifting in energy as its wavelength was stretched by the expansion of the Universe. In 1965, while working on a huge horn reflector antenna, Arno Penzias and Robert Wilson detected, for the first time, a black body radiation with a temperature ~3K (Penzias & Wilson, 1965). Now shifted to microwave frequencies, the cosmic microwave background (CMB) radiation confirmed the Big Bang theory as the underlying cosmological paradigm.

As the CMB was produced following a state of thermal equilibrium with baryonic matter, the measurement of tiny temperature fluctuations (of the order of $\Delta T/T \sim 10^{-5}$) in the CMB sky, reflect the variations in the matter density field at the time of decoupling. Furthermore, before decoupling, the pressure in the photon-baryon primordial plasma competed with the gravitational forces, creating spherical sound waves in the CMB anisotropies, leaving critical information about the density of baryons at the time of recombination and the amount of dark matter. These sound waves are known as baryon acoustic oscillations (BAOs). Indeed, measurements of the angular power spectrum of the CMB temperature anisotropies provide the strongest constraints on the Hot Big Bang and the ΛCDM model. Detailed CMB experiments have measured the temperature fluctuations in the CMB with increasing

Table 1.2.: The cosmological parameters inferred by the Planck Collaboration et al. (2016). Ω_m, Ω_Λ, Ω_b are the average densities of matter, dark energy, and baryonic matter in units of the critical density at redshift zero; H_0 is the Hubble constant, σ_8 is the square root of the linear variance of the matter distribution smoothed with a top-hat filter of radius 8 h^{-1} cMpc, n_s is the scalar power-law index of the power spectrum of primordial adiabatic perturbations

Cosmological Parameter	Value	Uncertainty
Ω_m	0.3089	$\pm$ 0.0062
Ω_Λ	0.6911	$\pm$ 0.0062
Ω_b	0.0485	$\pm$ 0.0009
$h \equiv H_0/(100\,\mathrm{km\,s^{-1}\,Mpc^{-1}})$	0.6774	$\pm$ 0.0046
σ_8	0.8159	$\pm$ 0.0086
n_s	0.9667	$\pm$ 0.0040

fidelity (Smoot et al., 1992; Komatsu et al., 2011; Planck Collaboration et al., 2016), estimating the cosmological parameters with unprecedented precision.

The current best constraints on the ΛCDM parameters come from the Planck space observatory (Planck Collaboration et al., 2016), which combine the CMB temperature anisotropies and polarisation, with other observational measurements (e.g. gravitational lensing data, supernovae type Ia luminosities, and BAO signatures in the clustering of galaxies). Table 1.2 lists the values of the cosmological parameters together with their exquisite uncertainties. The picture that has emerged from these experiments is that our Universe is spatially flat ($\kappa = 0$), $\sim 70\%$ of its energy density content at the present time is dark energy, in a form compatible with a cosmological constant, and $\sim 30\%$ is matter, out of which only $\sim 5\%$ is in the form of 'ordinary' baryonic matter, and the rest $\sim 25\%$ is dark matter.

1.2.1 Dark Energy

The discovery of the accelerating expansion of the Universe was a breakthrough achievement for modern cosmology (Riess et al., 1998; Perlmutter et al., 1999). Further observational evidence of the accelerated expansion comes from the evolution of the BAOs, comparing the sound horizon at the time of recombination and the sound horizon today. Measurements of the BAO peak using the clustering of galaxies confirmed both the photon-baryon primordial plasma model, and the late time acceleration due to dark energy (Cole et al., 2005; Eisenstein et al., 2005). Our standard cosmological model, ΛCDM, passed a rigorous theoretical and observational test with flying colours.

However, the nature of dark energy is still unknown. The simplest theoretical description of dark energy is Einstein's cosmological constant Λ, originally proposed to produce a static Universe within the framework of GR. At present, all cosmological observations are consistent with a cosmological constant, or a form of energy whose density remains constant as the Universe expands. One such form of energy is vacuum energy: the energy of a quantum field in its ground state (zero particles). Nevertheless, the model raises a number of fundamental problems. Predictions from quantum field theory for the vacuum energy density overestimate the observed value of Λ by many orders of magnitude (for a review see Weinberg, 1989; Carroll, 2001). In addition, the energy density of matter and the cosmological constant are within a factor of a two of each other at the present time, making our epoch unusual in the evolution of the Universe. This is known as the coincidence problem. These problems have motivated the search for alternative models of dark energy and modifications of gravity that might explain the acceleration of the universe more naturally. In many models, however, fine tuning of the model parameters is still required to explain their observed similarity (see for example Weinberg, 2000).

1.2.2 Dark Matter

The main motivation for the existence of cosmological dark matter is based on the need for a dominant, non-baryonic dark mass component, to reconcile the structure and dynamics of the observed luminous components in the Universe (i.e. stars and gas), with the gravitational forces inferred both on galactic, and cosmic, scales. The idea of a dark matter component trace back to the 1930s, when it was proposed as a means to explain the gravitational dynamics of stars within the Milky Way, and galaxies within galaxy clusters (Oort, 1932; Zwicky, 1933). This idea was later supported by observational measurements of flat rotational velocity profiles of stars in the outskirts of spiral galaxies, implying a mass profile linearly increasing with radius, far more extended than the stellar distribution (Babcock, 1939; Rubin & Ford, 1970). Further evidence of a 'missing mass' comes independently from analysing the distortion of the images of background galaxies around massive clusters in the foreground, via gravitational lensing. Measurements of the mass distribution of these clusters, enough to cause such lensed distortions, exceed the mass inferred from the baryonic distribution alone (e.g. Tyson et al., 1990).

The study of gravitationally collapsed structures provides another cosmological probe of the dark matter paradigm. Within a ΛCDM cosmology, the linear growth

of density perturbations is theoretically well understood. If one calculates the growth of density perturbations inferred from CMB experiments, one would expect very few collapsed structures at the present day. However, our Universe is filled with gravitationally collapsed structure, as the beautiful galaxy we live in. This discrepancy can be reconciled with the existence of a non-baryonic matter, which is not coupled to the photon-baryon primordial plasma. Hence, its density fluctuations can grow independently, and can be much larger at the time of decoupling. Furthermore, a Universe which is dominated by the leading theoretical model of dark matter, i.e. CDM, predicts the formation of large scale structure which is in striking agreement with the observed distribution of galaxies (e.g. Davis et al., 1985; Springel et al., 2006), including the detections of the BAO peak in the clustering of galaxies (Cole et al., 2005; Eisenstein et al., 2005).

It is usually assumed that dark matter is a fundamental particle that interacts only gravitationally with other particles. A large number of theoretical models have been put forward as candidates over the years. In particular, the mass of the proposed hypothetical particle, has important implications for formation of structure in the Universe. Although the dark matter particle remains currently undetected, numerical experiments suggest that it should be 'cold', i.e. it has a negligible thermal velocity at decoupling (e.g. Davis et al., 1985). The CDM model has been rigorously tested over past two decades, and it is now widely accepted as the standard model of cosmology.

1.3 The formation of galaxies in a ΛCDM Universe

The formation of galaxies is thought to be seeded by the tiny density fluctuations in the early Universe. Under the effect of gravitational forces, these primordial density perturbations grew in time, eventually becoming massive enough to overcome the expansion of the Universe, undergoing gravitational collapse to form a dark matter halo. Following the seminal work of White & Rees (1978), it is now widely accepted that galaxies form at the centre of these dark matter haloes.

Gas is subject to the same gravitational forces as the dark matter, tracing roughly the same structure formation. However, contrary to the dark matter, during gravitational collapse, the gas experience strong shocks and thermalises its kinetic infall energy.

The thermal pressure then prevents further gravitational collapse, and the gas reaches a hydrostatic equilibrium. Depending on the temperature, density and composition of the gas, a variety of cooling processes can take place, allowing the gas to further condense into the halo potential well. Eventually, self-gravity may dominate over the gravity of the dark matter halo, and the gas undergoes fragmentation and catastrophic collapse, leading to the formation of stars.

The physics of star formation are complex and are still not well understood. Nonetheless, strong empirical relationships between gas measurements and star formation rates have been observed, shedding some light into the nature of the formation of stars. For example, Kennicutt (1998) estimated that the surface density of star formation follows a power law relation with gas surface density. Furthermore, a fraction of the newly formed stars will explode in the form of supernovae, releasing large amounts of thermal energy into the interstellar medium (ISM). Together with photoionisation and stellar winds, this form of *stellar feedback* is thought to prevent further star formation in low mass galaxies (e.g. Dekel & Silk, 1986; White & Frenk, 1991; Benson et al., 2003). On the other hand, at higher galaxy masses, it is speculated that star formation is suppressed by feedback from accreting supermassive black holes (SMBHs, e.g. Bower et al., 2006; Croton et al., 2006). Indeed, observations of a tight correlation between the mass of a galaxy's central SMBH and key properties of its galactic host, such as the bulge mass and stellar velocity dispersion (e.g. Magorrian et al. 1998; Gebhardt et al. 2000), have led to the idea that SMBHs play a major role in the evolution of their host galaxies (e.g. Fabian 2012; Kormendy & Ho 2013; Heckman & Best 2014).

The understanding of all these processes and their complex interactions in a cosmological context is crucial to develop a comprehensive theory of galaxy formation.

1.4 The role of simulations

The formation and evolution of galaxies within dark matter haloes is thought to be a highly self-regulated process, in which galaxies tend to evolve towards a quasi-equilibrium state where the gas outflow rate balances the difference between the gas inflow rate and the rate at which gas is locked up in stars and black holes (e.g. White & Frenk, 1991; Finlator & Davé, 2008; Schaye et al., 2010; Davé et al., 2012).

Consequently, the physics of galaxy formation can be divided in two parts:

1. The formation and growth of dark matter haloes, which depends solely on the cosmological background.

2. Star formation and the regulation of the gas content in these haloes, that depends on complex baryonic processes such as radiative cooling, stellar mass loss, and feedback from stars and accreting SMBHs.

These processes happen on timescales that differ by several orders of magnitude, but are coupled together through the accretion rate of gas onto gravitationally bound haloes. This co-evolution process results in a tight correlation between the properties of galaxies and their dark matter haloes (see Wechsler & Tinker 2018 for a review).

In the following section, we summarise the different techniques that have been developed to solve the 'two parts' of the physics of galaxy formation.

1.5 Part 1: The formation and growth of dark matter haloes

Elegant analytical methods have been used to study the growth of primordial density fluctuations. In the linear regime (i.e. before gravitational collapse), we can calculate the evolution of the initial density field using linear perturbation theory. This problem is theoretically well understood. However, in the non-linear regime, the evolution of the density field becomes significantly more complicated, and perturbation theory is no longer valid. In this regime, no analytic solutions exist, and accurate modelling of the non-linear growth can only be achieved by numerical simulation.

1.5.1 Linear perturbation theory

Dark matter structures are assumed to have grown from small initial density perturbations. It is useful then to express the density, ρ, in terms of the density perturbation contrast against a density background,

$$\rho(\mathbf{x}, t) = \bar{\rho}(t)[1 + \delta(\mathbf{x}, t)]. \tag{1.13}$$

Modelling the evolution of the density as an ideal fluid, the relevant equations are: the continuity equation (conservation of mass), the Euler equation (momentum equation), and the Poisson equation (local density and gravitational field). In comoving coordinates, these equations are,

$$\text{Continuity:} \quad \frac{\partial \delta}{\partial t} + \frac{1}{a}\boldsymbol{\nabla} \cdot \left[(1+\delta)\mathbf{v}\right] = 0, \tag{1.14}$$

$$\text{Euler:} \quad \frac{\partial \mathbf{v}}{\partial t} + \frac{\dot{a}}{a}\mathbf{v} + \frac{1}{a}(\mathbf{v}\cdot\boldsymbol{\nabla})\mathbf{v} = -\frac{\boldsymbol{\nabla}\Phi}{a} - \frac{\boldsymbol{\nabla} P}{a\bar{\rho}(1+\delta)}, \tag{1.15}$$

$$\text{Poisson:} \quad \nabla^2\Phi = 4\pi\bar{\rho}a^2\delta, \tag{1.16}$$

where the differential operator $\boldsymbol{\nabla}$ is with respect to the comoving coordinates, $\partial/\partial t$ is at fixed comoving coordinates, Φ is the gravitational potential and $\mathbf{v}$ is the peculiar velocity describing the motion a fluid element relative to an observer comoving with the cosmological expansion. These equations can be further simplified by assuming that δ and $\mathbf{v}$ are small, so that we can drop second order terms.

For a pressureless fluid, such as e.g. dark matter, $P = 0$. Then, taking the divergence of the Euler equation, the time derivative of the continuity equation and substituting the gravitational potential using Poisson's equation, the differential equation that governs the time dependence of the growth of linear perturbations of the dark matter density field in a cosmological background can be written as,

$$\frac{\mathrm{d}^2\delta}{\mathrm{d}t^2} + 2\frac{\dot{a}}{a}\frac{\mathrm{d}\delta}{\mathrm{d}t} - 4\pi G\bar{\rho}\delta = 0. \tag{1.17}$$

An explicit solution for the growing mode of Eq. (1.17) was found by Heath (1977),

$$\delta(t) = D(t)\delta(t_0), \tag{1.18}$$

where $D(t)$ is the linear growth factor, which determines the normalisation of the linear matter power spectrum relative to the initial density perturbation power spectrum, and is computed by the integral,

$$D(t) \propto \frac{\dot{a}}{a}\int_0^t \frac{\mathrm{d}t'}{\dot{a}^2(t')}. \tag{1.19}$$

For a matter-dominated universe, an analytic expression of the linear growth factor can be found, which yields, $D(t) \propto t^{2/3} \propto a(t)$. For more 'complicated' cosmological models, the growing mode can be obtained from Eq. (1.19) numerically. In

Chapter 3 we will introduce a useful new approach to solve the Friedman equations that will allow us to formulate an analytic model for the growth of structure in the universe.

1.5.2 Non-linear growth

Analytical approximations using highly idealised models have been put forward to gain insight into the non-linear evolution of density perturbations. In particular, using a simple spherically symmetric model to describe the growth and collapse of a perturbation in a Gaussian random field, Press & Schechter (1974), developed a very useful formalism that allows us to estimate the mass function of collapsed objects. In the Press & Schechter theory, the co-moving abundance of haloes of mass M_h at time t is given by,

$$\frac{dn(M_h,t)}{dM_h} = \sqrt{\frac{2}{\pi}}\frac{\bar{\rho}}{M_h^2}\frac{\delta_c/D(t)}{S^{1/2}}\exp\left(-\frac{\left(\delta_c/D(t)\right)^2}{2S}\right)\left|\frac{\mathrm{d}\ln S^{1/2}}{\mathrm{d}\ln M_h}\right| \tag{1.20}$$

where $S = \sigma^2(M_h)$ is the variance of the density field on the length scale corresponding to the halo mass. According to the spherical collapse model, regions with $\delta(\mathbf{x},t) > \delta_c = 1.686$, will have collapsed to produce dark matter haloes by time t.

1.5.3 Dark Matter only simulations

The development of efficient numerical simulations have been pivotal in advancing our knowledge of structure formation in the Universe. The basic principle of numerical methods is to simulate a representative region of the Universe using N discrete point particles to sample the matter density field. Given a set of initial conditions (particle positions and velocities), the evolution of the particles is tracked by integrating their trajectories according to Newton's equations of motion, embedded within a cosmological background.

Dark matter only (DMO) simulations are a subset of N-body simulations where only gravitational forces are considered, so the particles are collisionless. This type of simulations has played a crucial role in establishing the cold dark matter paradigm (e.g. Davis et al., 1985; Frenk et al., 1988).

At present, the formation and evolution of dark matter haloes is considered, for the most part, a "solved problem" (see however, van den Bosch et al. 2018). Using extremely accurate measurements of the temperature anisotropies of the CMB as initial conditions (e.g. Planck Collaboration et al., 2016), many different groups have produced convergent results using large cosmological N-body simulations (e.g Springel et al., 2005b; Klypin et al., 2011; Trujillo-Gomez et al., 2011; Angulo et al., 2012; Fosalba et al., 2015).

1.6 Part 2: Star formation and the regulation of gas within dark matter haloes

Different approaches have been used to model the more complex baryonic physics of galaxy formation. The most widely used technique combines the evolution of dark matter with either a *semi-analytical* or *hydrodynamical* treatment of the baryonic processes involved. A key ingredient in both methods that has led us to a better understating of the physics of galaxy formation is the use of physically motivated models for feedback processes (see Somerville & Davé 2015; Naab & Ostriker 2017 for a comprehensive review).

1.6.1 Semi-analytical Models

Semi-analytic models (SAMs) follow the properties of haloes in the merger tree from DMO simulations (which encapsulates the merging and accretion history of the dark matter structures), and populates them with galaxies by solving a set of coupled differential equations (e.g. Cole et al., 1994; Somerville et al., 2008; Henriques et al., 2015; Lacey et al., 2016). The equations used to model the complex physical processes of galaxy formation in SAMs are motivated by empirical or theoretical considerations. These equations provide the prescription for the cooling of gas in haloes, star and black hole formation, feedback from star formation and active galactic nuclei (AGN), metal enrichment, etc. SAMs are typically characterised by a number of free parameters that can be constrained by comparing the model predictions with statistical properties of the galaxy population, such as the galaxy stellar mass function.

A great advantage of SAMs over hydrodynamical simulations is that they are computationally relatively inexpensive to run. Hence, SAMs can be applied to large cosmological volumes. This also makes them ideal for rapid parameter space exploration, allowing very good fits to observational datasets. On the other hand, some of the disadvantages of SAMs include that they cannot trace the flow of gas in and out of galaxies, they cannot predict the back reaction of baryons on the dark matter, and they do not include any spatial information about the gas distribution.

1.6.2 Hydrodynamical simulations

Hydrodynamical simulations attempt to simulate both the dark matter and the baryons together (e.g. Schaye et al., 2015; Davé et al., 2016; Dubois et al., 2016; Pillepich et al., 2018). This represents a much more demanding problem in terms of computational resources. The principle of hydrodynamic simulations is to take the initial conditions for a given cosmology, e.g. ΛCDM, and split the particles into two types of particles, gas and dark matter, according to the universal baryon fraction, i.e. $\bar{\rho}_{\rm baryon}(t)/\bar{\rho}_{\rm DM}(t)$. The evolution of the fluid is then tracked using Eqs. (1.14) to (1.16), given an equation of state for the gas elements.

In the context of numerical simulations, there exist two physically equivalent formalisms to solve the equations of hydrodynamics; *Lagrangian* simulations, which follow the properties of particles (discretising mass), and *Eulerian* simulations, which track fluid properties within static grid cells (discretising space). Often one is more powerful than the other for a particular application. For example, in Lagrangian simulations, such as *smoothed particle hydrodynamics* (SPH, Gingold & Monaghan 1977; Lucy 1977) the spatial resolution is naturally highest in high density regions, coinciding with structures of primary interest such as galaxies. Modern Eulerian simulations, such as *adaptive mesh refinement* codes (AMR Berger & Colella 1989), increase the spatial resolution in regions of particular interest by progressively refining grid cells, and are in general better at resolving fluid mixing, shocks and fluid instabilities than Lagrangian codes.

Many important physical processes in galaxy formation occur on scales too small to be resolved directly within large cosmologically representative volumes. In this regime, hydrodynamical simulations implement *subgrid physics models* to approximate the relevant processes that cannot be simulated directly (e.g. Crain et al., 2015; Pillepich et al., 2018). Very high-resolution simulations try and bridge

the gap between unresolved and resolved scales in cosmological scale simulations (e.g. Hopkins et al., 2011, 2014; Creasey et al., 2013, 2015).

While subgrid models resemble the expressions used in SAMs, in hydrodynamical simulations, local properties of baryonic particles can be used in the subgrid equations. Similar to SAMs, some of the subgrid physics prescriptions can be constrained using observations, for example the empirical Kennicutt-Schmidt law (Kennicutt, 1998). However, processes that are poorly understood, such as stellar and AGN feedback, need to be calibrated to match statistical properties of the galaxy population.

1.7 Thesis Structure

The primary aim of the work presented in this thesis is to test and understand the impact of the cosmological background on galaxy formation. We take the advantage of state of the art cosmological hydrodynamical simulations from the EAGLE suite to vary the cosmological parameters, in particular the cosmological constant, to test its effect on the efficiency of star formation, and draw conclusions about its observed value, and the physics driving galaxy formation.

The remainder of this thesis is organised as follows. In Chapter 2, we introduce the EAGLE simulation suite and the subgrid models used in the simulations. Using a modified version of the EAGLE simulations, in Chapter 3 we investigate the effect of the accelerated expansion of the Universe on the cosmic star formation rate. We study these effects beyond the present day by allowing the simulations to run forward into the future ($t > 13.8$ Gyr). We also develop a simple analytic model for the cosmic star formation rate that captures the suppression due to a cosmological constant. In Chapter 4, we predict the observed value of the cosmological constant, given a measure of the multiverse. In Chapter 5, we develop an analytic model of galaxy formation that connects the growth of dark matter haloes in a cosmological background, with the build up of stellar mass within these haloes. Because in Chapter 3 and Chapter 5 we show that feedback from accreting supermassive black holes has a dramatic impact in the efficiency of star formation in massive galaxies, in Chapter 6, we take a 'slight' detour to estimate the expected event rate of gravitational wave signals from mergers of supermassive black holes that could be resolved by a future gravitational wave detectors. We show that this can provide

a profound insight into the origin of supermassive black holes and the initial mass distribution of black hole seeds. Finally, in Chapter 7, we summarise the results of this thesis and present ideas for future research work.

The EAGLE simulation suite

2

> *But... EAGLE is the real Universe!*
>
> **— Richard Bower**

In this thesis, we make extensive use of the "Evolution and Assembly of GaLaxies and their Environment" (EAGLE) suite of cosmological simulations. These simulations consists of a large number of cosmological hydrodynamical simulations that follow the formation and evolution of cosmic structure and galaxies in cosmologically representative cubic volumes. Full details of the EAGLE simulations can be found in Schaye et al. (2015); Crain et al. (2015); here we provide only a brief review of the aspects of EAGLE most relevant to the studies presented in this thesis.

2.1 The EAGLE code

The EAGLE simulation consists of a large number of cosmological hydrodynamical simulations that include different resolutions, simulated volumes and physical models. These simulations use advanced SPH and state-of-the-art subgrid models to capture the unresolved physics. The EAGLE code contains three primary components: a gravity solver, a hydrodynamics solver, and subgrid physics modules.

2.1.1 Gravity solver

The EAGLE code uses a modified version of the GADGET-3 SPH code (last described by Springel 2005). The gravitational forces acting on each particle are calculated using a Tree-PM method, that combines tree-based and mesh-based methods (Bode et al., 2000; Bagla, 2002). Long range forces and periodic forces are obtained by mapping the density field onto a regular mesh and solving Poisson's Eq. (1.16) in Fourier space. The short range interactions are computed using an octree, where the volume is recursively subdivided into a hierarchy of cells. Cells that are close enough will allow their particles to interact directly using a direct summation algorithm, whilst

distant cells are calculated using multipole moments of the density field in the cells.

2.1.2 Hydrodynamics solver

While dark matter particles interact only gravitationally, i.e. they are collisionless, cosmic gas is described as a collisional ideal fluid. The evolution of the fluid is then described by Eqs. (1.14) to (1.16), together with an equation of state for the gas that relates the pressure, density and internal energy, u. The equation of state, typically $P = \rho(\gamma - 1)u$, where the adiabatic index is $\gamma = 5/3$ for a monatomic gas.

Using an SPH technique (Gingold & Monaghan, 1977; Lucy, 1977), the fluid is discretised into point mass particles, which transport the properties of the fluid. Continuous fluid properties, such as the density or pressure, are computed by interpolating the particle properties over a finite neighbourhood using a kernel function that depends solely on the separation of the particles and a smoothing length.

The EAGLE code uses a set of modifications to the SPH method, collectively referred to as ANARCHY (Dalla Vecchia et al. in preparation), which make use of the pressure-entropy formulation of SPH derived by Hopkins (2013), the artificial viscosity switch from Cullen & Dehnen (2010), an artificial conduction switch similar to that of Price (2008), the C_2 kernel of Wendland (1995), and the time-step limiters of Durier & Dalla Vecchia (2012). The effects of this state-of-the-art formulation of SPH on the galaxy properties are explored in detail by Schaller et al. (2015b).

2.1.3 Initial conditions

The initial conditions for the EAGLE simulations were created in three steps. First, a particle load, representing an unperturbed homogeneous periodic universe was produced. Secondly, a realisation of a Gaussian random density field with the appropriate linear power spectrum was created over the periodic volume. Thirdly, the displacements and velocities, consistent with the pure growing mode of gravitational instability, were calculated from the Gaussian realisation and applied to the particle load producing the initial conditions. The initial density perturbation power spectrum is commonly assumed to be a power-law, i.e. $P_i(k) \propto k^{n_s}$. From

the Planck results (Planck Collaboration et al., 2014), the spectral index n_s, has a value of $n_s = 0.9611$. A transfer function with the cosmological parameters shown in Table 1.2 was generated using CAMB (version Jan_12; Lewis et al. 2000). The linear matter power spectrum was generated by multiplying the initial power spectrum by the square of the dark matter transfer function evaluated at the present day $t = t_0$, i.e. $P(k, t) = P_i(k)T^2(k)D^2(t)$.[1]

2.1.4 Subgrid models

Processes that are not resolved by the simulations are implemented as subgrid physical models; they depend solely on local interstellar medium (ISM) properties. A full description of these subgrid models can be found in Schaye et al. (2015). In summary:

1. Radiative cooling and photoheating are implemented element-by-element as in Wiersma et al. (2009a), including the 11 elements found to be important, namely, H, He, C, N, O, Ne, Mg, Si, S, Ca, and Fe. Hydrogen reionization is implemented by switching on the full Haardt & Madau (2001) background at redshift $z = 11.5$.

2. Star formation is implemented stochastically following the pressure-dependent Kennicutt-Schmidt relation as in Schaye & Dalla Vecchia (2008). Above a metallicity-dependent density threshold $n_{\rm H}^*(Z)$,

$$n_{\rm H}^*(Z) = 0.1{\rm cm}^{-3}\left(\frac{Z}{0.002}\right)^{0.64} \tag{2.1}$$

   where Z is the gas metallicity (i.e. the fraction of the gas mass in elements heavier than helium). This threshold is designed to track the transition from a warm atomic to an unresolved, cold molecular gas phase (Schaye, 2004). The star formation rate is then computed by,

$$\dot{m}_* = m_{\rm g} A\left(1\,{\rm M}_\odot{\rm pc}^{-2}\right)^{-n}\left(\frac{\gamma}{G} f_{\rm g} P\right)^{(n-1)/2}, \tag{2.2}$$

   where $m_{\rm g}$ is the mass of the gas particle, $\gamma = 5/3$, $f_{\rm g}$ is the mass fraction in gas (assumed to be unity), and P is the pressure. The coefficients $A =$

[1] The CAMB input parameter file and the linear power spectrum are available at http://eagle.strw.leidenuniv.nl/

$1.515 \times 10^{-4} \mathrm{M}_{\odot} \mathrm{yr}^{-1} \mathrm{kpc}^{-2}$ and $n = 1.4$ are taken directly from observations assuming a Chabrier (2003) initial mass function (IMF). Gas particles have a probability of forming stars on a given time step determined by their pressure $\min\left(\dot{m}_{*} \Delta t / m_{\mathrm{g}}, 1\right)$. Furthermore, because the simulations cannot resolve the cold phase of the ISM (i.e. $T < 10^{4}\mathrm{K}$), in order to prevent fragmentation of gas and capture the unresolved turbulence, an effective equation of state is imposed, $P_{\mathrm{EOS}} \propto \rho_{\mathrm{g}}^{4/3}$ for gas with $\rho_{\mathrm{g}} > 0.1 \mathrm{cm}^{-3}$ and normalised to a temperature $T_{\mathrm{EOS}} = 8000\mathrm{K}$ at the density threshold.

3. Time-dependent stellar mass loss due to winds from massive stars and AGB stars, core collapse supernovae and type Ia supernovae, is tracked following Wiersma et al. (2009b).

4. When stellar particles more massive than $6\mathrm{M}_{\odot}$ reach an age of $3 \times 10^{7}\mathrm{yr}$, they will explode as type II supernovae, releasing $\approx 10^{51}\mathrm{erg}$ per supernova. Stellar feedback is treated stochastically, using the thermal injection method described in Dalla Vecchia & Schaye (2012). The gas surrounding the stellar particles is heated to a temperature ΔT. While the choice of ΔT allows to suppress numerical losses, the physical efficiency of feedback can be controlled by injecting more or less energy per feedback event, which is achieved by multiplying the energy per supernova by a factor of $f_{\mathrm{th}}(Z, n_{\mathrm{H}})$, which depends on the density and metallicity of the gas surrounding the stellar particle. This parameter is then calibrated to reproduce a set of observational constraints (Crain et al., 2015).

5. SMBH seeds of mass $\mathrm{M} = 1.48 \times 10^{5}\mathrm{M}_{\odot}$, are placed in haloes with a mass greater than $1.48 \times 10^{10}\mathrm{M}_{\odot}$ and tracked following the methodology of Springel et al. (2005a); Booth & Schaye (2009). Accretion onto SMBHs follows a modified version of the Bondi-Hoyle accretion rate which takes into account the circularisation and subsequent viscous transport of infalling material, limited by the Eddington rate as described by Rosas-Guevara et al. (2015)[2]. Additionally, BHs can grow by merging with other BHs as described in Schaye et al. (2015); Salcido et al. (2016).

6. Feedback from AGN is implemented following the stochastic heating scheme described by Schaye et al. (2015). Similar to the supernova feedback, a

[2]The EAGLE simulation do not include a boost factor for the accretion rate of BHs to account for an unresolved clumping factor.

fraction of the accreted gas onto the SMBH is released as thermal energy with a fixed heating temperature into the surrounding gas following Booth & Schaye (2009).

For the EAGLE simulations, the subgrid parameters were calibrated to reproduce three properties of galaxies at redshift $z = 0$: the galaxy stellar mass function, the galaxy size–stellar mass relation, and the black hole mass-stellar mass relation. The calibration strategy is described in detail by Crain et al. (2015), who also explores the effect of parameter variations.

2.2 Calibration philosophy and the predictive power of simulations

The recent success of galaxy formation models in matching observational data can, for the most part, be attributed to the implementation of more effective subgrid models for feedback processes. However, due to our lack of understanding of the physical processes that operate below the resolution limit, simulations such as EAGLE can only provide limited insight into the nature and source of these feedback processes. Current galaxy formation models cannot make *ab initio* predictions of galaxy properties such as stellar and black hole masses. Therefore, stellar and black hole feedback efficiencies in the simulations need to be calibrated to reproduce the correct observational properties.

The EAGLE simulations were calibrated on a small subset of the observational data, and validated on the rest. This provides confidence in the sense that EAGLE is not just a complicated fitting function. Hence, the simulations have predictive power on galaxy properties not included in the calibration strategy.

In particular, the EAGLE simulations were calibrated to reproduce the present-day galaxy stellar mass function, the amplitude of the galaxy-central black hole mass relation, and galaxy sizes. Other observables not considered in the calibration, such as the specific star formation rates of galaxies, passive fractions, the TullyFisher relation, galaxy colours, the column density distribution function of HI and the abundance of H_2, have been also found to be in good agreement with observations (Furlong et al., 2017; Furlong et al., 2015; Trayford et al., 2015; Lagos et al., 2015; Rahmati et al., 2015).

2.3 Summary

The EAGLE simulations comprise a set of state-of-the-art cosmological hydrodynamical simulation that use modern smoothed particle hydrodynamics and physically motivated subgrid models to capture the unresolved physics. These simulations have been shown to reproduce the observed galaxy population with unprecedented fidelity, providing a powerful tool to study galaxy formation and evolution.

Key observations, such as the present-day stellar mass function of galaxies, the dependence of galaxy sizes on stellar mass, and the amplitude of the central SMBH mass-stellar mass relation, as well as many other properties of observed galaxies and the intergalactic medium (both at the present day and at earlier epochs) are reproduced by the simulations (e.g. Furlong et al., 2017; Furlong et al., 2015; Trayford et al., 2015; Schaller et al., 2015a; Lagos et al., 2015; Rahmati et al., 2015, 2016; Bahé et al., 2016; Rosas-Guevara et al., 2016).

Is EAGLE the real Universe then? Despite the humorous assertion in the opening quote for this chapter, EAGLE is not the real Universe. There are known discrepancies between the simulation results and observational data. To mention some examples, the simulation slightly undershoots the "knee" of the galaxy stellar mass function ($\sim$ 0.2 dex underprediction of the observed number density). This translates to approximately 20% lower stellar mass density than inferred from observations (Schaye et al., 2015; Furlong et al., 2015). The evolution of the specific star formation rates broadly follows the trends seen in observational data, but with a normalisation offset of $0.2 - 0.5$ dex, depending on redshift (Schaye et al., 2015; Furlong et al., 2015). This, however, could be a calibration issue of the star formation indicators (see Driver et al., 2018). At redshift $z = 0$, the transition from active to passive galaxies occurs at slightly too high stellar masses (Schaye et al., 2015; Trayford et al., 2015). The present-day stellar mass-metallicity relation is flatter than the one inferred from observational data (Schaller et al., 2015c). This problem, however, seems to disappear at higher resolutions, suggesting it is an issue with the limited sampling of supernovae feedback events.

Since the EAGLE simulations reproduce a wide set of observational properties of the galaxy population, we may expect the physics of the real Universe to be reasonably well captured by the phenomenological sub-grid models implemented in the simu-

lations. In this thesis we will use this powerful tool to explore the interplay between cosmology and the formation of galaxies.

The continuous development of accurate and detailed theoretical predictions of models such as EAGLE, combined with the unprecedented amount of observational data available to us today, are the key to unravel the complex physics of galaxy formation.

3 The impact of dark energy on galaxy formation. What does the future of our Universe hold?

In this chapter we investigate the effect of the accelerated expansion of the Universe due to a cosmological constant, Λ, on the cosmic star formation rate. We utilise hydrodynamical simulations from the EAGLE suite, comparing a ΛCDM Universe to an Einstein-de Sitter model with $\Lambda = 0$. Despite the differences in the rate of growth of structure, we find that dark energy, at its observed value, has negligible impact on star formation in the Universe. We study these effects beyond the present day by allowing the simulations to run forward into the future ($t > 13.8$ Gyr). We show that the impact of Λ becomes significant only when the Universe has already produced most of its stellar mass, only decreasing the total co-moving density of stars ever formed by $\approx$15%. We develop a simple analytic model for the cosmic star formation rate that captures the suppression due to a cosmological constant. The main reason for the similarity between the models is that feedback from accreting black holes dramatically reduces the cosmic star formation at late times. Interestingly, simulations without feedback from accreting black holes predict an upturn in the cosmic star formation rate for $t > 15$ Gyr due to the rejuvenation of massive ($> 10^{11}$M$_\odot$) galaxies. We briefly discuss the implication of the weak dependence of the cosmic star formation on Λ in the context of the anthropic principle.

This chapter has been published as a paper in Monthly Notices of the Royal Astronomical Society (MNRAS):

- *The impact of Dark Energy on Galaxy Formation. What does the future of our Universe hold?*
  Salcido J., Bower, R. G., Barnes, L. A., Lewis, G. F., Elahi, P. J., Theuns, T., Schaller, M., Crain, R. A., Schaye, J., MNRAS 2018, Volume 477, Issue 3, Pages 3744-3759

3.1 Introduction

Precise observational data from the past two decades has allowed us to measure the cosmic history of star formation back to very early times ($z \approx 8$). The star formation rate (SFR) density of the Universe peaked approximately 3.5 Gyr after the Big Bang ($z \approx 2$), and declined exponentially thereafter (for a review see Madau & Dickinson, 2014).

Galaxy formation and evolution is a highly self-regulated process, in which galaxies tend to evolve towards a quasi-equilibrium state where the gas outflow rate balances the difference between the gas inflow rate and the rate at which gas is locked up in stars and black holes (BHs) (e.g. White & Frenk, 1991; Finlator & Davé, 2008; Schaye et al., 2010; Davé et al., 2012). Consequently, the cosmic SFR density is thought to be determined both by the formation and growth of dark matter haloes, and by the regulation of the gas content in these haloes. The former depends solely on cosmology, whereas the latter depends on baryonic processes such as radiative cooling, stellar mass loss, and feedback from stars and accreting black holes.

Which of these factors is most responsible for the decline in cosmic star formation? It could be driven by the 'freeze out' of the growth of large-scale structure, caused by the onset of accelerating cosmic expansion. As galaxies are driven away from each other by the repulsive force of dark energy, accretion and merging is slowed and galaxies are gradually starved of the raw fuel for star formation. Or, it could be caused primarily by the onset of efficient stellar and BH feedback.

The discovery of the accelerating expansion of the Universe was a breakthrough achievement for modern cosmology (Riess et al., 1998; Perlmutter et al., 1999). However, the driving force behind the acceleration (generically known as dark energy) is still unknown. At present, all cosmological observations are consistent with a cosmological constant, or a form of energy whose density remains constant as the Universe expands. One such form of energy is vacuum energy: the energy of a quantum field in its ground state (zero particles). The present best-fit cosmological model, known as the concordance model, or ΛCDM, includes both a cosmological constant Λ and Cold (i.e. non-relativistic) Dark Matter. This model has been very successful in matching the observational data.

Nevertheless, the model raises a number of fundamental problems. Predictions from quantum field theory for the vacuum energy density overestimate the observed value of Λ by many orders of magnitude (for a review see Weinberg, 1989; Carroll, 2001). In addition, the energy density of matter and the cosmological constant are within a factor of a few of each other at the present time, making our epoch unusual in the evolution of the Universe. This is known as the coincidence problem. These problems have motivated the search for alternative models of dark energy and modifications of gravity that might explain the acceleration of the universe more naturally. For example, quintessence models propose that the density of matter and dark energy track each other. In many models, however, fine tuning of the model parameters is still required to explain their observed similarity (see for example Weinberg, 2000).

An alternative approach is therefore to explain the observed value of Λ on anthropic grounds. This has already been applied very promisingly to the coincidence problem. Since the coincidence concerns the time that *we* observe the universe, the nature and evolution of observers in the Universe is highly relevant. For example Lineweaver & Egan (2007) argue that the production of planets in our Universe peaks when matter and dark energy are roughly coincident (see, however, Loeb et al., 2016).

For the cosmological constant and other fundamental parameters, anthropic reasoning requires a *multiverse*. Many models of inflation, such as eternal inflation, imply that the Universe as a whole is composed of a vast number of inflationary patches or sub-universes. Each sub-universe inherits a somewhat random set of physical constants and cosmic parameters from a wide range of possible values. Sub-universes in which the cosmological constant is large and positive will expand so rapidly that gravitational structures, such as galaxies, are unable to form (e.g. Weinberg, 1987; Martel et al., 1998; Efstathiou, 1995; Sudoh et al., 2017). Large negative values will cause the universe to collapse rapidly, also preventing the formation of galaxies. Only sufficiently small values of Λ will lead to the formation of universes that are able to host observers. This argument eliminates extreme values of Λ. For example, Weinberg (2000) estimates an upper bound on a positive vacuum energy density to allow for the formation of galaxies of about 200 times the present mass density.

Refining Weinberg's estimate requires us to more accurately explore the sensitivity of galaxy formation to the presence of Λ. Here, we use a suite of hydrodynamical simulations to take a first look at this problem by calculating the effect of the cosmological constant on galaxy and star formation in our Universe. Specifically,

we compare the formation of galaxies in our Universe with a hypothetical universe that is indistinguishable from ours at early times but has no cosmological constant. Because Λ is negligibly small in the early universe, these two universes will evolve in nearly identical ways for the first ≈ 2 Gyr of cosmic time (when the dark energy density is less than 0.03 times the matter density). This means that the epochs of nucleosynthesis, recombination[1], and reionization are indistinguishable.

In recent years, the accuracy of our understanding of galaxy formation has improved considerably, reaching the point at which it is possible to undertake this comparison meaningfully. The increased realism of simulated galaxies (in particular disc galaxies with more realistic sizes and masses) has been achieved due to the use of physically motivated subgrid models for feedback processes (e.g. Schaye et al., 2015; Dubois et al., 2016; Pillepich et al., 2018). One of the key ingredients that has allowed this progress is the inclusion of realistic models for the impact of feedback from the growth of super massive black holes (e.g. Bower et al., 2017). All successful models now demonstrate the need for active galactic nuclei (AGN) as an additional source of feedback that suppresses the formation of stars in high-mass haloes (e.g. Benson et al., 2003; Croton et al., 2006; Bower et al., 2006; Crain et al., 2015; Pillepich et al., 2018). One of the aims of the present chapter is to compare the impact of the cosmological constant with that resulting from the inclusion of black holes (BHs) in the simulation. In a previous study, van de Voort et al. (2011) found that by preventing gas from accreting onto the central galaxies in massive haloes, outflows driven by AGN play a crucial role in the decline of the cosmic SFR.

Different groups have used hydrodynamical simulations to study the effect of different dark energy or modified gravity models on cosmological, galactic and subgalactic scales (e.g. Puchwein et al., 2013; Penzo et al., 2014, 2016). Taking a different approach, in this chapter we investigate the effect of the accelerated expansion of the Universe on galaxy formation by asking the following question:

How different would the Universe be if there had been no dark energy?

For our study, we use a suite of large hydrodynamical simulations from the *Evolution and Assembly of GaLaxies and their Environment* (EAGLE) project (Schaye et al.,

[1]Of course, an observer in a $\Lambda = 0$ universe would measure a different angular power spectrum in the cosmic microwave background after 13.8 Gyr, because of the very different expansion history of the Universe at later times.

2015; Crain et al., 2015). Using state-of-the-art subgrid models for radiative cooling, star formation, stellar mass loss, and feedback from stars and accreting BHs, the simulations have reproduced many properties of the observed galaxy population and the intergalactic medium both at the present day and at earlier epochs (e.g. Furlong et al., 2017; Furlong et al., 2015; Trayford et al., 2015; Schaller et al., 2015a; Lagos et al., 2015; Rahmati et al., 2015, 2016; Bahé et al., 2016; Rosas-Guevara et al., 2016; Segers et al., 2016). Given that the physics of the real Universe is reasonably well captured by the phenomenological sub-grid models implemented in the simulations, with the use of appropriate assumptions, we can run the simulations beyond the present time, and explore the consequences of our models for the future. Furthermore, the simulation re-scaling strategy developed here, will be used in a companion paper (Barnes et al., 2018) considering a wider range of Λ values, and determining the likelihood distribution of possible Λ values conditioning the existence of observers.

The layout of this chapter is as follows: In Section 3.2, we develop a simple analytic model of the cosmic star formation rate that captures the suppression due to a cosmological constant. In Section 3.3, we briefly describe the simulations from which we derive our results and discuss our criteria for halo and galaxy definitions. In Section 3.3 we also describe our motivations to run our cosmological simulations into the future, and our assumptions in doing so. Section 3.4 provides a detailed discussion of our re-scaling strategy for the alternative cosmological models. In Section 3.5, we explore the dependence of the star formation history of the universe on the existence of a cosmological constant and the presence of BHs. We also explore their impact on other galaxy population properties, both up to the present time, and into the future. Finally, we summarise and discuss our results in Section 3.6.

3.2 A simple analytic model for the cosmic star formation rate density

3.2.1 Comparing different cosmological models

The star formation history of the Universe is determined by the interplay of cosmic expansion and the timescale at which cold gas can turn into stars. These processes

happen on timescales that differ by several orders of magnitude, but are coupled through the accretion rate of gas onto gravitationally bound haloes. The aim of our paper is to compare theoretical universes in which the star formation timescales are the same, but the cosmological timescales vary. We need, therefore, to be careful when comparing the different models, since the choice of coordinates that vary with cosmological parameters will obscure the similarities of the models. In particular, the expansion factor at the present day, a_0, is often treated as an arbitrary positive number, and it is common practice to set $a_0 = 1$. In this chapter, we need to take a different approach since we want to compare the properties of different universes at the same cosmic time (measured in seconds, or a multiple of key atomic transitions). Assuming a common inflationary origin, normalising out a_0 is not appropriate, since the expansion factor at the present day ($t_0 = 13.8$ Gyr), would be different for each universe.

We still need to define a scale on which to measure the size of the universes we consider. Using a hat notation ($\hat{}$) to denote quantities in our observable Universe, we set $\hat{a}_0 \equiv \hat{a}(t_0) = 1$. We want to emphasise that the cosmological models that we consider all start from very similar initial conditions. It therefore makes sense to normalise them to the same value of the expansion factor at an early time, t_1. We therefore set $a_1 \equiv a(t_1) = \hat{a}(t_1)$. We choose $\hat{a}_1 = 1/(1 + 127)$, corresponding to a redshift of $\hat{z} = 127$ for a present-day observer in our Universe[2]. At this moment, the age of the universe is $t_1 = 11.98$ Myr. This applies to all of the universes we consider since the cosmological constant term has negligible impact on the expansion rate at such early times.

Although time (in seconds) is the fundamental coordinate that we use to compare universes, it is sometimes useful, for example when comparing to observational data, to express time in terms of the redshifts measured by a present-day observer in our Universe, $\hat{z}$. We convert between cosmic time t (which is equivalent between universes) and $\hat{a}$ by inverting the time-redshift relation for our Universe:

$$\hat{z} = \frac{\hat{a}_0}{\hat{a}(t)} - 1 \tag{3.1}$$

It is important to note that $\hat{z}$ is not the redshift that would be measured by an observer in an alternative universe.

[2] $\hat{z} = 127$ was the reference simulation's starting redshift.

In this chapter, we will focus our comparison on two cosmological models, a standard ΛCDM universe as inferred by the Planck Collaboration et al. (2014), and an an Einstein deSitter (EdS) universe. Assuming both cosmological models have a common inflationary origin, the models can be normalised as follows:

1. For the ΛCDM model (see Table 3.1) we set $\hat{a}_0 = \hat{a}(t_0) = 1$, where $t_0 = 13.82$ Gyr is the present-day age of the universe. At time $t_1 = 11.98$ Myr, $\hat{a}_1 = \hat{a}(t_1) = 0.007813$. At this time, the expansion rate, as measured by the Hubble parameter is, $\hat{H}_1 = \hat{H}(t_1) = 54,377$ km/s/Mpc $= 55.6\,\mathrm{Gyr}^{-1}$.

2. We require the EdS model to have the same early expansion history, i.e., $a(t_1) = 0.007813$ and $H(t_1) = 55.6\,\mathrm{Gyr}^{-1}$. In this universe, at the present day (i.e. $t = t_0 = 13.82$ Gyr) the universe has a size, $a_0 = a(t_0) = 0.8589$ and an expansion rate, $H(t_0) = 0.0482\,\mathrm{Gyr}^{-1} = 47.16$ km/s/Mpc.

Figure 3.1 shows the cosmic scale factor as a function of time for the two cosmological models. As expected, at $t = t_0$, an EdS universe is smaller in size at the present day, as the cosmic expansion has not been accelerated by the effect of Λ. As the two universes evolve into the future, the size differences and relative expansion rates grow, e.g. at $t = 20$ Gyr, the scale factor for the ΛCDM models is ≈25% larger than for the EdS, and the expansion rate is ≈50% larger for our Universe.

3.2.2 Cosmological expansion history as a function of time

In the standard model of cosmology for a homogeneous and isotropic universe, the geometry of space-time is determined by the matter-energy content of the universe through the Einstein field equations as described by the Friedmann-Lemaître-Robertson-Walker metric in terms of the scale factor $a(t)$ and the curvature K, yielding the well-known Friedmann equation,

$$\left(\frac{\dot{a}}{a}\right)^2 = H^2(t) = \frac{8\pi G}{3}\rho - \frac{Kc^2}{a^2} + \frac{\Lambda c^2}{3}, \tag{3.2}$$

where $H(t)$ is the Hubble parameter. As the inflationary models predict that the Universe should be spatially flat, we only consider universes with no spatial curvature, i.e. $K = 0$.

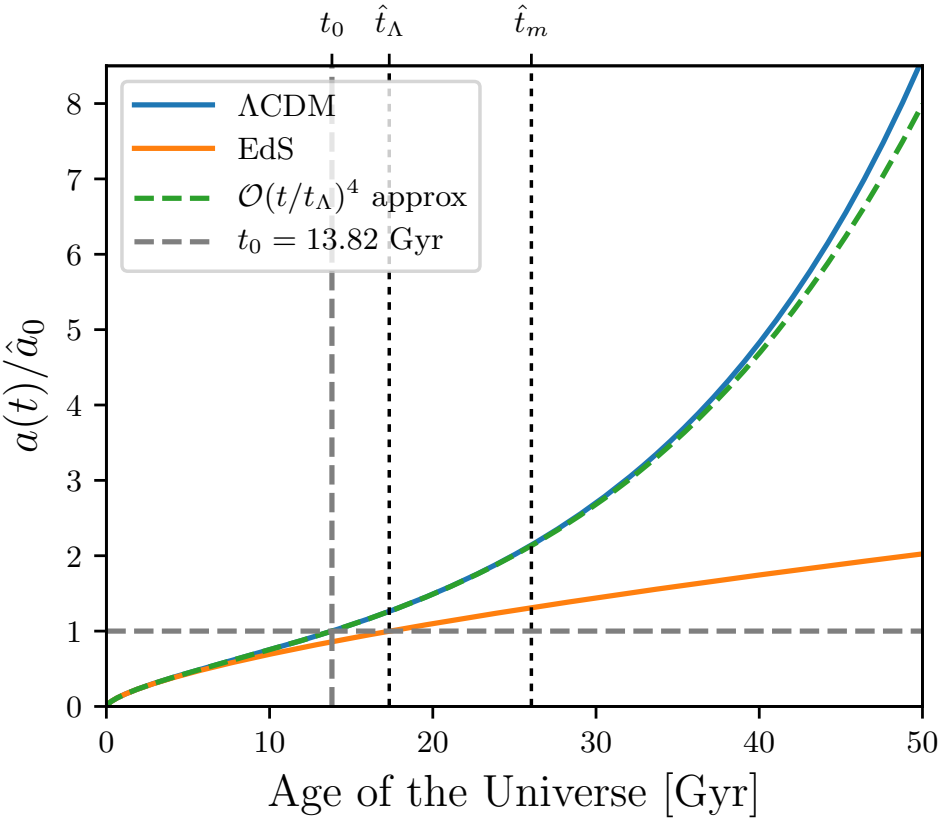

Fig. 3.1.: Cosmic scale factor as a function of time for two cosmological models. The model for the cosmological parameters for a standard ΛCDM universe as inferred by the Planck Collaboration et al. (2014) is shown in blue. An Einstein-de Sitter universe is shown in orange. Note that by construction the scale factors are indistinguishable when the universes are less than 1 Gyr old. The power series approximation of Eq. (3.10) is shown with a dashed green line.

The density of Eq. (3.2) includes the contribution of non-relativistic matter and radiation ($\rho_{\rm m}$ and $\rho_{\rm r}$). The radiation content of the Universe dominated its global dynamics at very early times ($a \to 0$), but its contribution is negligible thereafter. Ignoring $\rho_{\rm r}$ and using the energy density at an arbitrary time t_1, Eq. (3.2) can be written as,

$$\left(\frac{\dot{a}}{a}\right)^2 = \frac{8\pi G}{3}\rho_{\rm m,1}\left(\frac{a}{a_1}\right)^{-3} + \frac{\Lambda c^2}{3}, \tag{3.3}$$

where $\rho_{\rm m,1}$ is the matter density of the universe at $t = t_1$, and $a_1 = a(t_1)$. We choose t_1 such that it corresponds to a sufficiently early epoch, when the contribution of the cosmological constant term is negligible. As discussed in the previous section, at this time any universe closely approximates an EdS universe and we can assume that $a_1 = \hat{a}_1$ and $\rho_{\rm m,1} = \hat{\rho}_{\rm m,1} \implies \hat{\rho}_{\rm m,0}(\hat{a}_0/\hat{a}_1)^3 = \rho_{\rm m,0}(a_0/a_1)^3$. Then, Eq. (3.3) can be written as,

$$\left(\frac{\dot{a}}{a}\right)^2 = \frac{8\pi G}{3}\hat{\rho}_{\rm m,0}\left(\frac{a}{\hat{a}_0}\right)^{-3} + \frac{\Lambda c^2}{3}. \tag{3.4}$$

Note that in Eq. (3.4), the evolution of the scale factor for any arbitrary cosmology is written in terms of the matter density of our Universe at the present time $\hat{\rho}_{\rm m,0}$. We have left the factor of $\hat{a}_0$ explicit in the equation, but it can be set to $\hat{a}_0 = 1$, noting that $a_0 \neq 1$ for any cosmological model different to our Universe.

The LHS of Eq. (3.4), has units of time^{-2} and we will later find it useful to represent the RHS as the sum of two timescales. The cosmological constant is often written as an energy component with energy density $\rho_\Lambda = \Lambda c^2/8\pi G$, however, we can express this as a timescale as follows,

$$t_\Lambda = \sqrt{\frac{3}{\Lambda c^2}} = \frac{1}{H_0\sqrt{\Omega_{\Lambda,0}}}. \tag{3.5}$$

Similarly, the matter content of the Universe can be expressed as a timescale,

$$t_{\rm m} = \sqrt{\frac{3}{8\pi G\hat{\rho}_0}} = \frac{1}{\hat{H}_0\sqrt{\hat{\Omega}_{\rm m,0}}}. \tag{3.6}$$

Using the cosmological parameters for our Universe, $t_\Lambda = \hat{t}_\Lambda = 17.33$ Gyr and $t_m = \hat{t}_m = 26.04$ Gyr. For an EdS universe, $t_\Lambda \to \infty$.

Using this notation, Eq. (3.2) can be written as,

$$\left(\frac{\dot{a}}{a}\right)^2 = t_m^{-2}\left(\frac{a}{\hat{a}_0}\right)^{-3} + t_\Lambda^{-2}, \tag{3.7}$$

which can be solved analytically to express the expansion factor as a function of time and the parameters t_m and t_Λ:

$$a(t) = \left[\frac{1}{2}e^{-3t/2t_\Lambda}\left(e^{3t/t_\Lambda} - 1\right)\left(\frac{t_\Lambda}{t_m}\right)\right]^{2/3} \tag{3.8}$$

In the limit $t_\Lambda \to \infty$ this reduces to the familiar EdS solution,

$$\lim_{t_\Lambda \to \infty} a(t) = \left[\frac{3}{2}\frac{t}{t_m}\right]^{2/3} \tag{3.9}$$

In order to explore the significance of the t/t_Λ term more clearly, we can expand Eq. (3.8) as a Taylor series:

$$a(t) \approx \left[\frac{3}{2}\frac{t}{t_m}\right]^{2/3}\left(1 + \frac{1}{4}\left(\frac{t}{t_\Lambda}\right)^2 + \frac{1}{80}\left(\frac{t}{t_\Lambda}\right)^4 + \ldots\right) \tag{3.10}$$

The coefficients of the series decreased rapidly so that the first three terms provide a good approximation up to $t = 2t_\Lambda$ and beyond. Figure 3.1 shows how well this power series approximation works.

3.2.3 The growth of density perturbations

In the standard model of cosmology, structures such as galaxies and clusters of galaxies are assumed to have grown from small initial density perturbations. Expressing the density, ρ, in terms of the density perturbation contrast against a density background,

$$\rho(\mathbf{x}, t) = \bar{\rho}(t)[1 + \delta(\mathbf{x}, t)], \tag{3.11}$$

the differential equation that governs the time dependence of the growth of linear perturbations in a pressureless fluid, such as e.g. dark matter, can be written as (for a review see Peebles, 1980; Mo et al., 2010),

$$\frac{\mathrm{d}^2\delta}{\mathrm{d}t^2} + 2\frac{\dot{a}}{a}\frac{\mathrm{d}\delta}{\mathrm{d}t} - 4\pi G\bar{\rho}\delta = 0. \tag{3.12}$$

The growing mode of Eq. (3.12) can be written as,

$$\delta(t) = D(t)\delta(t_0), \tag{3.13}$$

where $D(t)$ is the linear growth factor, which determines the normalisation of the linear matter power spectrum relative to the initial density perturbation power spectrum, and is computed by the integral

$$D(t) \propto \frac{\dot{a}}{a} \int_0^t \frac{\mathrm{d}t'}{\dot{a}^2(t')}. \tag{3.14}$$

Using the hat notation as before, we normalise $D(t)$ so that,

- $\hat{D}(t_0) = 1$
- $D(t_1) = \hat{D}(t_1)$

In general, the growing mode can be obtained from Eq. (3.14) numerically. Figure 3.2 shows the growth factor as a function of cosmic time for the two cosmological models. As expected, the figure shows that linear perturbations grow faster in an EdS universe compared to those in a ΛCDM universe.

It is possible to gain more insight by integrating the power-series approximation for $a(t)$ from Eq. (3.10). Expanding the solution again as a power series in (t/t_Λ), retaining the leading terms, yields,

$$D(t) = \left[\frac{3}{2}\frac{t}{t_m}\right]^{2/3} \frac{2}{5} t_m^2 K_D \left(1 - 0.1591 \left(\frac{t}{t_\Lambda}\right)^2 + 0.0366 \left(\frac{t}{t_\Lambda}\right)^4\right), \tag{3.15}$$

where K_D is a normalisation constant. Requiring $\hat{D}(t_0) = 1$ gives $K_D = 4.70 \times 10^{-3}\,\mathrm{Gyr}^{-2}$. Figure 3.2 shows that Eq. (3.15) provides a good approximation up to $t = t_\Lambda$.

This demonstrates that although the t_Λ term slows down the growth of perturbations, its effect is less than 10% until $t \sim t_\Lambda \left(0.1/0.1591\right)^{1/2} \approx 0.8 t_\Lambda$ corresponding to ≈ 13.8 Gyr ($\approx \hat{t}_0$) in our Universe.

As we discuss in the following section, the quantity of fundamental interest for the accretion rate of dark matter haloes is the relative rate of growth of density perturbations, $\frac{1}{D}\frac{dD}{dt}$. We show this for the numerical solution in Fig. 3.3. We can also

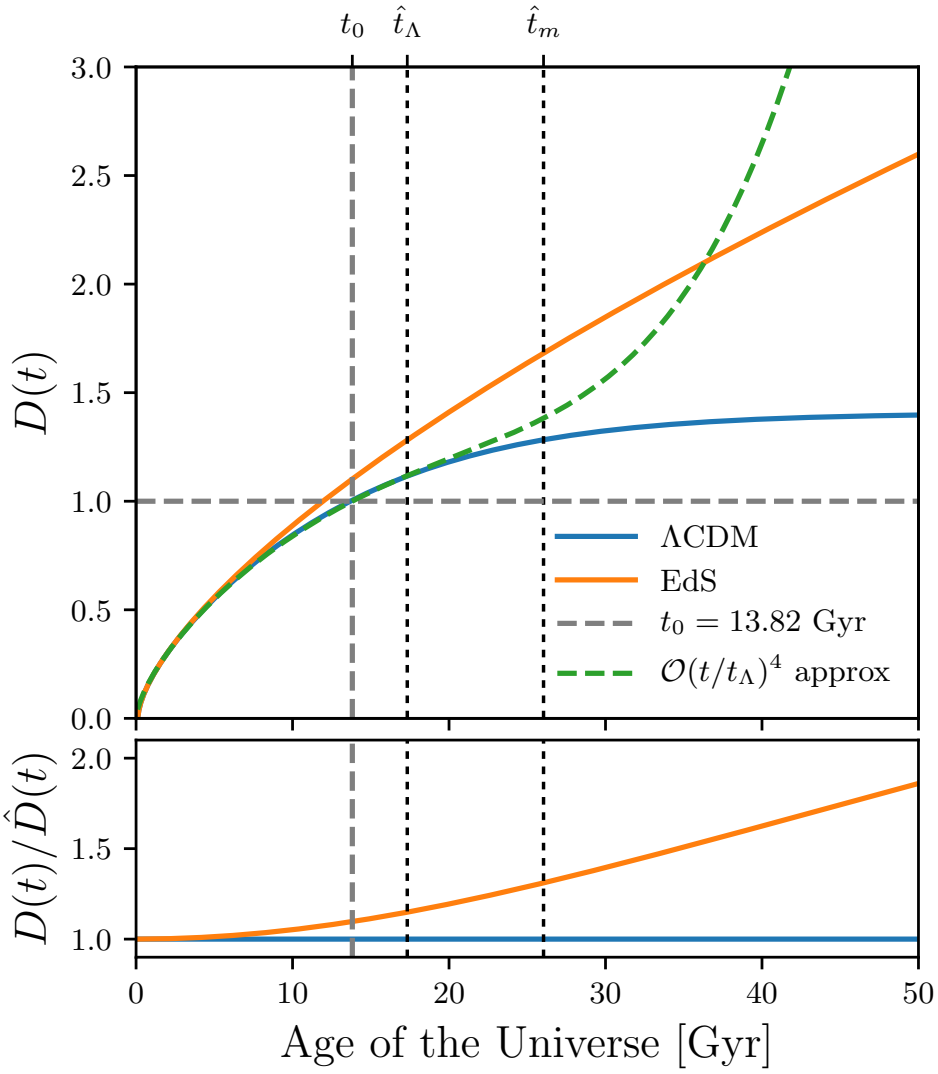

Fig. 3.2.: The linear growth factor for the ΛCDM and EdS cosmological models. The rates are all normalised such that $\hat{D}(t_0) = 1$, for the ΛCDM model, and $D(t_1) = \hat{D}(t_1)$. The bottom panel shows the growth factor at a given time, divided by the growth factor for ΛCDM. The presence of a cosmological constant suppresses the growth of structure in the ΛCDM model (blue) compared to that in the EdS model (orange). The power series approximation of Eq. (3.15) is shown with a dashed green line.

compute the relative growth rate by differentiating the power-series approximation of Eq. (3.15). Retaining the lowest order terms, we find,

$$\frac{1}{D}\frac{\mathrm{d}D}{\mathrm{d}t} = \frac{2}{3t}\left(1 - 0.4773\left(\frac{t}{t_\Lambda}\right)^2 + 0.1435\left(\frac{t}{t_\Lambda}\right)^4\right) \tag{3.16}$$

This expression does not depend on the constants t_m or K_D because we are focusing on the relative change in the growth factor. The impact of the cosmological constant term is relatively large, creating an ≈50% increase in growth rate for the EdS model compared to ΛCDM when $t \approx t_\Lambda$.

3.2.4 Impact on halo accretion rates

The growth rates of linear perturbations do not directly predict the growth rates of haloes, however, we can directly connect the two through the approach developed by Press & Schechter (Press & Schechter, 1974; Bond et al., 1991; Bower, 1991; Lacey & Cole, 1993). Correa et al. (2015) showed that the accretion rates of haloes can be written as (see also Neistein et al., 2006),

$$\frac{1}{M_h}\frac{\mathrm{d}M_h}{\mathrm{d}t} = \sqrt{\frac{2}{\pi}}\frac{(\delta_c/D)}{S(M_h)^{1/2}\left(q^\gamma - 1\right)^{1/2}}\frac{1}{D}\frac{\mathrm{d}D}{\mathrm{d}t}, \tag{3.17}$$

where M_h is the halo mass and $S(M_h)$ is the variance of the density field on the length scale corresponding the halo mass. δ_c is a parameter that represents a threshold in the linearly extrapolated density field for halo collapse. The parameters, q and γ, are related to the shape of the power-spectrum around the halo mass M_h. Approximating the scale dependence of the density field as a power-law, $S = S_0 M_h^{-\gamma}$, Correa et al. 2015 find $S \approx 3.98, \gamma \approx 0.3$ and $q \approx 3.16$, giving $\left[S(M_h)\left(q^\gamma - 1\right)\right]^{-1/2} \approx 0.78$ for $10^{12}\,\mathrm{M}_\odot$ haloes. These values depend only on the initial power spectrum (which we assume to be the same in all the universes we consider) and do not depend on the cosmological parameters. This formulation thus neatly separates the contribution of the power-spectrum shape from the cosmological parameters. We are therefore able to assume that q and γ are the same for all the universes that we consider, and focus on the dependence on $D(t)$.

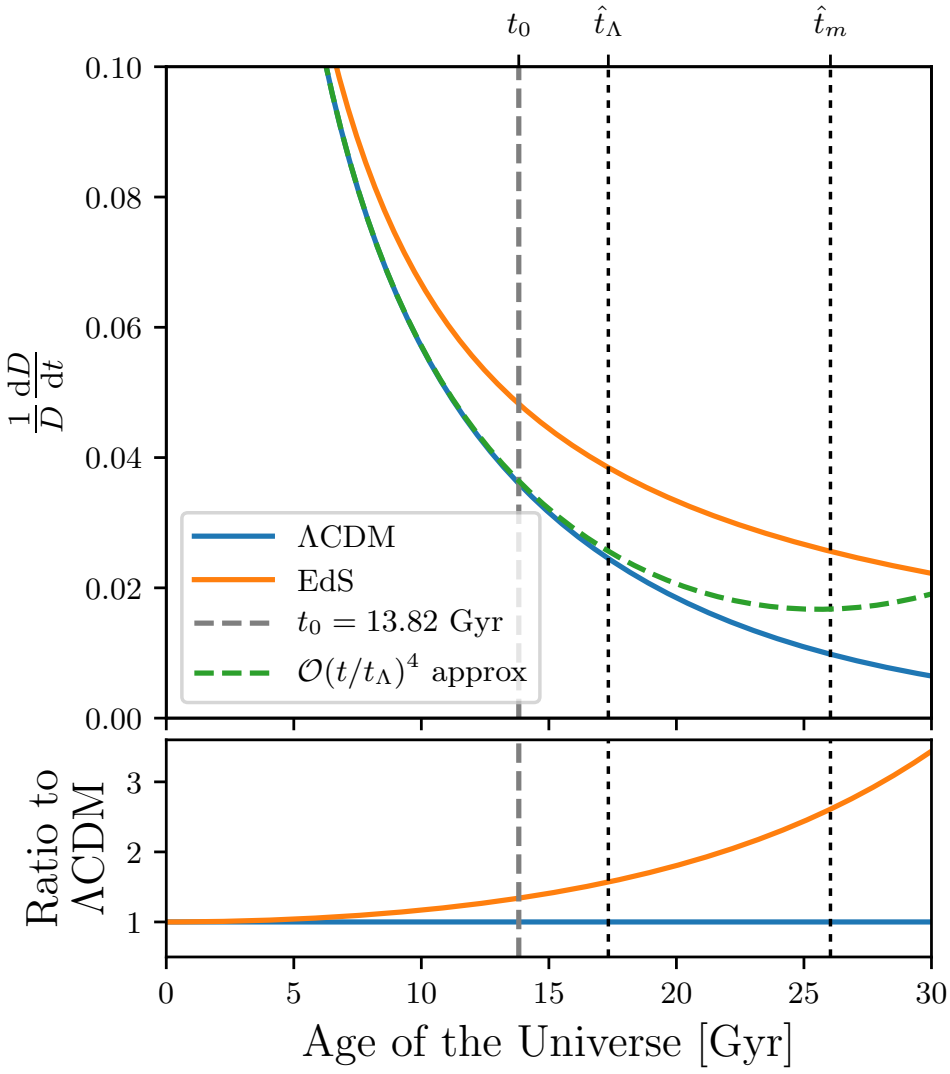

Fig. 3.3.: The relative rate of growth of density perturbations, $\frac{1}{D}\frac{\mathrm{d}D}{\mathrm{d}t}$ for the ΛCDM and EdS cosmological models. The bottom panel shows the ratio, at a given time. The presence of a cosmological constant slows down the growth of structure in the ΛCDM model (blue) compared to that in the EdS model (orange). The power series approximation of Eq. (3.16) is shown with a dashed green line.

For the numerical values of the power-spectrum parameters around a halo mass of $10^{12}\,\mathrm{M}_\odot$, Eq. 3.17 reduces to

$$\frac{1}{M_h}\frac{\mathrm{d}M_h}{\mathrm{d}t} = 1.0456\frac{1}{D^2}\frac{\mathrm{d}D}{\mathrm{d}t}. \tag{3.18}$$

This dependence can be understood as the combination of two factors. The first reflects the relative growth rate of density fluctuations $\frac{1}{D}\frac{\mathrm{d}D}{\mathrm{d}t}$. The second factor of $1/D$ comes from the rarity of haloes, reflecting the higher growth rate of fluctuations in the tail of the density field distribution.

Further insight can be gained by using the series approximation. This gives,

$$\frac{1}{M_h}\frac{\mathrm{d}M_h}{\mathrm{d}t} = \frac{566.61}{\sqrt{S}\,t^{5/3}t_m^{4/3}}\left(1 - 0.3182\left(\frac{t}{t_\Lambda}\right)^2 + 0.0563\left(\frac{t}{t_\Lambda}\right)^4\right). \tag{3.19}$$

This explicitly shows how the presence of a cosmological constant modulates the halo growth rate. In our Universe, the impact of the cosmological constant term is relatively modest, however; at $t = 13.8\,\mathrm{Gyr}$, we expect the difference to be 20%, growing to 40% at $t = 20\,\mathrm{Gyr}$.

As an example, in Fig. 3.4 we show the accretion rate of haloes of $M_h = 10^{12}\mathrm{M}_\odot$, both numerically and using Eq. (3.19).

3.2.5 Impact on the star formation rate of the Universe

In order to link the SFR of halos of mass M_h to their accretion rate, as a first approximation, we assume a time-independent galaxy specific star formation rate to host halo specific mass accretion rate relation (e.g. Behroozi et al., 2013a; Tacchella et al., 2013; Rodríguez-Puebla et al., 2016),

$$\frac{\dot{M}_*/M_*}{\dot{M}_h/M_h} = \frac{\partial \log M_*}{\partial \log M_h} = \epsilon(M_h), \tag{3.20}$$

where the star formation efficiency ϵ, of haloes of mass M_h, is the slope of the stellar-halo mass relation. From this equation, the star formation as a function of halo mass can be written as,

$$\dot{M}_*(M_h) = \epsilon_*(M_h)\dot{M}_h, \tag{3.21}$$

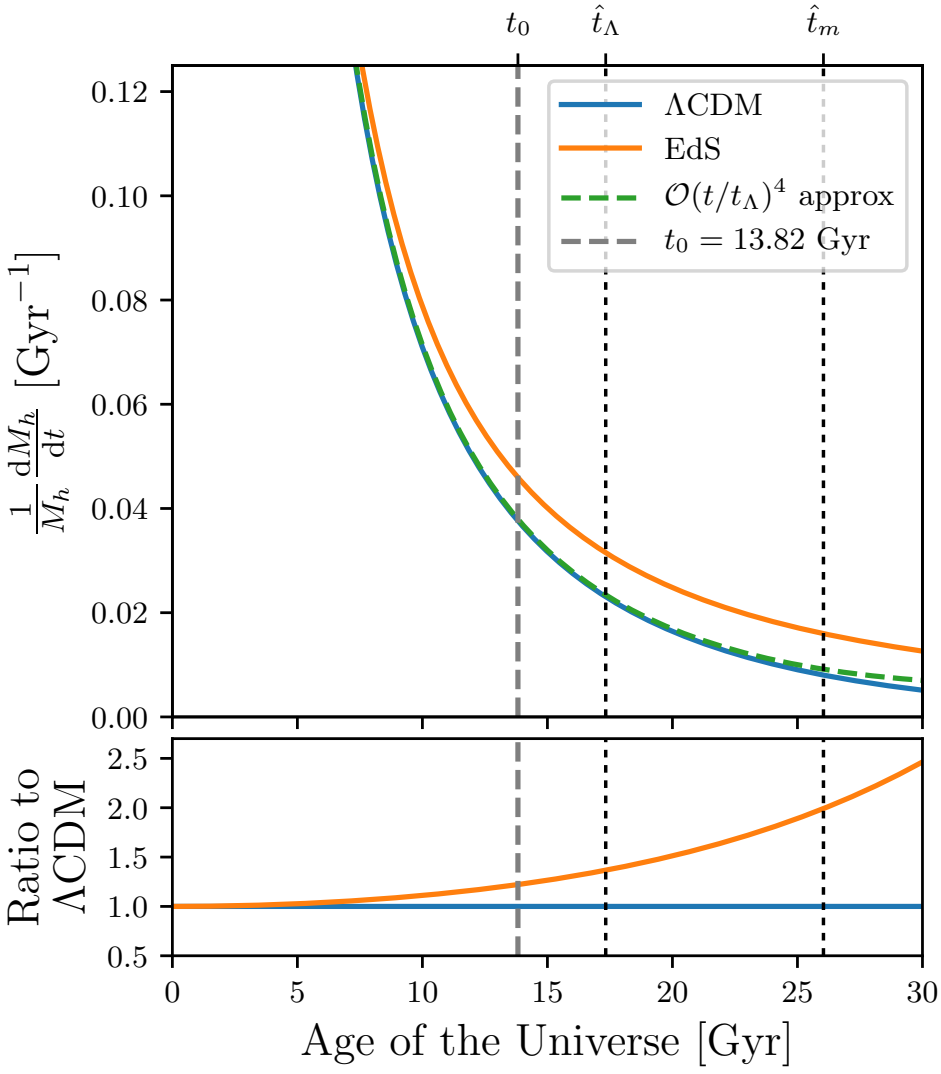

Fig. 3.4.: The specific accretion rate of haloes of mass $M_h = 10^{12}\mathrm{M}_\odot$, $\frac{1}{M_h}\frac{\mathrm{d}M_h}{\mathrm{d}t}$ for the ΛCDM and EdS cosmological models. The bottom panel shows the ratio at a given time. The presence of a cosmological constant slows down the specific accretion rates of halos in the ΛCDM model (blue) compared to that in the EdS model (orange). The power series approximation of Eq. (3.19) is shown with a dashed green line.

where $\epsilon_*(M_h) := \epsilon(M_h) \times (M_*/M_h)$ is completely defined by the stellar-halo mass relation. As there is no a priori knowledge of the functional form of $\epsilon_*(M_h)$, we use the abundance matching results from Behroozi et al. 2013b to estimate $\epsilon_*(M_h)$. The efficiency $\epsilon_*(M_h)$ peaks at masses similar to Milky-Way sized halos ($\sim 10^{12}$ M$_\odot$) and falls steeply for higher and lower masses. $\epsilon_*(M_h)$ can be well approximated by a broken power law as,

$$\epsilon_*(M_h) \propto \begin{cases} \left(\frac{M_h}{10^{12}\mathrm{M}_\odot}\right)^1 & \text{if } M_h \leq 10^{12}\mathrm{M}_\odot \\ \\ \left(\frac{M_h}{10^{12}\mathrm{M}_\odot}\right)^{-1} & \text{if } M_h > 10^{12}\mathrm{M}_\odot \end{cases} \tag{3.22}$$

At low masses, star formation rate is suppressed because of the efficiency of feedback from star formation, at higher masses the cooling of the inflowing gas is suppressed by heating from black holes (White & Frenk, 1991; Benson et al., 2003; Bower et al., 2006; Haas et al., 2013; Crain et al., 2015; Dubois et al., 2016; Bower et al., 2017).

In order to complete the analysis, we need to combine the specific halo mass accretion rate with an estimate of the halo abundance.

In the Press & Schechter analysis, the co-moving abundance of haloes of mass M_h at time t is given by (Press & Schechter, 1974; Bond et al., 1991; Bower, 1991; Lacey & Cole, 1993),

$$\frac{dn(M_h,t)}{dM_h} = \frac{\hat{\rho}_0}{M_h^2}\frac{\delta_c \gamma}{\sqrt{2\pi}S^{1/2}}\frac{1}{D}\exp\left(-\frac{\delta_c^2}{2SD^2}\right) \tag{3.23}$$

where we have assumed that the density power spectrum is a power law with exponent γ and written the co-moving density of the Universe as $\hat{\rho}_0$ following our convention. Note that we compute co-moving densities. At the same cosmic time, the different expansion rates will result in different physical (proper) halo and SFR densities, simply because of the more rapid expansion of the ΛCDM cosmology.

The total cosmic SFR density is given by the integral of all star formation in all haloes,

$$\dot{\rho}_*(t) = \int \dot{M}_*(M_h)\frac{\mathrm{d}n(M_h,t)}{\mathrm{d}M_h}\mathrm{d}M_h = \int \epsilon_*(M_h)\dot{M}_h\frac{\mathrm{d}n(M_h,t)}{\mathrm{d}M_h}\mathrm{d}M_h \tag{3.24}$$

Using the power series approximation Eq. (3.19) together with Eq. (3.22) and Eq. (3.23), the contribution to the cosmic SFR density from haloes of mass M_h (the integrand of Eq. (3.24)) is given by,

$$\begin{aligned}\frac{\mathrm{d}\dot{\rho}_*}{\mathrm{d}M_h} &= \epsilon_*(M_h)\left[\frac{1}{M_h}\frac{\mathrm{d}M_h}{\mathrm{d}t}\right] M_h \frac{\mathrm{d}n(M_h,t)}{\mathrm{d}M_h} \\ &= \epsilon_*(M_h)\frac{46230.9\hat{\rho}_0}{M_h S t^{7/3} t_m^{8/3}}\left(1 - 0.1590\left(\frac{t}{t_\Lambda}\right)^2 - 0.0056\left(\frac{t}{t_\Lambda}\right)^4\right) \\ &\times \exp\left[-\frac{232382}{S\,t^{4/3}t_m^{8/3}}\left(1 + 0.3182\left(\frac{t}{t_\Lambda}\right)^2 + 0.0028\left(\frac{t}{t_\Lambda}\right)^4\right)\right].\end{aligned} \tag{3.25}$$

The cosmological constant term enters through both the multiplier and the exponential terms, with a balance that depends on the halo mass through S (see Eq. (3.17)). While smaller haloes are more abundant than large objects, a smaller fraction of the inflowing material is converted into stars. As a result, the SFR density is dominated by the largest haloes in which star formation is able to proceed without generating efficient BH feedback. The smaller haloes only contribute significantly at very early times, when the abundance of larger objects is strongly suppressed by the exponential term. We see therefore that the level of suppression expected for $\approx 10^{12}\,\mathrm{M}_\odot$ haloes is representative of most of the SFR in the Universe.

The predictions for the contributions of different halo masses are shown in Fig. 3.5, together with the total expected cosmic SFR density, for the two cosmologies that we consider in this chapter. We will compare this approximation in Section 3.5 to the results from the EAGLE simulations.

3.3 The EAGLE Simulations

The simple analytic model provides a basis for interpreting the results, but it is highly simplified. We therefore compare the analytic model to numerical hydrodynamic simulations based on the EAGLE project. The EAGLE simulation suite[3] (Schaye et al., 2015; Crain et al., 2015) consists of a large number of cosmological hydrodynamical simulations that include different resolutions, simulated volumes and physical models. These simulations use advanced smoothed particle hydrodynamics (SPH)

[3] http://www.eaglesim.org

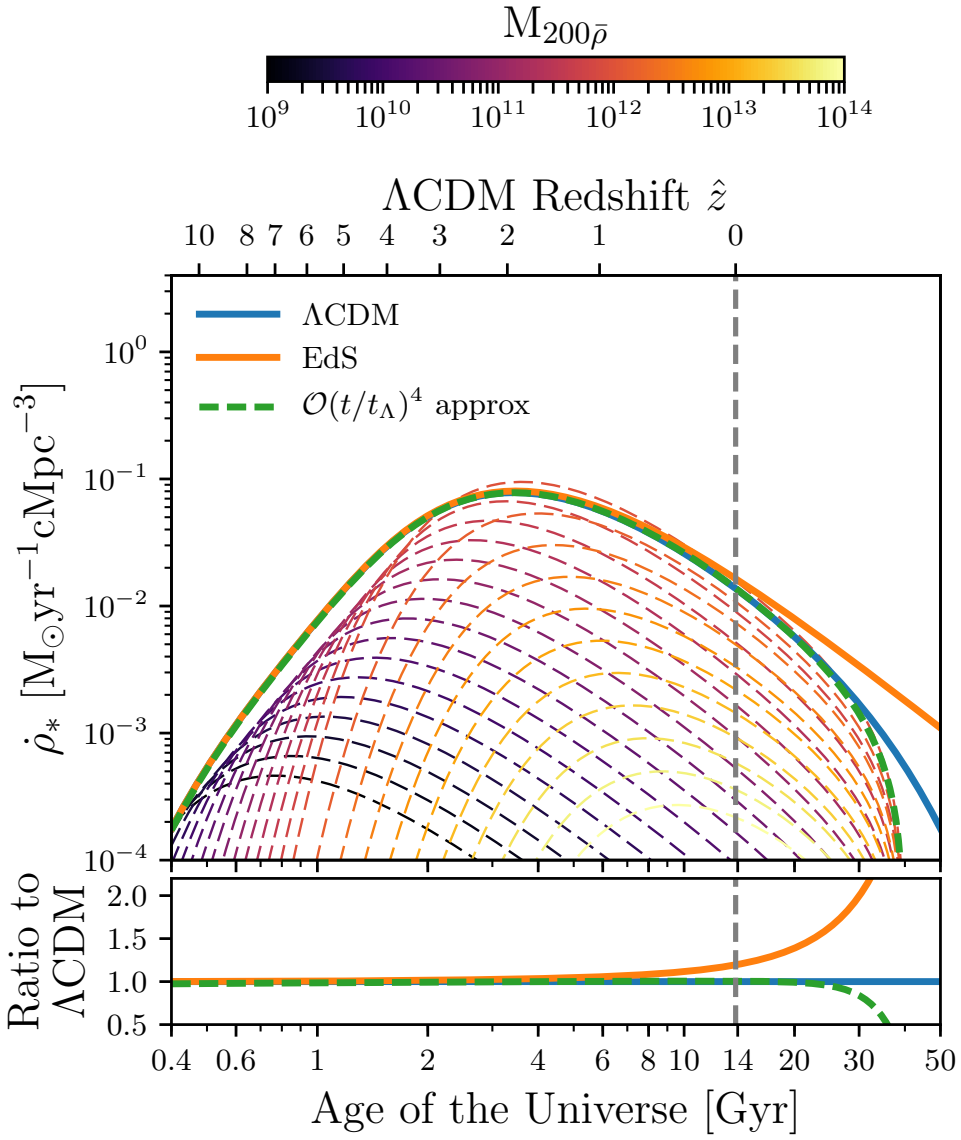

Fig. 3.5.: The predicted SFR history of the Universe, and the expected influence of the cosmological constant using the simple model developed in Section 3.2.5. Coloured lines show the contributions from dark matter haloes of different masses (per dex), using the star formation efficiency described by Eq. (3.25). The total SFR for the ΛCDM universe calculated numerically is shown in blue. An Einstein-de Sitter universe is shown in orange. The integrated SFR calculated using the approximation of Eqs. (3.24) and (3.25), is shown with a dashed green line. The bottom panel shows the ratio at a given time. The predicted suppression of SFR due to Λ at the present time is ≈19%. At $t \approx 30$ Gys the predicted SFR density for the EdS model is double than ΛCDM, and ≈6 times higher at $t = 50$ Gyr. The approximation of Eqs. (3.24) and (3.25) ceases to work for $t \gtrsim 25$ Gyr.

and state-of-the-art subgrid models to capture the unresolved physics. The simulation suite was run with a modified version of the GADGET-3 SPH code (last described by Springel 2005) and includes a full treatment of gravity and hydrodynamics. The calibration strategy is described in detail by Crain et al. (2015) who also presented additional simulations to demonstrate the effect of parameter variations.

The halo and galaxy catalogues for more than 10^5 simulated galaxies of the main EAGLE simulations with integrated quantities describing the galaxies, such as stellar mass, SFRs, metallicities and luminosities, are available in the EAGLE database[4] (McAlpine et al., 2016). A complete description of the code and physical parameters used can be found in Schaye et al. (2015).

The EAGLE reference simulations used cosmological parameters measured by the Planck Collaboration et al. (2014). In this chapter we introduce three main EAGLE simulations that use the same calibrated sub-grid parameters as the reference model, but change the cosmological model by setting the cosmological constant to zero, and/or removing feedback from BHs. The values of the cosmological parameters used for the simulations are listed in Table 3.1. The values of other relevant parameters adopted by all simulations featured in this study are listed in Table 3.2. Together these parameters determine the dynamic range and resolution that can be achieved by the simulations.

[4] http://www.eaglesim.org/database.php

Table 3.1.: The cosmological parameters for the EAGLE simulations used in this study. ΛCDM model refers to parameters inferred by the Planck Collaboration et al. (2014). EdS refers to an Einstein-de Sitter universe. Ω_m, Ω_Λ, Ω_b are the average densities of matter, dark energy, and baryonic matter in units of the critical density at redshift zero; H_0 is the Hubble constant, $\sigma_8(t_1)$ is the square root of the linear variance of the matter distribution at the initial cosmic time of the simulations ($t_1 = 11.98$ Myr) when smoothed with a top-hat filter of radius 11.8 cMpc ($8\,h^{-1}$ cMpc for a ΛCDM model), n_s is the scalar power-law index of the power spectrum of primordial adiabatic perturbations, and Y is the primordial abundance of helium. Values in bold show differences with respect to the ΛCDM values.

Cosmological Parameter	ΛCDM (Ref)	EdS
Ω_m	0.307	**1**
Ω_Λ	0.693	**0**
Ω_b	0.04825	**0.15717**
$h \equiv H_0/(100\,\mathrm{km\,s^{-1}\,Mpc^{-1}})$	0.6777	**0.3754**
$\sigma_8(t_1)$	0.0083	0.0083
n_s	0.9611	0.9611
Y	0.248	0.248

Table 3.2.: Box-size, number of particles, initial baryonic and dark matter particle mass, co-moving and Plummer-equivalent gravitational softening, inclusion of AGN feedback, cosmological model and Hubble parameter for the EAGLE simulations used in this chapter. Values in bold show differences with respect to the Ref simulation. The three bottom small box models were used for convergence tests.

Identifier	L [cMpc]	N	$m_{\rm gas}$ [$M_\odot$]	$m_{\rm DM}$ [$M_\odot$]	$\epsilon_{\rm com}$ [ckpc]	$\epsilon_{\rm prop}$ [pkpc]	AGN	Cosmology	h
ΛCDM (Ref)	50	2×752^3	1.81×10^6	9.70×10^6	2.66	0.70	Yes	Planck 14	0.6777
ΛCDM (No AGN)	50	2×752^3	1.81×10^6	9.70×10^6	2.66	0.70	**No**	Planck 14	0.6777
EdS	50	2×752^3	1.81×10^6	9.70×10^6	2.66	0.70	Yes	**EdS**	**0.3754**
EdS (No AGN)	50	2×752^3	1.81×10^6	9.70×10^6	2.66	0.70	**No**	**EdS**	**0.3754**
Λ = 0 L12 h0_3754	12.50	2×188^3	1.81×10^6	9.70×10^6	2.66	0.70	Yes	**EdS**	**0.3754**
Λ = 0 L12 h0_6777	8.43	2×188^3	1.81×10^6	9.70×10^6	**1.79**	0.70	Yes	**EdS**	0.6777
Λ = 0 L12 h0_4716	10.73	2×188^3	1.81×10^6	9.70×10^6	**2.28**	0.70	Yes	**EdS**	**0.4716**

Fig. 3.6 Shows the projected gas density for the ΛCDM and EdS cosmological models both at the present day and into the future. At $t = 13.8$ Gyr, the general appearance of both models is similar, but over the next 6.8 Gyr, the effect of Λ becomes more significant slowing down the growth of structure.

3.3.1 Subgrid models

Processes that are not resolved by the simulations are implemented as subgrid physical models; they depend solely on local interstellar medium (ISM) properties. A full description of these subgrid models can be found in Schaye et al. (2015). In summary:

1. Radiative cooling and photoheating are implemented element-by-element as in Wiersma et al. (2009a), including the 11 elements found to be important, namely, H, He, C, N, O, Ne, Mg, Si, S, Ca, and Fe. Hydrogen reionization is implemented by switching on the full Haardt & Madau (2001) background at the proper time corresponding to redshift $z = 11.5$ in our ΛCDM Universe.

2. Star formation is implemented stochastically following the pressure-dependent Kennicutt-Schmidt relation as in Schaye & Dalla Vecchia (2008). Above a metallicity-dependent density threshold $n_{\rm H}^*(Z)$, which is designed to track the transition from a warm atomic to an unresolved, cold molecular gas phase (Schaye, 2004), gas particles have a probability of forming stars determined by their pressure.

3. Time-dependent stellar mass loss due to winds from massive stars and AGB stars, core collapse supernovae and type Ia supernovae, is tracked following Wiersma et al. (2009b).

4. Stellar feedback is treated stochastically, using the thermal injection method described in Dalla Vecchia & Schaye (2012).

5. Seed BHs of mass $\mathrm{M} = 1.48\times10^5\mathrm{M}_\odot$, are placed in haloes with a mass greater than $1.48\times10^{10}\mathrm{M}_\odot$ and tracked following the methodology of Springel et al. (2005a); Booth & Schaye (2009). Accretion onto BHs follows a modified version of the Bondi-Hoyle accretion rate which takes into account the circularisation and subsequent viscous transport of infalling material, limited by

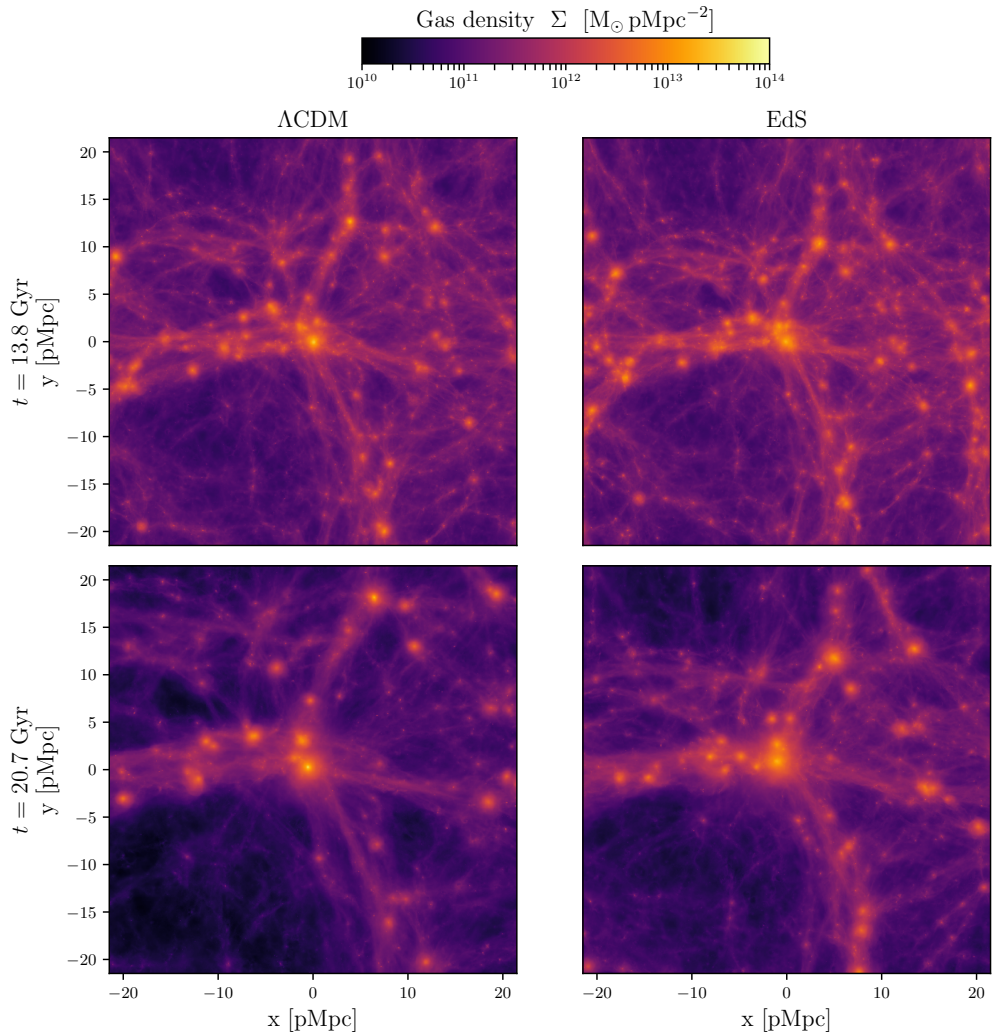

Fig. 3.6.: The evolution of the projected gas density for each EAGLE model centred on the most massive halo at the present time ($t = 13.8$ Gyr). The length of each image is 43 (proper) Mpc on a side, to highlight the difference on cosmic expansion. Left: ΛCDM universe. Right: EdS universe. Top: Cosmic time $t = 13.8$ Gyr. Bottom: Cosmic time $t = 20.7$ Gyr. The colour coding represents the (proper) surface gas density projected along the line of sight. At $t = 13.8$ Gyr, the general appearance of both models is similar, as the phases of the initial fluctuations are the same. Over the next 6.8 Gyr, the effect of Λ becomes more significant, slowing down the growth of structure compared to the EdS model.

the Eddington rate as described by Rosas-Guevara et al. (2015)[5]. Additionally, BHs can grow by merging with other BHs as described in Schaye et al. (2015); Salcido et al. (2016).

6. Feedback from AGN is implemented following the stochastic heating scheme described by Schaye et al. (2015). Similar to the supernova feedback, a fraction of the accreted gas onto the BH is released as thermal energy with a fixed heating temperature into the surrounding gas following Booth & Schaye (2009).

For the EAGLE simulations, the subgrid parameters were calibrated to reproduce three properties of galaxies at redshift $z = 0$: the galaxy stellar mass function, the galaxy size–stellar mass relation, and the black hole mass-stellar mass relation[6]. The calibration strategy is described in detail by Crain et al. (2015), who explores the effect of parameter variations.

3.3.2 Halo and galaxy definition

Haloes were identified running the "Friends-of-Friends" (FoF) halo finder on the dark matter distribution, with a linking length equal to 0.2 times the mean inter-particle spacing. Galaxies were identified as self-bound over-densities within the FoF group using the SUBFIND algorithm (Springel et al., 2001; Dolag et al., 2009). A 'central' galaxy is the substructure with the largest mass within a halo. All other substructures within a halo are 'satellite' galaxies.

Comparing haloes from simulations with different cosmologies is not a well-defined task, as halo masses are usually defined in terms of quantities that depend on the specific cosmological parameters. Typically, this is done by growing a sphere outwards from the potential minimum of the dominant dark matter sub-halo out to a radius where the mean interior density equals a fixed multiple of the critical or mean density of the Universe, causing an artificial 'pseudo-evolution' of dark matter halos by changing the radius of the halo (Diemer et al., 2013). Star formation, however, is governed by the amount of gas that enters these halos and reaches their central regions. Wetzel & Nagai 2015 show that the growth of dark matter haloes is subject to this 'pseudo-evolution', whereas the accretion of gas is not. Because gas

[5]The EAGLE simulation do not include a boost factor the accretion rate of BHs to account for an unresolved clumping factor.
[6]BH feedback efficiency left unchanged from Booth & Schaye (2009).

is able to cool radiatively, it decouples from dark matter, tracking the accretion rate near a radius of $R_{200\bar{\rho}}$, the radius within which the mean density is 200 times the mean density of the universe, $\bar{\rho}$. As we try to connect the accretion of dark matter haloes to star formation, we define halo masses as the total mass within $R_{200\bar{\rho}}$,

$$M_{200_{\bar{\rho}}} = 200\frac{4\pi}{3}R^3_{200\bar{\rho}}\bar{\rho}. \tag{3.26}$$

Additionally, as $\bar{\rho} = \Omega_m(t)\rho_c(t)$ is given in co-moving coordinates, the mean density of the universe remains constant in time for each cosmological model.

Following Schaye et al. 2015 and Furlong et al. 2015, galaxy stellar masses are defined as the stellar mass associated with the subhalo within a 3D 30 proper kilo parsec (pkpc) radius, centred on the minimum of the subhalo's centre of gravitational potential. This definition is equivalent to the total subhalo mass for low-mass objects, but excludes diffuse mass around very large subhaloes, which would contribute to the intracluster light (ICL).

3.3.3 Continuing the simulations into the future

As Λ continues driving the accelerated expansion of the universe, the linear growth of density perturbations, $D(t)$ is suppressed (see Eq. (3.15)). Further insight can be obtained if we analyse the evolution of the potential perturbations given by the perturbed Poisson equation for an expanding space,

$$\nabla^2\Phi = 4\pi G\bar{\rho}_{\rm p}a^2D\delta_0, \tag{3.27}$$

where the Laplace operator is with respect to comoving coordinates, and the mean density $\bar{\rho}_{\rm p}$ is given in proper coordinates. As $\bar{\rho}_{\rm p}$ evolves $\propto a^{-3}$, it follows that $\nabla^2\Phi \propto D/a$. Using Eq. (3.10) and Eq. (3.15) we can see that for an EdS universe, both D and a are $\propto t^{2/3}$ and the potentials are expected to stop evolving (they are frozen in). On the other hand, the suppression of growth of density perturbations due to a cosmological constant causes a decay in the potentials as the universe expands. As shown in Fig. 3.2, according to linear theory, these two scenarios have comparable growth factors at the present time (≈10% difference, see Eq. 3.15), but the difference becomes increasingly important in the future. Furthermore, star formation is expected to eventually exhaust the finite reservoir of cold gas in galaxies,

shutting off the production of stars in the universe forever (e.g. Fukugita et al., 1998; Loeb et al., 2016).

In order to study the impact of Λ in galaxy formation beyond the present day, and hence explore the uniqueness of the present epoch, and in order to determine the total mass of stars ever produced by the universe, we allow the simulations to run into the future, i.e. $t > t_0$ (e.g. Barnes et al., 2005; Loeb et al., 2016). The subgrid models for star formation, stellar mass loss, stellar feedback, BH seeding and feedback from AGN were kept as described in Section 3.3.1 as the simulations ran into the future. On the other hand, as there is no information about the UV and X-ray background radiation from quasars and galaxies into the future, for simplicity, we assumed that the background radiation freezes out, i.e. we kept its value at $t = t_0$ constant into the future. We consider this to be a good simplification as the UV background only affects star formation in very low mass haloes, and hence does not affect the cosmic SFR at late times (e.g. Schaye et al., 2010).

3.4 Simulations re-scaling

In this section we describe our simulation re-scaling strategy. At early epochs, the universe was matter dominated, and so we can neglect the contribution of Λ. Hence, any universe with non zero matter density, i.e. $\rho_{\mathrm{m},0} \neq 0$, will be close to an EdS universe at early epochs. Therefore, we can assume identical initial conditions for all cosmological models of interest here.

The initial conditions for the reference ΛCDM model were created in three steps. First, a particle load, representing an unperturbed homogeneous periodic universe was produced. Secondly, a realisation of a Gaussian random density field with the appropriate linear power spectrum was created over the periodic volume. Thirdly, the displacements and velocities, consistent with the pure growing mode of gravitational instability, were calculated from the Gaussian realisation and applied to the particle load producing the initial conditions. The initial density perturbation power spectrum is commonly assumed to be a power-law, i.e. $P_i(k) \propto k^{n_s}$. From the Planck results (Planck Collaboration et al., 2014), the spectral index n_s, has a value of $n_s = 0.9611$. A transfer function with the cosmological parameters shown in Table 3.1 was generated using CAMB (version Jan_12; Lewis et al. 2000). The linear matter power spectrum was generated by multiplying the initial power spec-

Table 3.3.: Parameters re-scaled in the initial conditions. Hat notation indicates parameters for our Universe.

Parameter	Units	Re-scaling factor
Box size	cMpc h^{-1}	$(\hat{h}^{-1}h) \times (\hat{a}_1 a_1^{-1})$
Particle Masses	$M_\odot\, h^{-1}$	$(\hat{h}^{-1}h)$
Particle Coordinates	cMpc h^{-1}	$(\hat{h}^{-1}h) \times (\hat{a}_1 a_1^{-1})$
Particle Velocities	cMpc s^{-1}	$(\hat{a}_1 a_1^{-1})^{1/2}$

trum by the square of the dark matter transfer function evaluated at the present day $t = t_0$, i.e. $P(k,t) = P_i(k)T^2(k)D^2(t)$.[7]

The EAGLE version of GADGET uses an internal system of units that includes both co-moving coordinates and the dimensionless Hubble parameter, h. For the alternative cosmological models, we have the freedom to choose the present time t_0 for each simulation, and we re-scale all the initial condition such that they are identical in physical *"h-free"* units at an early time $t_1 = 11.98$ Myr. Table 3.3 shows the parameters that have been re-scaled in the initial conditions.

The same tables of radiative cooling and photoheating rates as a function of density and temperature were used for all cosmological models. The corresponding redshifts for the cooling tables were re-scaled such that they correspond to the same cosmic time for each cosmology. That is, using Eq. (3.8), we find the scale factor, a, for which the alternative cosmology satisfies,

$$t(\hat{a}) = t(a). \tag{3.28}$$

The average baryonic density Ω_b has been re-scaled in such way that the baryon fraction ($f_\mathrm{b} = \Omega_\mathrm{b}/\Omega_\mathrm{m}$) is equal in both cosmologies, i.e.

$$\frac{\hat{\Omega}_\mathrm{b}}{\hat{\Omega}_\mathrm{m}} = \frac{\Omega_\mathrm{b}}{\Omega_\mathrm{m}}. \tag{3.29}$$

Table 3.4 shows additional parameters that have been re-scaled to be equivalent in h-free physical units. Finally, hydrogen and HeII reionization were also re-scaled in such way that redshifts correspond to the same cosmic time.

[7] The CAMB input parameter file and the linear power spectrum are available at http://eagle.strw.leidenuniv.nl/

Table 3.4.: Additional parameters re-scaled in the simulations. Hat notation indicates parameters for our Universe.

Parameter	Units	Re-scaling factor
Co-moving Softening	ckpc h^{-1}	$(\hat{h}^{-1}h) \times (\hat{a}_1 a_1^{-1})$
Max Softening	pkpc h^{-1}	$(\hat{h}^{-1}h)$
Seed BH Mass	$M_\odot\, h^{-1}$	$(\hat{h}^{-1}h)$
Min M_{FOF} for New BH	$M_\odot\, h^{-1}$	$(\hat{h}^{-1}h)$

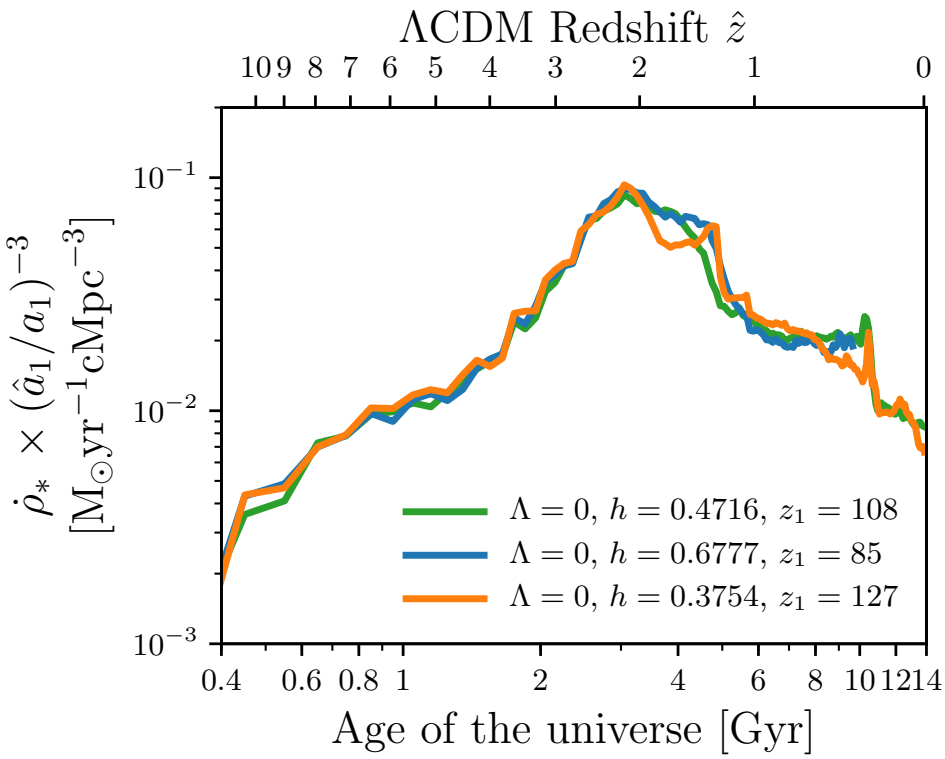

Fig. 3.7.: Global SFR density for three EdS models scaled by the ratio of the initial scale factors for each model. The initial conditions for each model have been re-scaled such that the time at which we start the simulations remains unchanged, i.e. $t(a_1) = 11.98\,\mathrm{Myr}$.

In order to demonstrate that this re-scaling strategy works correctly, Fig. 3.7 shows the global SFR density for the three small box EdS simulations used for convergence (see Table 3.2). They each represent the same physical scenario, but choose a different proper time to be "today", t_0. This has the effect of altering the values of the Hubble parameter h and the redshift of the initial conditions, so that the simulations begin at proper time $t(a_1) = 11.98$ Myr in all models. Despite the small size of the simulation boxes (hence the noisy curves), the figure shows consistent SFRs as a function of cosmic time for the three models. Therefore, our re-scaling strategy allows us to simulate any cosmological model, regardless of the value of h.

3.5 Results: The Evolution of Star Formation

3.5.1 The past history of the cosmic star formation rate

Figure 3.8 shows the global SFR density as a function of cosmic time for our simulation models. For comparison, observations from Cucciati et al. (2012) [FUV], Bouwens et al. (2012) [UV], Robertson et al. (2013) [UV] and Burgarella et al. (2013) [FUV + FIR] are shown as well. Solid lines in the figure show the evolution of the (co-moving) cosmic SFR density for the reference ΛCDM EAGLE run (blue), and for an EdS universe (orange). Dashed lines show simulation models without feedback from AGN. Dotted lines show the prediction for the cosmic SFR density using Eq. (3.25). We focus first on the evolution of the models up to the present age of the universe, $t = t_0 = 13.8$ Gyr.

In linear time, the SFR rises very rapidly and most of the plot is dominated by the slow decline (for an example, see Furlong et al. 2015). Hence, in order to emphasis the growth and decline of the SFR, and to reproduce the familiar shape of the star formation history (Madau & Dickinson, 2014), the horizontal time axis has been plotted in a logarithmic scale for $t \leq 8$ Gyr. In order to explore the SFR in detail at the present epoch and into the future, the horizontal time axis changes to a linear scale for $t > 8$ Gyr. The black vertical dotted line shows the transition from logarithmic to linear scale. For reference, the redshifts, $\hat{z}$, for an observer at t_0 in the ΛCDM universe, are given along the top axis. As discussed in detail in Furlong et al. (2015), the reference simulation (solid blue line) reproduces the shape of the observed SFR density remarkably well, with a small offset of 0.2 dex at $t \gtrsim 2$ Gyr.

While the simulations agree reasonably well with the observational data at redshifts above 3, we caution that these measurements are more uncertain.

Remarkably, the shape of the cosmic SFR history is very similar for both the ΛCDM and EdS models: the SFR density peaks ≈3.5 Gyr after the Big Bang and declines slowly thereafter. The similarity of the universes prior to the peak is expected, since the Λ term in the Friedman equation is sub-dominant in both cases. At later times, however, we might naively have expected the decline to be more pronounced in the ΛCDM cosmology, since the growing importance of the Λ term slows the growth of density perturbations.

From Fig. 3.2, the linear growth factors of the two cosmological models differ by ≈10% at the present time, and so we might have expected a similar difference in the (co-moving) cosmic SFR density (≈15%, read from Fig. 3.8). This naive expectation is not borne out because of the complexity of the baryonic physics. Because of stellar and AGN feedback, haloes have an ample reservoir of cooling gas that is able to power further star formation regardless of the change in the cosmic halo growth rate.

Our simulation demonstrates that the existence of Λ does play a small role in determining the (co-moving) cosmic SFR density. However, these differences are minor. In order to put the differences into context, we compare with a pair of simulations in which the BH feedback is absent. These runs are shown as dashed lines in the plot. We focus here on the behaviour before $t = 13.8$ yrs. As can be seen, the absence of AGN feedback has a dramatic effect on the shape of the cosmic star formation density (Schaye et al., 2010; van de Voort et al., 2011). Interestingly, however, while the normalisation of the SFR density is considerably higher, the time of the peak is similar. BH feedback is not solely responsible for the decline in star formation after $t \approx 3.5$ Gyr. This hints that the existence of the peak results from the interaction of the slowing growth rates of haloes (after the peak) and the star formation timescale (set by the ISM physics) which limits the rate at which the galaxy can respond to convert in-falling material into stars (before the peak).

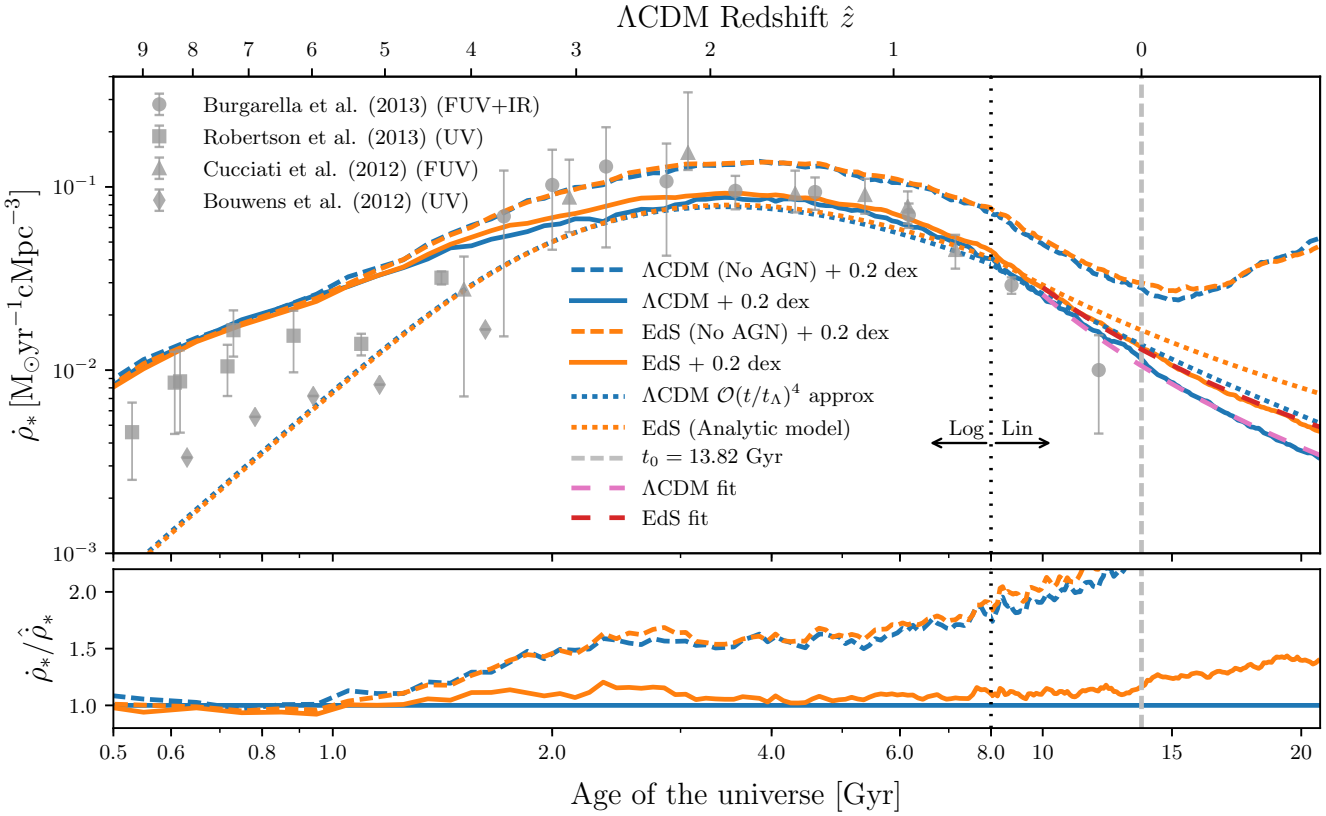

Fig. 3.8.: Global SFR densities. The EAGLE reference and the EdS models are shown in solid blue and orange lines respectively. Observational data from Cucciati et al. (2012) [FUV], Bouwens et al. (2012) [UV], Robertson et al. (2013) [UV] and Burgarella et al. (2013) [FUV + FIR] are shown as symbols. The EAGLE reference simulation (solid blue) reproduces the shape of the observed SFR density remarkably well, with a small offset of 0.2 dex at $t \gtrsim 2$ Gyr (for clarity, all EAGLE models have been shifted by 0.2 dex). The analytical model of Eqs. (3.24) and (3.25) is shown with dotted lines for both cosmologies. Power law fittings for the SFR density for $t > 8$ Gyr, as per Eq. (3.30), for the ΛCDM and EdS models are shown in pink and red lines respectively. The horizontal time axis has been plotted in a logarithmic scale for $t \leq 8$ Gyr changing to a linear scale for $t > 8$ Gyr. The black vertical dotted line shows the transition from logarithmic to linear scale.

Table 3.5.: Power law parameter fitting for the median SFR shown in Fig. 3.8.

Model	a	c	k
	$[M_\odot yr^{-1} cMpc^{-3}]$	$[Gyr^{-1}]$	
ΛCDM	5.42	0.81	2.77
EdS	3.99	0.94	2.41

The SFR history predicted by the simple model developed in Section 3.2.5 (dotted curves) is in remarkable agreement with the observational data and predicts the relative difference of the cosmological simulations, both at the present time, and into the future. We want to emphasise that the model is not a parametric fit to the data, but rather an analytical model derived from a simple relation of star formation to halo mass accretion.

3.5.2 The future of the cosmic star formation rate ($t > 13.8$ Gyr)

In order to explore whether the relative SFR densities will diverge as the impact of Λ becomes more pronounced, we ran the simulations for both cosmological models into the future (i.e. beyond a cosmic time of $t = 13.8$ Gyr). As the simulations run into the future, the small differences seen at $t = 13.8$ Gyr become larger, reading an ≈40% difference at $t = 1.5 \times t_0 = 20.7$ Gyr, which is in agreement with the predictions shown in Fig. 3.5.

The decline in the SFR density can be approximated by a power law for both the reference ΛCDM and EdS models (red and pink dashed lines),

$$\dot{\rho}_* = a(ct)^{-k}, \tag{3.30}$$

with the parameters a, c and k given in Table 3.5. We used the reduced chi-squared statistic for goodness of fit testing. We use this fitting function to extrapolate the results from the simulations further into the future.

We note here a striking feature of the universes with no BH feedback: the SFR increases again in the future, both for the ΛCDM and EdS cosmologies. In Section 3.5.4 we discuss how this effect originates from massive galaxies ($M_* > 10^{11} M_\odot$) that rejuvenate in the future. As it is not clear from the simulation whether

the SFR will continue to rise, or when it would start declining, we have not fitted any functional form to the "No AGN" models.

3.5.3 The stellar mass density

To study the build up of stellar mass, we present the growth in stellar mass density, ρ_*, across cosmic time in Fig. 3.9. The colour coding is the same as in Fig. 3.8. The lower panel shows the ratio of the stellar density compared to the reference ΛCDM model. Furlong et al. (2015) show that the reference EAGLE simulation is in good agreement with the observed growth of stellar mass across cosmic time. In contrast to Furlong et al. (2015), where the stellar mass density was obtained from aperture measurements to facilitate comparison with observations, we calculate ρ_* by integrating the SFR density from Fig. 3.8,

$$\rho_* = \int_0^t \dot{\rho}_* \mathrm{d}t', \tag{3.31}$$

in order to provide an estimate of the total mass of stars produced by the universe[8]. For the models with AGN feedback, we have extrapolated the power law fit described in Section 3.5.1 far into the future, up to 10 trillion years, and considered this as the "Total stellar mass density" of the universe. As suggested by the analytic model in Eq. (3.25), in universes with feedback from star formation and AGN, the cosmic SFR density is expected to continue decreasing into the future. At late times, the SFR becomes orders of magnitude lower than that of the peak at 3.5 Gyr. Figure 3.9 shows that the total stellar mass density is dominated by the contribution from the peak in star formation and reaches a plateau at $t \approx t_0$. Hence, the formal uncertainties in the extrapolation into the future are unimportant for the predicted total stellar mass density. The right-hand axis of Fig. 3.9 represents the percentage of the total stellar density compared to ΛCDM. For the reference ΛCDM model, the universe has already produced most ($\approx$88%) of its eventual stellar mass by the present day, adding up very little stellar mass into the future. Although there is no Λ to slow down the formation of cosmic structure, the EdS model closely resembles a ΛCDM cosmology with only $\approx$15% more stellar mass produced.

As discussed in Section 3.3.3, a universe with Λ has a very different expansion history compared to one without dark energy. This produces a different growth of

[8] As we are interested in total mass of stars *produced* by the universe, Eq. (3.31) ignores stellar mass loss.

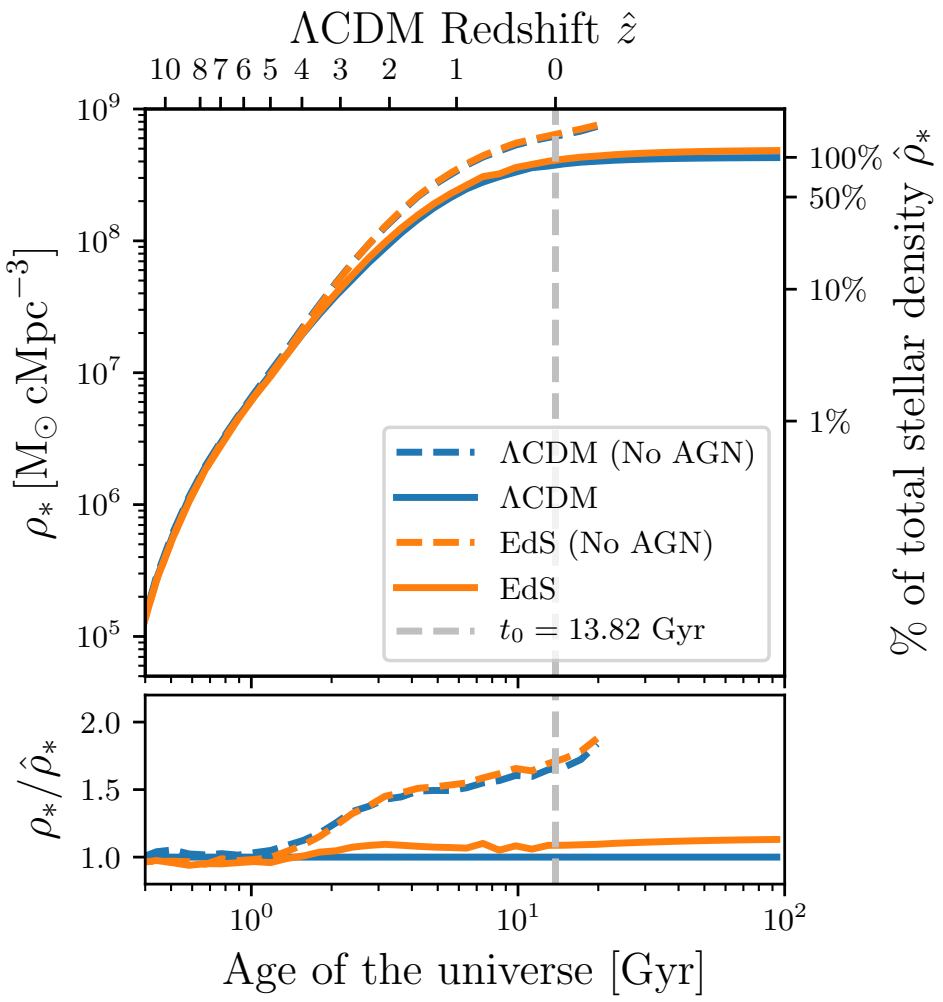

Fig. 3.9.: The stellar mass density as a function of time in the EAGLE simulation models. The colour coding is the same as in Fig. 3.8. The right-hand axis represents the percentage of the total stellar density compared to the ΛCDM model. Both the ΛCDM and EdS models have already produced most of the stars in the universe by the present day, building up very little stellar mass into the future. The models without AGN feedback quickly deviate from the reference model, producing almost twice the mass in stars by the end of the simulation (≈20.7 Gyr). The figure shows that the effect of dark energy on the overall star formation is negligible.

density perturbations, in particular into the future (see Figs. 3.1 and 3.2). Nevertheless, as seen in Fig. 3.9, since both cosmologies have already produced most of the stars in the universe by the present day, when the contribution of Λ is becoming increasingly important, the effect of dark energy on the overall star formation, is negligible.

In contrast, the models without feedback from BHs (dashed curves) quickly deviate from the reference model, starting from $t \sim 1$ Gyr, producing almost twice the mass in stars by the end of the simulations, 20.7 Gyr after the Big Bang.

3.5.4 Other galaxy population properties

In this section we will compare the galaxy population properties of the two simulation models at the present time, and into the future. In particular, we compare the galaxy stellar mass function (GSMF), and the specific star formation rate (SSFR) of galaxies. To compare with observational data, in each of the figures discussed below, the left panel shows properties at $t = 12.5$ Gyr, equivalent to redshift $\hat{z} = 0.1$ for an observer at the present time in a ΛCDM universe. The right panel shows the same property but at $t = 1.5 \times t_0 = 20.7$ Gyr. To guide the eye, each property for the reference ΛCDM model at $t = 12.5$ Gyr is plotted with a black line in each plot at $t = 1.5 \times t_0 = 20.7$ Gyr. Finally, we have also included the ratios of each quantity to the reference ΛCDM model at the corresponding time at the bottom of each panel.

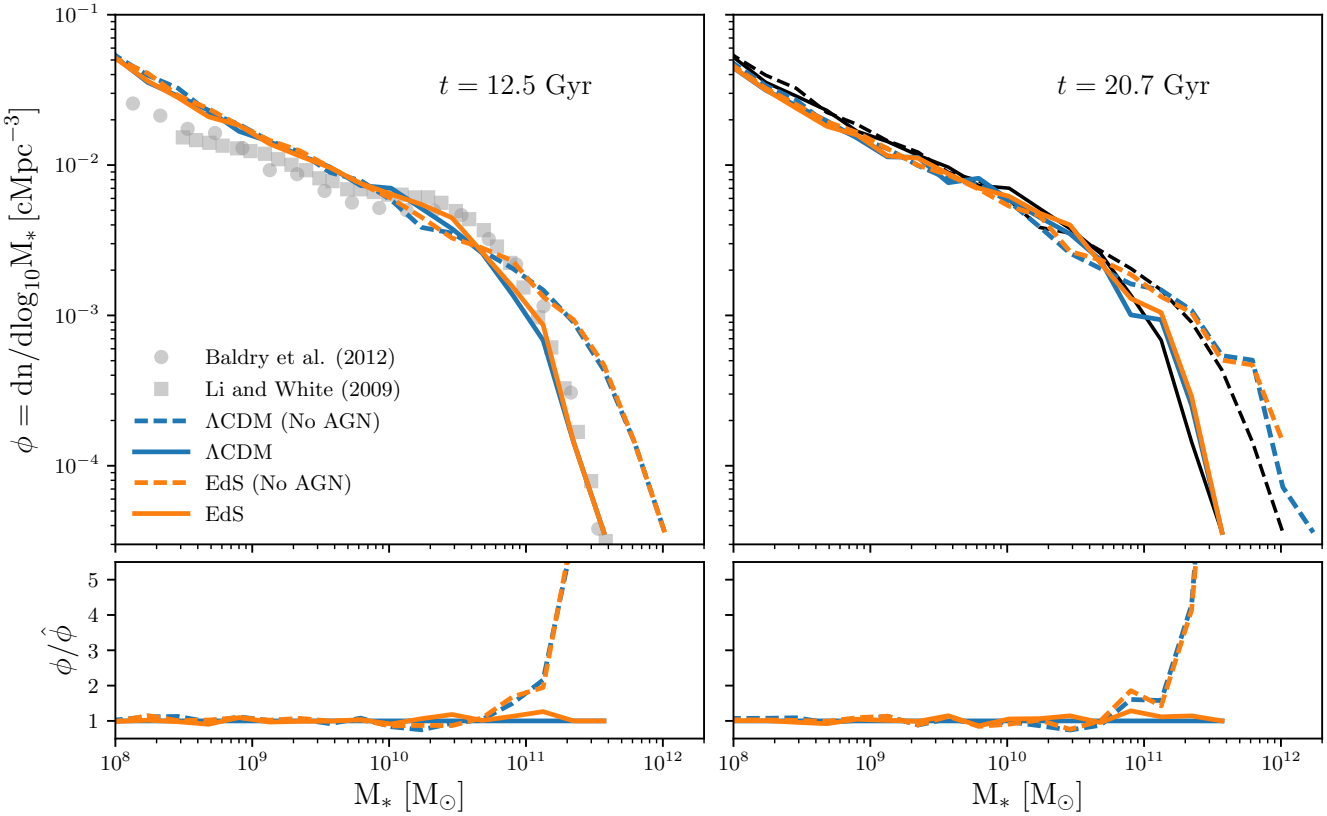

Fig. 3.10.: The GSMF at $t = 12.5$ Gyr, equivalent to redshift $\hat{z} = 0.1$ for an observer at the present time in a ΛCDM universe (left), and $t = 1.5 \times t_0$ (right) for the EAGLE simulation models. The colour coding is the same as in Fig. 3.8. Observational data from Baldry et al. (2012) and Li & White (2009) is shown as symbols. The reference and "No AGN" ΛCDM models at $t = 12.5$ Gyr are plotted in the right panel for reference (solid and dashed black lines respectively). The effect of dark energy on the GSMF is negligible, with very little evolution into the future. As expected, the models without AGN feedback predict a higher number density of massive galaxies ($M_* > 10^{11}\mathrm{M}_\odot$). This effect becomes more significant into the future, going from ≈0.7 dex to ≈1.1 dex.

The galaxy stellar mass function

The effect of Λ on the GSMF can be seen in Fig. 3.10. The colour coding is the same as in Fig. 3.8. For comparison, observational data from Baldry et al. (2012) and Li & White (2009) is shown as well. As discussed in Schaye et al. (2015), the observed GSMF at redshift 0.1 was used to infer the free parameters of the subgrid physics used in the simulation. The reference EAGLE model reproduces the shape of the observed GSMF reasonably well, with a slight under-abundance of galaxies at its knee.

Figure 3.10 shows that the effect of Λ on the GSMF is negligible, with very little evolution into the future. The models without AGN feedback predict a higher number density of massive galaxies ($M_* > 10^{11}\mathrm{M}_\odot$) compared to the models with AGN feedback. This effect becomes more significant into the future, going from 0.7 dex to 1.5 dex. The origin of this difference is explored in the next section.

Specific star formation rates

Galaxies can be broadly classified into largely distinct star-forming and passive populations according to their SSFR,

$$\mathrm{SSFR} = \frac{\dot{M}_*}{M_*}. \tag{3.32}$$

For star-forming galaxies, there is a well-defined star forming sequence, with SSFR observed to be approximately constant as a function of stellar mass (e.g. Noeske et al., 2007; Karim et al., 2011). Figure 3.11 shows the SSFR for star-forming galaxies in the simulations as a function of galaxy stellar mass at the present day, and into the future. The colour coding is the same as in Fig. 3.8. The horizontal dotted lines correspond to the SSFR cut (10^{-2} Gyr^{-1}) used to separate star forming from passive galaxies in our Universe. For comparison, observational data from Gilbank et al. (2010) is shown as well. Furlong et al. (2015) show that the SFFR in the reference simulations at the present day is similar to observations in the local universe, with an offset of 0.3 dex. This is possibly consistent with the systematic uncertainties in the calibration of the observation diagnostics. At low masses there is an increase in SSFR with stellar mass; however, this has been found

to be a resolution-dependent effect. Hence, we have plotted the results with lighter coloured lines (similar to Schaye et al., 2015). The models without feedback from AGN have higher SSFR for $M_* > 10^{10}\mathrm{M}_\odot$, whereas the effect of Λ on the SSFR of galaxies is negligible.

Figure 3.11 shows the galaxy population property that has the strongest evolution into the future. We find that over the next 6.8 Gyr the SSFR will drop by $\approx$0.4 dex.

Interestingly, the models without AGN feedback predict an increase of the SSFR of galaxies with $M_* > 10^{11}\mathrm{M}_\odot$ in the future. The figure shows that the increase in SFR shown in Fig. 3.8, and the higher number density of massive galaxies in Fig. 3.10, originate from massive galaxies that rejuvenate in the future. A plausible explanation for this phenomenon is that, according to simple radiative cooling models, in massive galaxies and clusters, a hot gaseous atmosphere should lose energy by the emission of radiation, and if there is no heating mechanism to compensate the cooling (e.g. AGN feedback), cooling flows should form (Fabian, 1994; Peterson & Fabian, 2006), triggering star formation. This result will be explored in more detail in a follow-up paper.

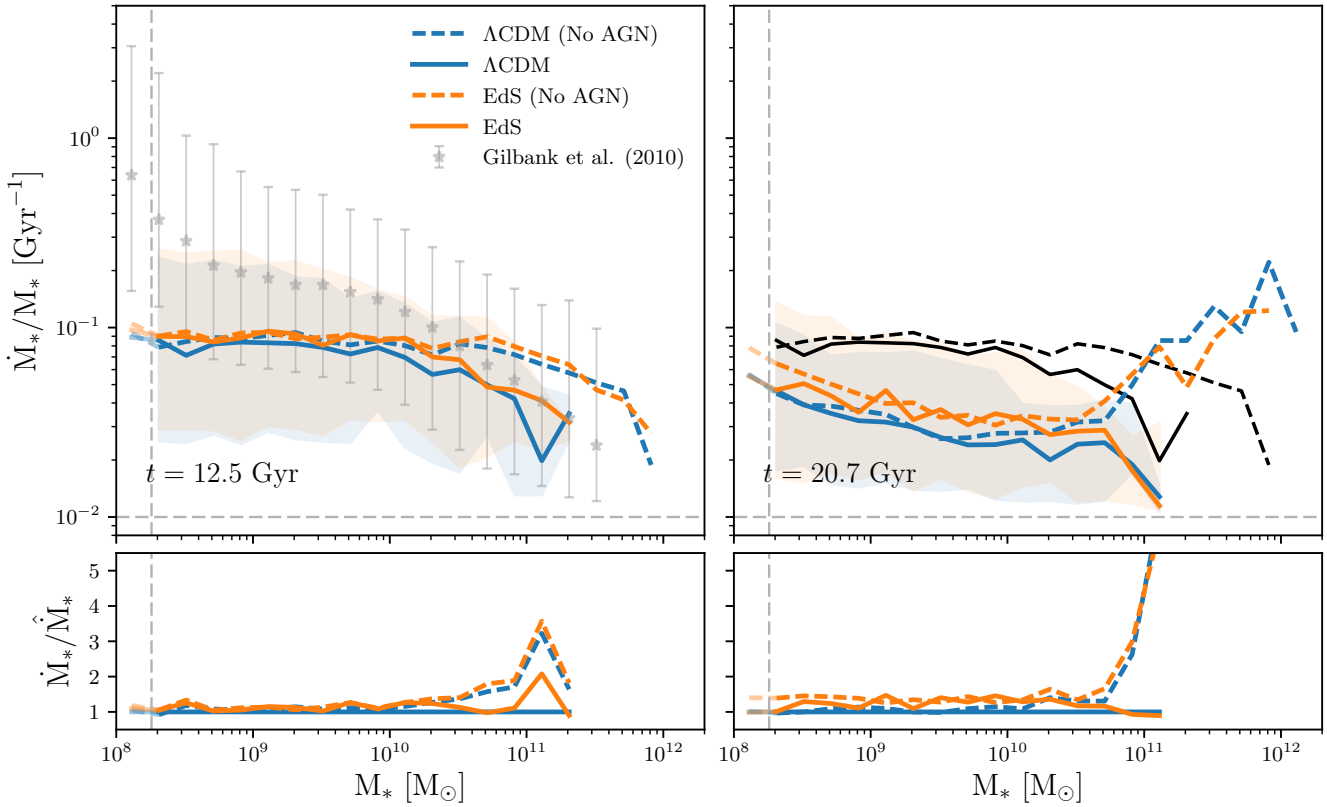

Fig. 3.11.: The SSFR of star forming galaxies at $t = 12.5$ Gyr, equivalent to redshift $\hat{z} = 0.1$ for an observer at the present time in a ΛCDM universe (left), and $t = 1.5 \times t_0$ (right) for the EAGLE simulation models. The colour coding is the same as in Fig. 3.8. Observational data from Gilbank et al. (2010) is shown as symbols. The reference and "No AGN" ΛCDM models at $t = 12.5$ Gyr are plotted in the right panel for reference (solid and dashed black lines respectively). The solid curves show the median relation for star forming galaxies, defined as those with an SSFR above the limit specified by the horizontal dashed line (10^{-2}Gyr^{-1}). The faint shaded regions enclose the 10th to 90th percentiles for the ΛCDM and EdS Models. Lines are light coloured when the stellar mass falls below that corresponding to 100 baryonic particles, to indicate that resolution effects will be important. The figure shows that the effect of dark energy on the GSMF is negligible. The models without AGN feedback predict a higher SSFR for massive galaxies ($M_* > 10^{10}$M$_\odot$). The right panel shows that the overall SSFR drops from $t = 12.5$ Gyr to $t = 1.5 \times t_0$. For the "No AGN" models, however, the SSFR increases for massive galaxies ($M_* > 10^{11}$M$_\odot$).

3.6 Discussion and Conclusions

In this chapter, we explored the dependence of the star formation history of the universe on the existence of a cosmological constant and feedback from accreting BHs. We base our results on the EAGLE simulation code, that has been shown to compare favourably to observational data, and thus, to provide a good description of the formation of galaxies in our Universe. Feedback from supermassive BHs has been shown to be a key ingredient in achieving this match by suppressing star formation in massive haloes (e.g. Bower et al., 2006; Harrison, 2017), while the accelerating expansion rate of the Universe suppresses the accretion rates of haloes at late times (e.g. Jenkins et al., 1998; Huterer et al., 2015). Our study allows us to assess the relative importance of these ingredients.

The universes that we consider are indistinguishable at early times. They share a common epoch of equality and recombination, and have equal amplitudes and spectrum of density fluctuations at early times. We take care to compare the evolution of models with equivalent starting points, and to demonstrate that the simulation code correctly scales the different values of the present-day expansion rate (Hubble parameter). When comparing the universes, it is important that we compare properties at a fixed cosmic time. Since the processes of stellar (and biological) evolution provide a common clock, independent of the large-scale cosmological expansion, these provide an astrophysically relevant comparison.

We have also developed an analytic model derived from a simple relation of star formation to halo mass accretion rate. Despite its simplicity, the model reproduces the overall shape of evolution of the cosmic SFR density. The model and the simulations allow us to explore the effect of a cosmological constant term on the cosmic SFR density.

Our main conclusions are as follows:

- We find that the existence of the cosmological constant has little impact on the star formation history of the Universe. The SFR is suppressed by $\approx$15% at the present time, and we find that the properties of galaxies are almost indistinguishable in the two universes.

- To explore whether this is due to the relatively recent dominance of the dark energy density in our Universe, we continued the simulations 6.8 Gyr into the future. Even after this time, the co-moving SFR densities differ only by ≈40%. Clearly, the cosmological constant has only a marginal effect on the stellar content of the Universe.

- Using the analytic model, we can recognise that the existence of the peak in the SFR density results from the interaction of the star formation efficiency (set by the ISM physics) which limits the rate at which the galaxy can respond to convert in-falling material into stars, the relative abundance of efficiently star forming haloes (i.e. of masses $\approx 10^{12}\,M_{\odot}$), and only at late times, the slowing growth rates of haloes due to the cosmological constant.

- By extrapolating fits to the evolution of the co-moving SFR density into the future, we show that, in our Universe, more than ≈88% of the stars that will ever be produced, have already been formed by the present cosmic time. In the absence of dark energy, only ≈15% more stellar mass would have been formed in the same time. The difference is small, bringing into question whether the 'coincidence problem' (the comparable energy densities of matter and dark energy) can be explained by an anthropic argument: the existence of dark energy (at the observed value) has negligible impact on the existence of observers or the ability of humanity to observe the cosmos. In Barnes et al. (2018) we explore this argument in more detail by considering a wider range of Λ values, and determining the likelihood distribution of possible Λ values conditioning the existence of observers.

- In comparison, the existence of BHs has a major impact on the Universe. In the absence of AGN feedback, the co-moving SFR density is enhanced by a factor of 2.5 at the present day.

- Even in a universe without BHs or dark energy, we find that the co-moving SFR density peaks at 3.5 Gyr (z≈2 according to a present-day observer in our Universe). The decline in star formation is however slower at more recent times.

- For hypothetical universes without feedback from accreting BHs, there is a *comeback* of SFR, which increases again in the future. This effect originates

from massive galaxies ($M_* > 10^{11} M_\odot$) that rejuvenate as there is no heating mechanism to compensate the cooling, in turn, triggering star formation.

4 Galaxy formation efficiency and the Multiverse explanation of the cosmological constant

Models of the very early universe, including inflationary models, are argued to produce varying universe domains with different values of fundamental constants and cosmic parameters. Using the cosmological hydrodynamical simulation code from the EAGLE collaboration, we investigate the effect of the cosmological constant on the formation of galaxies and stars. We simulate universes with values of the cosmological constant ranging from $\Lambda = 0$ to $\Lambda_0 \times 300$, where Λ_0 is the value of the cosmological constant in our Universe. Because the global star formation rate in our Universe peaks at $t = 3.5$ Gyr, before the onset of accelerating expansion, increases in Λ of even an order of magnitude have only a small effect on the star formation history and efficiency of the universe. We use our simulations to predict the observed value of the cosmological constant, given a measure of the multiverse. Whether the cosmological constant is successfully predicted depends crucially on the measure. The impact of the cosmological constant on the formation of structure in the universe does not seem to be a sharp enough function of Λ to explain its observed value alone.

This chapter has been published as a paper in Monthly Notices of the Royal Astronomical Society (MNRAS):

- *Galaxy formation efficiency and the multiverse explanation of the cosmological constant with EAGLE simulations*
  Barnes, L., Elahi, P. J, **Salcido J.**, Bower R. G., Lewis, G. F., Theuns, T., Schaller, M., Crain, R. A., Schaye, J., MNRAS 2018, Volume 477, Issue 3, Pages 3727-3743

The simulations and data analysis described in this chapter are the direct work of the author, in collaboration with the supervisors named above, along with other researchers at the University of Sydney, Western Sydney University and the University of Western Australia.

4.1 Introduction

Cosmological inflation, it has been argued, naturally predicts a vast ensemble of varying universe domains[1], each with different cosmic conditions and even different fundamental constants (see the review of Linde, 2017). A typical mechanism for generating these universes is as follows (Guth, 2007). The inflaton field undergoes quantum fluctuations, and so we might expect some parts of the universe to still be inflating while other parts have entered a post-reheating "big bang" phase. The universe as a whole consists of post big-bang universes filled with ordinary matter and radiation, surrounded by an ever-inflating background.

In evaluating such models, predicting what we would expect to observe is necessarily tied to where observers are formed in the multiverse. In this instance, anthropic reasoning is inevitable (Carter, 1974; Carr & Rees, 1979; Davies, 1983; Barrow & Tipler, 1986). With different cosmic and fundamental constants in different parts of the multiverse, the values we expect to observe are unavoidably tied to their ability to support the complexity required by life.

These multiverse models could successfully explain the fine-tuning of the universe for life: small changes in their values can suppress or erase the complexity upon which physical life as we know it, or can imagine it, depends. The scientific literature on the fine-tuning of the universe for life has been reviewed in Hogan (2000); Barnes (2012); Schellekens (2013); Meißner (2014); Lewis et al. (2016). For example, as pointed out by Davies & Unwin (1981); Sakharov (1984); Linde (1984); Banks (1985); Linde (1987); Weinberg (1987, 1989), only a small subset of values of the cosmological constant (Λ) permit structure to form in the universe at all. Universes in which the cosmological constant is large and positive will expand so rapidly that gravitational structures, such as galaxies, are unable to form. Large negative values will cause space to recollapse rapidly, also preventing the formation of galaxies.

If inflation creates a huge number of variegated universe domains, then a structure-permitting value of the cosmological constant will probably turn up *somewhere*. Any observers will see a universe with at least some structure. In thus way, the seemingly improbable suitability of our universe for life is rendered more probable.

[1] For simplicity, we call such regions "universes".

As Weinberg (1987) noted, we can test a particular multiverse model via its prediction of the distribution of universe properties. Observers will inhabit universes drawn in a highly-biased way from the population of universes, but we can calculate the typical properties of a universe that contains observers. In this way, we can calculate the likelihood of our observations, and so compare multiverse models. For example, a model in which 99% of observers measure a value of the cosmological constant as large as our value should (other things being equal) be preferred over a model in which only 1% of observers make such a measurement. Whether these consistency tests can give absolute (rather than just relative) support to the idea of a multiverse is the subject of some debate (Ellis & Silk, 2014; Barnes, 2017).

To test the relative merits of multiverse models in this way, we need to know how life, or at least the cosmic structures that are the likely preconditions for life, depend on the fundamental constants of nature and cosmic parameters. In the case of the cosmological constant, the large-scale structure of the universe is most directly affected. Galaxies are the sites of star formation, and stars provide both a steady source of energy and the heavier elements from which planets and life forms are made.

Within an anthropic approach, we can also shed light on the coincidence problem: we live at a time in the universe when the energy density of the cosmological constant and the energy density of matter are within a factor of two of each other (Lineweaver & Egan, 2007). The coincidence problem has motivated a search to alternative modification to gravity that might explain the value of the cosmological constant more naturally. Although, alternative models, such as quintessence can explain why the relative densities of matter and cosmological constant densities track each other, fine tuning of the model parameters is still required to explain their observed similarity (Zlatev et al., 1999; Zlatev & Steinhardt, 1999; Dodelson et al., 2000; Chimento et al., 2003).

Investigations of the effect of the cosmological constant on galaxy formation have thus far relied on analytic models of increasing levels of sophistication. Efstathiou (1995) located galaxies at the peaks of the smoothed density field of the universe, and found that — assuming that the cosmological constant is positive, observers should expect to see $\Omega_\Lambda \approx 0.67 - 0.9$. Peacock (2007) extended this approach to negative values of the cosmological constant, finding a significant probability that $\Omega_\Lambda < 0$ is observed. These approaches have been extended by Garriga & Vilenkin

(2000); Garriga et al. (2000); Tegmark et al. (2006); Bousso & Leichenauer (2009, 2010); Piran et al. (2016); Sudoh et al. (2017); Adams et al. (2017).

The modern approach to galaxy formation uses supercomputer simulations that incorporate the effects of gravity, gas pressure, gas cooling, star formation, black hole formation, and various kinds of feedback from stars and black hole accretion. It has been long known that feedback is very important to explaining the star formation history of our universe; models without feedback are too effective at forming stars, compared to observations (White & Rees, 1978; Dekel & Silk, 1986; White & Frenk, 1991; Somerville & Davé, 2015). One of the key ingredients that has allowed this progress is the inclusion of realistic models for the impact of feedback from the growth of black holes. All successful models now demonstrate the need for Active Galactic Nuclei (AGN) as an additional source of feedback that suppresses the formation of stars in high-mass haloes (Benson et al., 2003; Croton et al., 2006; Bower et al., 2006). Although this idea was initially developed using semi-analytic models, this has now been confirmed in a wide range of numerical simulations (eg. Dubois et al., 2016; Bower et al., 2017; Pillepich et al., 2018).

Here, we will use the EAGLE project's galaxy formation code to calculate the effect of the cosmological constant on the formation of structure in different post-inflation universes. Each of our models will be practically indistinguishable at early times, including nucleosynthesis and the epoch of recombination. Their histories diverge at later times due to the onset of cosmological constant-powered accelerating expansion. In Section 4.2, we describe the EAGLE galaxy formation code and the suite of simulations that we have run. In Section 4.3, we describe the effect of changing the cosmological constant on the global accretion and star-forming properties of the universe. Section 4.4 looks at the effect on an individual galaxy, and its relation to its environment. In Section 4.5, we use our simulations to derive prediction from models of the multiverse.

4.2 Galaxy Formation Simulation Code

The Virgo Consortium's EAGLE project (*Evolution and Assembly of GaLaxies and their Environment*) is a suite of hydrodynamical simulations that follow the formation of galaxies and supermassive black holes in cosmologically representative volumes of a standard ΛCDM universe. The details of the code, and particularly the

sub-grid models, are described in Schaye et al. (2015), and are based on the models developed for OWLS (Schaye et al., 2010), and used also in GIMIC (Crain et al., 2009) and cosmo-OWLS (Le Brun et al., 2014). The simulations code models the effect of radiative cooling for 11 elements, star formation, stellar mass loss, energy feedback from star formation, gas accretion onto and mergers of supermassive black holes (BHs), and AGN feedback.

The initial conditions for the EAGLE simulations were set up using a transfer function generated using CAMB (Lewis et al., 2000) and a power-law primordial power spectrum with index $n_s = 0.9611$. Particles were arranged in a glass-like initial configuration were displaced according to second-order Lagrangian perturbation theory (Jenkins, 2010).

Black holes are seeded in all dark matter haloes with masses greater than $10^{10} h^{-1}\,\mathrm{M}_\odot = 1.48 \times 10^{10}\,\mathrm{M}_\odot$. The halo finding algorithm is described in Schaye et al. (2015); in short, the code regularly runs the friends-of-friends (FoF) finder (Davis et al., 1985) with linking length 0.2 on the dark matter distribution. When analysing the simulations in following sections, we are interested in membership with any halo, rather than distinguishing substructures, so we use the FOF algorithm to identify haloes.

4.2.1 Cosmological Parameters and Scale Factor

We need to choose the cosmological parameters for our simulation. The problem with the standard set of cosmological parameters ($\Omega_m, \Omega_\Lambda, \Omega_b, h$) is that they are all time dependent. In the model universes that we will consider, there is no unique "today" at which we can compare sets of parameters. We follow Tegmark et al. (2006) by defining cosmological parameters that are constant in time. We use only one time-dependent parameter, which is cosmic time t. The constant parameters are listed in Table 4.1. Note that the cosmological constant (Λ) and its associated energy density are related linearly, $\Lambda = 8\pi G \rho_\Lambda / c^2$.

Table 4.1.: Free parameters in the FLRW model, defined so that they are constant in time, at least since very early times. The measured value derives from the Planck Collaboration et al. (2014) cosmological parameters, as used by the EAGLE project: $(\Omega_m, \Omega_\Lambda, \Omega_b, h, \sigma_8, n_s, Y) = (0.307, 0.693, 0.04825, 0.6777, 0.8288, 0.9611, 0.248)$.

Parameter		Measured value
ρ_Λ	Cosmological constant energy (mass) density	5.98×10^{-27} kg m^{-3}
ξ_b	Baryon mass per photon ρ_b/n_γ	1.01×10^{-36} kg m^{-3}
ξ_c	Cold dark matter mass per photon ρ_c/n_γ	5.43×10^{-36} kg m^{-3}
κ	Dimensionless spatial curvature (in Planck units) $k/a^2T_0^2$	$\lvert\kappa\rvert \lesssim 10^{-60} \approx 0$

How do we solve the Friedmann equations, given the dimensionless cosmological parameters in Table 4.1, so that we can derive the usual cosmological parameters for the simulation? We have the freedom to choose "today", that is, we can rescale $a(t)$ to make $a(t_0) = 1$ for any time t_0. A useful way to proceed initially is to define t_0 to be the time at which the energy densities of the cosmological constant and matter are equal. Then, we calculate the matter densities,

$$\rho_{\mathrm{m},0} = \rho_\Lambda \tag{4.1}$$

$$\xi_\mathrm{m} \equiv \xi_\mathrm{b} + \xi_\mathrm{c} \;\Rightarrow\; \rho_{\mathrm{b},0} = \frac{\xi_\mathrm{b}}{\xi_\mathrm{m}}\rho_{\mathrm{m},0}\,; \quad \rho_{\mathrm{c},0} = \frac{\xi_\mathrm{c}}{\xi_\mathrm{m}}\rho_{\mathrm{m},0} \tag{4.2}$$

Then, we calculate the photon number density at t_0, and from it the CMB temperature (T_0) and the radiation (photons and neutrinos) energy density,

$$n_{\gamma,0} = \rho_{\mathrm{b},0}/\xi_\mathrm{b} = \rho_{\mathrm{c},0}/\xi_\mathrm{c} = \rho_{\mathrm{m},0}/\xi_\mathrm{m} \tag{4.3}$$

$$n_{\gamma,0} = \frac{2\zeta(3)}{\pi^2}\left(\frac{k_B T_0}{\hbar c}\right)^3 \tag{4.4}$$

$$\rho_{\mathrm{r},0} = g\frac{\pi^2}{30}k_B T_0\left(\frac{k_B T_0}{\hbar c}\right)^3 \tag{4.5}$$

$$\text{where} \quad g = 2 + 2\,\frac{7}{8}\,3\,\left(\frac{4}{3}\right)^{4/3}\,. \tag{4.6}$$

We can then solve the Friedmann equation,

$$H^2 = \left(\frac{1}{a}\frac{\mathrm{d}a}{\mathrm{d}t}\right)^2 = \frac{8\pi G}{3}(\rho_\mathrm{m} + \rho_\mathrm{r} + \rho_\Lambda + \rho_k) \tag{4.7}$$

$$= \frac{8\pi G}{3}(\rho_{\mathrm{m},0}a^{-3} + \rho_{\mathrm{r},0}a^{-4} + \rho_\Lambda + \rho_{k,0}a^{-2}) \tag{4.8}$$

$$\text{where} \quad \rho_k = -\kappa\frac{3}{8\pi G}\left(\frac{k_B T_0}{\hbar}\right)^2\,. \tag{4.9}$$

We can calculate the critical density, $\rho_{\mathrm{crit},0} = 3H_0^2/8\pi G = \rho_{\mathrm{m},0} + \rho_{\mathrm{r},0} + \rho_\Lambda + \rho_{k,0}$ and then the usual cosmological parameters $\Omega_\mathrm{m} = \rho_{\mathrm{m},0}/\rho_{\mathrm{crit},0}$, and similarly for Ω_r, Ω_c, Ω_b, Ω_Λ, and Ω_k. With these parameters, FLRW codes can solve the Friedmann equations[2].

[2]There are two potential complications. If we consider a universe with no cosmological constant ($\rho_\Lambda = 0$) then the choice of "initial" matter density is effectively arbitrary. Secondly, if the universe recollapses, then it may never reach the time at which $\rho_{\mathrm{m},0} = \rho_\Lambda$. The most general way to find some matter density at which we can apply the technique above is to write the Friedmann equation in terms of the CMB temperature T_0. We can then solve for the CMB temperature at turnaround $H(t) = 0$, and from this calculate the minimum matter density of the universe.

Having solved the Friedmann equations for $a(t)$, we can rescale to change the time of "today" to be any other time (t_0'): $a_{\rm new}(t) = a(t)/a(t_0')$, and recalculate the various density parameters appropriately. We will describe our choices for the normalisation of $a(t)$ in Sections 4.2.3and 4.2.4.

4.2.2 Initial Conditions and Sub-Grid Physics

We use the same initial conditions for each simulation. For the range of cosmological constants we consider here, there has been minimal effect on the evolution of the universe at the start of the simulation. Specifically, we use the same initial conditions for the SPH particles *in physical coordinates*: in the EAGLE code, like its GADGET ancestor, we need to convert code quantities into physical quantities taking into account the initial scale factor (a_i) and the Hubble parameter (h) of the original simulation: distance ($d_{\rm phys} = a_i h^{-1} d_{\rm code}$), velocity ($v_{\rm phys} = v_{\rm code}\sqrt{a_i}$), and mass ($m_{\rm phys} = h^{-1} m_{\rm code}$).

We must also be careful regarding parameters in our sub-grid physics recipes. The sub-grid physics of the EAGLE code has been checked, and the necessary parameters rescaled as necessary to keep the same *physical* values. We also discovered a few cases in which it was assumed that $\rho_\Lambda \neq 0$, which needed to be remedied for the test runs below.

Note the assumptions that we are making when we change the cosmological constant, but keep the physical parameters of the subgrid model unchanged. This is potentially worrisome, given that these parameters are often inferred, not from first principles, but by calibrating against observations of galaxy populations in our Universe. Our assumptions are twofold. First, we assume that the subgrid model is sufficiently sophisticated that it captures the relevant physics. For example, we assume that star formation in any cosmology occurs when the local density is sufficiently high. It is appropriate to apply such a model to other universes. Secondly, we assume that the parameters inferred from observations are the same as would be inferred from a first-principles calculation; they do not depend on the cosmological constant for such small-scale processes. For example, the *local* matter density above which star formation occurs should only depend on conditions within 10-100pc scale molecular clouds, far below cosmological scales. We can plausibly use the same threshold for different cosmologies.

Using the same subgrid parameters would create a problem only if our overall cosmology is wrong, for it could be the case that we have inferred the wrong value of some subgrid parameter to partially compensate for an incorrect expansion history of the universe. In this case, of course, the entire EAGLE simulation suite would need to be redone, as would almost every other cosmological simulation. We will leave that worry for another day.

4.2.3 Testing our Modifications

The freedom to choose "today" t_0 in our simulation gives us a way to confirm that our modifications are correct. Setting $\rho_\Lambda = 0$ and $\kappa = 0$, and noting that ρ_r is negligible for the time covered by the simulation, we simulate structure formation in an Einstein de-Sitter (EdS) Universe. We can use this freedom to define three different sets of simulation initial conditions.

A. The initial time of the simulation has the same scale factor as the corresponding Planck cosmology simulation, $a_{i,A} = 1/(1 + z_{i,A}) = 1/128$. We solve for the proper initial time $t_{\rm init}$ in the Planck cosmology, and then require that $a_{\rm EdS}(t)$ is normalised so that $a_{\rm Planck}(t_{\rm init}) = a_{\rm EdS}(t_{\rm init})$. This requires that we set Hubble parameter to $h_A = 0.375$.

B. We alter the initial redshift of the simulation so that 'today' ($z = 0$, $a = 1$) is at $t_0 = 13.8$ Gyr. This requires that we set the initial redshift of the simulation to $z_{i,B} = 108$ and the Hubble parameter to $h_B = 0.4716$.

C. The Hubble parameter h of the simulation has the same value as the corresponding Planck cosmology simulation, $h_{\rm Planck} = 0.6777$. Having found the time in the EdS universe when $h_C = 0.6777$, we normalise the scale factor so that $a_{\rm EdS} = 1$ at that time. This requires that we set the initial redshift to $z_{i,C} = 85.4$.

The simulations A, B and C are trying to solve the same *physical* problem, and should produce the same properties of the universe as a function of proper time. If we have not correctly accounted for factors of h (Croton, 2013) or confused comoving/physical quantities in our calculations, then these two simulations should diverge. Inevitably, there will be numerical differences: because the "time" variable of the simulation is actually $\log a$, the time stepping is not identical.

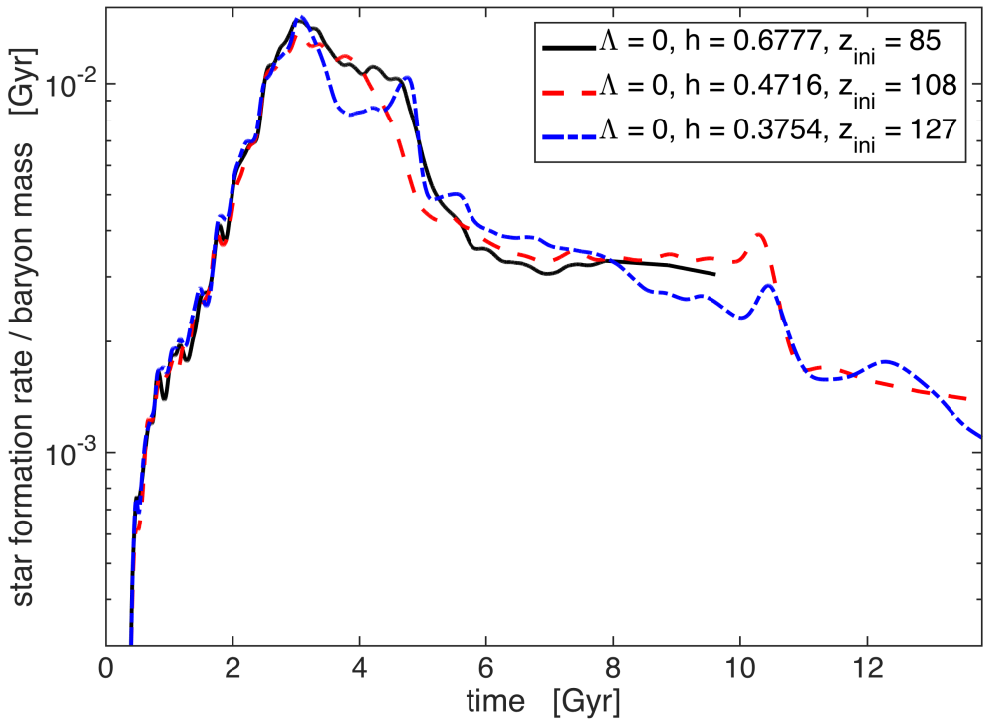

Fig. 4.1.: The star formation rate efficiency (that is, star formation rate divided by the total baryon mass in the simulation box), for three simulations with $\Lambda = 0$ but different choices for "today" (at which $a(t_0) = 1$). While there is scatter between the different simulations, they show an overall star formation history that is consistent. The scatter is comparible in magnitude to that caused by using a different seed for the random number generator associated with subgrid physics.

Figure 4.1 shows the star formation rate efficiency (that is, SFR divided by the total baryon mass in the simulation box), for three simulations (A, B and C) with $\Lambda = 0$. While there is scatter between the different simulations, they show an overall star formation history that is consistent. We have also run simulations that alter the seed for the random number generator. The scatter that this produces for a single set of parameters is similar in magnitude to the differences between the simulations A, B and C. We conclude that the code is functioning as expected.

In a companion paper (Salcido et al., 2018), we consider a more detailed comparison between the EdS cosmology and our universe, to quantify the effect of the cosmological constant on galaxy formation in our universe.

4.2.4 Simulation Suite

The EAGLE reference simulations used cosmological parameters measured by the Planck Collaboration et al. (2014). We run seven EAGLE simulations that modify the cosmological constant, while keeping the same baryon mass per photon (ξ_b), cold dark matter mass per photon (ξ_c), and spatial curvature ($\kappa = 0$) unchanged. We also use the same physical sub-grid parameters as the reference model. The values of the cosmological and numerical parameters used for the simulations are listed in Table 4.2.

As noted in Section 4.2.1, we can solve the Friedmann equations for $a(t)$ with an arbitrary normalisation, and then rescale appropriately. For our cosmological simulations, we choose the initial scale factor (or equivalently, redshift $z_{\rm initial}$) to be the same for all values of Λ. In our universe, $z_{\rm initial} = 127$ corresponds to a proper time of $t_{\rm init} = 11.5$ Myr. Thus, for a given value of Λ for which we have the scale factor $a(t)$ with any arbitrary normalisation, we rescale so that $a(t_{\rm initial}) = 1/(1 + z_{\rm initial})$.

In fact, we can solve for the new cosmological parameters $(H_0', \Omega_\Lambda', \Omega_{\rm m}')$ in terms of their values in our universe $(H_0, \Omega_\Lambda, \Omega_{\rm m})$ analytically in this case. We require the expansion of the universe to be the same at early times, which implies that $H_0^2\Omega_{\rm m}$ is equal for all universes. In addition, we increase the physical energy density of

dark energy by a factor f: $\Lambda_{\rm new} = f\Lambda_0$, which implies that $H_0'^2\Omega_\Lambda' = fH_0^2\Omega_\Lambda$. Combining these equations gives,

$$H_0' = H_0\sqrt{\Omega_{\rm m} + f\Omega_\Lambda} \qquad \Omega_{\rm m}' = \frac{\Omega_{\rm m}}{\Omega_{\rm m} + f\Omega_\Lambda} \tag{4.10}$$

Using these equations gives the cosmological parameters in Table 4.2, as a function of Λ.

We are interested in star formation across cosmic time, and so we want to run the simulation as far as possible into the future. This becomes increasingly difficult as the universe transitions into its era of accelerating expansion. The internal-time variable in the code is $\log(a)$, and when a begins to increase exponentially in cosmic time (t), it takes more and more internal-time steps to cover the same amount of cosmic time. Furthermore, because the internal spatial variable is *comoving* distance, objects that have a constant proper size are shrinking in code units. In our experience, in the accelerating era, the densest particles in the simulations are assigned very short internal-time steps. The simulation slows to a crawl, spending inordinate amounts of CPU time on a small number of particles at the centres of isolated galaxies.

In future work, we will look for ways to overcome these problems. Here, we have been able to run the simulation far enough into the future that, particularly for large values of the cosmological constant, quantities such as the collapse fraction and the fraction of baryons in stars have approached constant values. The endpoint of the $\Lambda_0 \times 30$, $\Lambda_0 \times 100$ and $\Lambda_0 \times 300$ simulations can be seen in the figures in following sections. We have captured the initial burst of galaxy and star formation in these universes, and the accelerating expansion of space makes any future accretion negligible. Each galaxy becomes a separate 'island universe'. Nevertheless, the far-future ($\gg$ 20 Gyr) fate of baryons in haloes is not captured by our simulations. Very slow processes that are difficult to capture in any simulation (let alone one in a cosmological volume) become relevant: gas cooling on very long time scales, a trickle of star formation, rare supernovae in low density environments, accretion of diffuse gas onto stellar remnants and black holes. These processes could be relevant to our models of observer creation over all of cosmic time; we will return to these issues in Section 4.5.3.

Table 4.2.: Cosmological and numerical parameters for our simulations: Box-size ("comoving", that is, the size of the box today in the Reference Λ_0 simulation), number of particles, and cosmic parameters ($h, \Omega_m, \Omega_b, \Omega_\Lambda$). (Larger 50 Mpc boxes were run and are analysed in more detail in Salcido et al. (2018). For our purposes, their results were consistent with the 25 Mpc simulations we use here.) Note that these numbers use the convention for 'today' defined in Section 4.2.4: the proper age of the universe when $a_{\rm initial} = 1/(1 + z_{\rm initial})$ is the same for all models. The parameter σ_8 is the rms linear fluctuation in the mass distribution on scales of 8 h^{-1} Mpc, calculated using CAMB (Lewis et al., 2000). Note that this parameter varies between cosmologies due to differences in the growth of matter fluctuations, and differences in the averaging scale due to the different values of h. As noted in Section 4.2.4, we do *not* run CAMB again to generate new initial conditions for each of our simulations; we use the same initial snapshot (particle positions and velocities) for each simulation. For all simulations, the initial baryonic and dark matter particle mass, "comoving" and Plummer-equivalent gravitational softening, and initial redshift are as follows: $m_{\rm gas} = 1.81 \times 10^6\,{\rm M}_\odot$, $m_{\rm DM} = 9.70 \times 10^6\,{\rm M}_\odot$, $\epsilon_{\rm com} = 2.66$ kpc, $\epsilon_{\rm prop} = 0.70$ kpc, $z_{\rm initial} = 127$. Not listed are the three simulations used for the convergence test (Figure 4.1), which use smaller boxes: $L = 12.5$ cMpc, $N = 2 \times 188^3$.

Sim. Name	L [cMpc]	N	h	Ω_m	Ω_b	Ω_Λ	σ_8
EdS_25 ($\Lambda = 0$)	25	2×376^3	0.3755	1.0	0.1572	0	0.6826
Ref_25 (Λ_0)	25	2×376^3	0.6777	0.307	0.04825	0.693	0.8288
$\Lambda_0 \times 3$	25	2×376^3	1.047	0.1287	0.0202	0.8713	0.8913
$\Lambda_0 \times 10$	25	2×376^3	1.823	0.0424	0.00667	0.9576	0.8955
$\Lambda_0 \times 30$	25	2×376^3	3.113	0.01455	0.00229	0.98545	0.8434
$\Lambda_0 \times 100$	25	2×376^3	5.654	0.00441	6.93×10^{-4}	0.99559	0.7476
$\Lambda_0 \times 300$	25	2×376^3	9.779	0.00147	2.32×10^{-4}	0.99853	0.6446

4.3 Changing the Cosmological Constant: Global Properties

We vary the cosmological constant between zero and several hundred times larger than the value in our Universe. We do not consider negative values of the cosmological constant here, as it would require significant changes to the time stepping in the code to handle the transition from expansion to contraction.

Figure 4.2 shows the deceleration parameter $q \equiv -\ddot{a}/(aH^2)$ and the linear growth factor $D(t)$ as a function of cosmic time, for different values of the cosmological constant. As the cosmological constant increases, the time at which the expansion of the universe begins to accelerate ($q < 0$) moves to earlier times as $t_{\rm accel} \sim 1/\sqrt{G\rho_\Lambda}$. Once accelerated expansion begins, the formation of structure freezes and accretion stops. We can see this in linear perturbation theory, where all modes grow in proportion to the growth factor $D(t)$; we normalise $D(t)$ so the curves are equal at early times, and $D(t_0) = 1$ in our Universe today. We see that once the expansion of the universe begins to accelerate, the growth factor approaches a constant, and structures ceases to grow.

In this section we will characterise the details of structure formation in these universes. Ordinarily, one describes these properties using comoving quantities, such as the comoving halo number density and comoving star formation rate density. One immediate problem is that the term "comoving" is meaningless when different universes are being compared. There is no "today" that is common to all models, relative to which we can define comoving volumes, densities and the like. There is nothing special, cosmically speaking, about 13.8 Gyr or 2.725 K. We can arbitrarily change the comoving density of star formation, for example, by choosing a different cosmic time in a given universe to be "today", which makes the comparison of comoving densities meaningless.

To overcome this, we will calculate quantities relative to the physical *mass* (total or baryonic) in the simulation box[3]. This provides a meaningful comparison between the simulated universes, and like comoving densities it does not automatically scale

[3] We could define comoving densities relative to the initial physical volume of the simulation box, which is the same in all models. But while this allows a meaningful comparison, the initial cosmic time is still arbitrary. Choosing an earlier time would increase all the "comoving" densities, which makes their value in a given universe difficult to interpret. Calculating specific (per unit mass) quantities overcomes this problem.

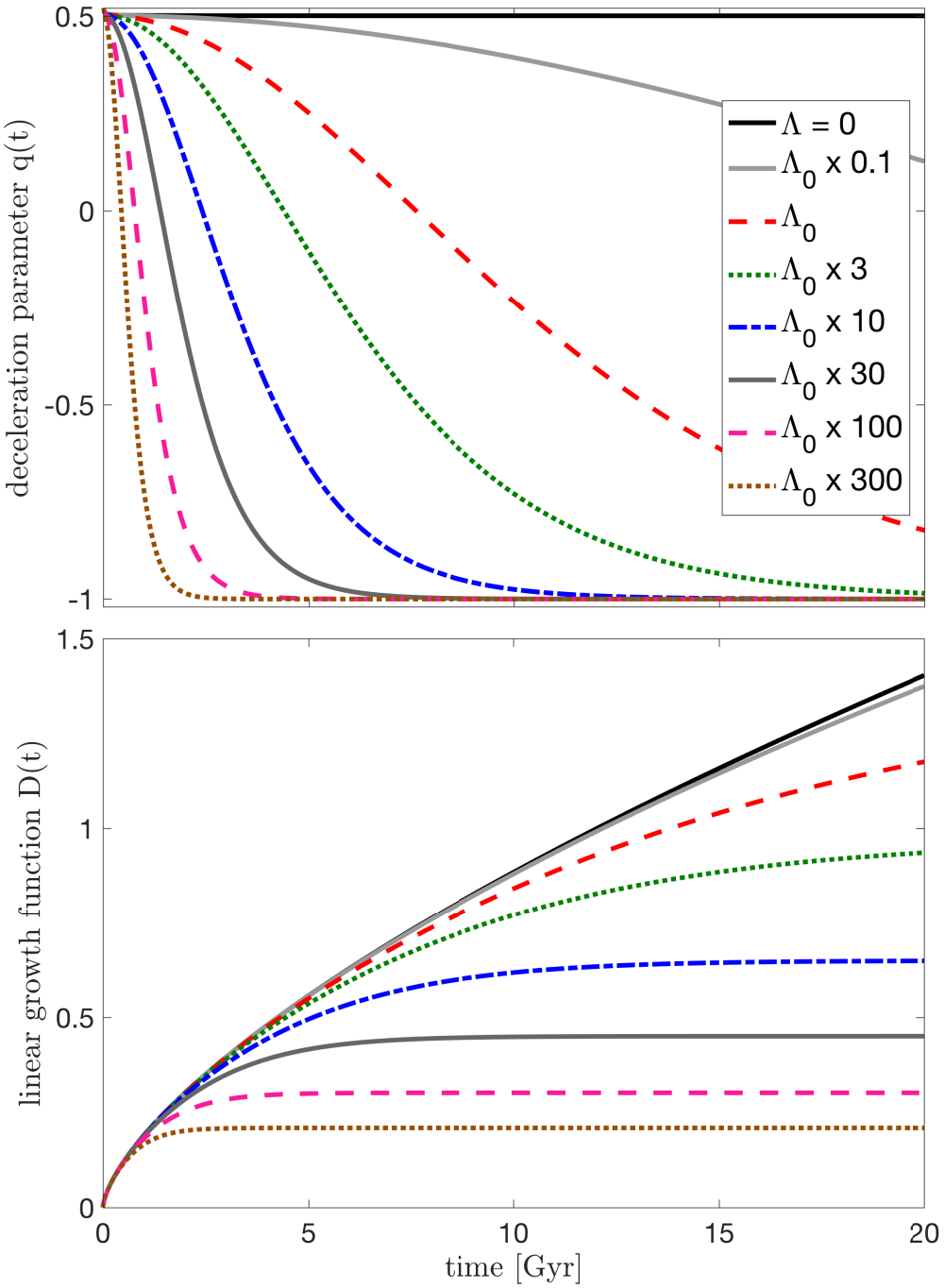

Fig. 4.2.: The deceleration parameter $q \equiv -\ddot{a}/(aH^2)$ (*top*) and the linear growth factor $D(t)$ (*bottom*) as a function of cosmic time, for different values of the cosmological constant. Note that $q = 1/2$ at all times for the $\Lambda = 0$ cosmology. As the cosmological constant increases, the time at which the expansion of the universe begins to accelerate ($q < 0$) moves to earlier times as $t_{\rm accel} \sim 1/\sqrt{G\rho_\Lambda}$. Once accelerated expansion begins, the formation of structure freezes and accretion stops, and $D(t)$ approaches a constant.

with expansion of the universe. We can ask, for example, what fraction of the total baryonic mass in the universe is in the form of stars as a function of cosmic time? What fraction has been converted into metals?

4.3.1 Mass accretion

Formally, in a cold dark matter universe, every particle is in a dark matter halo of *some* mass. That is, the collapse fraction of the universe is always unity; from Press & Schechter (1974) theory,

$$F(> M|t) = \mathrm{erfc}\left(\frac{\delta_{\mathrm{crit}}(t)}{\sqrt{2}\sigma(M,t)}\right), \tag{4.11}$$

where $F(> M|t)$ is the fraction of matter at cosmic time t that is part of a collapsed halo of mass greater than M, $\delta_{\mathrm{crit}}(t)$ is the critical linear overdensity of a collapsed object, and $\sigma(M,t)$ is the standard deviation of the cosmic matter field when smoothed on a scale that encloses mass M. The matter variance $\sigma(M,t) \to \infty$ as $M \to 0$, thus $F(> 0|t) = 1$ at all times.

In the simulation, however, there is a minimum dark matter halo mass that can be resolved by the particles. Given that each dark matter particle has mass $m_{\mathrm{DM}} = 9.7 \times 10^6\,\mathrm{M}_\odot$ and we require 32 particles to identify a halo, we can resolve haloes with mass greater than $m_{\mathrm{min}} = 3.1 \times 10^8\,\mathrm{M}_\odot$. Summing the total mass in these haloes, then, gives the collapse fraction for resolved haloes: $F(> m_{\mathrm{min}}|t)$. This approximately excludes haloes that are too small to form stars, so gives us the fraction of mass in the universe that resides in potentially star-forming haloes; the remainder can be considered as the inter-galactic medium.

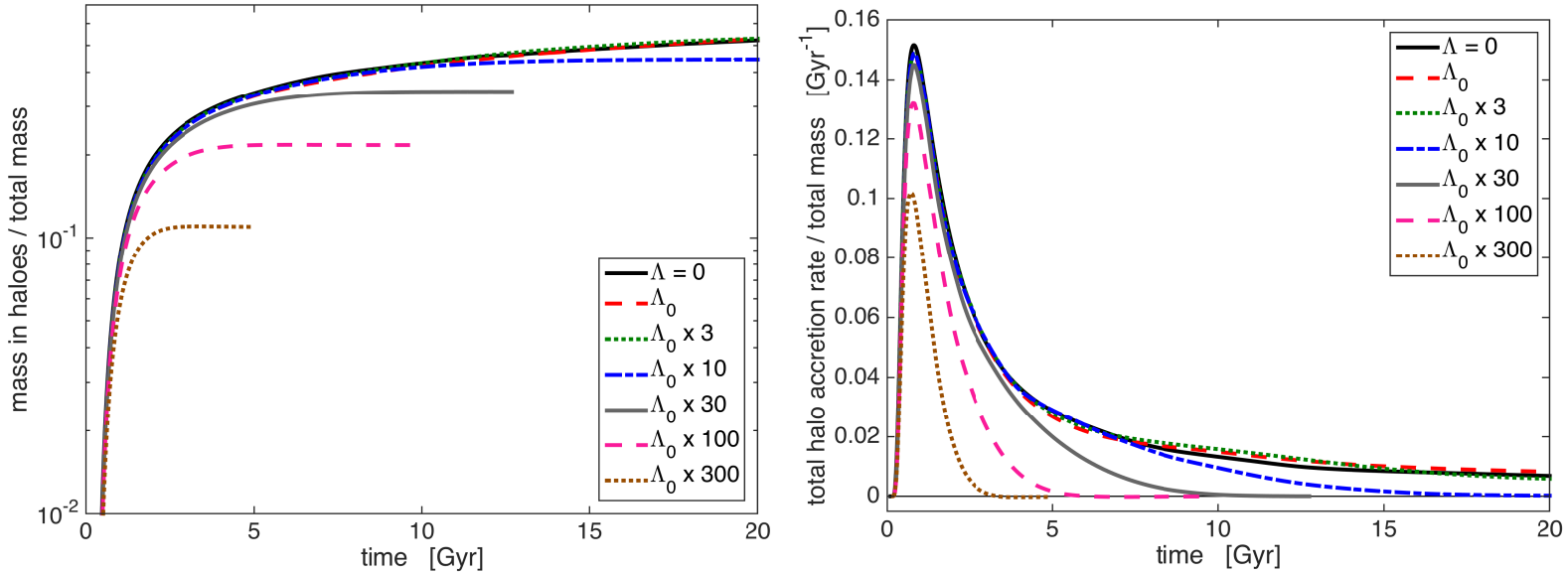

Fig. 4.3.: *Left:* The fraction of mass in each simulation that is part of a resolved halo: $F(> m_{\rm min}|t)$, where $m_{\rm min} = 3.1 \times 10^8\,{\rm M}_\odot$. This minimum mass is a consequence of the numerical resolution of the simulations, but is consistent across all of them and approximately excludes haloes that are too small to form stars. The result is a measure of the fraction of mass in the universe that resides in potentially star-forming haloes. *Right:* The specific total halo accretion rate, that is, the time derivative of the left hand curve. The rate peaks at $t = 0.8$ Gyr in our Universe ($\Lambda = \Lambda_0$). Even for a universe with a cosmological constant ten times larger than ours ($\Lambda_0 \times 10$), there is minimal difference in total halo mass fraction even after 20 Gyrs, well into the accelerating phase of the universe's expansion.

Figure 4.3 shows (*left*) the fraction of the total mass in the universe that has collapsed into resolved haloes, and (*right*) the specific total halo accretion rate, that is, the time derivative of the left hand curve. In this figure and those following, the time derivative is calculated after smoothing the accretion fraction. Even for a universe with a cosmological constant ten times larger than ours ($\Lambda_0 \times 10$), there is minimal difference in total halo mass fraction even after 20 Gyrs, well into the accelerating phase of the universe's expansion. The initial peak in the accretion rate at $t = 0.8$ Gyr remains largely unchanged even in a universe with a cosmological constant 30-100 times larger than ours. In a universe with $\Lambda = \Lambda_0 \times 100$, a fifth of the mass in the universe accretes into haloes with $m > m_{\rm min} = 3.1 \times 10^8\,{\rm M}_\odot$.

4.3.2 Baryon flow

Baryons are subject to physical forces other than gravity: the smoothing effect of gas pressure, cooling and heating from radiation, star formation, supernovae-driven galactic winds, black hole feedback and more. Figure 4.4 shows *left* the fraction of the baryonic mass (in the form of stars and gas) in the simulation that is inside dark matter haloes with $m > m_{\rm min} = 3.1 \times 10^8\,{\rm M}_\odot$ as a function of cosmic time, and *right* the specific rate of baryon accretion (i.e. per unit total baryon mass).

We see the same peak in the accretion rate at $t = 0.8$ Gyr, and when there is zero cosmological constant, the baryon accretion rate increases in a similar way to the total accretion rate (Figure 4.3). As the cosmological constant increases, it has a much larger effect on the baryons than the dark matter. In fact, for $\Lambda = \Lambda_0 \times 10$, the rate of baryon accretion becomes negative, as baryons are — on average — being ejected from galaxies.

We can understand this effect as follows. We can write the acceleration (a_g) of a test mass at distance r from a large mass M under the Newtonian gravitational force with a cosmological constant term,

$$a_g = -G\frac{M}{r^2} + \frac{\Lambda c^2}{3} r \,. \tag{4.12}$$

If we consider a large collapsed mass, then the distance (d_0) at which the force on a test mass is balanced between attraction to the central mass and repulsion by the cosmological constant is found by setting $a_g = 0$,

$$d_0 = 1.1 \text{ Mpc} \left(\frac{M}{10^{12} \text{ M}_\odot}\right)^{1/3} \left(\frac{\Lambda}{\Lambda_0}\right)^{-1/3}, \tag{4.13}$$

or equivalently in terms of the ratio $\rho_\Lambda / \rho_{\Lambda_0}$. In our universe, this is ~ 4 times larger than the virial radius of the halo (which also scales as the $1/3$ power of mass). In universes in which the cosmological constant is larger, these distances are comparable.

As seen in Figure 4.4, this does not dramatically affect the growth of the dark matter halo. But baryonic matter ejected from galaxies in galactic winds or outflows, if it reaches the outer parts of the halo, is liable to be lost. Rather than raining back down on the galaxy after a delay of ~ 1 Gyr (Oppenheimer & Davé, 2008; Oppenheimer et al., 2010; van de Voort, 2017), this material is lost, drawn away into the expansion of the universe by the repulsive effect of the cosmological constant (Barnes et al., 2006).

As we will see in the next subsection, in universes for which ($\Lambda \gtrsim \Lambda_0 \times 10$), the initial burst of star formation in the universe occurs when the universe has begun to expand exponentially. This rapid star formation, combined with black hole feedback, launches outflows that are carried away by the accelerating expansion. This effect overwhelms accretion by gravitational attraction, causing the net accretion rate to become negative. The result is that there is not a simple, linear relationship between dark matter halo growth and baryon accretion that holds for all values of the cosmological constant.

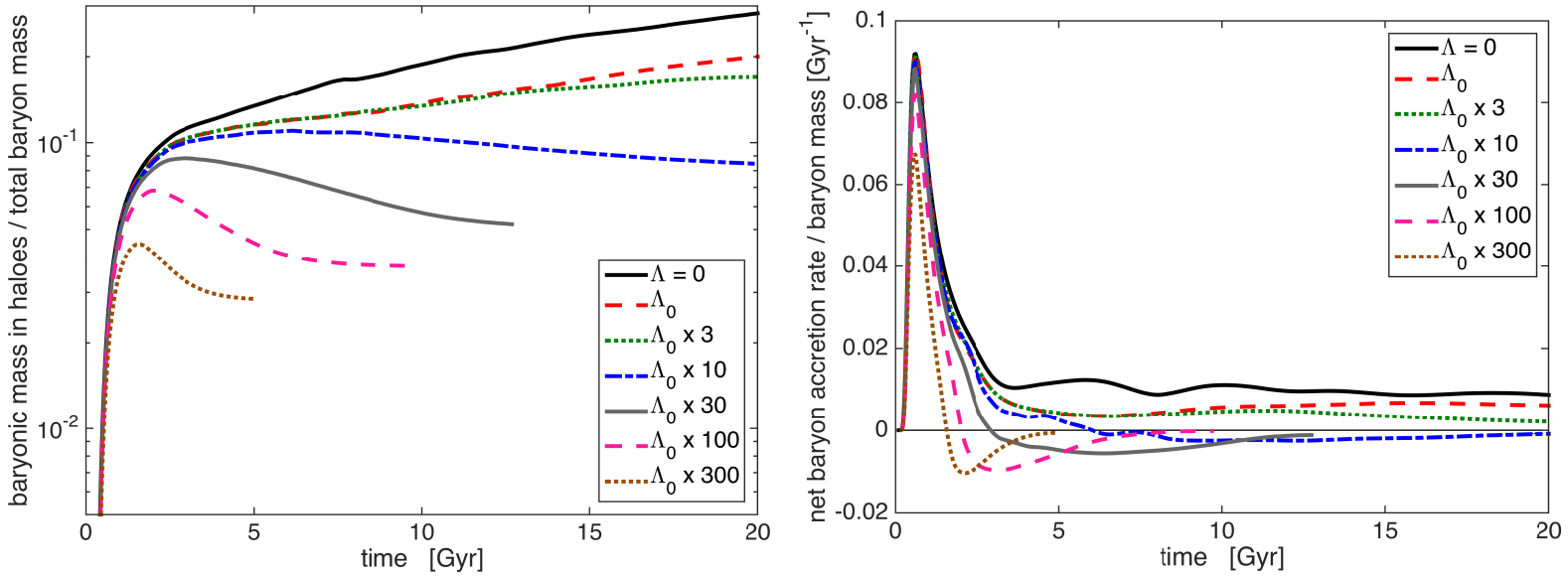

Fig. 4.4.: *Left* the fraction of the baryonic mass in the simulation that is inside dark matter haloes with $m > m_{\rm min} = 3.1 \times 10^8\,{\rm M}_\odot$ as a function of cosmic time, and *Right* the specific rate of baryon accretion. The rate peaks at $t = 0.6$ Gyr in our Universe ($\Lambda = \Lambda_0$).

4.3.3 Star formation

Some of the baryons that accrete into haloes will form stars. Figure 4.5 shows (*left*) the fraction of cosmic baryons that are in the form of stars as a function of cosmic time, and (*right*) the star formation rate efficiency, which takes into account star birth only. Note that, as it is commonly used in the galaxy formation literature, "specific star formation" refers to the star formation rate of a galaxy divided by its *stellar* mass. To avoid confusion, we will call the star formation mass (rate) per unit total baryon mass the star formation (rate) efficiency.

The star formation rate efficiency peaks at $t \approx 3.5$ Gyr. This is a delayed consequence of the peak in the mass accretion rate at $t = 0.8$ Gyr. As the cosmological constant increases, the haloes are starved both by the cessation of fresh accretion from the intergalactic medium and the lack of recycling of outflowing gas, noted above. The result is a significant curtailing of the star formation rate efficiency. While the $\Lambda = 0$ universe has turned $\sim 4\%$ of its baryons into stars by $t = 20$ Gyr, for $\Lambda_0 \times 100$, this fraction is essentially constant after 10 Gyr at 0.5%. This factor of 8 decrease contrasts with the factor of 2.4 decrease in the total mass accretion.

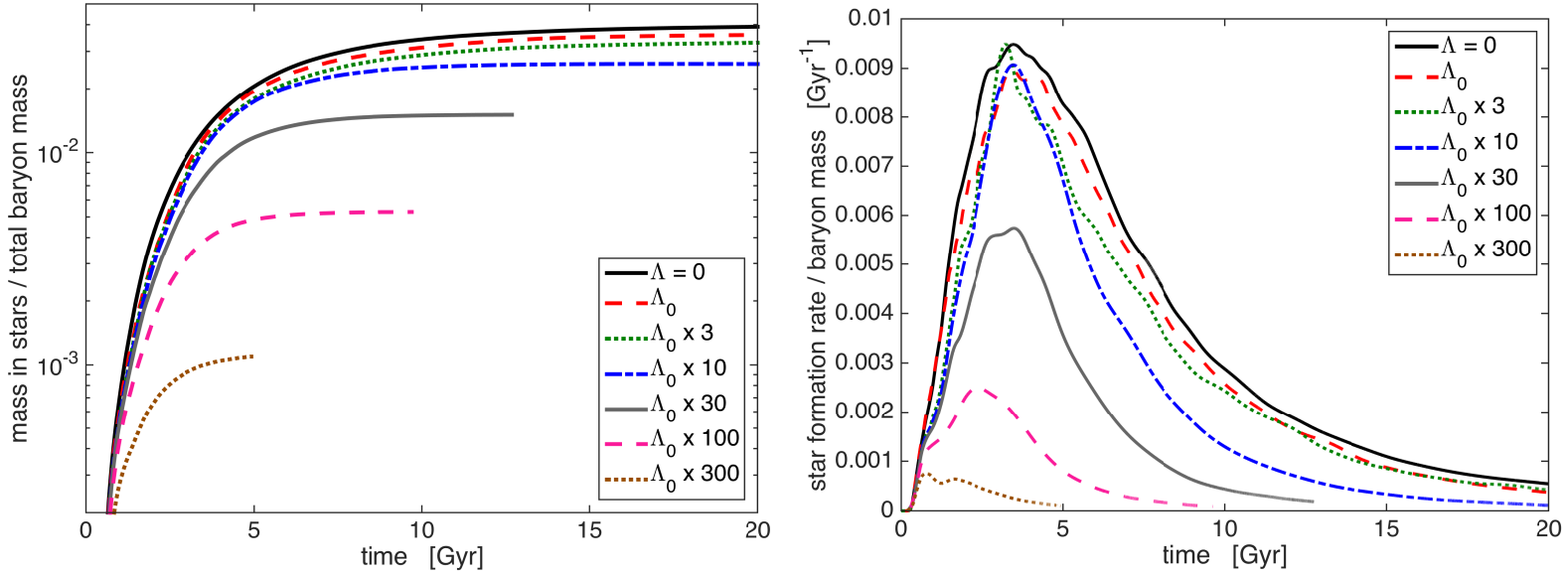

Fig. 4.5.: *Left:* the fraction of cosmic baryons by mass that are in the form of stars as a function of cosmic time. *Right:* the star formation rate efficiency, which takes into account both star birth only. The rate peaks at $t = 3.5$ Gyr in our Universe ($\Lambda = \Lambda_0$).

4.3.4 Cosmic metal production

Planets and their occupants are formed from the products of stellar nucleosynthesis. The EAGLE code, in addition to primordial H and He, follows 9 metals: C, N, O, Ne, Mg, Si, S, Ca, and Fe. Figure 4.6 shows (*left*) the fraction of cosmic baryons that are in the form of metals in collapsed haloes, and (*right*) the halo metal production rate. Note that this includes metals in all phases: inside stars, in dense star-forming clouds, and in the hot, non-star forming interstellar gas. The halo metal production rate reflects the balance between metal production in stars, recycling back into the inter-stellar medium by winds and supernovae, re-incorporation into later generation stars, ejection from haloes in galactic winds, and reaccretion into haloes.

As star formation peaks (Figure 4.5), metals are being produced in stars and returned to the IGM in supernovae and planetary nebulae. This feedback also loads metals into the galactic winds that drive baryons out of haloes (Figure 4.4). As with the baryon accretion rate, the net accretion rate becomes negative for certain values of Λ as metals are ejected in winds at a higher rate than they are produced and reaccreted. Our universe turns approximately a fraction 1.2×10^{-3} by mass of its baryons into halo metals by 20 Gyr, while for $\Lambda_0 \times 100$ the fraction asymptotes by 10 Gyr to 1.5×10^{-4}. This factor of 10 difference contrasts with the factor of 2.5 difference with regards to the total fraction of mass in haloes.

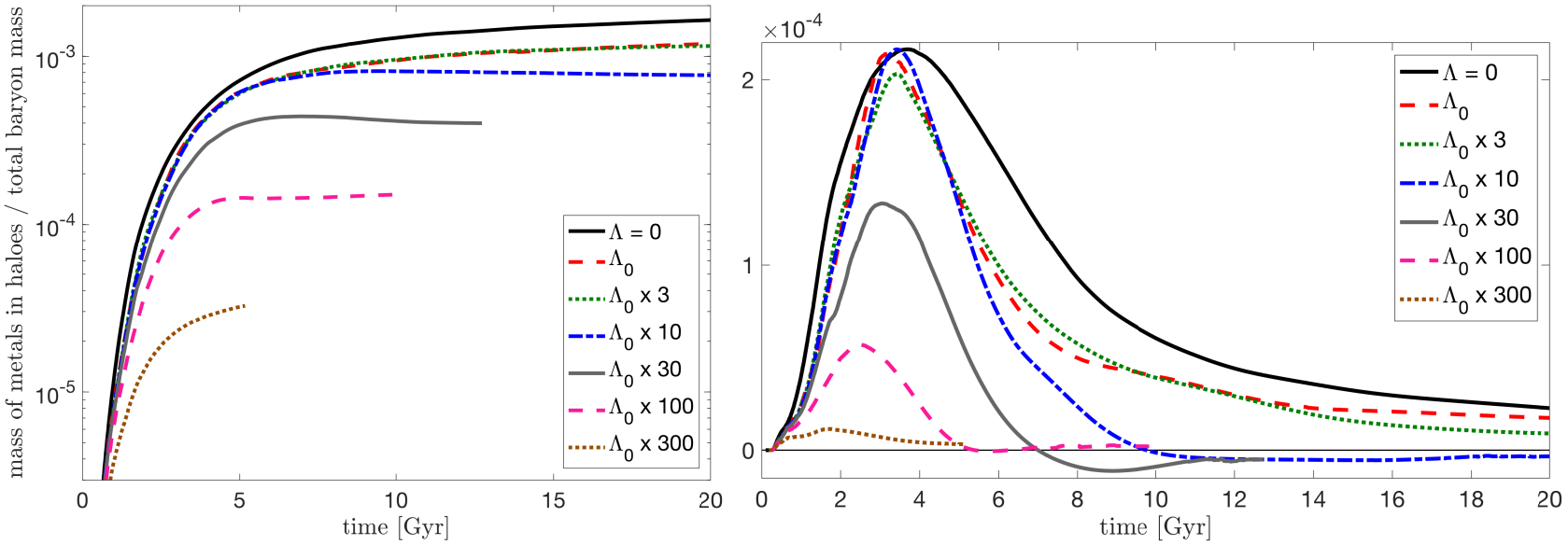

Fig. 4.6.: *Left:* The fraction of cosmic baryons that are in the form of metals in collapsed haloes. Right: the halo metal production rate. The rate peaks at $t = 3.2$ Gyr in our Universe ($\Lambda = \Lambda_0$), and the peak is steadily diminished as the cosmological constant increases.

4.4 Accretion and star formation in individual haloes

In this section, we will consider the evolution of a comoving region of space that, in our universe, evolves into a Milky Way-mass halo ($2 \times 10^{12}\,\mathrm{M}_\odot$) by the present day. Figure 4.7 shows the projected gas density in a comoving region around the halo equal to 4 Mpc today in our universe; the cosmic time and proper size of the region are shown above each panel. The *left* panels show an EdS universe ($\Lambda = 0$); the *right* panels show a $\Lambda_0 \times 30$ universe.

The top two panels show this region of the universe at cosmic time $t = 0.757$ Gyr, while the $\Lambda_0 \times 30$ is still in its early decelerating phase. The proper sizes of the boxes are within 1% of each other, and the distributions of matter are very similar. We see the usual picture of small haloes collapsing and hierarchically merging into larger haloes.

The middle two panels show this region of the universe at cosmic time $t = 6.5$ Gyr. The $\Lambda_0 \times 30$ is undergoing accelerating expansion, so the proper size of the region is 2.3 times larger than in the EdS universe, and the linear growth factor is 33% smaller. The large central halo in the EdS simulation has drawn in more matter from its surroundings, and is still being drawn towards a second halo at the bottom of the panel.

The bottom two panels show this region of the universe at cosmic time $t = 12.5$ Gyr. The accelerating expansion of the $\Lambda_0 \times 30$ means that the proper size of the comoving region is 10 times larger than in the EdS universe. The typical Newtonian force between two masses in the region is thus 100 times smaller, and the linear growth factor is 2.3 times smaller. The difference in the distribution of matter is quite dramatic: in the $\Lambda_0 \times 30$ universe, there has been little evolution of the structure of the universe since $t = 6.5$ Gyr. The matter in the vertical filaments has not fallen into the large halo, starving the galaxy of gas. In the EdS universe, the halo has been drawn closer to the second halo at the bottom of the panel; the filament of matter between them has largely fallen into one of the haloes.

To highlight the difference between the final states of the galaxies at the centre of the halo, Figure 4.8 shows a region of constant proper size (0.5 Mpc) around the

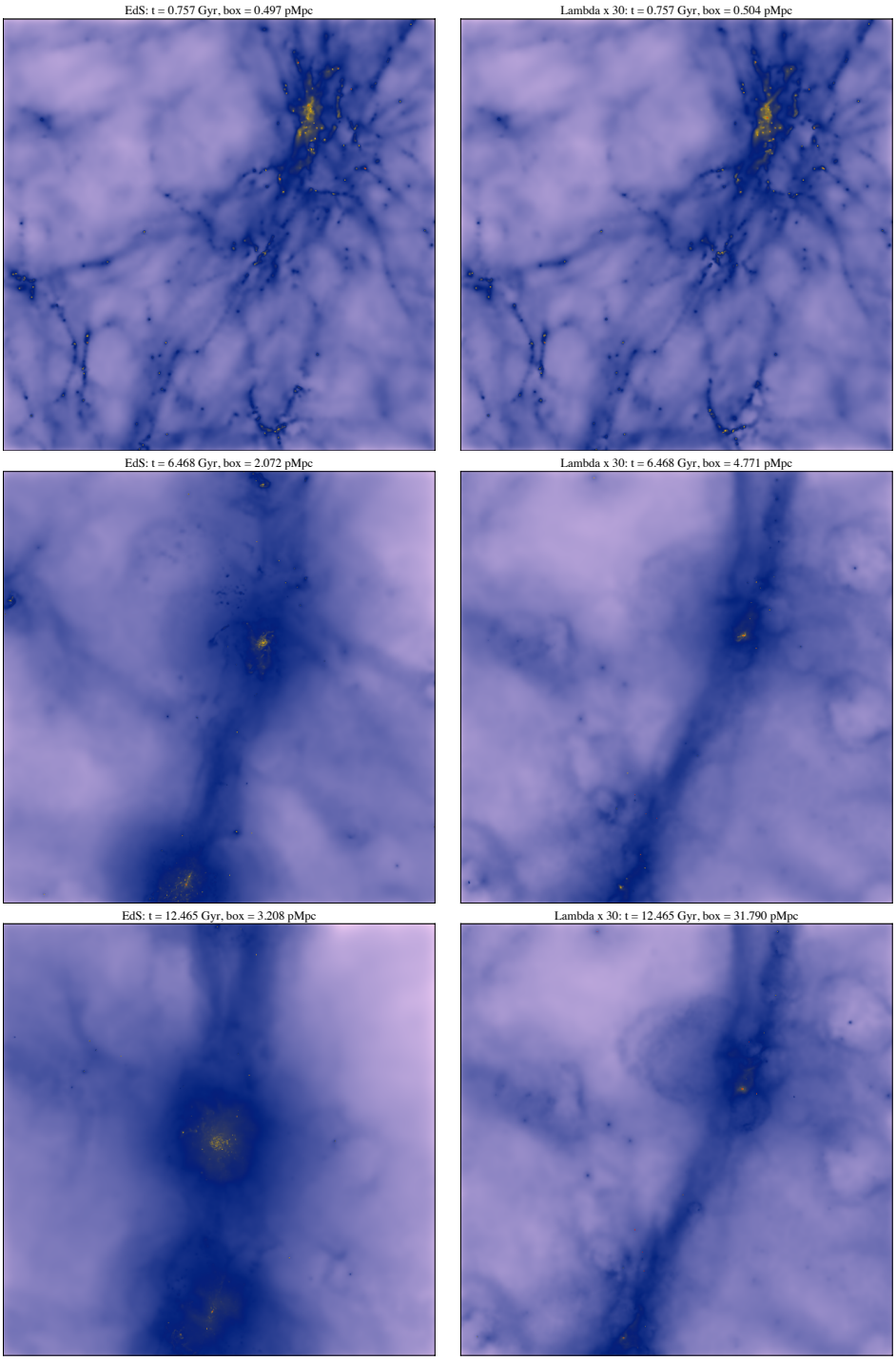

Fig. 4.7.: The evolution of the projected gas density of a comoving region of space that, in our universe, evolves into a Milky Way-mass halo by the present day. The comoving size is 4 Mpc in our Universe. The proper time and proper size of the region are shown above each panel. *Left:* an EdS universe ($\Lambda = 0$); *Right:* a $\Lambda_0 \times 30$ universe. The colour scaling on each row is held constant.

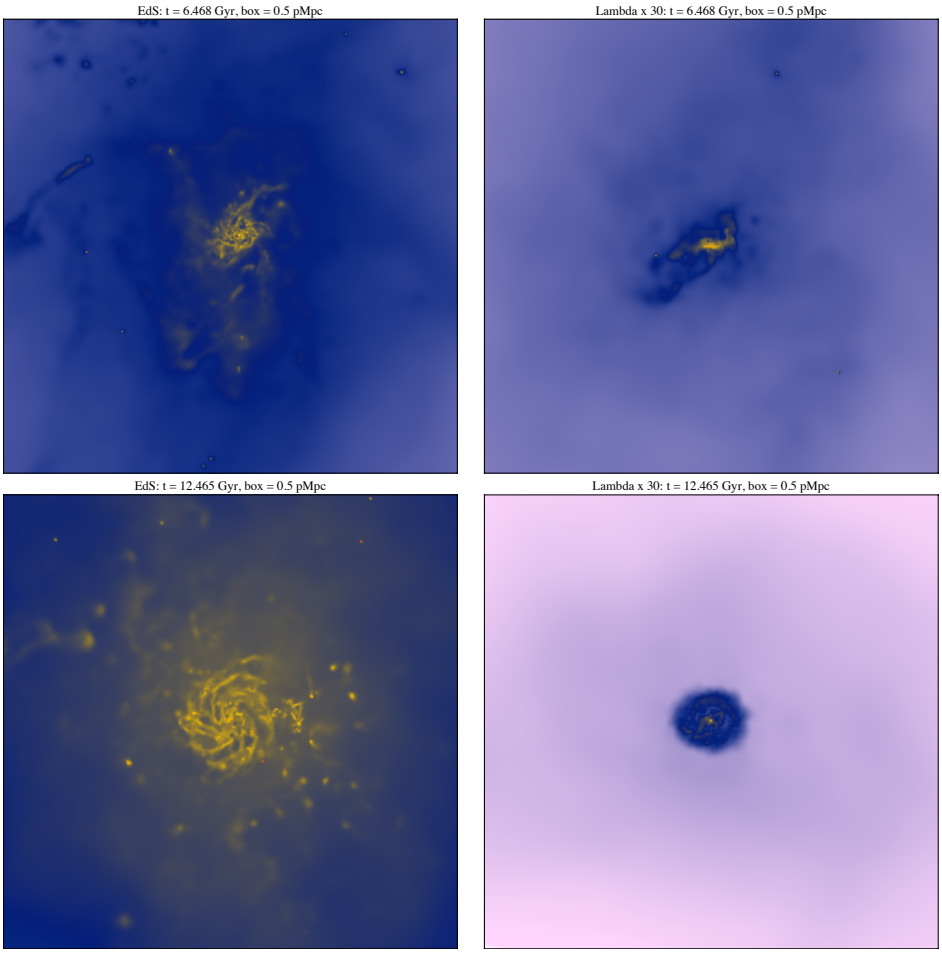

Fig. 4.8.: The evolution of the projected proper gas density in a region of fixed proper size (0.5 Mpc) around the central galaxies in the panels in Figure 4.8. The proper time is shown above each panel. *Left:* an EdS universe ($\Lambda = 0$); *Right:* a $\Lambda_0 \times 30$ universe.

central galaxy in the regions shown in Figure 4.8. The colour scaling in all four panels is held constant.

The top two panels show this region of the universe at cosmic time $t = 6.5$ Gyr. Both show a galaxy in formation, being fed by streams of gas. But already we can see that the EdS galaxy (*left*) is larger, and is surrounded by a much higher density circumgalactic medium. In the $\Lambda_0 \times 30$ universe (*right*), the free fall time from the edge of the isolated region around the galaxy is a few Gyr, and so the halo accretes as much material as is available on this timescale. Accordingly, the total mass of the halo only grows by only $\sim 1\%$ in the 6 Gyr between the two snapshots shown in Figure 4.8, to a final mass of $8 \times 10^{11}\,\mathrm{M}_\odot$. In this isolation, the gas collapses into one monolithic disk. In the same time in the EdS simulation, the halo has doubled in mass to $4 \times 10^{12}\,\mathrm{M}_\odot$ at $t = 12.5$ Gyr, and is still growing.

4.5 Implications for multiverse models

4.5.1 The measure of the multiverse

We can use our calculations to make predictions from multiverse models. Given a model that predicts an ensemble of universes with a distribution of values for the cosmological constant, we can ask what fraction of *observers* will inhabit a universe with a particular value of Λ.

If the model in question predicts a *finite* ensemble of universes, inhabited by a finite number of observers, then this calculation is straightforward. Scientific theories are tested by predicting observations, and so all observers are treated as of equal importance for the purposes of calculating the likelihood[4]. We thus use a counting metric to calculate the likelihood,

$$p_{\rm obs}(\Lambda|MB)\,{\rm d}\Lambda = \frac{n_{\rm obs}([\Lambda, \Lambda + {\rm d}\Lambda])}{n_{\rm obs}}\,, \tag{4.14}$$

where M is the multiverse model, B is any relevant background information (which should not give away any clues about the properties of the actual universe), $n_{\rm obs}([\Lambda, \Lambda + {\rm d}\Lambda])$ is the number of observers (or observer-moments) that exist in a universe with cosmological constant in the range $[\Lambda, \Lambda + {\rm d}\Lambda]$, and $n_{\rm obs}$ is the total number of observers in the multiverse.

To evaluate these quantities, we calculate (at least approximately) the rate at which observers are produced per unit time per unit comoving volume, for a given set of cosmic and fundamental parameters: ${\rm d}^2 n_{\rm obs}/{\rm d}t{\rm d}V$. So long as the universe has finite age, or if the rate at which observers are produced approaches zero quickly

[4] We will ignore the complication of asking: what exactly counts as an observer? We cannot predict the occurrence of observers in sufficient detail to make any difference. That is, we might wonder whether any complex life form counts as an observer (an ant?), or whether we need to see evidence of communication (a dolphin?), or active observation of the universe at large (an astronomer?). Our model does not contain anything as detailed as ants, dolphins or astronomers, so we are unable to make such a fine distinction anyway. In any case, such a distinction is unlikely to bias our calculation toward any particular value of the cosmological constant.

enough into the future, then the integral over cosmic time of this rate will be finite. Then, the likelihood of the cosmological constant is,

$$p_{\rm obs}(\Lambda|MB)\,{\rm d}\Lambda = \frac{\int_0^{t_{\rm max}} V(t;\Lambda)\,p_V(\Lambda|t)\frac{{\rm d}^2 n_{\rm obs}}{{\rm d}t\,{\rm d}V}\,{\rm d}t\,{\rm d}\Lambda}{\iint_0^{t_{\rm max}} V(t;\Lambda)\,p_V(\Lambda|t)\frac{{\rm d}^2 n_{\rm obs}}{{\rm d}t\,{\rm d}V}\,{\rm d}t\,{\rm d}\Lambda}\,, \tag{4.15}$$

where $t_{\rm max}$ is the maximum age of the universe (possibly infinite), $V(t;\Lambda)$ is the total comoving volume of the universe, $p_V(\Lambda|t)\,{\rm d}\Lambda$ is the fraction of the universe by comoving volume at time t in which the value of the cosmological constant is in the range $[\Lambda, \Lambda + {\rm d}\Lambda]$. The comoving volume depends on the arbitrary normalization of $a(t)$, but this cancels in the equation above.

However, most proposed multiverses are not finite. In eternally-inflating universes, for example, it is argued that not only does the multiverse consist of an infinite number of universes, but each universe is infinitely large (Vilenkin & Winitzki, 1997; Garriga & Vilenkin, 2001; Knobe et al., 2003; Freivogel et al., 2006; Guth, 2007; Ellis & Stoeger, 2009). Thus, the number of universes with a given value of Λ, times the average number of observers in those universes, divided by the total number of observers in the multiverse, is $\infty \times \infty/\infty$.

These infinities need to be managed with a *measure*; see, among others, Vilenkin (1995); Garriga et al. (2006); Aguirre et al. (2007); Vilenkin (2007b,a); Gibbons & Turok (2008); Page (2008); Bousso et al. (2009); de Simone et al. (2010); Freivogel (2011); Bousso & Susskind (2012); Garriga & Vilenkin (2013); Page (2017). Simplistically, this measure can be thought of in two ways. Firstly, a multiverse model could motivate confining our attention to a finite region of the universe with volume $V(t;\Lambda)$ (as a function of time and Λ). Then, we can use the finite calculation for the likelihood (Equation 4.15). Secondly, the measure could specify the fraction of the volume of the universe in which cosmic parameters are in a given range, even though the total volume of the universe is infinite. This is used to weight the integral, effectively "cancelling" the infinite quantity $V(t;\Lambda)$ from the numerator and denominator of Equation (4.15), which gives,

$$p_{\rm obs}(\Lambda|MB)\,{\rm d}\Lambda = \frac{\int_0^{t_{\rm max}} p_V(\Lambda|t)\frac{{\rm d}^2 n_{\rm obs}}{{\rm d}t\,{\rm d}V}\,{\rm d}t\,{\rm d}\Lambda}{\iint_0^{t_{\rm max}} p_V(\Lambda|t)\frac{{\rm d}^2 n_{\rm obs}}{{\rm d}t\,{\rm d}V}\,{\rm d}t\,{\rm d}\Lambda}\,. \tag{4.16}$$

Here, rather than focus on a specific multiverse model, we will consider three measures. Following Weinberg (1987); Efstathiou (1995); Peacock (2007); Bousso

& Leichenauer (2010), we note that nothing in fundamental physics picks out a value of the cosmological constant as privileged, including the value zero. This, in particular, rules out the use of a logarithmic prior. In the range of Λ that we consider, which is very small compared to the Planck scale, we approximate the distribution as flat on a linear scale. The difference between the measures is the quantity with respect to which the distribution is flat.

1. *Mass-weighted:* there is a uniform probability that a given mass element in the universe will inhabit a region with a given value of the cosmological constant. Note that, for reasons discussed in Section 4.3, specifying that there is uniform probability with respect to *comoving* volume is not sufficient, as there is no universal 'today' relative to which we can define volume[5]. We use the constraint of constant mass to define comoving volumes between universes.

2. *Causal patch:* This measure was proposed to solve the quantum xeroxing paradox in black holes (Susskind et al., 1993; Bousso, 2006; Bousso et al., 2006), treating the de-Sitter horizon in a universe with Λ analogously to a black hole horizon. We ask: what is the volume of the region of the universe at time t that can causally affect a given comoving world line in the future of t? The comoving extent of the region is,

$$\chi_{\rm patch}(t) = \int_t^{t_{\rm max}} \frac{{\rm d}t}{a(t)} \,. \tag{4.17}$$

   Then, for the spatially flat universes that we consider here, the volume is $V = (4\pi/3)\chi^3(t)$, which goes in Equation (4.15). Note that Equation (4.17) depends on the arbitrary normalisation of $a(t)$, but this is cancelled out when it is multiplied by the observer creation rate: ${\rm d}^2 n_{\rm obs}/\,{\rm d}t\,{\rm d}V$. The comoving size of the causal patch is shown in Figure 4.9 (*left*, relative to the normalisation of $a(t)$ from Section 4.2.1). Also shown (*middle*) is the physical mass contained within the causal patch (which is not relative to the normalisation of $a(t)$).

3. *Causal diamond:* This measure is based on the principle that spacetime regions that are causally inaccessible should be disregarded (Bousso, 2006; Bousso et al., 2007). We consider a comoving world line in a universe, extending from the end of inflation (reheating at $t = t_{\rm rh}$) to the distant future.

[5] Put another way, we are free to renormalise $a(t)$, but this normalisation could depend on Λ. This will not cancel out in equation (4.16), making the calculated probability arbitrary.

What is the volume (at time t) of the region of the universe that is enclosed by a photon that departs the world line at its beginning and returns at the end? We can write,

$$\chi_{\text{diamond}}(t) = \min\{\chi_{\text{patch}}(t), \eta(t)\}\,, \tag{4.18}$$

$$\text{where} \quad \eta(t) = \int_{t_{\text{rh}}}^{t} \frac{\mathrm{d}t}{a(t)} \tag{4.19}$$

As for the causal patch, the volume $V = (4\pi/3)\chi^3(t)$ is used in Equation (4.15). The causal diamond is shown in Figure 4.9. Also shown is the physical mass contained within the causal diamond (*right*).

We stress, however, that the measure is not a "degree of freedom" in a multiverse model. It must not be inferred from or fit to observations, and the fact that a particular measure gives good agreement with observations is *no* reason to prefer that measure. The reason is that any value of Λ can be made practically certain with an appropriately jerry-rigged measure. If a model *derives* its prediction from observations, then its predictions cannot then be tested by those same observations. A multiverse model is supposed to tell us about the global structure of the universe. There should not be any assumptions that need to be added "on top", because there are no physical facts left to specify, at least on relevant cosmological scales. The measure should follow naturally — in some sense — from the multiverse model[6].

[6] To put this another way, suppose a multiverse model specified the global structure of the universe in painstaking detail: the value of cosmic parameters and properties at every place and time. What would it mean to apply two different measures to this model, to derive two different predictions? How could all the physical facts be the same, and yet the predictions of the model be different in the two cases? What is the measure *about*, if not the universe? Is it just our own subjective opinion? In that case, you can save yourself all the bother of calculating probabilities by having an opinion about your multiverse model directly.

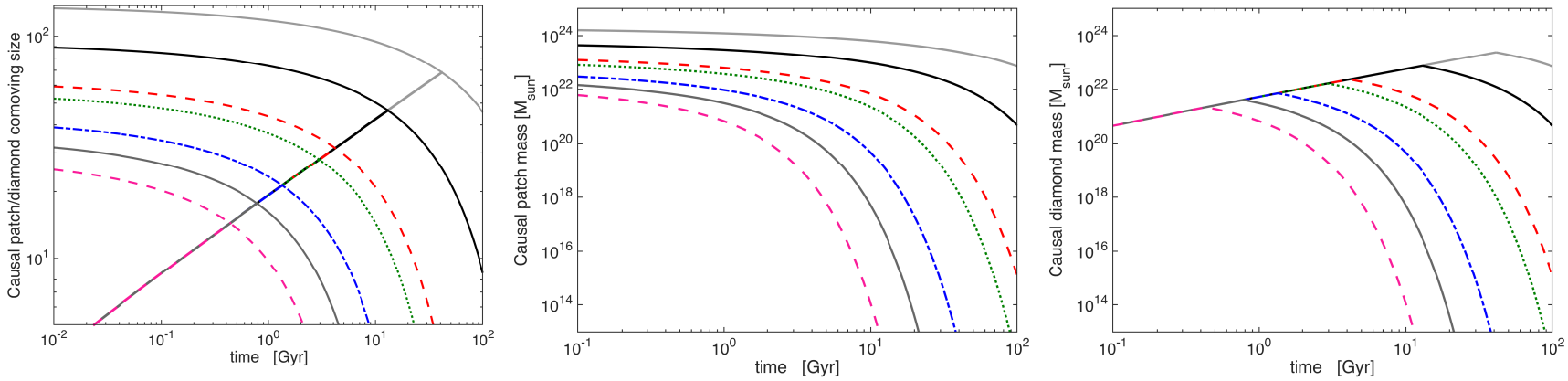

Fig. 4.9.: *Left:* Comoving causal patch and causal diamond vs proper time (Gyrs) for different values of the cosmological constant shown in the legend. The decreasing curves are the causal patch. Increasing (overlapping) curves are the quantity $v(t)$ from Equation (4.18); the causal diamond is the minimum of these two curves at a given time. The comoving distance is relative to the chosen normalisation of $a(t)$, as described in Section 4.2.1. Also shown are the physical mass inside the causal patch (*middle*) and causal diamond (*right*) as a function of cosmic time, which are independent of the normalisation.

4.5.2 Models of observers

We need to connect the presence of observers to local conditions in our simulations. This will, inevitably, be a combination of approximation and guesswork. Note that any constant factor in the observer creation rate will cancel in Equations 4.15 and 4.16, so an absolute rate is not required. We consider three models of observers, linked to the production of energy and chemical elements.

1. *Star formation + fixed delay:* Following Bousso & Leichenauer (2010), we consider a model in which observers follow the formation of a star with a fixed time delay of 5 Gyr. We also considered a time delay of 10 Gyr, but it made minimal difference to our conclusions. This is inspired by the time taken for intelligent life to form on Earth after the birth of the Sun.

2. *Star formation + main-sequence lifetime:* As first argued by Carter (1983, see also Barrow & Tipler 1986), if the formation of life is extremely improbable — that is, if the average timescale for its formation is much longer than the lifetimes of stars — then it will form at the last available moment, so to speak. Most stars will host lifeless planets, but where life forms it will do so at a time that is of order of the main-sequence lifetime of the star. As a first approximation, we assume that there is a constant probability per unit time of life forming around stars of all masses. The observer creation rate for each star population that forms is proportional to the fraction of stars (by number) that are still on the main sequence after time Δt,

$$f_{\rm ms}(\Delta t) = \frac{\int \theta(t_{\rm ms}(M) - \Delta t)\, \xi(M)\, {\rm d}M}{\int \xi(M)\, {\rm d}M}\,, \tag{4.20}$$

   where $\xi(M)$ is the stellar initial mass function (IMF), $t_{\rm ms}(M)$ is the main-sequence lifetime of a star of mass M, the limits of the integral are the minimum and maximum stellar masses, and $\theta(x)$ is the Heaviside step function, so that only those stars whose main-sequence lifetimes are longer than the time since the population was born contribute. We use the Chabrier (2003) initial mass function, and a simple relationship between mass and main-sequence lifetime drawn from the analytic model of Adams (2008) normalised to $t_{\rm ms} = 10$ Gyr at Solar mass; this broadly consistent with Portinari et al. (1998). Of particular importance are the maximum and minimum stellar masses. To be consistent with the IMF used to calibrate the EAGLE

simulations, we choose the minimum and maximum stellar masses to be: $M_{\rm min} = 0.1\,{\rm M}_\odot$ and $M_{\rm max} = 100\,{\rm M}_\odot$. The resulting main-sequence fraction is shown in Figure 4.10.

Folding in the star formation (birth) rate density ($\dot{\rho}_{\rm star}$), we calculate the global observer creation rate. A stellar population that formed at time Δt before the present time t provides a relative contribution of $f_{\rm ms}(\Delta t)$ to the observer creation rate,

$$\frac{{\rm d}^2 n_{\rm obs}}{{\rm d}t\ {\rm d}V}(t) \propto \int_0^t \dot{\rho}_{\rm star}(t') f_{\rm ms}(t - t')\ {\rm d}t' \ . \tag{4.21}$$

Note that, since the time at which observers exist is irrelevant to the mass-weighted measure, the"Star formation + fixed delay" and "Star formation + main-sequence lifetime" models give identical results. This is not the case for the causal patch and causal diamond measures — a later observer at the same comoving position may be outside the patch/diamond, and so does not contribute to the integral in Equation (4.15).

3. *Star formation + metals:* The raw materials for life are the product of stellar-nucleosynthesis, and in particular metals that have been ejected from stars and returned to the interstellar medium. Planets, it is believed, form from the debris disks around newly-formed stars, and stars with higher metallicity are known to be more likely to have giant planets (Gonzalez, 1997; Fischer & Valenti, 2005). However, this result is less clear for smaller rocky planets (Buchhave & Latham, 2015; Wang & Fischer, 2015). There must, of course, be some metallicity dependence, since the probability of a rocky planet forming in a zero-metallicity debris disk is zero. We make the simple assumption that the probability of a rocky planet forming around a star is proportional to the metallicity of the star-forming gas, $Z_{\rm SF}$, so that the observer creation rate at time t is proportional to the number of planets that exist around main-sequence stars,

$$\frac{{\rm d}^2 n_{\rm obs}}{{\rm d}t\ {\rm d}V}(t) \propto \int_0^t Z_{\rm SF}(t')\ \dot{\rho}_{\rm star}(t') f_{\rm ms}(t - t')\ {\rm d}t' \ . \tag{4.22}$$

where $Z_{\rm SF}(t')$ is the metallicity of star-forming gas at at time t'.

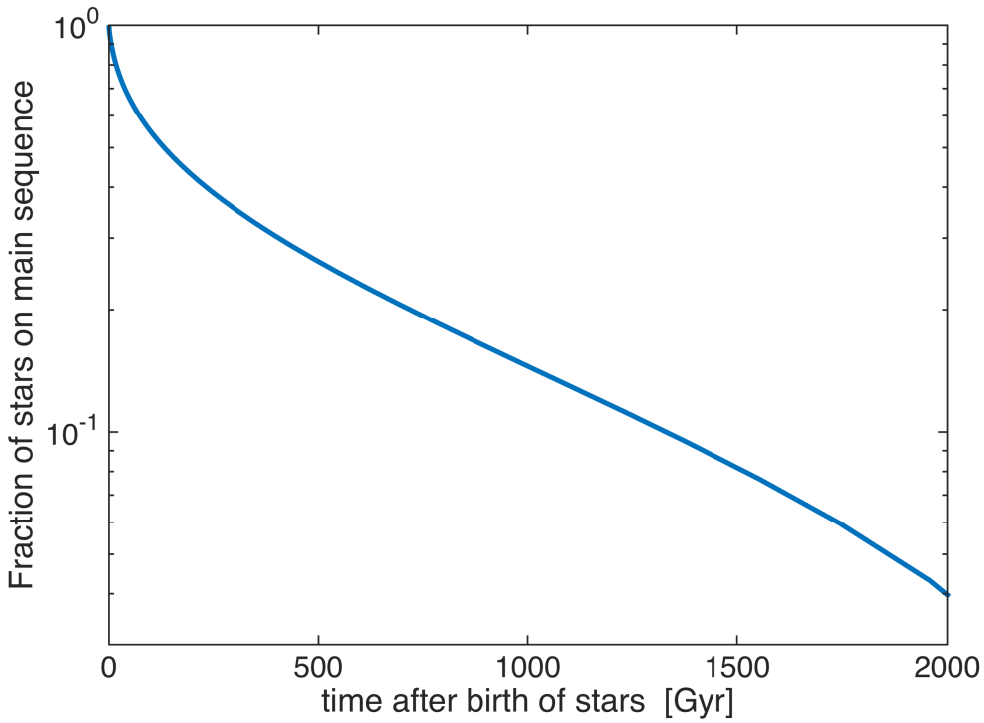

Fig. 4.10.: The fraction of stars by number that are still on the main sequence of their evolution after time Δt. We assume a Chabrier (2003) IMF, and a relationship between mass and main-sequence lifetime from Adams (2008), normalised to $t_{\rm ms} = 10$ Gyr at Solar mass. To be consistent with the IMF used to calibrate the EAGLE simulations, we choose the minimum and maximum stellar masses to be: $M_{\rm min} = 0.1\,{\rm M}_\odot$ and $M_{\rm max} = 100\,{\rm M}_\odot$.

4.5.3 Extrapolation

The integral in Equations 4.15 and 4.16 is over all of cosmic time, but our simulations only extend to a finite time. They capture the initial burst of star formation in our universe, and so are converging thanks to the isolation of haloes by the acceleration of the expansion of space. There will, however, be a trickle of star formation into the future in our galaxies, which our simulations do not capture. Looking at the decline of star formation in the $\Lambda \geq \Lambda_0 \times 10$ simulations, we extrapolate our simulations using an exponential decrease in star formation (rate) efficiency (SFE) with time [SFE $= a \exp(-bt)$], for constants a and b that are derived from the final few Gyr of the simulation. For our simulations, $Z_{\mathrm{SF}}(t)$ has converged; extrapolating by fitting an exponential makes only a negligible difference.

We also use the $\Lambda = 0$ simulation to calculate the relevant quantities for $0 < \Lambda < \Lambda_0$. For $\Lambda < \Lambda_0 \times 0.1$, the time at which the universe begins to accelerate is greater than the limits of our simulation, at which time the star formation rate efficiency has peaked and is declining. By using the $\Lambda = 0$ simulation, there will be no difference in the observer model, but there will be a difference in the causal patch and causal diamond because these depend on Λ. Note that the both of these measures diverge for $\Lambda = 0$, so we only consider universes with $\Lambda > 0$.

As noted in Section 4.2.4, in the far future of our simulations, a variety of very slow (on Gyr timescales) processes may become relevant but are not captured by our simulations. In particular, in the distant future of the $\Lambda = 0$ cosmology, the growth function grows without limit and it is likely that close to 100% of the mass in the universe is found in galaxies. However, in an old, extremely diffuse galactic disk, baryons may be more likely to accrete directly onto dead stellar remnants and black holes than collapse into a fresh star. What is the long-term fate of the interstellar medium in our isolated galaxies? Further modelling may be able to derive the expected fraction of baryons that will form stars into the distant future, and in particular, stars that are likely to host planets. Here, in the absence of such a model, we will simply extrapolate the simulations.

4.5.4 Predicting the cosmological constant

Figure 4.11 shows the integrand in the numerator of Equation 4.15 or 4.16, which combines the observer creation rate, the measure, and the chosen comoving volume

(if needed). We will call this the 'relative observer creation rate'. The value of Λ is shown in the legend in the top left panel. The first row shows the mass-weighted measure, derived directly from the star formation rate efficiencies in Figure 4.5 and metal fraction in Figure 4.6. The second row shows the causal patch measure, and the third row shows the causal diamond measure.

The columns show the different observer models. The first column shows the star formation + fixed delay model, the second column shows the star formation + main-sequence lifetime model, and the third column shows the star formation + metals model.

The first row (mass weighted) shows most directly the effects of the different observer models. The grey $\Lambda_0 \times 0.01$ model is indistinguishable from the $\Lambda_0 \times 0.1$ model because they both use the results of the $\Lambda = 0$ simulation, as described above. In the second column, we can see the effect of folding in the main-sequence stellar lifetime. The decline in the observer creation rate follows the decline in the main-sequence fraction, as the initial burst of stars formed in the first 10 Gyr after the big bang grow old. Because of the abundance of small, long-lived stars, observers are created even at very late times in the universe (Loeb et al., 2016). The addition of metal-weighting further diminishes observer creation in large Λ universes, as they have fewer stars and fewer bound metals to make planets around their stars.

The second and third rows show the causal patch and causal diamond measures. Note that the $\Lambda_0 \times 0.01$ and $\Lambda_0 \times 0.1$ curves are distinguishable because of the difference in the comoving volume $V(t; \Lambda)$. For each observer model, these measures show similar trends. The smaller comoving volume at earlier times in the causal diamond moves the peak to slightly later times, but otherwise the two measures are very similar. The main effect of these measures is to decrease the relative observer creation rate exponentially once the expansion of the universe begins to accelerate. This somewhat cancels out the effect of the longer main-sequence lifetimes in the second and third observer models.

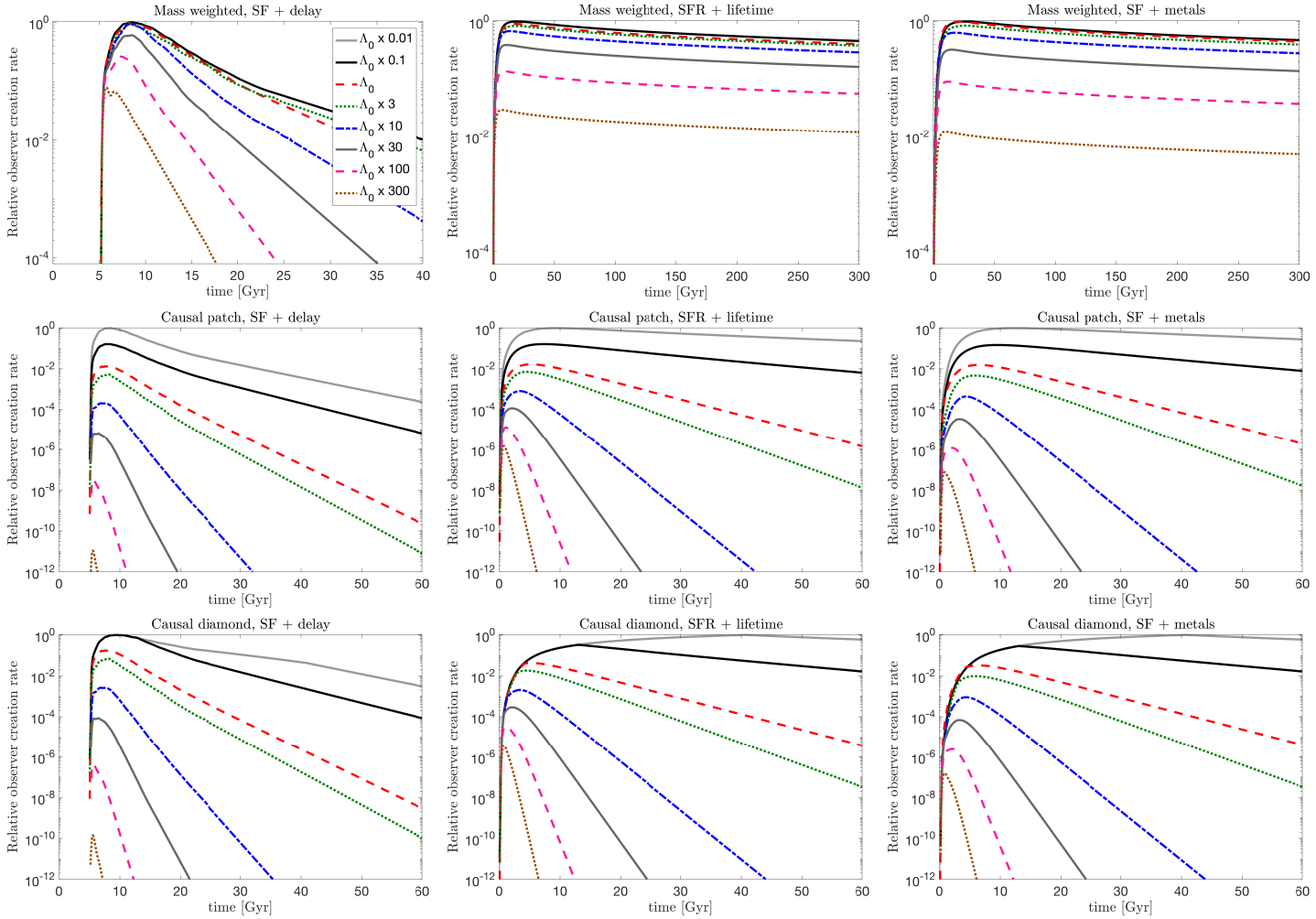

Fig. 4.11.: The 'relative observer creation rate', which is the integrand of Equation 4.15 or 4.16. The value of Λ is shown in the legend in the top left panel. The first row shows the mass-weighted measure, derived directly from the star formation rate efficiencies in Figure 4.5 and metal fraction in Figure 4.6. The second row shows the causal patch measure, and the third row shows the causal diamond measure. The columns show the different observer models. The first column shows the star formation + fixed delay model, the second column shows the star formation + main-sequence lifetime model, and the third column shows the star formation + metals model.

Table 4.3.: Median and "one-sigma" (68%) probability limits of the cosmological constant for the three multiverse measures and three observer models. For the causal patch and causal diamond measures, the value in brackets shows the median value of the cosmological constant using the observer creation rate (per unit mass) from the $\Lambda = 0$ simulation. This illustrates the effect of these measures.

median $\Lambda/\Lambda_0 \pm 68\%$	Mass weighted	Causal patch	Causal diamond
SF + delay	59^{+135}_{-49}	$0.34^{+0.62}_{-0.3}$ (0.37)	$0.65^{+2.5}_{-0.52}$ (0.68)
SF + lifetime	59^{+135}_{-49}	$0.089^{+0.76}_{-0.08}$ (0.095)	$0.25^{+0.71}_{-0.24}$ (0.28)
SF + metals	45^{+118}_{-37}	$0.07^{+0.71}_{-0.066}$ (0.072)	$0.17^{+0.7}_{-0.16}$ (0.18)

Figure 4.12 shows the relative probabilities $p(\Lambda|MB)$ from Equation 4.15 or 4.16; each line integrates a panel of Figure 4.11 over cosmic time. We plot the probability per unit log Λ, and normalise by setting the maximum value to one, rather than integrating over the limited range of Λ. Note that in the *left* plot (mass weighted measure), the 'SF + delay' and 'SF + lifetime' curves are indistinguishable — the integral over cosmic time is not affected by the 5 Gyr delay, and cancels out the effect of $f_{\rm ms}$. For the range of Λ we consider, the median and "one-sigma" (68%) values are shown in Table 4.3.

As we have noted previously, the decline in star formation in our universe after $t = 3.5$ Gyr is not due to the effect of the cosmological constant (Salcido et al., 2018). Universes without a cosmological constant show a similar decline. The initial burst of star-formation in the universe, then, is not dramatically affected by moderate increases in Λ. Only for $\Lambda \gtrsim \Lambda_0 \times 30$ do we see a significant effect on the total number of stars in the universe. Thus, in the mass-weighted measure, the probability distribution for Λ is reasonably flat to large values ($\sim \Lambda_0 \times 30$). The median value in this case is 60 times larger than the observed value. Adding metal-weighting to the observer model increases the suppressing effects of Λ, but the median value is still ~45 times larger than the observed value. While these distributions are broad, most of the probability is at large values of Λ. Table 4.4 shows the the probability that the cosmological constant observed by a typical observer is less than or equal to the value in our universe (Λ_0) for the three multiverse measures and three observer models. For the mass weighted measure, this probability is small (2%).

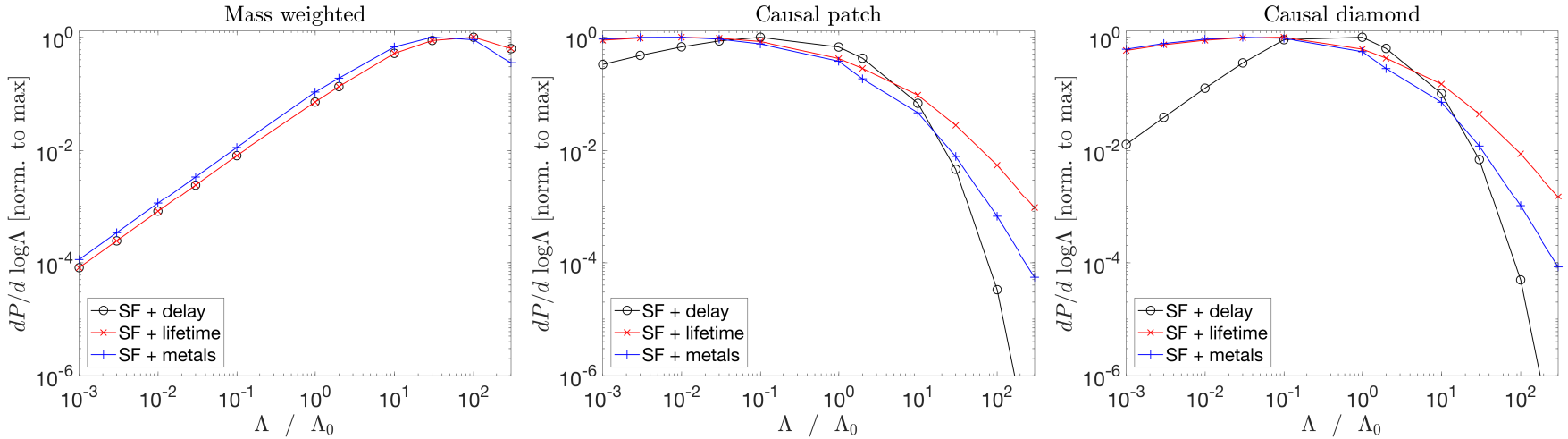

Fig. 4.12.: The relative probabilities per unit log Λ from Equation 4.15 or 4.16; each line integrates a panel of Figure 4.11 over cosmic time. The *left* panel shows the mass weighted measure the *middle* panel shows the causal patch measure, and the *right* panel shows the causal diamond measure.

Note that the results above are for the parameter range $\Lambda_0 \times 0.01 < \Lambda < \Lambda_0 \times 300$. The results for small values of Λ have converged, but increasing the upper limit increases the median value. If we extrapolate the probability distribution to larger values of Λ, we find that the median value for Λ is ~200 Λ_0 for the mass-weighted measure.

For the causal patch and causal diamond measures, the fact that the comoving volume in the measure decreases with time suppresses large values of the cosmological constant, independently of the effect on the observer creation rate $\mathrm{d}^2 n_{\mathrm{obs}} / \mathrm{d}t\, \mathrm{d}V$. This leads to the $\gtrsim 50\%$ probabilities for small values of the cosmological constant (Table 4.4). To illustrate the effect of the measure, we calculate the median value of the cosmological constant using the observer creation rate (per unit mass) from the $\Lambda = 0$ simulation. The results are shown in brackets in Table 4.3. These values are consistently larger than the actual median value, but only by a small factor. Thus, the causal patch and causal diamond measures are playing the dominant role in setting the expected value of the cosmological constant. The predicted value of Λ is set by the time at which the star formation efficiency peaks in universes with small values of Λ, which is set by other cosmological and physical parameters. The decline of star formation efficiency with Λ plays a secondary role.

Our results are broadly consistent with the analytic model of Bousso & Leichenauer (2010), who find that for fixed values of the primordial inhomogeneity Q and spatial curvature, and for $\Lambda > 0$, the causal patch and causal diamond measures predict a value of $0.1 \lesssim \Lambda/\Lambda_0 \lesssim 10$, depending on the model for observers. As noted there, the suppression of structure formation by accelerating expansion is only important for a cosmological constant of order $\Lambda_0 \times 100$. Thus, the agreement between our calculations is due to the "geometric" effects of the causal patch and causal

Table 4.4.: The probability that the cosmological constant observed by a typical observer is less than or equal to the value in our universe (Λ_0) for the three multiverse measures and three observer models. For the causal patch and causal diamond measures, these probabilities are greater than 50%, but the value for the mass-weighted measure is small.

Prob $\Lambda \leq \Lambda_0$	Mass weighted	Causal patch	Causal diamond
SF + delay	1.9%	86%	73%
SF + lifetime	1.9%	90%	86%
SF + metals	2.5%	93%	90%

diamond measures; the astrophysics of galaxy formation does not prefer values of the cosmological constant less than $\Lambda_0 \times 100$.

4.6 Conclusions

Models of the very early universe, including inflationary models, are argued to produce varying universe domains with different values of fundamental constants and cosmic parameters. In such models, predicting observations *necessarily* involves understanding where observers are created in the multiverse. In particular, this anthropic approach has been used to predict the value of the cosmological constant.

Using the cosmological hydrodynamical simulation code from the EAGLE collaboration, we have investigated the effect of the cosmological constant on the formation of galaxies and stars. This SPH code follows the gravitational collapse of matter in an expanding universe, incorporating sub-grid recipes for radiative cooling for 11 elements, star formation, stellar mass loss, energy feedback from star formation, gas accretion onto and mergers of supermassive black holes, and AGN feedback. We simulate universes with values of the cosmological constant ranging from $\Lambda = 0$ to $\Lambda_0 \times 300$, where Λ_0 is the values of the cosmological constant in our Universe. For larger values of the cosmological constant, the time at which the expansion of the universe begins to accelerate declines as $t_\Lambda \propto (\Lambda/\Lambda_0)^{-1/2}$.

Our Universe shows a peak in the global star formation rate at $t = 3.5$ Gyr, coming after the peak in the halo matter accretion rate at $t = 1$ Gyr. By the time the expansion of our Universe begins to accelerate (at $t = 7.6$ Gyr), the global halo mass accretion rate has dropped to about 10% of its earlier maximum, and most of the mass that will ever accrete into haloes has already accreted. As a result, increases in Λ of even an order of magnitude have a small effect on the star formation efficiency of the universe.

One interesting effect that affects the raw materials of life is stellar and AGN feedback. In our Universe, these processes slow star formation by sending baryons back into the outer parts of the halo and the local intergalactic medium. This material is largely recycled into the galaxy after ~ 1 Gyr, and forms a later generation of stars. But in universes with $\Lambda \gtrsim \Lambda_0 \times 10$, much of this material is lost to the intergalactic medium, carried away by the accelerating expansion of the universe rather than

reaccreting. The net baryon accretion rate becomes negative as more material is lost to galactic winds than is accreted/reaccreted.

In universes with larger values of Λ, galaxies quickly become isolated from their cosmic surroundings. The familiar ecosystem of galaxies in our universe, which balance accretion, major and minor merging, galactic cannibalism, star formation, galactic winds, and reaccretion, is reduced to a closed box, as galaxies become island universes, surrounded by vacuum and isolated from the rest of the matter in the universes. They burn through their finite matter supply, forming stars at a decreasing rate.

We use our simulations to predict the observed value of the cosmological constant, given a measure of the mulitiverse. We considered three simple but plausible models for where we would expect observers to be created in our simulations, and three measures of the multiverse.

In the mass-weighted measure, with a uniform probability that a given mass element in the universe will inhabit a region with a given value of the cosmological constant, the predicted size of Λ is determined by the decline in the star formation efficiency of the universe. For the reasons described above, this is relatively flat as a function of Λ, and so the predicted (median) value is $50 - 60$ times larger than the observed value. The probability of observing a value as small as our cosmological constant Λ_0 is $\sim 2\%$. In this case, an anthropic argument for value of Λ, while doing much better than the famous 120 orders-of-magnitude discrepancy from quantum field theory, is not a particularly successful prediction.

For the causal patch and causal diamond measures, which consider a subset of the universe that depends on Λ, the predicted value is within a factor of a few of the observed value. But, this has very little to do with the decline in the star formation efficiency (and so, presumably, observer creation rate) with Λ. It is a result of the rapid decrease in the size of the causal patch/diamond with increasing cosmological constant.

We stress again: this is no reason to prefer the causal patch and causal diamond measures. This is not an observational test of these measures. A specific multiverse model must justify its measure on its own terms, since the freedom to choose a measure is simply the freedom to choose predictions ad hoc.

We conclude that the impact of the cosmological constant on the formation of structure in the universe does not straightforwardly explain the small observed value of Λ. The prediction depends crucially on the measure. If the observer creation rate had been sufficiently sharply peaked at values near Λ_0, the measure would not much matter. But in fact, in the absence of a multiverse model that can convincingly justify a measure, it is not clear whether the anthropic prediction Λ is successful. Future work will consider varying more cosmological and fundamental parameters, to shed more light on which kind of universe is to be expected from a multiverse.

5 The UNIVERSEAPP: A mathematical model of galaxy formation

In this chapter, we introduce the UNIVERSEAPP (the **Universe** on **A P**iece of **P**aper), an analytic model that connects the growth of dark matter haloes in a cosmological background, with the build up of stellar mass within these haloes. The model identifies the physical processes that drive the Galaxy-Halo co-evolution through cosmic time. Galaxy formation is revealed as a simple process where the instantaneous star formation efficiency within halos is only a function of their virial temperature. Despite its simplicity, the model reproduces self-consistently the shape and evolution of the cosmic star formation rate density, the specific star formation rate of galaxies, and the galaxy stellar mass function, both at the present time and at high redshift.

This chapter is work currently in progress, and will be submitted soon in the form of a paper to Monthly Notices of the Royal Astronomical Society (MNRAS).

5.1 Introduction

The galaxy-halo connection and co-evolution is perhaps one of the most fundamental features (or predictions) of every galaxy formation model. In our current paradigm of galaxy formation, every galaxy forms within a dark matter halo. However, understanding the relationship between a dark matter halo and the galaxies it hosts is not a trivial exercise due to our lack of understanding of the complex baryonic process involved.

In a standard Lambda Cold Dark Matter (ΛCDM) cosmology, gravitationally bound dark matter structures build up hierarchically, primarily by the smooth accretion of surrounding matter, and by the continuous merging of smaller structures (Qu et al., 2017). The formation and evolution of galaxies within these haloes is thought to be a highly self-regulated process, in which galaxies tend to evolve towards a quasi-equilibrium state where the gas outflow rate balances the difference between

the gas inflow rate and the rate at which gas is locked up in stars and black holes (BHs) (e.g. White & Frenk, 1991; Finlator & Davé, 2008; Bouché et al., 2010; Schaye et al., 2010; Davé et al., 2012). Consequently, galaxy formation is thought to be determined on the one hand by the formation and growth of dark matter haloes, which depends solely on the cosmological background, and on the other hand, by the regulation of the gas content in these haloes, that depends on complex baryonic processes such as radiative cooling, stellar mass loss, and feedback from stars and accreting BHs. This co-evolution process results in a tight correlation between the properties of galaxies and their dark matter haloes (see Wechsler & Tinker 2018 for a review).

In principle, galaxy formation modelling should aim to reproduce the relation between stellar mass and halo mass inferred from observations. However probing the dark matter distribution and its evolution represents an observational challenge. Direct observational probes include galaxy-galaxy lensing (e.g. Brainerd & Specian, 2003; Hoekstra et al., 2004; Hudson et al., 2015) and the kinematics of satellite galaxies (e.g. Zaritsky et al., 1993; van den Bosch et al., 2004; Norberg et al., 2008). However, direct observation techniques are limited to low redshifts ($z < 1$), due to the difficulty of resolving individual distant galaxies. Indirect methods include, for example, comparing the abundance and clustering properties of galaxy samples with predictions from a phenomenological halo models (e.g. Neyman & Scott, 1952; Berlind & Weinberg, 2002; Cooray & Sheth, 2002; Cowley et al., 2018). This method however, depends heavily on the underlying modelling and assumptions, for example, the bias with which halos trace the underlying matter distribution.

From the theoretical point of view, the formation and evolution of dark matter haloes is considered a "solved problem" (see however, van den Bosch et al. 2018). Using extremely accurate measurements of the density perturbations imprinted onto the cosmic microwave background radiation fluctuations as initial conditions (e.g. Planck Collaboration et al., 2014), many different groups have produced convergent results using large cosmological N-body simulations (e.g Springel et al., 2005b; Klypin et al., 2011; Trujillo-Gomez et al., 2011; Angulo et al., 2012; Fosalba et al., 2015).

On the other hand, different approaches have been used to model the more complex baryonic physics of galaxy formation. The most widely used technique combines the evolution of dark matter with either a *semi-analytical* (e.g. Cole et al., 1994;

Somerville et al., 2008; Henriques et al., 2015; Lacey et al., 2016) or *hydrodynamical* (e.g. Schaye et al., 2015; Davé et al., 2016; Dubois et al., 2016; Pillepich et al., 2018) treatment of the baryonic processes involved. A key ingredient in both methods that has led us to a better understating of the physics of galaxy formation is the use of physically motivated models for feedback processes (see Somerville & Davé 2015; Naab & Ostriker 2017 for a comprehensive review).

Another useful method, known as *empirical modelling*, takes the advantage of the vast number of observational data sets from galaxy surveys and relate statistical galaxy scaling relations to the evolution of dark matter haloes without assuming strong physical priors (e.g. Behroozi et al., 2013b; Moster et al., 2013; Rodríguez-Puebla et al., 2016; Behroozi et al., 2018; Moster et al., 2018). This "simple", yet powerful, approach could reveal undiscovered properties of baryonic physics (e.g. Behroozi et al., 2013a).

While all of these approaches have been very productive, the increasing complexity of the models make it difficult to pinpoint and understand the fundamental physics driving the results. In this chapter, we examine this issue in detail. We developed the UniverseApp, a fully analytic model of galaxy formation derived from a simple relation of the star formation to halo growth rate that disentangle the role of cosmology from the role of astrophysics in the galaxy formation process. Our model restricts the role of baryonic astrophysics to setting the relation between galaxies and their halos. With this simple relation, we can use an analytic approximation of the growth of dark matter halos to predict galaxy properties. By providing a set of analytic equations, the model can be easily "inverted" and allows for rapid experiments to be conducted, providing a great tool to explore the differential effects of baryonic physics, averaged over galaxy scales. Despite its simplicity, the model reproduces self-consistently the shape and evolution of the cosmic star formation rate (SFR) density, the specific star formation rate (sSFR) of galaxies, and the galaxy stellar mass function (GSMF), both at the present time and at high redshift.

As the UniverseApp model is highly simplified model, we compare our results to the numerical hydrodynamic simulations, the EAGLE project. The EAGLE simulation suite[1] (Schaye et al., 2015; Crain et al., 2015) consists of a large number of cosmological hydrodynamical simulations that include different resolutions, simulated volumes and physical models. These simulations use advanced smoothed particle hydrodynamics (SPH) and state-of-the-art subgrid models to capture the

[1] http://www.eaglesim.org

unresolved physics. A complete description of the code and physical parameters used can be found in Schaye et al. (2015). Here we compare to the EAGLE reference simulations that used cosmological parameters inferred by the Planck Collaboration et al. (2014). The calibration strategy is described in detail by Crain et al. (2015) who also presented additional simulations to demonstrate the effect of parameter variations.

Throughout this chapter, we adopt a flat, ΛCDM cosmology with parameters ($\Omega_m = 0.307$, $\Omega_\Lambda = 0.693$, $h = 0.6777$, $\sigma_8 = 0.8288$, $n_s = 0.9611$) consistent with the Planck Collaboration et al. 2014 results.

The layout of this chapter is as follows: In Section 5.2 we introduce the UNIVERSEAPP model. We present two models of instantaneous star formation efficiency: A time-independent efficiency which depends only on halo mass. And a time-evolving efficiency that depends on the virial temperature of the halo. In Section 5.3, we explore the effect of the different efficiency parameters in the galaxy formation outputs. Namely, the cosmic star formation rate density, the specific star formation rate of galaxies, and the galaxy stellar mass function. In Section 5.4 we compare the results from the UNIVERSEAPP to different datasets of observational data. We also discuss the need for a time-evolving efficiency in order to reproduce the rapid evolution of the galaxy stellar mass function. We discuss the limitations of our model, and conclude in Section 6.5.

5.2 An analytic model of galaxy formation

5.2.1 The instantaneous star formation efficiency

The formation, evolution and abundance of dark matter haloes can be predicted accurately when the cosmology and dark matter model (i.e. cold, warm, self-interacting, etc.) is known. However, the galaxy content of haloes is very sensitive to the baryonic processes involved in the formation of galaxies. One approach of galaxy formation modelling is to aim to reproduce the relation between stellar mass and halo mass inferred from observations. If this is achieved, other fundamental observables should be reproduced as well.

Here, we assume an instantaneous star formation efficiency which captures all the physical processes involved in the conversions of gas into stars, i.e. cooling, star formation law, feedback mechanisms, etc. We can relate the galaxy SFR to the host halo mass accretion rate as,

$$\dot{M}_*(M_h) = \epsilon_* \dot{M}_h, \tag{5.1}$$

where the instantaneous star formation efficiency, ϵ_*, could be a complex function of many parameters. We will consider two models of ϵ_*, a time-independent efficiency which depends only on halo mass, and a time-evolving efficiency that depends on the virial temperature of the halo.

- *Halo mass-dependent efficiency*

  In order to model ϵ_*, we first assume a time-independent relation of the galaxy specific SFR to the host halo specific mass accretion rate (e.g. Rodríguez-Puebla et al., 2016; Salcido et al., 2018; Tacchella et al., 2018). We can write Eq. (5.1) as,

$$\begin{aligned} \dot{M}_*(M_h) &= \left(\frac{\mathrm{d}\log_{10} M_*}{\mathrm{d}\log_{10} M_h}\right) \frac{M_*}{M_h} \dot{M}_h \\ &= \varepsilon(M_h) \frac{M_*}{M_h} \dot{M}_h \\ &= \epsilon_*(M_h) \dot{M}_h. \end{aligned} \tag{5.2}$$

  where, $\varepsilon(M_h)$ is the logarithmic slope of the stellar to halo mass relation (SHMR). Here, $\epsilon_*(M_h)$ is completely determined by the SHMR. Using abundance matching techniques to infer the functional form of $\epsilon_*(M_h)$ (e.g. Behroozi et al., 2013b; Rodríguez-Puebla et al., 2016), it has been estimated to peak at masses similar to Milky-Way sized halos ($\sim 10^{12}\,\mathrm{M}_\odot$) and fall steeply for higher and lower masses. We model $\epsilon_*(M_h)$ using the double power law parametrisation proposed by Moster et al. 2010,

$$\epsilon_*(M_h) = 2\epsilon_\mathrm{N} \left[\left(\frac{M_h}{M_\mathrm{crit}}\right)^{-\alpha} + \left(\frac{M_h}{M_\mathrm{crit}}\right)^{\beta} \right]^{-1}, \tag{5.3}$$

  where ϵ_N is the normalisation parameter, α and β determine the slope of the efficiency at low and high masses respectively, and M_crit locates the transition, or peak efficiency. Figure 5.1 shows an illustration of the model parameters. To match observational data, the values of α and β are typically positive, i.e. at low masses, SFR is suppressed because of the efficiency of feedback from star formation, at higher masses the cooling of the inflowing gas is suppressed

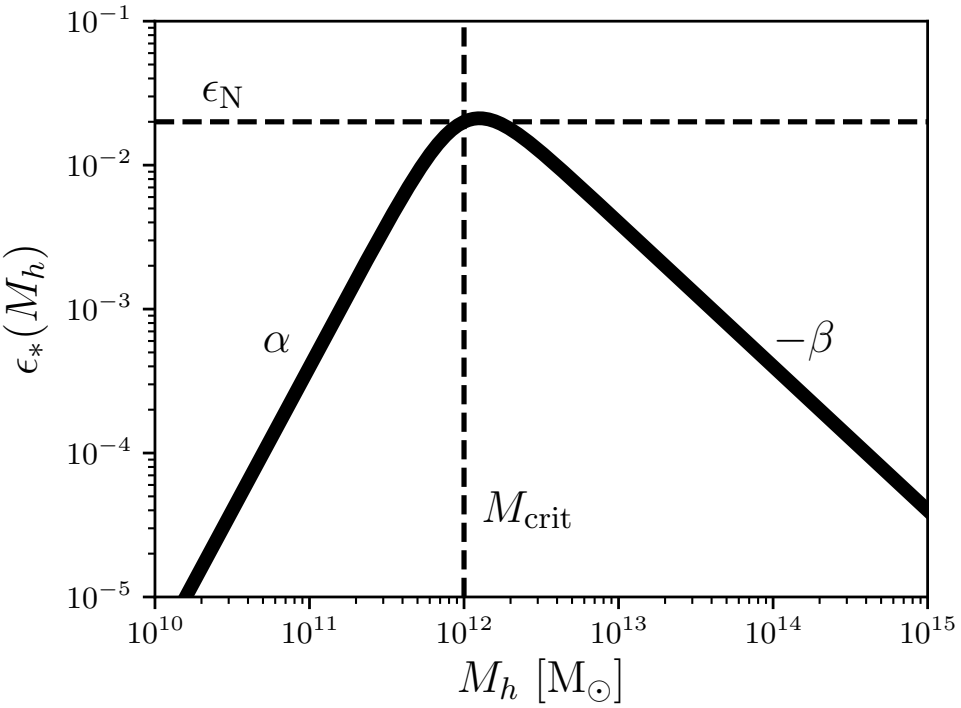

Fig. 5.1.: Parametrisation of the instantaneous star formation efficiency $\epsilon_*(M_h)$ provided in Eq. (5.3). $\epsilon_{\rm N}$ is the normalisation parameter, α and β determine the slope of the efficiency at low and high masses respectively, and $M_{\rm crit}$ locates the transition, or peak efficiency.

by heating from BHs (e.g. White & Frenk, 1991; Benson, 2012; Bower et al., 2006; Haas et al., 2013).

As we will show in Section 5.3, a halo mass-dependent efficiency turns out the be a good approximation of the SFR of galaxies because most of the stellar mass builds up when the mass of the halo has roughly its current value. However, a time-independent efficiency model significantly under predicts the abundance galaxies at high redshifts, which hints to the need of a time-evolving efficiency model. "Traditional" empirical modelling (e.g Moster et al., 2018; Behroozi et al., 2018) would relax the physical priors and let, in this case, the four efficiency parameters in the model to evolve freely in time. Instead, we propose a physically motivated efficiency model that naturally evolves with cosmic time.

- *Virial temperature-dependent efficiency*

Cooling and heating processes (which dictate the star formation efficiency of a cloud of gas), are most clearly described by entropy; cooling always reduces the local entropy of a system, whilst heating always raises it. On the other hand, idealised gravitational collapse is assumed to be adiabatic (i.e. entropy is conserved). Assuming a uniform density distribution, the entropy configuration of a gravitationally collapsed halo is completely characterised by its virial temperature. We present an instantaneous star formation efficiency model characterised by a time-independent critical virial temperature $T_{\rm crit}$. That is, there exists a critical halo virial temperature at which there is a transition from where star formation driven outflows get hotter than the virial temperature of the halo and can buoyantly escape (i.e. supernovae energy, or entropy, is much greater than the halo binding energy), to where outflows are no longer buoyant, and gas stalls inside the halo triggering star formation and BH growth.

We model the virial temperature-dependent instantaneous star formation efficiency as a function of the halo's virial temperature using the same double power law parametrisation as in Eq. (5.3),

$$\epsilon_*(T_{\rm vir}) = 2\epsilon_{\rm N}\left[\left(\frac{T_{\rm vir}}{T_{\rm crit}}\right)^{-\alpha} + \left(\frac{T_{\rm vir}}{T_{\rm crit}}\right)^{\beta}\right]^{-1}, \tag{5.4}$$

We will further discuss this model in Section 5.4.1, and show that it reproduces the observational data both at the present time and at high redshift.

5.2.2 Halo definition

Dark matter haloes are typically identified by growing a sphere outwards from the potential minimum of the dark matter halo out to a radius where the mean interior density equals a fixed multiple of the critical or mean density of the Universe, causing an artificial 'pseudo-evolution' of dark matter halos by changing the radius of the halo (Diemer et al., 2013). Star formation, however, is governed by the amount of gas that enters these halos and reaches their central regions. Wetzel & Nagai 2015 show that the growth of dark matter haloes is subject to this 'pseudo-evolution', whereas the accretion of gas is not. Because gas is able to cool radiatively, it decouples from dark matter, tracking the accretion rate near a radius of $R_{200\bar{\rho}}$, the

radius within which the mean density is 200 times the mean density of the universe, $\bar{\rho}$. As we try to connect the accretion of dark matter haloes to star formation, we define halo masses as the total mass within $R_{200\bar{\rho}}$,

$$M_h = 200\frac{4\pi}{3}R^3_{200\bar{\rho}}\bar{\rho}, \tag{5.5}$$

where $\bar{\rho}(t) = \hat{\rho}_0 a(t)^{-3}$.

We assume that during gravitational collapse, the gas experience strong shocks and thermalises its kinetic infall energy to the virial temperature of the halo, given by,

$$T_{\rm vir} = \frac{\mu m_p G M_h}{5 k_{\rm B} r_h(t)}, \tag{5.6}$$

where we have assumed a uniform cloud of monatomic gas, M_h is the mass of the halo, μ is the mean molecular weight of the gas in the halo, which we have assumed $\mu \approx 0.6$ for a fully ionized plasma of primordial composition, $k_{\rm B}$ is the the Boltzmann constant, m_p the proton mass, and $r_h(t)$ is the virial radius of the halo, defined in Eq. (5.5). For a given halo mass, the radius of the halo $r_h(t)$ changes with time as the mean density of the Universe evolves.

5.2.3 The UniverseApp model

We now present the main components of the fully analytical UniverseApp model, which are summarised in the schematic diagram of Fig. 5.2. The derivation of the equations presented here can be found in Appendix A.

By using the Taylor expansion solution of the Friedmann equation introduced in Salcido et al. 2018, the formation and evolution of dark matter haloes are fully described analytically by the components in the blue block of Fig. 5.2, given that the cosmological parameters $\hat{\rho}_0$[2], Λ, H_0 and the shape of the matter power-spectrum, parametrised by the variance of the smoothed density field $S = \sigma^2(M_h)$, which we approximate[3] as a power law $S \approx S_0 M_h^{-\gamma}$ with slope γ, are known. All astrophysical processes enter into the model by the instantaneous star formation efficiency ϵ_* (shown in green), which is fully described by the SHMR in the four free parameters $M_{\rm crit}$ or $T_{\rm crit}$, $\epsilon_{\rm N}$, α and β in Eqs. (5.3) and (5.4).

[2] We use a hat notation (ˆ) to denote quantities in our observable Universe.

[3] Approximating the scale dependence of the density field as a power-law around $10^{12}\,{\rm M}_\odot$ haloes, Correa et al. 2015 find $S_0 \approx 10^{4.2}$, $\gamma \approx 0.3$.

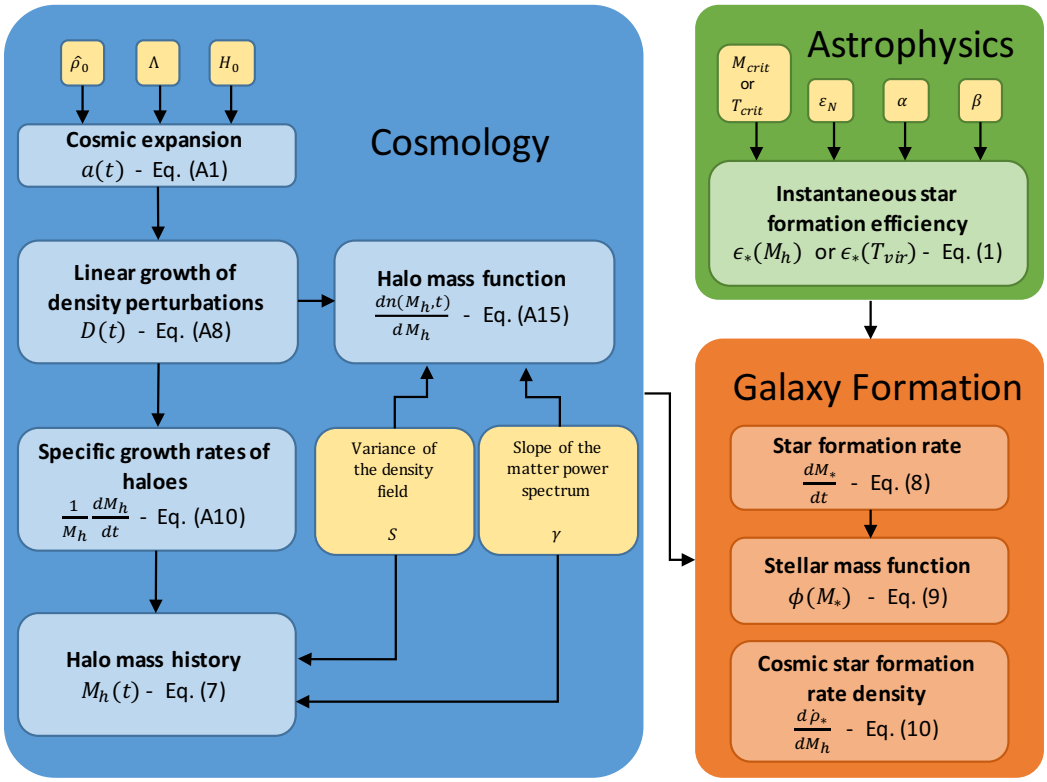

Fig. 5.2.: A schematic diagram of the UniverseApp analytic model of galaxy formation. The blue block components depend only on cosmology. By using the Taylor expansion solution to the Friedmann equations in (Salcido et al., 2018), all the cosmological components can be calculated analytically for every cosmological parameters ρ_0, Λ, H_0 and the shape of the power-spectrum parametrised by S and γ. All astrophysical processes (green) enter into the model by the instantaneous star formation efficiency ϵ_*, which is fully described by the four free parameters $M_{\rm crit}$ or $T_{\rm crit}$, $\epsilon_{\rm N}$, α and β in Eq. (5.3) or Eq. (5.4). The galaxy formation outputs are summarised in the orange block.

- *Halo mass history*

The mass of a halo as a function of time is given by,

$$M_h(t) = \left[-\frac{424.958\gamma}{\sqrt{S_0}{t_m}^{4/3}} \left(t_0^{-2/3} \left(1 + 0.1590 \left(\frac{t_0}{t_\Lambda} \right)^2 - 0.0112 \left(\frac{t_0}{t_\Lambda} \right)^4 \right) \right. \right. \\ \left. \left. -t^{-2/3} \left(1 + 0.1590 \left(\frac{t}{t_\Lambda} \right)^2 - 0.0112 \left(\frac{t}{t_\Lambda} \right)^4 \right) \right) + M_0^{-\gamma/2} \right]^{-2/\gamma}, \tag{5.7}$$

where $t_0 = 13.8$ Gyr, is the present cosmic time, $t_\mathrm{m} = \sqrt{3/8\pi G\hat{\rho}_0}$, $t_\Lambda = \sqrt{3/\Lambda c^2}$, $\hat{\rho}_0$ is the matter density of our Universe at the present time, and Λ is the value of the cosmological constant. Substituting the numerical values for the cosmological parameters for a standard ΛCDM universe as inferred by the Planck Collaboration et al. (2014) in Eq. (5.7), i.e. t_m=26.039, t_Λ=17.3317, γ=0.3, t_0=13.8 and S_0=$10^{4.2}$, Fig. 5.3 shows the individual mass histories for halos of a given mass M_0 at the present cosmic time (represented by the colour coding). An Einstein-de Sitter universe is shown in dashed lines.

- *The galaxy star formation rate*

The stellar evolution of individual halos through cosmic time is given by the integral of,

$$\frac{\mathrm{d}M_*}{\mathrm{d}t} = \epsilon_* \left[\frac{1}{M_h} \frac{\mathrm{d}M_h}{\mathrm{d}t} \right] M_h \\ = \epsilon_* \frac{566.61}{\sqrt{S_0}\, t^{5/3} t_m^{4/3}} \left(1 - 0.3182 \left(\frac{t}{t_\Lambda} \right)^2 + 0.0563 \left(\frac{t}{t_\Lambda} \right)^4 \right) M_h(t)^{\left(\frac{\gamma}{2}+1\right)}, \tag{5.8}$$

where ϵ_* is given by Eq. (5.3) or Eq. (5.4), and $M_h(t)$ by Eq. (5.7).

- *The galaxy stellar mass function*

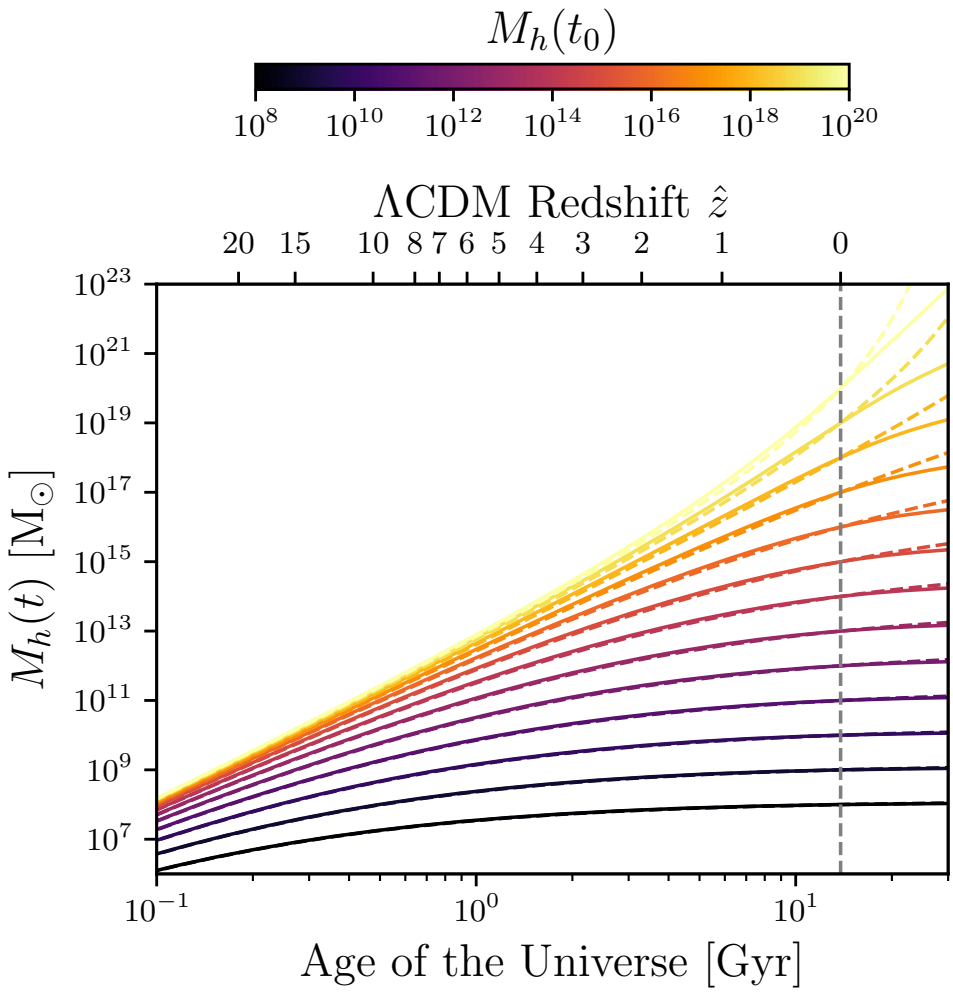

Fig. 5.3.: Average halo mass as a function of cosmic time derived in Eq. (5.7). A model for the cosmological parameters for a standard ΛCDM universe as inferred by the Planck Collaboration et al. (2014) is show with solid lines. An Einstein-de Sitter universe is shown in dashed lines. Colour coding represents different halo mass at the present time $M_0 = M_h(t_0)$.

The GSMF could be obtained by convolving the mass function of dark matter haloes and the SHMR,

$$\begin{aligned}\phi(M_*) = \frac{\mathrm{d}N}{\mathrm{dlog}_{10}M_*(M_h)} &= \frac{\mathrm{d}N}{\mathrm{dlog}_{10}M_h}\left(\frac{\mathrm{dlog}_{10}M_*}{\mathrm{dlog}_{10}M_h}\right)^{-1} \\ &= \frac{\mathrm{d}N}{\mathrm{dlog}_{10}M_h}\varepsilon(M_h)^{-1},\end{aligned} \tag{5.9}$$

where, $\varepsilon(M_h)$ can be thought as a galaxy formation efficiency of haloes of mass M_h, and can be obtained by the integral of Eq. (5.8).

- *The cosmic star formation rate density*

The cosmic SFR density is given by the integral of,

$$\begin{aligned}\frac{\mathrm{d}\dot{\rho}_*}{\mathrm{d}M_h} &= \epsilon_*\left[\frac{1}{M_h}\frac{\mathrm{d}M_h}{\mathrm{d}t}\right]M_h\frac{\mathrm{d}n(M_h,t)}{\mathrm{d}M_h} \\ &= \epsilon_*\frac{46230.9\hat{\rho}_0}{M_h S t^{7/3} t_m^{8/3}}\left(1-0.1590\left(\frac{t}{t_\Lambda}\right)^2-0.0056\left(\frac{t}{t_\Lambda}\right)^4\right) \\ &\times\exp\left[-\frac{232382}{S\,t^{4/3}t_m^{8/3}}\left(1+0.3182\left(\frac{t}{t_\Lambda}\right)^2+0.0028\left(\frac{t}{t_\Lambda}\right)^4\right)\right].\end{aligned} \tag{5.10}$$

Here again, ϵ_* could be modeled using either Eq. (5.3) or Eq. (5.4). The differential form of Eq. (5.10) explicitly shows the contribution from haloes of different masses M_h, to the total cosmic SFR density.

Equations (5.7) to (5.10), together with a model of the instantaneous star formation efficiency, Eq. (5.3) or Eq. (5.4), provide a full mathematical framework to explore the effects of cosmology and baryonic physics on galaxy formation. In the next section, we will explore the effect of the different efficiency parameters on the galaxy SFR, GSMF and the cosmic SFR density.

5.3 The impact of the instantaneous star formation efficiency

We now use the UniverseApp to explore the effect of the different efficiency parameters in the galaxy formation outputs in the orange block of Fig. 5.2. It is

Table 5.1.: Instantaneous star formation efficiency parameters for the six idealised models.

	$\epsilon_{\rm N}$	$M_{\rm crit}$	α	β
Fiducial	0.02	10^{12}	1	1
Constant	0.02	10^{12}	0	0
No AGN	0.02	10^{12}	1	0
No SN	0.02	10^{12}	0	1
$M_{\rm crit} = 10^{10}$	0.02	10^{10}	1	1
$M_{\rm crit} = 10^{14}$	0.02	10^{14}	1	1

common to characterise galaxy properties over halo masses, and for simplicity, in this section we will only use a halo mass-dependent star formation efficiency model (i.e. we will model ϵ_* using Eq. (5.3)).

It has been estimated that the SHMR peaks at masses similar to Milky-Way sized halos ($\sim 10^{12}\,{\rm M}_\odot$). Typically, at low masses, the SFR is suppressed because of the efficiency of stellar feedback. On the other hand, at higher masses the cooling of the inflowing gas is suppressed by heating from supermassive BHs (e.g. White & Frenk, 1991; Benson, 2012; Bower et al., 2006). The "Fiducial" model captures this behaviour with both α and β being positive and equal to 1.

We consider five variants to explore the physics of galaxy formation. An extreme idealised case label as "Constant", describes a model where a fixed fraction of the baryon budget is turned into stars, regardless of the halo mass. The "No AGN" model describes a scenario where the efficiency of feedback process is weak for massive objects. Physically, this could be thought as a model where feedback from active galactic nuclei is inefficient. The "No SN" model describes a scenario where the efficiency of feedback process is weak in small haloes. Physically, this could be thought as a model where feedback from supernovae is inefficient[4]. Two additional models labelled "$M_{\rm crit} = 10^{10}$" and "$M_{\rm crit} = 10^{14}$" explore the effect of changing the critical, or transition, halo mass. We show in Fig. 5.4 the instantaneous star formation efficiency for the six models, and their parameters are summarised in Table 5.1.

[4]This model would also require that accretion onto BHs in low mass galaxies is suppressed (see Dubois et al., 2016; Bower et al., 2017; Habouzit et al., 2017; McAlpine et al., 2018)

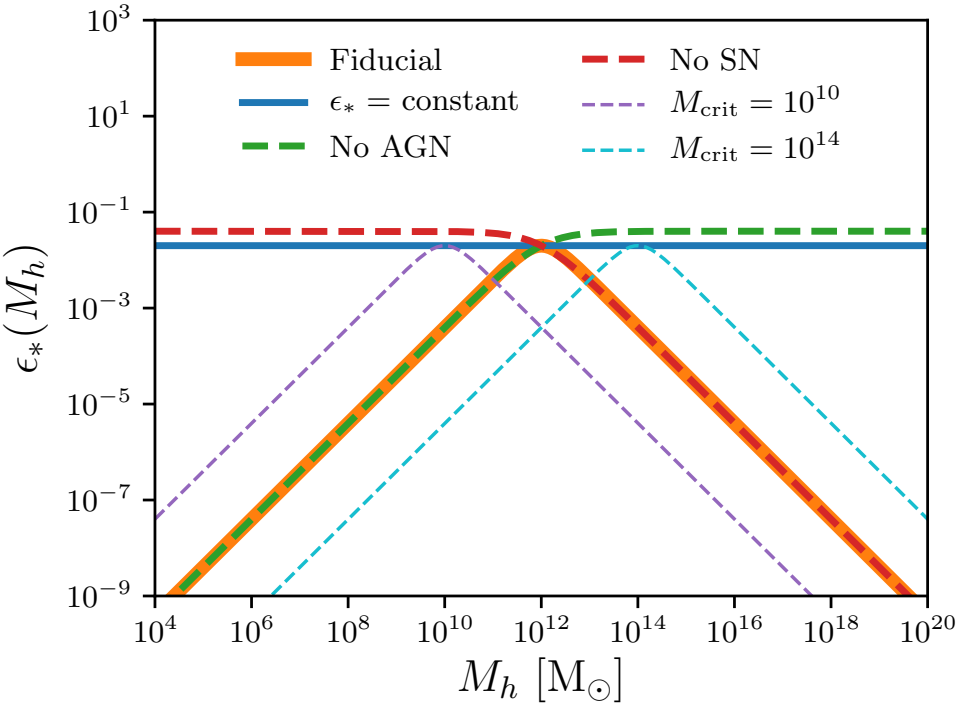

Fig. 5.4.: The instantaneous star formation efficiency ϵ_* as a function of halo mass for the six models described in Table 5.1.

5.3.1 The build up of stellar mass

We begin by exploring the effect of the efficiency parameters in star formation in individual galaxies. Using the six efficiency models, the build up of stellar mass in individual haloes can be calculated self-consistently by integrating Eq. (5.8).

Fig. 5.5 shows an example of the evolution of the stellar mass in a halo of mass $M_0 = 10^{13}\mathrm{M}_\odot$ at the present time for the six efficiency models. It can be seen in the figure, that for the constant efficiency model, the stellar mass inside the halo grows steadily with time, and starts to slow down only at late times due to the cosmic expansion. For the fiducial model, the build up of stellar mass is faster (steeper slope). Once the critical halo mass is reached ($M_{\rm crit} = 10^{12}\mathrm{M}_\odot$, corresponding to $M_* \approx 10^{10}\mathrm{M}_\odot$ for this model), the stellar mass plateaus. The No AGN model has a similar behaviour at early times, but once the critical halo mass is reached, star formation does not slow down and the halo reaches a higher stellar mass. On the other hand, the No SN model produces much more stellar mass at early times, but once the critical halo mass is reached, star formation slows down, and the halo reaches a similar final stellar mass as the fiducial model. The two models with

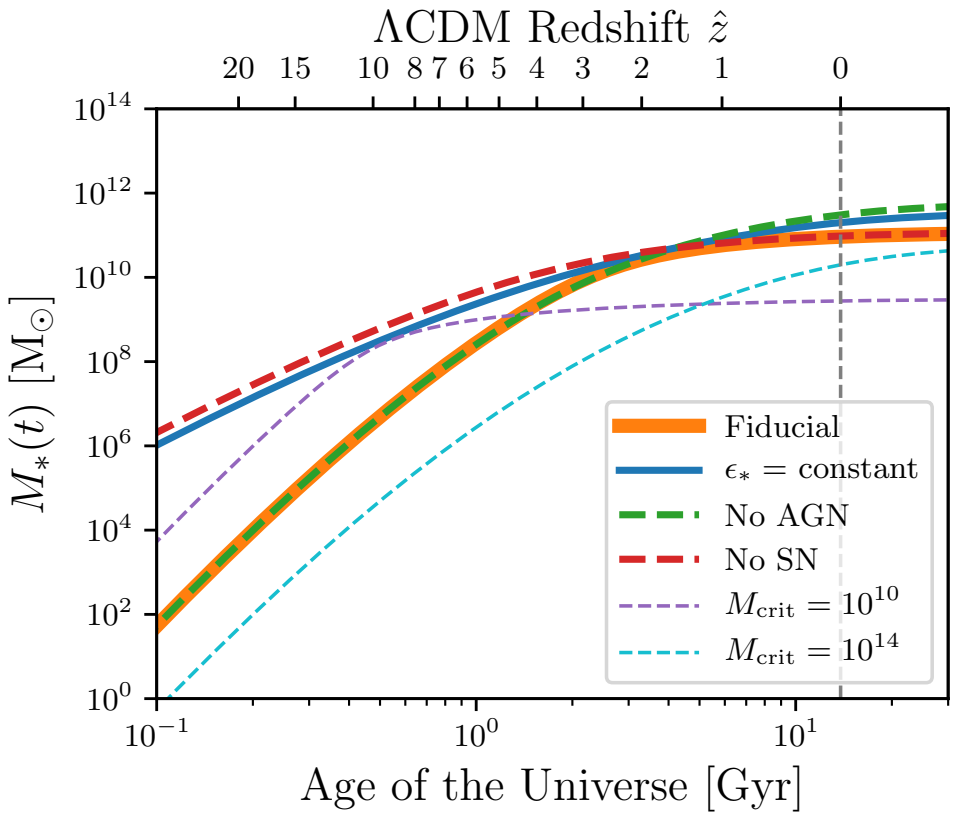

Fig. 5.5.: An example of the evolution of the stellar mass in a halo of mass $M_0 = 10^{13}\mathrm{M}_\odot$ at the present time. The different colours represent the different efficiency models.

different $M_{\rm crit}$ present a similar behaviour to the fiducial model, i.e. once the halo reaches the critical mass, it hardly produces any additional stellar mass.

5.3.2 The stellar mass function

As shown in the previous section, we can use Eq. (5.8) to calculate the stellar mass of any halo as a function of time. This allows us to obtain the SHMR and convolve it with the halo mass function in Eq. (A.15) to calculate the GSMF.

Fig. 5.6 shows the GSMF at the present time for the six efficiency models. As it has been pointed out before (e.g Bower et al., 2006; Mutch et al., 2013), if feedback process are inefficient both at the low mass and high mass end, i.e. a constant fraction of the baryon budget is turned into stars in every halo, then, the GSMF does not exhibit the characteristic knee obtained in observations (constant model shown in blue). Once feedback process are implemented, the location of the knee of the GSMF is determined by the the critical mass in the star formation efficiency

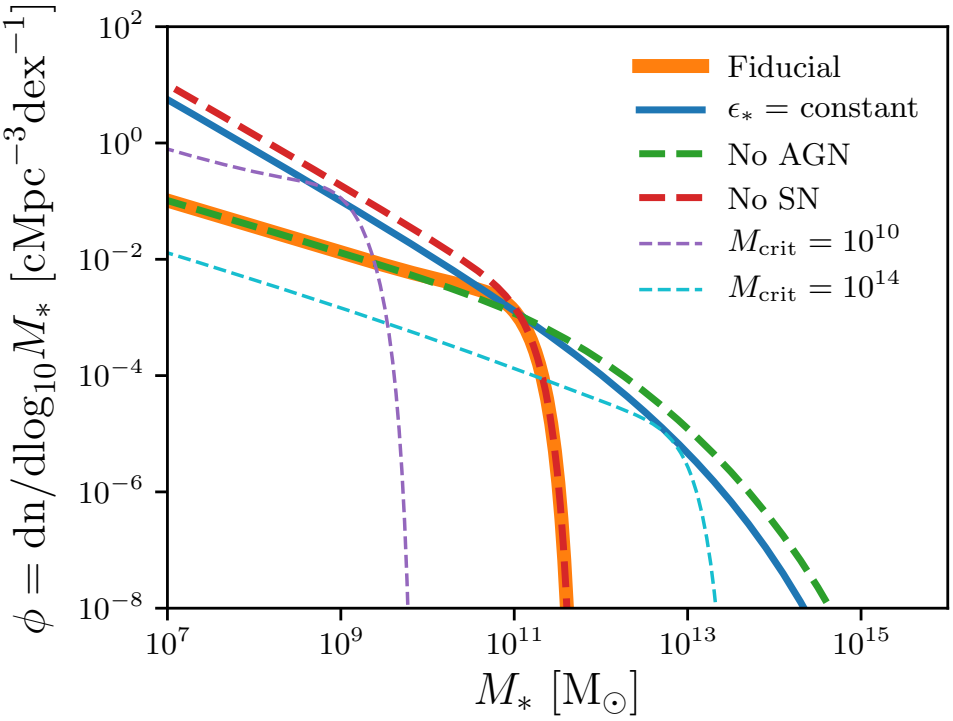

Fig. 5.6.: The GSMF at the present time. The different colours represent the different efficiency models.

(fiducial, $M_{\mathrm{crit}} = 10^{10}$ and $M_{\mathrm{crit}} = 10^{14}$). The No AGN model has the same shallow slope at the faint end of the GSM function as the fiducial model, with a slight bend at high masses driven only by the halo mass function. The No SN model presents the same knee as the fiducial model, but the slope of the faint end of the GSM function is much steeper.

5.3.3 The cosmic SFR density

The cosmic history of star formation is perhaps one of the most fundamental observables of our Universe. It has been observed to peaked approximately 3.5 Gyr after the Big Bang ($z \approx 2$), and declined exponentially thereafter (for a review see Madau & Dickinson, 2014). Different groups have tried to model the complex physics driving the cosmic SFR by using, for example, full hydrodynamical simulations (e.g. Schaye et al., 2015; Davé et al., 2016; Dubois et al., 2016; Pillepich et al., 2018). The UniverseApp provides a simple model that disentangle the role of cosmology from the role of astrophysics, which in turn, allows us to examine the effect of the different efficiency parameters on the cosmic SFR density.

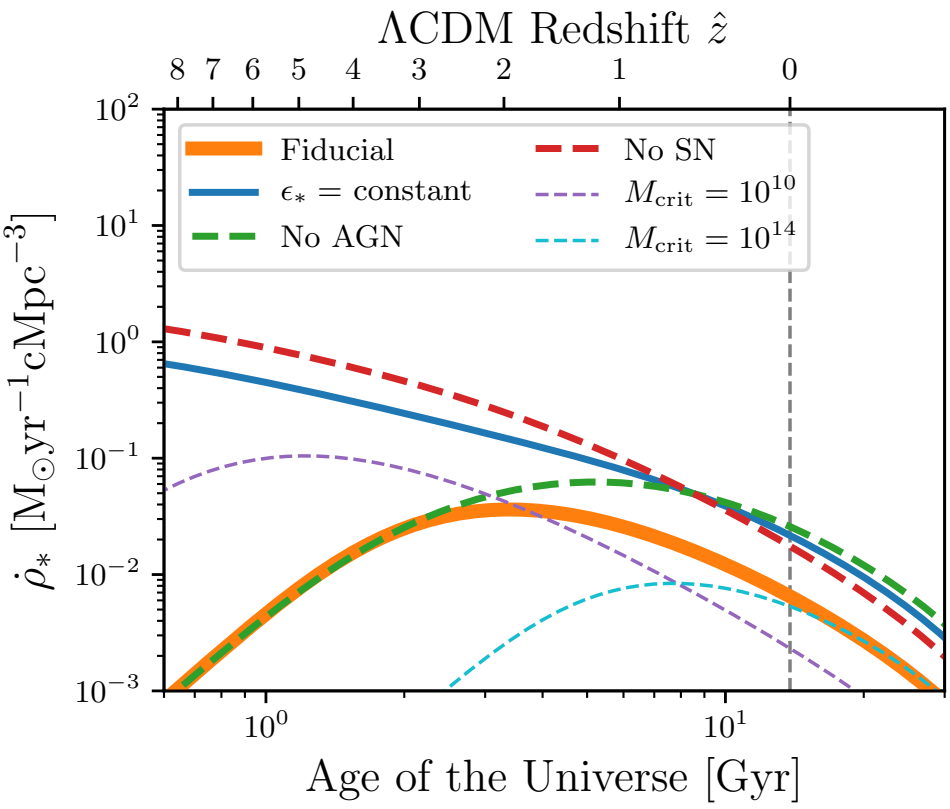

Fig. 5.7.: The cosmic SFR density for the six efficiency models.

We begin by noting that Eq. (5.10) has two main terms. First, a multiplier term that originates from both, the halo accretion rate, and the halo mass function, and is $\propto t^{-7/3}$. This, comes from the dynamical timescale of the universe getting larger. Second, an exponential term contribution due to the build up of halos in the halo mass functions that is $\propto e^{-t^{-4/3}}$. For a given halo mass then, the exponential term dominates at early times, and the contribution to the cosmic SFR density is driven by the exponential build up of haloes. At late times, the exponential term asymptotically tends to a constant value, and the further evolution of the cosmic SFR is dominated by the multiplier term, i.e., it behaves as a power law. As discussed in Salcido et al. 2018, the contribution of dark energy is only relevant at late times, and at its observed value, it has a negligible impact on star formation in the Universe.

Figure 5.7 shows the integrated cosmic SFR density for the six efficiency models computed using Eq. (5.10). For the fiducial model, while smaller haloes are more abundant than large objects, a smaller fraction of the inflowing material is converted into stars. As a result, the SFR density is dominated by the largest haloes in which star formation is able to proceed without generating efficient feedback. The smaller haloes only contribute significantly at very early times, when the abundance of larger

objects is strongly suppressed by the exponential term in the mass function. We see therefore that the contribution of halos of mass $\approx M_{\rm crit} = 10^{12}\,{\rm M}_{\odot}$, is representative of most of the SFR in the model.

If star formation is efficient at all halo masses (constant model), then the cosmic SFR behaves like a power law with time, which only deviates from this behaviour at late times due to the contribution of the cosmological constant.

Examining the No SN model reveals that origin of the observed peak in the cosmic history of star formation is the efficient feedback in low mass galaxies. Without a mechanism to suppress star formation in small haloes, the history of the cosmic SFR density would not have its characteristic peak. Supernovae feedback is then mainly responsible for shaping the cosmic SFR density of the Universe. On the other hand, examining the No AGN model reveals that efficient feedback in high mass haloes only has a moderate effect on shaping the cosmic star formation. Without a mechanism to prevent star formation in massive galaxies, the cosmic SFR density would still exhibit a peak, only changing mildly its amplitude and localisation. However, the slope of the decline would be similar (orange vs green dashed lines).

Finally, changing the transition mass $M_{\rm crit}$ has a great impact on the localisation of the SFR peak. As in the fiducial model, the contribution of halos of mass $\approx M_{\rm crit}$, is representative of most of the SFR in each model.

5.4 Fitting observations

In this section we compare the results from the UniverseApp to different datasets of observational data. We begin by calibrating our model the GSMF at $\hat{z} = 0$ using observations from the Galaxy And Mass Assembly (GAMA) survey (Baldry et al., 2012) and the Sloan Digital Sky Survey (SDSS) (Moustakas et al., 2013). We use the reduced chi-squared statistic to derive the best-fitting instantaneous star formation efficiency $\epsilon_*(M_h)$. Because the model is fully analytic, this calibration process is fast and easy to perform. Figure 5.8 shows the best fit model in orange. The best best fit efficiency parameters are shown in Table 5.2.

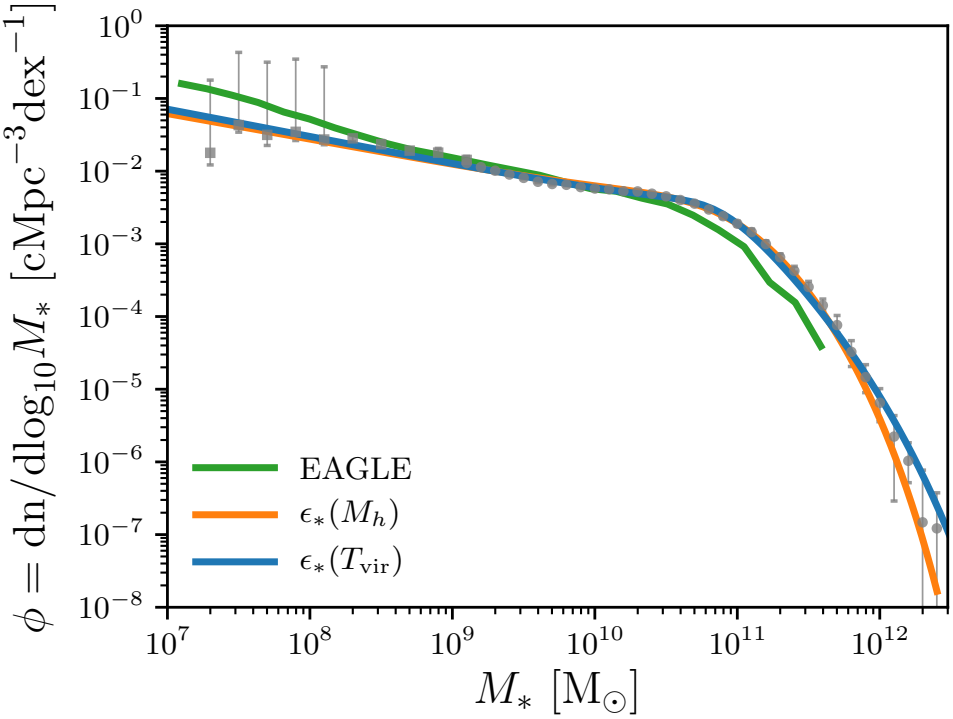

Fig. 5.8.: GSMF for the best fit parameters in Table 5.2.

Table 5.2.: Best fit parameters for a time-independent star formation efficiency model $\epsilon_*(M_h)$.

ϵ_{N}	$M_{\mathrm{crit}}\,[\mathrm{M_\odot}]$	α	β	χ^2_ν
0.028	$10^{11.68}$	1.537	0.656	1.50

5.4.1 The need for an evolving efficiency

Having stablished the best-fitted efficiency parameters for the UniverseApp model, we can study the evolution of the model outputs. By construction, $\epsilon_*(M_h)$ is only a function of halo mass and is fixed in time. Hence, the evolution of the GSFM depends only on the evolution of the abundance of halos of mass M_h as a function of time, as described by the halo mass function. Figure 5.9 shows the evolution of the predicted GSMF for the halo mass-dependent star formation efficiency model in dashed lines. Colour coding represents different redshifts for a ΛCDM universe. Observation data from Baldry et al. 2012; Moustakas et al. 2013; Tomczak et al. 2014; Ilbert et al. 2013; Muzzin et al. 2013; Song et al. 2016 is show in coloured symbols.

While the observed data at high redshift is highly uncertain, the halo mass-dependent model significantly under predicts the abundance of distant galaxies. This hints to the need of a time-evolving efficiency model. "Traditional" empirical modelling (e.g Moster et al., 2018; Behroozi et al., 2018) would relax the physical priors and let, in this case, the four efficiency parameter in the model to evolve freely in time. Instead, we propose a physically motivated efficiency model that naturally evolves with cosmic time.

The three phases of galaxy formation

Using a simple analytical model, Bower et al. 2017 described the build up of gas within haloes using the interaction between buoyant, high entropy star formation driven outflows and the rate of cosmic gas inflow. In low mass systems the adiabat of star formation driven outflows exceeds that of the halo's diffuse corona, and can buoyantly escape (i.e gas gets hotter than the virial temperature of the halo). In turn, the density within the halo remains low. As the halo grows, a hot corona forms and the star formation driven outflows are no longer buoyant relative to their surroundings (i.e the virial temperature of the halo is higher than that of the stellar feedback outflows). This triggers the build up of a high density of gas within the halo. By equating the adiabat of stellar feedback outflows to that of the galaxy's diffuse corona, Bower et al. 2017 predicted a critical halo mass ($M_{\rm crit} \approx 10^{12}\,{\rm M}_\odot$ with a redshift dependance) for this transition.

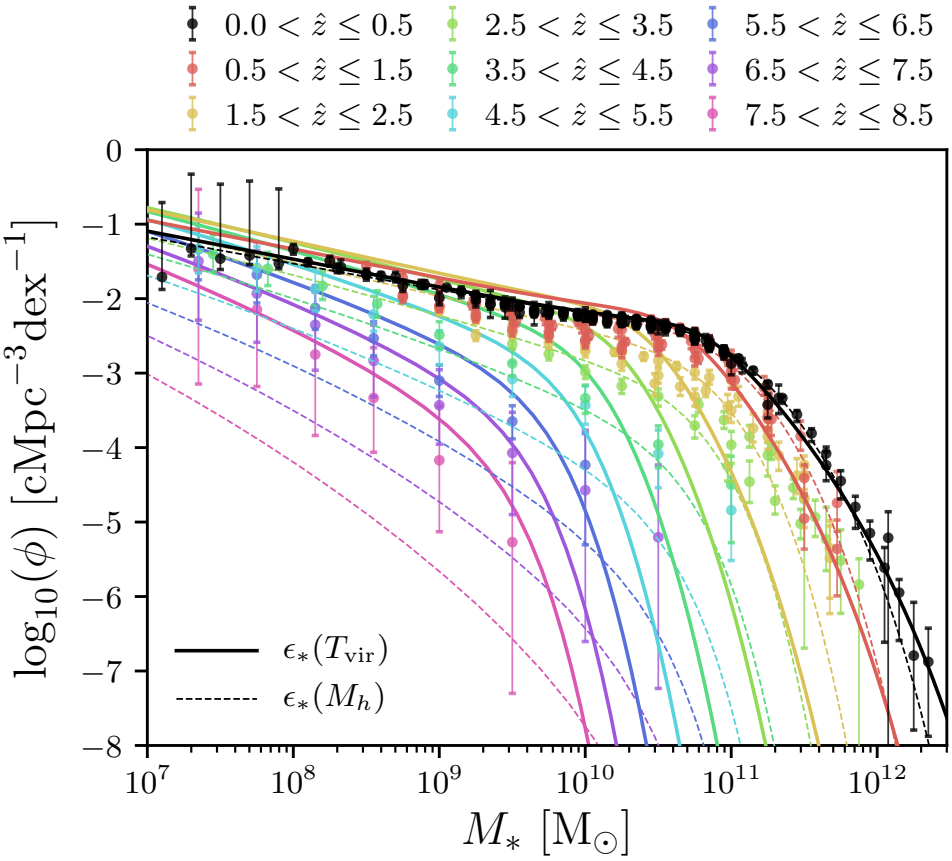

Fig. 5.9.: Evolution of the predicted GSMF for the halo mass-dependent, and the virial temperature-dependent star formation efficiency models. Colour coding represents different observed redshifts. Observation data with their associated uncertainties from Baldry et al. 2012; Moustakas et al. 2013; Tomczak et al. 2014; Ilbert et al. 2013; Muzzin et al. 2013; Song et al. 2016 is show in coloured symbols. The halo mass-dependent model is shown in dashed lines ($\epsilon_*(M_h)$). The virial temperature-dependent model is shown in solid lines ($\epsilon_*(T_{\rm vir})$). While both models have been calibrated to reproduce the GSMF at low redshift, the halo mass-dependent model significantly under predicts the abundance of galaxies at high redshift.

An instantaneous star formation efficiency model characterised by a time-independent critical virial temperature, $T_{\rm crit}$, assumes that there exists a critical halo virial temperature at which there is a transition from where star formation driven outflows can buoyantly escape, to where outflows are no longer buoyant, and gas stalls inside the halo. Using the viral temperature of the halo provides a natural evolution of the star formation efficiency, because for a fixed halo mass, early collapsed haloes are more compact (denser), and one might expect a higher efficiency (for haloes with $T_{\rm vir} < T_{\rm crit}$).

In this simple picture, we can distinguish three phases of galaxy formation, characterised by the virial temperature of the halo:

- **Stellar feedback regulated phase:** buoyant star formation driven outflows effectively regulate the gas content of galaxies residing in haloes with virial temperature $T_{\rm vir} < T_{\rm crit}$. In this phase, the density within the halo remains low, resulting in limited star formation and starved BH growth.

- **Efficient star forming/rapid growing black hole phase:** as haloes grow, the virial temperature increases to the point that the stellar outflows are no longer buoyant relative to their surroundings, and therefore stall (i.e $T_{\rm vir} \approx T_{\rm crit}$). The density of gas builds up within the halo triggering high star formation rates and rapid BH growth.

- **AGN feedback regulated phase:** In haloes with $T_{\rm vir} > T_{\rm crit}$, the central BH is massive enough to produce efficient AGN feedback, in turn, regulating the gas content of the halo and preventing further star formation.

An additional advantage of using the virial temperature to characterise the star formation efficiency, is that we can add a proxy for the effect of cosmic reionisation. Ultraviolet radiation from the first stars formed reionised neutral hydrogen, raising its entropy to a temperature of $\approx 10^4$K. This process prevented further cooling, hence preventing star formation, in haloes with $T_{\rm vir} < 10^4$K (Doroshkevich et al., 1967; Couchman & Rees, 1986; Rees, 1986; Efstathiou, 1992; Loeb & Barkana, 2001). As a result of this suppression of star formation, only a fraction of the haloes with present-day mass $\approx 10^{10}$M$_\odot$ form a galaxy, and no galaxies form below a halo mass of $\approx 10^7$M$_\odot$ (Sawala et al., 2013, 2016; Fitts et al., 2017; Bose et al., 2018). We therefore include the effect of reionisation by setting $\epsilon_*(T_{\rm vir} < 10^4{\rm K}) = 0$.

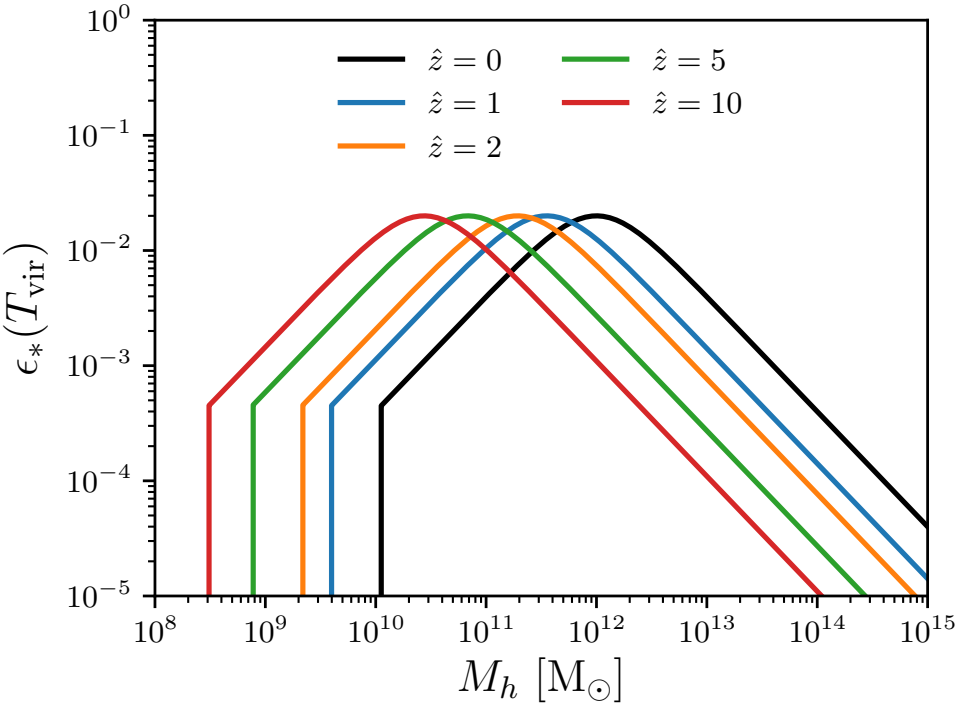

Fig. 5.10.: Evolution of the instantaneous star formation efficiency, $\epsilon_*(T_{\rm vir})$, as a function of halo mass for different redshifts in a ΛCDM universe. The sharp cut in efficiency in low mass halos is the effect of cosmic reionisation, $\epsilon_*(T_{\rm vir} < 10^4{\rm K}) = 0$.

Table 5.3.: Best fit parameters for an evolving star formation efficiency model $\epsilon_*(T_{\rm vir})$.

$\epsilon_{\rm N}$	$T_{\rm crit}$ [K]	α	β	χ^2_ν
0.022	$10^{5.34}$	2.377	0.840	1.59

We again calibrate the $\epsilon_*(T_{\rm vir})$ model to the GSMF at $\hat{z} = 0$ using the reduced chi-squared statistic to derive the best-fitting parameters. The best fit efficiency parameters are shown in Table 5.3. As we have discussed, using the virial temperature of the halo to characterise the star formation efficiency, provides a natural time evolution of the efficiency in cosmic time. Figure 5.10 shows the evolution of the instantaneous star formation efficiency as a function of halo mass for different redshifts in a ΛCDM universe. The sharp cut in efficiency in low mass haloes is the effect of setting $\epsilon_*(T_{\rm vir} < 10^4{\rm K}) = 0$.

It is important to highlight that the models were calibrated to reproduce only the observed GSMF at redshift $z = 0$. Figure 5.8 shows the best fit virial temperature model in blue. The figure shows that both, the halo mass-dependent efficiency $\epsilon_*(M_h)$, and the virial temperature-dependent efficiency $\epsilon_*(T_{\rm vir})$ models, provide a good fit to the present-day GSMF (see also the reduced chi squared statistics in Table 5.2 and Table 5.3). Remarkably, Fig. 5.9 shows that a star formation efficiency

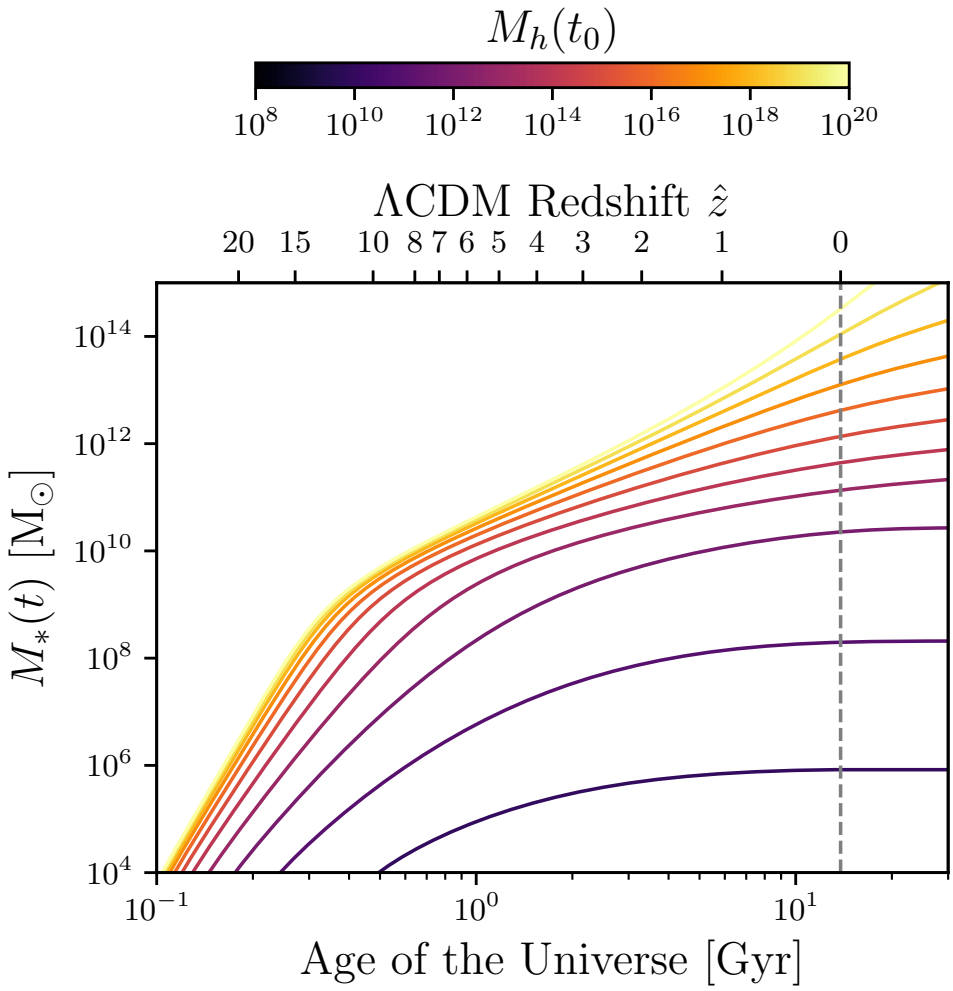

Fig. 5.11.: Evolution of the stellar mass within haloes using the best-fit virial temperature efficiency model (Table 5.3). Colour coding represents different present-day halo mass $M_h(t_0)$. Solid lines represent a ΛCDM universe. An EdS universe is shown in dashed lines. Halos of a present-day mass $\lessapprox 10^{10}\mathrm{M}_\odot$ do not host any galaxies. The effect of the cosmological constant is negligible in the build up of stellar mass.

as a function of the virial temperature of the halo reproduces the abundance of galaxies both at low and high redshift.

Figure 5.11 shows the build up of the stellar mass within haloes using the best-fit virial temperature efficiency model, and calculated integrating Eq. (5.8). Colour coding represents different present-day halo mass $M_h(t_0)$ on a ΛCDM cosmology. As expected, haloes of a present-day mass $\lessapprox 10^{10}\mathrm{M}_\odot$ do not host any galaxies. The transition of the star formation efficiency at T_{crit} can be clearly seen in very massive haloes, where there is a rapid rise of stellar mass, then, when the halo reaches the critical temperature, the build up of stellar mass slows down significantly.

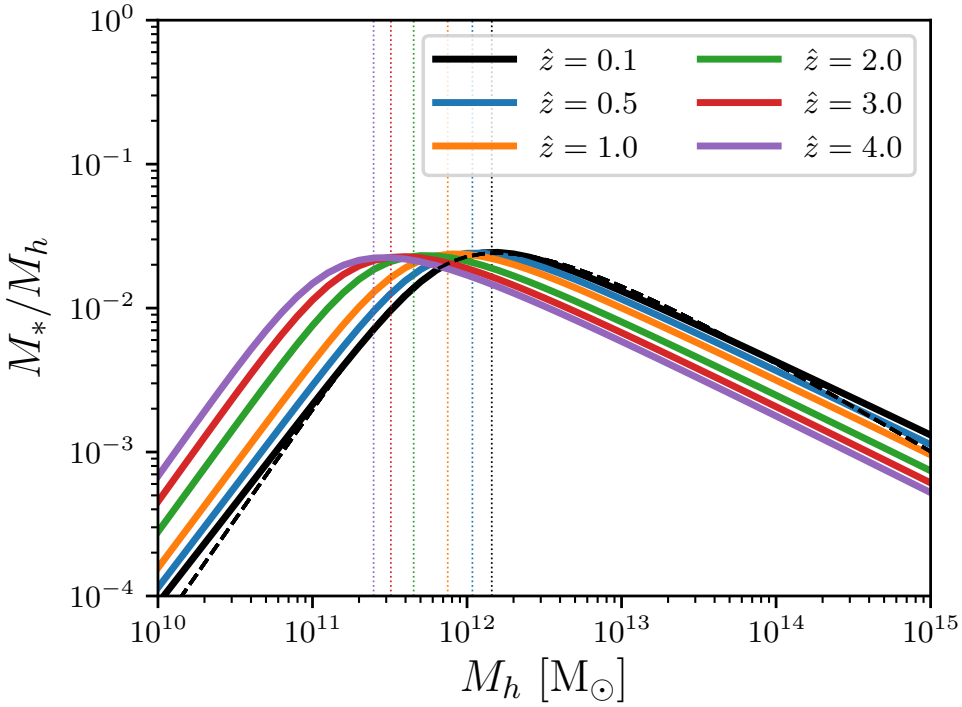

Fig. 5.12.: Predicted SHMR for the time-independent, and evolving star formation efficiency models. Colour coding represents different observed redshifts. The halo mass-dependent model is shown as a dashed black line. Vertical dotted lines indicate the critical mass derived in Bower et al. 2017.

Figure 5.12 shows the predicted SHMR from both efficiency models. Colour coding represents different observed redshifts. The critical halo mass predicted in Bower et al. 2017 is shown in vertical dotted lines. Recently, McAlpine et al. 2018 showed that the critical halo mass predicted in Bower et al. 2017 agrees remarkably well with the triggering of a rapid black hole growth phase in the EAGLE simulations.

The UNIVERSEAPP model using a virial temperature efficiency predicts a SHMR relation that differs from observational contains using abundance and clustering properties of galaxy samples with predictions from a phenomenological halo models. For example, recently Cowley et al. 2018 calculated that the peak of the SHMR shifts to higher masses for earlier times. As we discussed before, these methods however, depend heavily on the underlying modelling and assumptions. More sophisticated empirical models (e.g. Behroozi et al., 2018; Moster et al., 2018) find that the peak in the SHMR movies first to higher masses for low redshifts, and then to lower masses at high redshifts.

Figure 5.13 shows the predicted cosmic SFR for the two efficiency models. Using the UNIVERSEAPP model, we can clearly see the contribution to the total SFR density

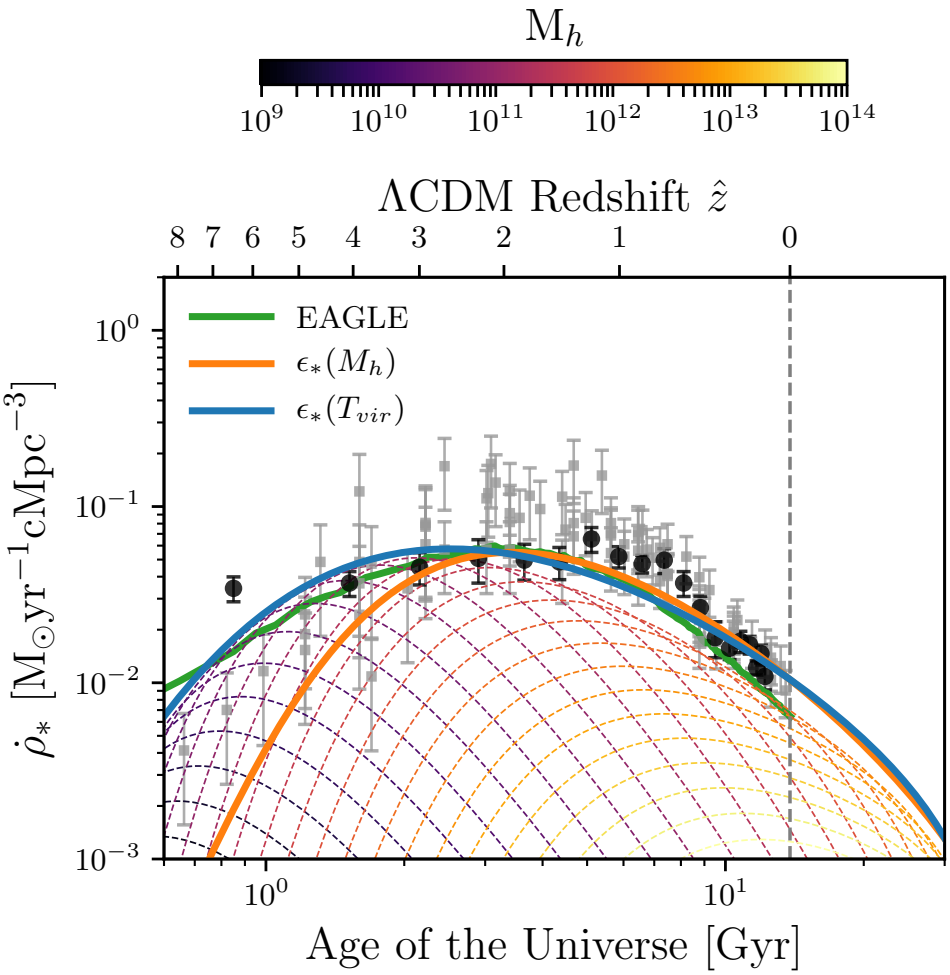

Fig. 5.13.: The predicted SFR history of the Universe for the two efficiency models presented in this chapter. Coloured lines show the contributions from dark matter haloes of different masses (per dex), using the star formation efficiency described by Eq. (5.10), and using the virial temperature efficiency model. The total SFR for the virial temperature efficiency model is shown in blue. The time-independent efficiency model is shown in orange. Results from the EAGLE simulation are shown in green for reference. Observational data compiled by Behroozi et al. 2013b is shown as grey symbols. Observational data from Driver et al. 2018 is shown as black symbols.

from dark matter haloes of different masses (per dex), shown as coloured dashed lines (only shown for the virial temperature-dependent efficiency model). The total SFR for the virial temperature efficiency model is shown in blue. The halo mass-dependent efficiency model is shown in orange. Results from the EAGLE simulation are shown in green for reference. Observational data compiled by Behroozi et al. 2013b is shown as grey symbols. The latest observational results from the GAMA survey from Driver et al. 2018 are shown as black symbols. The UNIVERSEAPP model using a virial temperature efficiency reproduces the amplitude and shape of the observed SFR density remarkably well, while the halo mass-dependent efficiency model, produces a lower SFR at high redshift.

Finally, in Fig. 5.14 we show the SSFR of galaxies different redshifts. The UNIVERSEAPP model using a virial temperature efficiency is shown in solid lines. The halo mass-dependent model is shown in dashed lines. Results from the EAGLE simulations are shown in dotted lines for reference. The halo mass-dependent model agrees surprisingly well with the sophisticated physics and full hydrodynamic simulations used in EAGLE. On the other hand, the virial temperature efficiency model, predicts significantly lower SSFR. This is, perhaps counterintuitive, since the virial temperature model is more efficient in low mass haloes at higher redshifts. This is because galaxies of a fixed stellar mass are hosted by more massive haloes, so experience a greater cosmological accretion rate and must increase their SFR to achieve self-regulation.

5.5 Discussion and Conclusions

In our current paradigm of galaxy formation, every galaxy forms within a dark matter halo. Due to the tight correlation observed between the properties of galaxies and their host haloes, it is natural to expect that individual galaxy assembly could be correlated with halo assembly (see Wechsler & Tinker 2018 for a review).

In this chapter, we developed a fully analytic model of galaxy formation that connects the growth of dark matter haloes in a cosmological background, with the build up of stellar mass within these haloes. The model restricts the role of baryonic astrophysics to setting the relation between galaxies and their halos. We assume an instantaneous star formation efficiency which captures all the physical processes

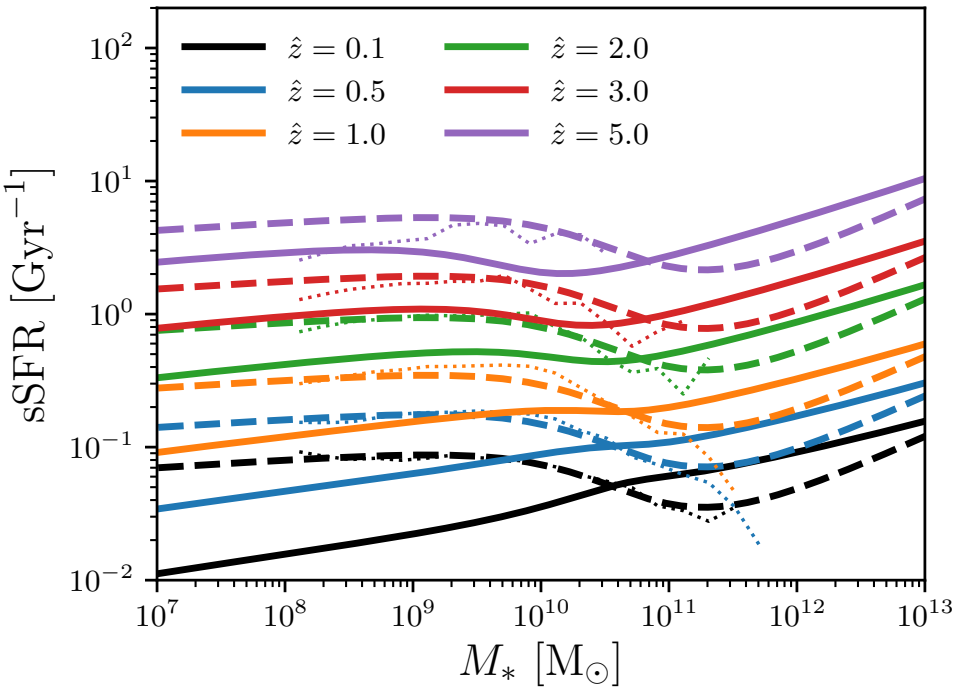

Fig. 5.14.: The sSFR of galaxies at different redshifts for an observer at the present time in a ΛCDM universe. The UniverseApp model using a virial temperature efficiency is shown in solid lines. The halo mass-dependent model is shown in dashed lines. Results from the EAGLE simulations are shown in dotted lines for reference.

involved in the conversions of gas into stars, i.e. cooling, star formation law, feedback mechanisms, etc.

We show that galaxy formation is revealed as a simple process where the instantaneous star formation efficiency within halos is only a function of their virial temperature. We show that all the complex physics of galaxy formation, the interplay between cosmology and baryonic process can be understood as a single differential equation. Despite its simplicity, the model reproduces self-consistently the shape and evolution of the cosmic star formation rate density, the specific star formation rate of galaxies, and the galaxy stellar mass function, both at the present time and at high redshift.

The instantaneous star formation efficiency model characterised by a time-independent critical virial temperature, $T_{\rm crit}$, assumes that there exists a critical halo virial temperature at which there is a transition from where star formation driven outflows can buoyantly escape, to where outflows are no longer buoyant, and gas stalls inside the halo. In this simple picture, we can distinguish three phases of galaxy formation: A stellar feedback regulated phase, where buoyant star formation driven outflows

effectively regulate the gas content of galaxies residing in haloes with virial temperature $T_{\rm vir} < T_{\rm crit}$. An efficient star forming/rapid growing black hole phase, where stellar outflows are no longer buoyant relative to their surroundings, and therefore stall (i.e $T_{\rm vir} \approx T_{\rm crit}$). The density of gas builds up within the halo, triggering high star formation rates and rapid BH growth. Finally, an AGN feedback regulated phase, where the central BH is massive enough to regulate the gas content of the halo, preventing further star formation.

Our model is limited to the connection between haloes and central galaxies only. Subhaloes and satellite galaxies are subject to complex processes, such as tidal and ram pressure stripping, which are not included. Furthermore, for simplicity, our model neglects the effect of stellar mass loss and stellar build up by mergers. Nevertheless, the model can be easily extended to include such processes. Finally, one of the main advantages of the model is that by providing a set of analytic equations, the model can be easily "inverted" and allows for rapid experiments to be conducted, providing a great tool to explore the differential effects of baryonic physics, averaged over galaxy scales.

6

Music from the heavens - Gravitational waves from supermassive black hole mergers in the EAGLE simulations

In this chapter, we estimate the expected event rate of gravitational wave signals from mergers of supermassive black holes that could be resolved by a space-based interferometer, such as the Evolved Laser Interferometer Space Antenna (eLISA), utilising the reference cosmological hydrodynamical simulation from the EAGLE suite. These simulations assume a ΛCDM cosmogony with state-of-the-art subgrid models for radiative cooling, star formation, stellar mass loss, and feedback from stars and accreting black holes. They have been shown to reproduce the observed galaxy population with unprecedented fidelity. We combine the merger rates of supermassive black holes in EAGLE with the latest phenomenological waveform models to calculate the gravitational waves signals from the intrinsic parameters of the merging black holes. The EAGLE models predict ~ 2 detections per year by a gravitational wave detector such as eLISA. We find that these signals are largely dominated by mergers between seed mass black holes merging at redshifts between $z \sim 2$ and $z \sim 1$. In order to investigate the dependence on the assumed black hole seed mass, we introduce an additional model with a black hole seed mass an order of magnitude smaller than in our reference model. We also consider a variation of the reference model where a prescription for the expected delays in the black hole merger timescale has been included after their host galaxies merge. We find that the merger rate is similar in all models, but that the initial black hole seed mass could be distinguished through their detected gravitational waveforms. Hence, the characteristic gravitational wave signals detected by eLISA will provide profound insight into the origin of supermassive black holes and the initial mass distribution of black hole seeds.

This chapter has been published as a paper in Monthly Notices of the Royal Astronomical Society (MNRAS):

- *Music from the heavens - gravitational waves from supermassive black hole mergers in the EAGLE simulations*
  Salcido J., Bower R. G., Theuns T., McAlpine S., Schaller M., Crain R. A., Schaye J., Regan J., MNRAS 2016, Volume 463, Issue 1, Pages 870-885

6.1 Introduction

In our current understanding of extragalactic astrophysics supermassive black holes (SMBHs) reside at the centres of most galaxies at $z = 0$ and were responsible for powering the luminous quasars observed within the first billion years of the Universe (e.g. Fan 2006; Volonteri & Bellovary 2012). Observations of a tight correlation between the mass of a galaxy's central SMBH and key properties of its galactic host, such as the bulge mass and stellar velocity dispersion (e.g. Magorrian et al. 1998; Gebhardt et al. 2000; Ferrarese & Merritt 2000; Gültekin et al. 2009), have led to the idea that SMBHs play a major role in the evolution of their host galaxies (e.g. Bower et al. 2006; Volonteri & Bellovary 2011; Fabian 2012; Alexander & Hickox 2012; Kormendy & Ho 2013). It seems, therefore, that feedback from active galactic nuclei (AGN), galaxy mergers, and the growth of SMBHs are closely intertwined (e.g. Kauffmann & Haehnelt 2000; King 2003; Di Matteo et al. 2005; Booth & Schaye 2009; Fanidakis et al. 2011).

In a standard Lambda Cold Dark Matter (ΛCDM) cosmology cosmic structures build up hierarchically by the continuous merging of smaller structures and the accretion of surrounding matter. In this hierarchical scenario central SMBHs follow a similar build-up process and are the result of a complex evolution, in which black hole (BH) seeds grow both through accretion episodes and mergers with other BHs. However, constraining the formation mechanisms of BHs represents a major observational challenge. The direct detection of gravitational wave (GW) signals from SMBH mergers may prove to be a viable way to discriminate among the different BH seed formation models (e.g. Volonteri, 2010; Amaro-Seoane et al., 2012). The discovery of the GW source GW150914 by the LIGO collaboration provided the first observational evidence for the existence of binary BH systems that inspiral and merge within the Hubble time (Abbott et al., 2016). The gravitational radiation emitted during the merging of SMBHs in the centres of colliding galaxies will produce some of the *'loudest'* events in the Universe, which can provide us

with unique information about the nature of BHs and also provides a test of our understanding of gravity and galaxy evolution.

In the last decade major efforts have been made to predict the event rate of GWs in the frequency band of a space-based GW detector such as the Evolved Laser Interferometer Space Antenna (eLISA, Amaro-Seoane et al. 2012, 2013). These predictions range from a few, up to a few hundred events per year, depending on the assumptions underpinning the calculation of the SMBHs coalescence rate. Early works derived the SMBH coalescence rate from observational constraints such as the observed quasar luminosity function (Haehnelt, 1994), whilst more recent studies have utilised semi-analytical galaxy formation models and/or hybrid models that combine cosmological N-body simulations with semi-analytical recipes for the SMBH dynamics (e.g. Wyithe & Loeb, 2003; Enoki et al., 2004; Koushiappas & Zentner, 2006; Sesana et al., 2007; Micic et al., 2007; Sesana et al., 2009; Barausse, 2012; Klein et al., 2016). In contrast to semi-analytic models, hydrodynamical simulations follow the dynamics of the cosmic gas by direct numerical integration of the equations of hydrodynamics capturing non-linear processes that cannot be described by simple mathematical approximations. Hence a more complete and consistent picture of the evolution of SMBHs and their host galaxies can be obtained.

The *Evolution and Assembly of GaLaxies and their Environment* (EAGLE) project (Schaye et al., 2015; Crain et al., 2015) consists of a suite of hydrodynamical simulations of a ΛCDM cosmogony. Using state-of-the-art subgrid models for radiative cooling, star formation, stellar mass loss, and feedback from stars and accreting BHs, the simulations reproduce the observed galaxy population with unprecedented fidelity. Key observations, such as the present-day stellar mass function of galaxies, the dependence of galaxy sizes on stellar mass, and the amplitude of the central BH mass-stellar mass relation, as well as many other properties of observed galaxies and the intergalactic medium (both at the present day and at earlier epochs) are reproduced by the simulations (e.g. Furlong et al., 2017; Furlong et al., 2015; Trayford et al., 2015; Schaller et al., 2015a; Lagos et al., 2015; Rahmati et al., 2015, 2016; Bahé et al., 2016; Rosas-Guevara et al., 2016). In this study we introduce the first estimate of the event rate of GWs expected from SMBH mergers utilising large-scale cosmological hydrodynamical simulations. We compute that the event rate of GW signals is low enough to produce a set of events that are resolvable by a space-based interferometer, such as eLISA.

The layout of this chapter is as follows: In Section 6.2 we provide a brief summary of the basic equations of the GW signals produced by the SMBH coalescence process. Section 6.3 presents a brief overview of the EAGLE simulation suite, including the list of simulations used in this study, a discussion of the BH seeding mechanism and growth, as well as the calculated SMBH merger rates from the simulations. In Section 6.4 we present the predicted GW signals from the simulations and discuss our main results. We discuss the limitations of our analysis, making some remarks on the simulations and the SMBH seeding model adopted in EAGLE and conclude in Section 6.5.

6.2 Gravitational Wave emission from SMBH mergers

Studying SMBH mergers involve physical processes that cover many orders of magnitude in physical size. From mergers of dark matter haloes and galaxies driven by the cosmic web at large scales (>Mpc), to the final SMBH merger via the emission of GWs that occurs at sub-parsec scales. The overall scenario was first outlined by Begelman, Blandford & Rees (1980). When two dark matter halos merge, the galaxies that they host will eventually merge by the effect of dynamical friction. After the galaxy merger, the central SMBHs are brought near the centre of the main halo due to dynamical friction against the dark matter, background stars, and gas. The efficiency of dynamical friction decreases when the SMBHs become close and form a bound binary (Mayer et al., 2007). The dynamical evolution of the SMBH binary is expected to be radically different in gas-rich and gas-poor galaxies. In gas-rich galaxies planet-like migration can effectively dissipate energy and angular momentum from the binary, leading to a short coalescence time-scale, typically in the order of $\sim 10^7 - 10^8$ yrs (Escala et al. 2005; Colpi 2014 but see e.g. Tamburello et al. 2017). In gas-poor systems, the evolution of the binary is largely determined by three-body interactions with the background stars, leading to a long coalescence timescale of the order of a few Gyrs. At milliparsec separations, GW emission drives the final coalescence process (see Colpi & Dotti 2011, Mayer 2013 and Colpi 2014 for a review on SMBH dynamics in galaxy mergers).

The BH binary merging process can be divided in three distinct phases which are illustrated by Fig. 6.1:

1. The **inspiral phase**, during which the distance between the bound SMBH binary is larger than the Last Stable Circular Orbit ($R_{\rm LSCO}$) and the mutual gravitational field strength is weak. Since the location of the LSCO is very difficult to calculate for a binary BH system, here $R_{\rm LSCO}$ is approximated by the limiting case of a test particle orbiting a non-rotating BH, $R_{\rm LSCO} = 6GM_1/c^2 = 3R_S$, where R_S is the Schwarzschild radius of the most massive BH in the binary. Post-Newtonian equations provide an accurate representation of the dynamical evolution of the binary in this phase. The GW signals emitted during the inspiral phase have a characteristic shape with slowly increasing frequency and amplitude.

2. In the highly non-linear **merger phase** SMBHs approach to within the last stable circular orbit ($\leq R_{\rm LSCO}$) and the dynamics evolve to a rapid plunge and coalescence. In this regime the event horizons of the BHs overlap and the geometry of the local spacetime becomes extremely complicated. Analytical schemes break down in this regime and numerical relativity (NR) is needed to model the dynamics through the merger phase.

3. Finally, the **quasi-normal-ringdown phase**, where the resulting BH settles down to a rotating Kerr BH emitting GWs due to its deviations from the final axisymmetric state. Perturbation theory can be applied to obtain the quasi-normal modes in this phase. The GW signal emitted during the ringdown phase has a characteristic shape consisting of the superposition of exponentially damped sinusoids.

In general relativity the *'no-hair'* theorem posits that BHs are entirely characterised by only three parameters, namely their mass, spin, and electric charge. For astrophysical BHs the electric charge is usually expected to be negligible (Misner et al., 1973, pp. 875-876). Therefore each coalescing SMBH is fully characterised by the total mass $M_{\rm total} = M_1 + M_2$, the mass ratio M_1/M_2 of the binary and the BH spin angular momenta $\vec{S}_1$ and $\vec{S}_2$. M_1 is defined as the more massive member of the BH binary ($M_1 \geq M_2$). The most general detectable signal from a SMBH binary is a function of the intrinsic properties of the binary, the merger redshift z, and the observer's orientation. In this study for simplicity we focus on non-spinning SMBH binaries as potential sources of GWs. In Appendix B we extend our analysis to investigate the case of rapidly spinning coalescing SMBHs. The inclusion of the

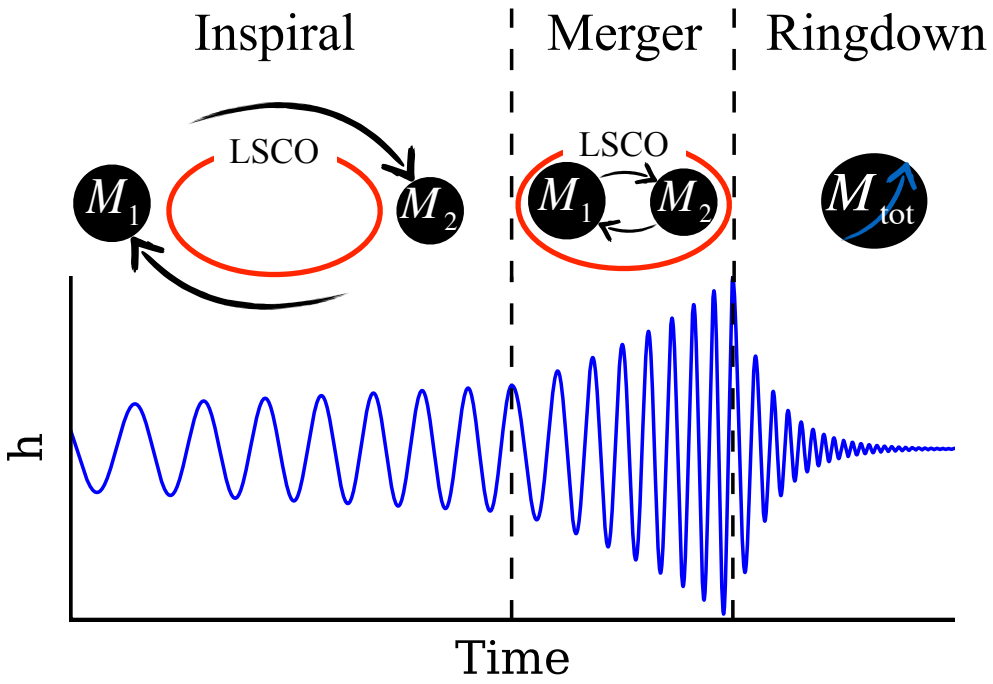

Fig. 6.1.: Schematic diagram of the phase evolution (inspiral, merger, and ringdown) of a non-spinning SMBH binary coalescence process. The Last Stable Circular Orbit (LSCO) of the binary is shown as the red curve. The resulting SMBH may be rapidly rotating even if the progenitor BHs had very small or no spin (Flanagan & Hughes, 1998). Below each phase an example of the *strain* amplitude, h, as a function of time is shown for the dominant spherical harmonic mode of the GW signal from the non spinning SMBH binary. This specifies the fractional change in the relative displacement between freely falling test masses in a detector due to the GW.

signal from the ringdown phase increases the signal-to-noise ratio (S/N) of observed binaries and enable measurements of the parameters of the resulting SMBH (Klein et al., 2016).

6.2.1 Characteristic strain

It is difficult to determine accurately the total gravitational energy radiated as GWs in a BH binary coalescence and modelling the GW signal from these processes still represents a challenge for GW astronomy (Ohme, 2012; Hannam, 2014).

In general, the total energy radiated during a BH coalescence will be some fraction, ϵ, of the total rest mass energy of the binary ($M_{\rm total}c^2$) that depends on the mass ratio M_1/M_2, the orbital angular momentum and the initial spin of the BHs.

In GW astronomy it is common to describe the amplitude of a source using the dimensionless *strain* as a function of time, $h(t)$. This specifies the fractional change in the relative displacement between two test masses, $h(t) = \Delta L(t)/L_0$, where L is the distance between free-falling masses that constitute the GW detector. The dimensionless characteristic strain amplitude, h_c, is not the instantaneous strain of a source but rather an accumulated signal, intended to include the effect of integrating a signal during the inspiralling phase. The characteristic strain amplitude, h_c, is defined as

$$\left[h_c(f_s)\right]^2 = 4f^2\left|\tilde{h}(f_s)\right|^2, \tag{6.1}$$

where $\tilde{h}(f_s)$ is the Fourier transform of the strain signal, $\tilde{h}(f_s) = \mathcal{F}\{h(t)\}(f_s) = \int_{-\infty}^{\infty} h(t)e^{-2\pi i f_s t}\mathrm{d}t$, and $f_s = f_{\rm obs}(1+z)$ is the rest-frame frequency of the signal (Moore et al., 2015).

We employ the most recent phenomenological frequency-domain gravitational waveform model for non-precessing BH binaries described in Khan et al. (2016) (commonly referred to as "PhenomD"). The PhenomD model provides the waveform families in the Fourier domain of the dominant spherical-harmonic modes of the GW signal in aligned-spin systems in terms of the signal amplitude, $A(f_s)$, and phase, $\phi(f_s)$, given by

$$\tilde{h}(f_s) = A(f_s)e^{-i\phi(f_s)}. \tag{6.2}$$

In this hybrid model, the inspiral and merger-ringdown parts of the signal are modelled separately in two frequency regimes of the waveform. The first region covers the inspiral signal, up to the merger frequency

$$f_{\rm merger} = 0.018\, c^3/GM_{\rm total}, \tag{6.3}$$

which is approximately the frequency at the LSCO of a test particle orbiting a non-rotating BH ($R_{\rm LSCO} = 6GM_1/c^2$) (Flanagan & Hughes, 1998). In the inspiral region, analytic post-Newtonian prescriptions and effective-one-body methods are used to describe the signal.

The second region (which is is further sub-divided into intermediate and merger-ringdown regions) uses phenomenological models calibrated to pure NR simulations to describe the signal. The full waveform strain signal is parameterised by the physical parameters of the BH binary, total mass ($M_{\rm total} = M_1 + M_2$), luminosity distance ($D_{\rm L}(z)$), symmetric mass ratio ($\eta = M_1 M_2/M_{\rm total}^2$), and the dimensionless spin parameters defined as

$$\chi_i = \frac{\vec{S}_i \cdot \hat{L}}{M_i^2}, \tag{6.4}$$

where $\chi_i \in [-1, 1]$ and the BH spin angular momenta, $\vec{S}_i$, are assumed to be parallel to the direction of the orbital angular momentum, $\hat{L}$.

The loss of energy through GWs leads to a decrease in the separation of the BH binary and hence the orbital frequency increases. For Keplerian circular orbits the frequency of the GWs is twice the orbital frequency ($f_s = 2f_{\rm orbit}$). Integrating the frequency evolution of the inspiral phase, or chirp, $\dot{f} = {\rm d}f/{\rm d}t$, we can estimate the time it takes for the binary to evolve between any two frequencies. It can be shown (Shapiro & Teukolsky, 1983; Tinto, 1988) that for BH binaries on Keplerian circular orbits

$$\begin{aligned} t(f_2) - t(f_1) = &\frac{5}{256}\frac{c^5}{G^{5/3}}\frac{(M_1 + M_2)^{1/3}}{M_1 M_2} \\ &\times (2\pi)^{-8/3}\left(f_1^{-8/3} - f_2^{-8/3}\right). \end{aligned} \tag{6.5}$$

The intrinsic duration of the inspiral phase is then given by

$$\tau_{\rm inspiral} = t(f_{\rm merger}) - t(f_{\rm min}), \tag{6.6}$$

where the value of $f_{\rm min}$ at which the inspiral spectrum starts is uncertain. Since $f_{\rm merger}$ is set by Eq. (6.3), $f_{\rm min}$ is a free parameter in our calculations. Clearly, choosing $f_{\rm min}$ very close to $f_{\rm merger}$ gives short inspiral times. On the other hand, $f_{\rm min} \ll f_{\rm merger}$ will produce the opposite effect. Following the approach of Koushiappas & Zentner (2006), we choose $f_{\rm min}$ to be close to $f_{\rm merger}$ to ensure reasonable values for the time that the BH binary systems spend in the inspiral phase, which are also comparable to the orbital frequency at the BH binary hardening radius (Quinlan, 1996). We have chosen $f_{\rm min} = 1 \times 10^{-3}\, c^3/GM_{\rm total}$ for our analysis.

The intrinsic duration of the merger phase is approximated by (Koushiappas & Zentner, 2006),

$$\tau_{\rm merger} \sim 14.7 \left(\frac{M_{\rm total}}{1 \times 10^5\, {\rm M}_\odot} \right) [{\rm sec}]\,. \tag{6.7}$$

Khan et al. (2016) show that the phenomenological approach is capable of describing waveforms from BH binaries with a high degree of physical fidelity. The range of calibration of the model is: mass-ratio $\in [1, 18]$ and spins $\in [-0.95, 0.98]$. Nonetheless, the model can be evaluated at any physically allowed mass-ratio. In our study, it was required to extend the use of the PhenomD model outside its calibration region for some SMBH binary cases, which can produce physically plausible results that are reasonable for our event rate estimations. However, individual binary parameter estimation would require one to check the model in this region against fully general relativistic NR calculations. More details about the PhenomD model can be found in Khan et al. (2016).

In Fig. 6.2 we show some examples of the dimensionless characteristic strain amplitude h_c produced by massive BH coalescence events with different masses and occurring at different redshifts, calculated with the equations given in this section.

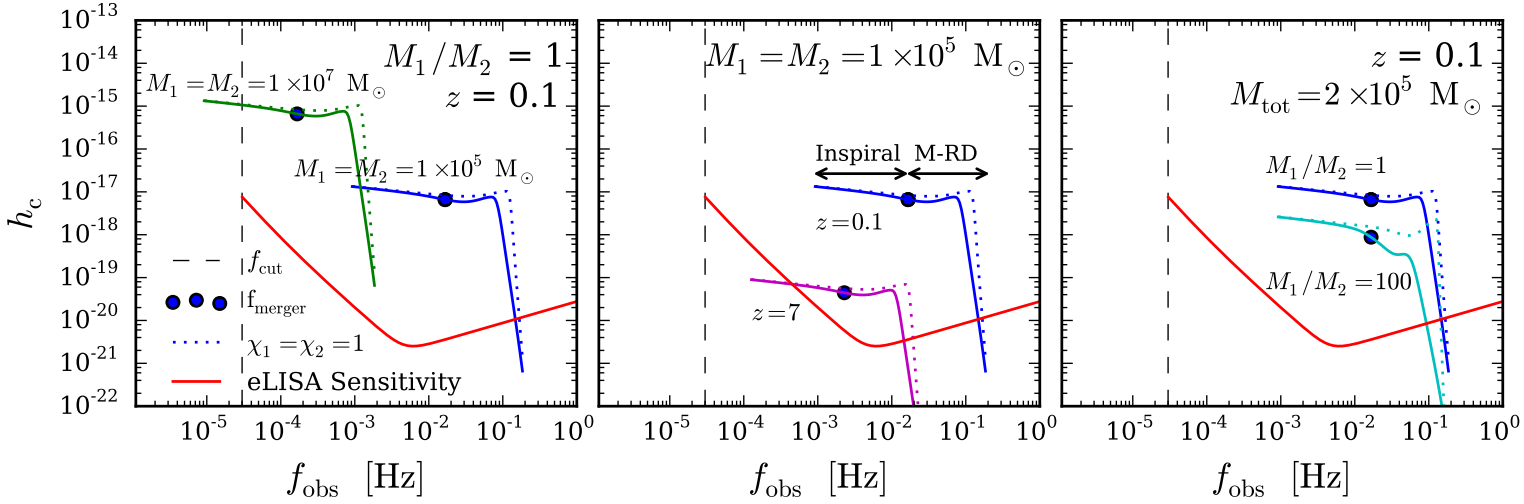

Fig. 6.2.: Example of the dimensionless characteristic strain amplitude, h_c, produced by non-spinning SMBH coalescence events ($\chi_i = 0$). Maximally spinning SMBHs aligned with the orbital angular momentum of the binary are shown in dotted lines ($\chi_i = 1$). In all panels the inspiral and merger-ringdown phases are shown for an equal mass BH binary (Mass ratio $M_1/M_2 = 1$, $M_1 = M_2 = 1 \times 10^5$ M$_\odot$) that merge at redshift $z = 0.1$ as reference (blue line). The frequency at the transition from the inspiral phase to the merger phase ($f_{merger} = 0.018\, c^3/GM_{total}$) is highlighted with a blue dot. The sensitivity curve of eLISA was calculated from the analytic approximation provided by Amaro-Seoane et al. (2013). The black dashed line indicates the low-frequency cut-off of the sensitivity curve $f_{cut} = 3 \times 10^{-5}$ Hz. GW signals above the sensitivity curve and to the right of the low-frequency cut-off can be resolved from the eLISA data stream. *LEFT PANEL:* The effect of increasing the total mass of the SMBH binary. An equal mass SMBH binary (Mass ratio $M_1/M_2 = 1$) with $M_1 = M_2 = 1 \times 10^7$ M$_\odot$ that merges at redshift $z = 0.1$ is shown in green. *MIDDLE PANEL*: The effect of redshift. An equal mass SMBH binary (Mass ratio $M_1/M_2 = 1$, $M_1 = M_2 = 1 \times 10^5$ M$_\odot$) merging at redshift $z = 7$ is shown in magenta. *RIGHT PANEL*: The effect of mass ratio. A BH binary with total mass $M_{total} = 2 \times 10^5$ M$_\odot$ and mass ratio $M_1/M_2 = 100$ merging at redshift $z = 0.1$ is shown in cyan.

6.2.2 The eLISA sensitivity curve

The Evolved Laser Interferometer Space Antenna is a space-based mission designed to measure gravitational radiation over a broad band of frequencies ranging between $f \sim 0.1$ mHz to $f \sim 1$ Hz. The final design specification of the mission are yet to be evaluated, including key features like the low-frequency acceleration noise, mission lifetime, the length of the interferometer arms, and the number of laser links between the spacecraft (Klein et al., 2016). In our study we will use the New Gravitational Observatory (NGO) concept, which was proposed to the European Space Agency (ESA) during the selection process for the L1 large satellite mission. We refer the reader to Amaro-Seoane et al. (2013) for a detailed description of the eLISA concept and architecture.

According to the design requirements, the sensitivity that eLISA will be able to achieve in dimensionless characteristic strain noise amplitude is

$$h_n(f_{\rm obs}) = \sqrt{S_n(f_{\rm obs}) f_{\rm obs}}, \tag{6.8}$$

where the strain noise power spectral density $S_n(f_{\rm obs})$ is given by the analytical approximation,

$$\begin{aligned} S_n(f_{\rm obs}) =& \frac{20}{3} \frac{4 \times S_{\rm acc}(f_{\rm obs}) + S_{\rm sn}(f_{\rm obs}) + S_{\rm omn}(f_{\rm obs})}{L^2} \\ & \times \left(1 + \left(\frac{f_{\rm obs}}{0.41 \left(\frac{c}{2L} \right)} \right)^2 \right), \end{aligned} \tag{6.9}$$

where $f_{\rm obs}$ is the observed frequency and $L = 1 \times 10^9$ m is the optical path-length between the free-falling masses. At low frequencies the noise spectrum of the instrument is dominated by residual acceleration noise of the test masses caused by force gradients arising due to the relative movement of the spacecraft with respect to the test masses

$$S_{\rm acc}(f_{\rm obs}) = 1.37 \times 10^{-32} \left(1 + \frac{10^{-4}\text{Hz}}{f_{\rm obs}} \right) \left(\frac{\text{Hz}}{f_{\rm obs}} \right)^4 \left[\text{m}^2\text{Hz}^{-1} \right]. \tag{6.10}$$

For $f_{\rm obs} \gtrsim 5 \times 10^{-3}$ Hz, the arm length measurement noise dominates, for which the quantum mechanical photon shot noise is

$$S_{\rm sn}(f_{\rm obs}) = 5.25 \times 10^{-23} \left[{\rm m^2 Hz^{-1}}\right]. \tag{6.11}$$

At higher frequencies the sensitivity decreases again, due to the arm-length response to multiple wavelengths of GWs. This effect is included with other combined measurement noise in,

$$S_{\rm omn}(f_{\rm obs}) = 6.28 \times 10^{-23} \left[{\rm m^2 Hz^{-1}}\right]. \tag{6.12}$$

The eLISA sensitivity curve obtained from Eq. (6.8) is plotted as the red curves in Fig. 6.2.

The measurement frequency bandwidth requirement for the detector is (10^{-4} Hz to 1 Hz) with a target of (3×10^{-5} Hz to 1 Hz) (Amaro-Seoane et al., 2013). For our analysis we adopt the target frequency cut $f_{\rm cut} = 3 \times 10^{-5}$ Hz.

6.2.3 Resolved events

An advantage of using the characteristic strain to describe the amplitude of GW sources given the sensitivity of the detector is that the S/N averaged over all possible orientations of the source and interferometer can be written as

$${\rm S/N} = \sqrt{\int_f^{f+\Delta f} \left[\frac{h_c(f'_{\rm obs})}{h_n(f'_{\rm obs})}\right]^2 \frac{df'_{\rm obs}}{f'_{\rm obs}}}, \tag{6.13}$$

which allows one to assess by eye the detectability of a given source if h_c is plotted against the observed frequency (Moore et al., 2015).

The resolution frequency bin, Δf, is set by the minimum frequency resolvable by the instrumentation. It is the inverse of the mission lifetime $\Delta f \sim 1/T_{\rm obs}$, where $T_{\rm obs}$ is the length of observation (Gair et al., 2013). For small Δf, we can assume

a constant ratio $k = h_c(f'_{\rm obs})/h_n(f'_{\rm obs})$. Then, by changing the integration limits as $f + \Delta f = f(1+\alpha)$, where $\alpha = \Delta f/f$, we can rewrite Eq. (6.13) as

$$\begin{aligned}(\mathrm{S/N})^2 &= k^2 \int_f^{f(1+\alpha)} \frac{df'_{\rm obs}}{f'_{\rm obs}} \\ &= k^2 \ln(1+\alpha).\end{aligned} \tag{6.14}$$

The eLISA mission has an expected duration of 3 years. Therefore $\Delta f \sim 1/T_{\rm obs} = 1/(3\mathrm{yrs}) \approx 10^{-8}\,\mathrm{Hz}$. If we impose $S/N \gtrsim 5$ for all the frequency bandwidth ($3 \times 10^{-5}\,\mathrm{Hz}$ to $1\,\mathrm{Hz}$) in Eq. (6.14), this results in $k \gtrsim 1.76$. In the examples shown in Fig. 6.2 it can be seen that once any given GW signal crosses the detector sensitivity curve, the ratio of the signal to the sensitivity curve, k, rapidly increases by a few orders of magnitude. Therefore we can safely assume that all GW signals above the sensitivity curve (i.e. $h_c(f_{\rm obs}) \geq h_n(f_{\rm obs})$) can be detected by eLISA.

6.2.4 Event rate

We calculate the number of detected sources (i.e. $h_c(f_{\rm obs}) \geq h_n(f_{\rm obs})$) per redshift interval $z+\Delta z$ and co-moving volume V_c, and denote this quantity as $\bar{N}(z, k \geq 1)/\Delta z V_c \approx d^2\bar{n}(z, k \geq 1)/dz dV_c$. Integrating over all redshifts, the estimated event rate of detected GW sources per observed time is given by

$$\frac{d\bar{N}}{dt_{\rm obs}} = \int_0^\infty \frac{d^2\bar{n}(z, k \geq 1)}{dz dV_c} \frac{dz}{dt} \frac{dV_c}{dz} \frac{dz}{(1+z)}. \tag{6.15}$$

The total number of observed events in a given observation time is simply

$$N_{\rm total} = \int_0^{T_{\rm obs}} \frac{d\bar{N}}{dt_{\rm obs}} dt_{\rm obs}, \tag{6.16}$$

where $T_{\rm obs} = 3\,\mathrm{yrs}$ is the length of the mission. We now seek to estimate this quantity using the merger rates of SMBHs in the EAGLE cosmological hydrodynamical simulations.

6.3 The EAGLE Simulations

The EAGLE simulation suite[1] (Schaye et al., 2015; Crain et al., 2015) consists of a large number of cosmological hydrodynamical simulations that include different resolutions, simulated volumes and physical models. These simulations use advanced smoothed particle hydrodynamics (SPH) and state-of-the-art subgrid models to capture the unresolved physics. Radiative cooling (Wiersma et al., 2009a), star formation (Schaye & Dalla Vecchia, 2008; Schaye, 2004), metal enrichment (Wiersma et al., 2009b), energy input from stellar feedback (Dalla Vecchia & Schaye, 2012), BH growth (Rosas-Guevara et al., 2015; Schaye et al., 2015), and feedback from active galactic nuclei (Schaye et al., 2015) are included. The simulation suite was run with a modified version of the GADGET-3 SPH code (last described by Springel 2005) and includes a full treatment of gravity and hydrodynamics. The modifications to the SPH method, collectively referred to as ANARCHY (Dalla Vecchia et al. in preparation), make use of the pressure-entropy formulation of SPH derived by Hopkins (2013), the artificial viscosity switch from Cullen & Dehnen (2010), an artificial conduction switch similar to that of Price (2008), the C_2 kernel of Wendland (1995), and the time-step limiters of Durier & Dalla Vecchia (2012). The effects of this state-of-the-art formulation of SPH on the galaxy properties are explored in detail by Schaller et al. (2015b). The calibration strategy is described in detail by Crain et al. (2015) who also presented additional simulations to demonstrate the effect of parameter variations.

The halo and galaxy catalogues for more than 10^5 simulated galaxies of the main EAGLE simulations with integrated quantities describing the galaxies, such as stellar mass, star formation rates, metallicities and luminosities, are available in the EAGLE database[2] (McAlpine et al., 2016). A complete description of the code and physical parameters used in the EAGLE simulations can be found in Schaye et al. (2015), here we present a brief overview of the BH seeding and growth mechanisms. Cosmological parameters for a standard ΛCDM universe were adopted by these simulations. The values of the key cosmological parameters implemented are $\Omega_\mathrm{m} = 0.307$, $\Omega_\Lambda = 0.693$, $\Omega_\mathrm{b} = 0.04825$, $h = 0.6777$ and $\sigma_8 = 0.8288$, as inferred by the Planck Collaboration et al. (2014).

[1] http://www.eaglesim.org
[2] http://www.eaglesim.org/database.php

The label for each simulation denotes the comoving cubic box length and the cube root of the number of particles in the simulation. For example, Ref-L100N1504 corresponds to a simulation volume of $(100\,\mathrm{cMpc})^3$ (where cMpc denotes co-moving megaparsecs) using 1504^3 particles of dark matter and an equal number of baryonic particles. A prefix distinguishes the subgrid variations. For example, the prefix '*Ref-*' refers to a simulation using the reference model.

We compare the predicted GW signals from two EAGLE models, our reference simulation Ref-L100N1504, and a modified version of the Ref-L050N0752 model which uses the same calibrated subgrid parameters as the reference model, but smaller BH seeds, as described in Section 6.3.1. We have labeled this model SS-L050N0752. Additionally, in order to test for convergence with simulated volume size and resolution, the Ref-L050N0752, Ref-L025N0376 and Recal-L025N0752 models are compared in Appendix B. As discussed by Schaye et al. (2015), the '*Recal-*' higher-resolution simulation uses values of the subgrid parameters that were recalibrated following the same procedure used for the reference simulation, enabling the user to test the "weak convergence" properties of the simulations. In Table 6.1 we summarise the simulation models used in this chapter, including the comoving cubic box length, initial baryonic and non-baryonic particle masses, Plummer-equivalent gravitational softening lengths and BH seed mass. Together these parameters determine the dynamic range and resolution that can be achieved by the simulations.

Table 6.1.: Box-size, number of particles, initial baryonic and dark matter particle mass, co-moving and Plummer-equivalent gravitational softening, and BH seed mass for the EAGLE simulations used in this chapter. Values in bold show differences with respect to the Ref-L100N1504 simulation.

Simulation	L [cMpc]	N	$m_{\rm gas}$ [$M_\odot$]	$m_{\rm DM}$ [$M_\odot$]	$\epsilon_{\rm com}$ [ckpc]	$\epsilon_{\rm prop}$ [ckpc]	$m_{\rm seed}$ [$M_\odot$]
Ref-L100N1504	100	2×1504^3	1.81×10^6	9.70×10^6	2.66	0.70	1.475×10^5
SS-L050N0752	**50**	2×752^3	1.81×10^6	9.70×10^6	2.66	0.70	$\mathbf{1.475 \times 10^4}$
Ref-L050N0752	**50**	2×752^3	1.81×10^6	9.70×10^6	2.66	0.70	1.475×10^5
Ref-L025N0376	**25**	2×376^3	1.81×10^6	9.70×10^6	2.66	0.70	1.475×10^5
Recal-L025N0752	**25**	2×752^3	$\mathbf{2.26 \times 10^5}$	$\mathbf{1.21 \times 10^6}$	**1.33**	**0.35**	1.475×10^5

6.3.1 Black hole seeding

To explain the population of luminous quasars in the high-redshift Universe ($z \geq 6$) SMBHs must have formed early and grown rapidly (e.g. Volonteri & Bellovary 2012). Different formation and evolution mechanisms for BH seeds have been proposed to explain the rapid growth that enables these seeds to grow to masses of $10^9\,\mathrm{M}_\odot$ in less than one billion years. These SMBHs may have originated from the remnants of the very first generation of stars, runaway collisions of stars and/or stellar mass BHs, direct collapse of supermassive stars, or from an even more exotic process (refer to Volonteri 2010 for a review on formation models for SMBHs). We now briefly review the most promising models for forming SMBH seeds in the early Universe:

1. *Remnants of the first generation of stars*

   BH seeds may have formed from remnants of Population III stars (e.g. Madau & Rees, 2001; Volonteri et al., 2003). If stars more massive than $\sim 250\,\mathrm{M}_\odot$ formed from primordial gas, they are predicted to directly collapse into BH seeds with masses of $\sim 100\,\mathrm{M}_\odot$. However, it is still unclear if most of the first stars were born with such large masses (e.g. Clark et al., 2011; Greif et al., 2011). Additionally, in order to grow to masses in excess of $10^9\,\mathrm{M}_\odot$ as early as redshift $z \sim 6$ seeds would require to grow close to the Eddington rate for the majority of their lifetime. The shallow potential wells in which Population III stars form makes this scenario rather unattractive (e.g. Johnson et al., 2008; Alvarez et al., 2009; Volonteri et al., 2016). Growth through super-Eddington accretion phases may solve this conflict (e.g. Volonteri et al., 2015; Lupi et al., 2016; Inayoshi et al., 2016). However, further theoretical work on this mechanism and its sustainability is required.

2. *Collapsing nuclear star clusters*

   In this model, stellar-dynamical instabilities in proto-galactic discs may lead to infall without fragmentation of low metallicity gas, increasing the central galactic density (e.g. Seth et al., 2008; Devecchi & Volonteri, 2009; Devecchi et al., 2012; Lupi et al., 2014; Katz et al., 2015). Within the nuclear region a dense stellar cluster forms. As the central cluster undergoes core collapse,

runaway collisions of stars may lead to the formation of a single SMBH seed with a mass up to $\sim 10^3\,\mathrm{M}_\odot$.

3. *Direct collapse of supermassive stars*

   It has been proposed that in high-redshift haloes radiation emitted by nearby star-forming galaxies could cause the photo-dissociation of H_2. This prevents the temperature of primordial gas from reaching very low values and thus elevates the Jeans mass, allowing the formation of a large central mass, possibly evolving into a supermassive star (e.g. Omukai, 2001; Wise et al., 2008; Regan & Haehnelt, 2009; Agarwal et al., 2014; Sugimura et al., 2014; Regan et al., 2016). Another mechanism to form a supermassive star is by rapid funnelling of low metallicity gas in low angular momentum haloes with global or local dynamical instabilities (e.g. Loeb & Rasio, 1994; Koushiappas et al., 2004; Begelman et al., 2008). Once a supermassive star forms its core may collapse to form a small BH within the radiation-pressure-supported object. In this scenario the central BH can accrete the entire envelope and form a SMBH seed of mass $\sim 10^3\,\mathrm{M}_\odot$ up to $\sim 10^5\,\mathrm{M}_\odot$.

Constraining the formation mechanisms of BH seeds represents a major observational challenge. As we will show, the detection of GW signals from SMBH coalescences represents a promising way to discriminate among different theoretical formation models by determining the mass function of seed BHs.

Since the SMBH seed formation processes are not resolved by cosmological simulations, it is assumed that every halo above a certain threshold mass hosts a central BH seed. For a comprehensive description of the BH seeding mechanisms in these simulations see Springel et al. 2005a, Di Matteo et al. 2008, Booth & Schaye 2009, and Schaye et al. 2015. In the Ref-L100N1504 model high-mass BH seeds[3] ($m_{\mathrm{seed}} = 1.475 \times 10^5 \mathrm{M}_\odot$) are placed at the centre of every halo with total mass greater than $m_{\mathrm{halo,th}} = 1.475 \times 10^{10} \mathrm{M}_\odot$ that does not already contain a BH. For the SS-L050N0752 model the BH seed mass is $m_{\mathrm{seed}} = 1.475 \times 10^4 \mathrm{M}_\odot$. We choose to place BH seeds in haloes of mass $m_{\mathrm{halo,th}} = 1.475 \times 10^{10}\,\mathrm{M}_\odot$ (which corresponds to $m_{\mathrm{halo,th}} \sim 1.5 \times 10^3\, m_{\mathrm{DM}}$ for the reference models and $m_{\mathrm{halo,th}} \sim 1.2 \times 10^4\, m_{\mathrm{DM}}$ for the high-resolution *'Recal'* model) to ensure that the structure of haloes containing BHs is always well resolved. Halos are selected for seeding by regularly running

[3] $m_{\mathrm{seed}} = 1.475 \times 10^5 \mathrm{M}_\odot = 1 \times 10^5 \mathrm{M}_\odot h^{-1}$, where $h = 0.6777$.

the "Friends-of-Friends" (FoF) halo finder on the dark matter distribution, with a linking length equal to 0.2 times the mean inter-particle spacing.

6.3.2 Black hole dynamics and delays

Our aim is to calculate the GW signals from the merger rates of SMBHs across cosmic time, which depend crucially on how many galaxies host BHs and on the galaxy merger history. Therefore, full cosmological models including BH physics are necessary to study the merger rates of SMBHs. Nonetheless, given the limited spatial resolution in large scale cosmological simulations, information on the small-scale dynamical evolution of SBMH binaries is lost. To overcome this limit and obtain realistic SMBH dynamics and merger rates we employ advection schemes that correct the motion of BH particles and apply a time delay corrections to the BH merger timescales to account for the unresolved small-scale dynamical evolution of the binaries.

In the simulations, when a halo grows above the threshold mass $m_{\rm halo,th}$, its highest-density gas particle is converted into a collisionless BH particle with subgrid mass $m_{\rm BH} = m_{\rm seed}$. Since the BH seed mass is usually significantly lower than the baryonic particle mass ($m_{\rm seed} \ll m_{\rm gas}$), the use of a subgrid mass is necessary for BH-specific processes such as accretion (Springel et al., 2005a). On the other hand, gravitational interactions are computed using the BH particle mass.

Since the simulations cannot model the dynamical friction acting on BHs with masses $\lesssim m_{\rm gas}$, BHs with mass < 100 times the initial gas particle mass $m_{\rm gas}$ are re-positioned to the local potential minimum. To prevent BHs in gas poor haloes from jumping to nearby satellites, we limit this process to particles whose velocity relative to the BH is smaller than $0.25c_{\rm s}$, where $c_{\rm s}$ is the local sound speed, and whose distance is smaller than three gravitational softening lengths. Tracking the evolution of BH orbits in individual galaxy mergers during code development showed this eliminated spurious repositioning events in fly-by encounters. However, within ~kpc separations, repositioning of BHs to account for unrealistic dynamics in cosmological scale simulations may cause spurious SMBH mergers and/or SMBHs to merge sooner than what is predicted by their orbital decay time-scale (Tremmel et al., 2015). Hence, a SMBH merger time delay is needed to correct for this effect.

Two BHs merge if they are separated by a distance that is smaller than both the SPH smoothing kernel of the BH, $h_{\rm BH}$, and three gravitational softening lengths (this criteria gives a median separation of $\sim$ 1pkpc at all redshifts and halo masses). $h_{\rm BH}$ is chosen such that within a distance $h_{\rm BH}$ from the BH there are $N_{\rm ngb} = 58$ weighted SPH neighbours. Furthermore, in order to prevent BHs from merging during fly-by encounters we impose a limit on the allowed relative velocity of the BHs, required to be smaller than the circular velocity at the distance $h_{\rm BH}$ ($v_{\rm rel} < \sqrt{G M_1 h_{\rm BH}^{-1}}$, where G is the gravitational constant and M_1 is the mass of the most massive BH in the pair). Triple BH mergers can happen in a single time-step in the simulations. However, due to their extreme rarity, we do not consider these events in our analysis.

As we briefly discussed in Section 6.2, after two galaxies merge a variety of effects can affect the dynamical evolution of the SMBH binary and finally lead (or not) to a merger within a Hubble time. Dynamical friction, three-body interactions with stars, interactions with gas, including planet-like migration and/or orbital decay of the binary due to the clumpy gas and the heating of the cold layer of the disc by BH feedback can either prevent or promote the SMBH merger (Colpi & Dotti, 2011; Mayer, 2013; Colpi, 2014; Tamburello et al., 2017). A binary could stall at $\sim$ pc separations, which is known as the "final-parsec" problem (Begelman et al., 1980). However, a later galaxy merger may trigger the SMBH merger (Hoffman & Loeb, 2007). Given the uncertainties in these mechanisms, and the potential variability from galaxy to galaxy, we adopt simplified prescriptions to estimate the SMBH merger time delays based on the gas content in the nuclear region of the resulting galaxy after the merger, similar to the method adopted by Antonini et al. (2015).

- *Gas rich galaxies*: For galaxies with gas mass within a 3D aperture with radius 3 pkpc greater than or equal to the total BH mass ($M_{\rm gas@3pkpc} \geq M_1 + M_2$), a 0.1 Gyr delay was added to the BH merger time recorded in the simulation.

- *Gas poor galaxies*: For galaxies with gas mass within a 3D aperture with radius 3 pkpc less than the total BH mass ($M_{\rm gas@3pkpc} < M_1 + M_2$), a 5 Gyr delay was added to the BH merger time recorded in the simulation.

As we will discuss in Section 6.4, we find that adding a significant delay in gas-poor galaxies gives a very similar result of the expected rate of GW signals than our model assuming no delays.

6.3.3 Black hole growth

Once seeded, BHs are free to grow via gas accretion at a rate that depends only on the local hydrodynamical properties, namely: the mass of the BH, the local density and temperature of the surrounding gas, the velocity of the BH relative to the ambient gas, and the angular momentum of the gas with respect to the BH. Accretion onto BHs follows a modified version of the Bondi-Hoyle accretion rate which takes into account the circularisation and subsequent viscous transport of infalling material, limited by the Eddington rate (as described by Rosas-Guevara et al. 2015). Additionally, BHs can grow by merging with other BHs as described in the previous section.

It is important to highlight that the sub-grid physics in the EAGLE simulations were calibrated to reproduce the observed galaxy stellar mass function at redshift $z = 0.1$, the amplitude of the galaxy stellar mass-central BH mass relation and galaxy sizes (Crain et al., 2015). Although not part of the calibration procedure, Rosas-Guevara et al. 2016 show that the simulations also reproduce the observed BH mass function at $z = 0$ and show good agreement with the observed AGN luminosity functions in the hard and soft X-ray bands. Additionally, Trayford et al. (2016) shows the important role of BH growth in quenching star formation and establishing the high-mass red sequence of galaxies in EAGLE.

Figure 6.3 shows the halo mass-central BH mass relation at redshift $z = 0$ for the EAGLE simulations discussed here. The halo mass, M_{200}, is defined as the total mass within the radius within which the mean density is 200 times the critical density of the Universe.

Regardless of the initial seed mass, BHs that reside in low-mass haloes barely grow because star formation driven outflows are efficient and able to prevent large reservoirs of cold low angular momentum gas accumulating around the BH. Then, the accretion behaviour changes dramatically in haloes with mass $\sim 10^{12}\mathrm{M}_{\odot}$. At this halo mass, the hot gas in the corona causes the star formation driven outflows to stall and conditions become optimal for BH accretion, and BHs grow rapidly. The growth of BHs residing in haloes more massive than $\sim 10^{12}\mathrm{M}_{\odot}$ is self-regulated by AGN feedback and BHs reach similar masses regardless of their initial seed mass. The physical origin of this transition is further discussed by Bower et al. (2017). As a result of this transition there are two prominent populations of SMBHs in the

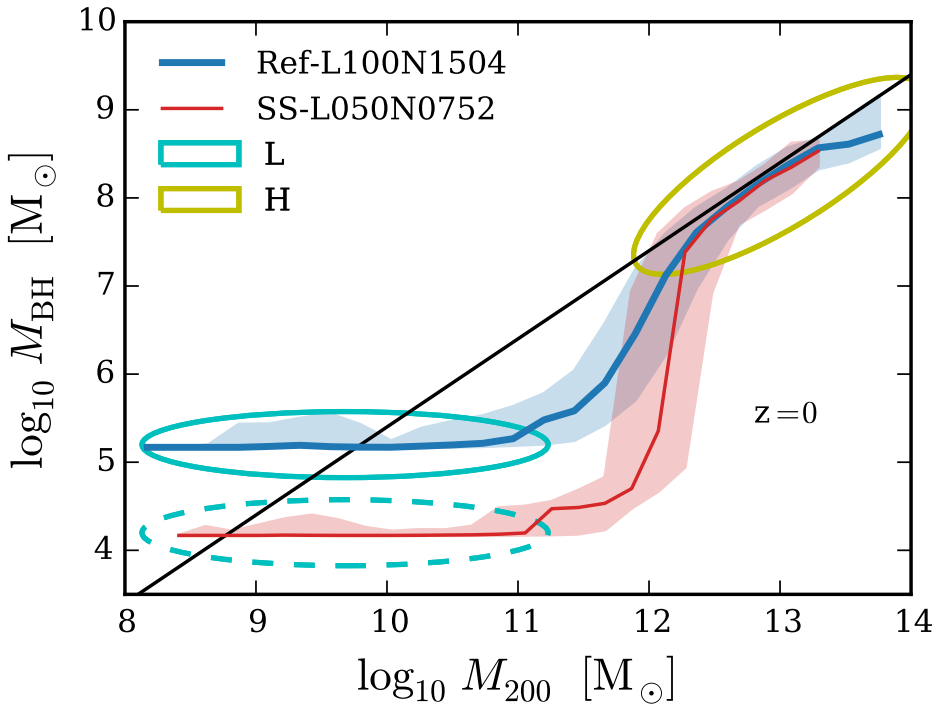

Fig. 6.3.: Halo mass-central BH mass relation for two EAGLE simulations at redshift $z = 0$. Lines represent the median of the distribution for each simulation. Only bins containing 5 objects or more have been plotted. The shaded region encloses the 10^{th} to 90^{th} percentiles for each model. The black line is shown as reference for a relationship $M_{BH} \propto M_{200}$. Regardless of the initial BH seed mass the halo mass-BH mass relation exhibits a steep slope in haloes with mass $\sim 10^{12} M_{\odot}$. At this halo mass, the hot gas in the corona causes the star formation driven outflows to stall and conditions become optimal for BH accretion, and BHs grow rapidly (Bower et al. in preparation). For BHs hosted by haloes more massive than $\sim 10^{12} M_{\odot}$ the growth is self-regulated by AGN feedback. Two prominent populations of SMBHs are highlighted: BHs not much more massive than the seed mass (**L** for 'low mass') and very massive BHs with masses $> 10^7 M_{\odot}$ (**H** for 'high mass').

simulations. These are highlighted in the figure: BHs not much more massive than the seed mass (**L** for 'low mass') and very massive BHs with masses $> 10^7$ $M_\odot$ (**H** for 'high mass').

6.3.4 Black hole coalescence

For each SMBH merger that takes place in the simulations we store the mass of both SMBHs, M_1 and M_2, and the redshift z at which the merger event takes place. On Fig. 6.4 we show the 2D histogram of the mass of each BH member for all the mergers in the EAGLE simulation models considered here. The total number of BH mergers in each simulation model is indicated in the figure. For Ref-L100N1504 a total of $N_{\rm BHM} = 54,850$ BH mergers take place across cosmic time. A factor of ≈ 8 fewer mergers occur in the small seeds ($N_{\rm BHM} = 7,045$) model almost entirely due to the factor of 8 smaller volume of the simulation. Three prominent populations of characteristic SMBH binaries build up. These are the result of the halo mass-central BH mass relation in EAGLE, shown in Fig. 6.3. The groups are: SMBH binaries that involve two BHs not much more massive than the seed mass (**L**+**L**); high mass ratio binaries where M_1 is massive ($> 10^7 M_\odot$) and M_2 is not much more massive than the seed mass (**L**+**H**); the case where both BHs are massive, with masses between 10^7 and 10^8 $M_\odot$ (**H**+**H**).

In Fig. 6.5 we show the co-moving number density distribution as a function of the more massive member of the BH binaries, M_1, plotted for five non-contiguous ranges in the mass of the least massive member, M_2. The (**L**+**L**) and (**L**+**H**) populations of binaries correspond to the left and right peaks of the distribution in the top two panels. The population (**H**+**H**) is shown in the bottom two panels. Naturally, the larger simulation volume samples more massive structures, hence the observed BH coalescence distribution in each panel extends to higher values of M_1. Since we keep the same vertical axis range for all five panels we can compare the contribution of each mass bin to the total SMBH merger rate. The population of binaries where both BHs are massive (**H**+**H**), shown in the bottom panel, is at least two orders of magnitude smaller than that of high mass ratio binaries (**L**+**H**) and SMBH binaries that involve two BHs not much more massive than the seed mass (**L**+**L**), shown in the top two panels of the figure.

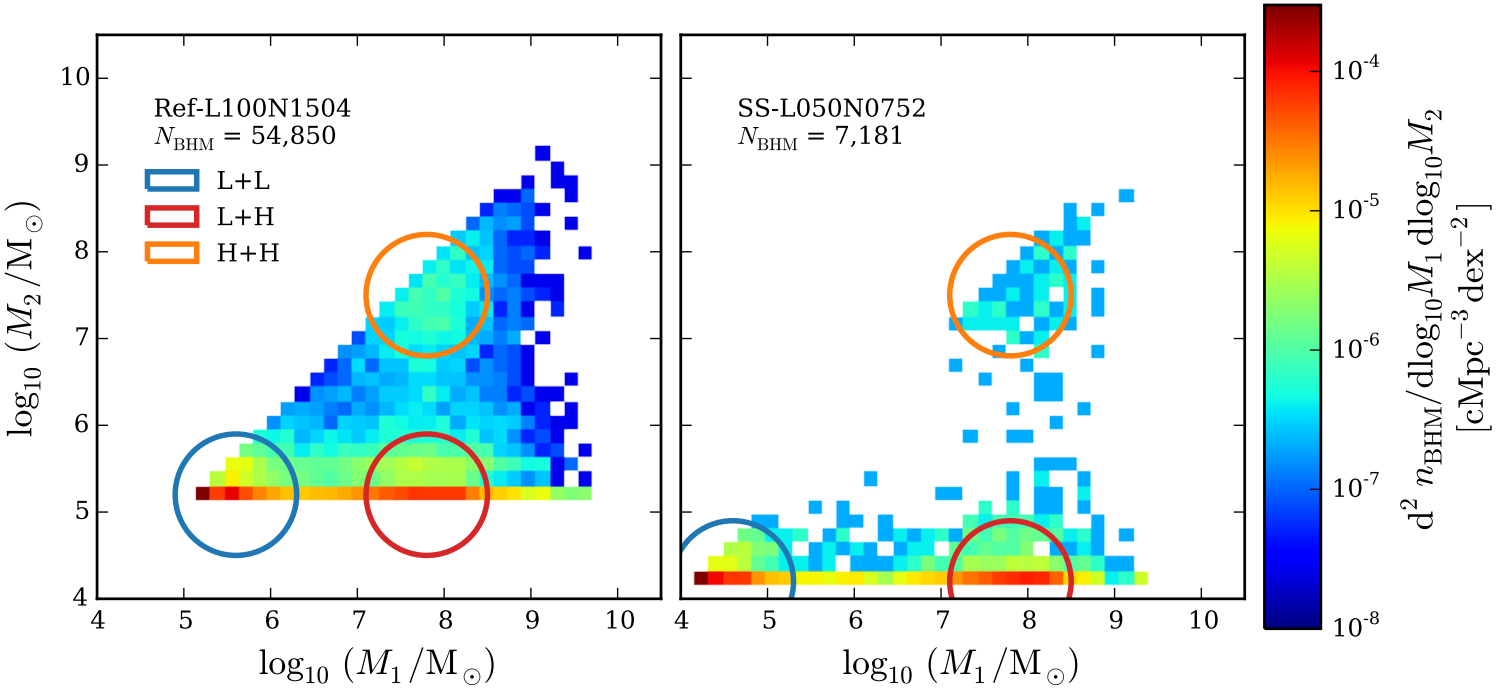

Fig. 6.4.: 2D histogram of all BH mergers for all redshifts in the EAGLE simulations. Ref-L100N1504 (left panel) and SS-L050N0752 (right panel). M_1 is the more massive member of the SMBH binary ($M_1 \geq M_2$). The total number of coalescence events in each simulation model, $N_{\rm BHM}$, is shown in the top left corner of each panel. Colour coding represents the number density of SMBH mergers per binary mass bin. As a result of the transition in the Halo mass-central BH mass relation shown in Fig. 6.3, there are three prominent populations of SMBH binaries in the simulations, which are highlighted in the figure: SMBH binaries that involve two BHs not much more massive than the seed mass (**L**+**L**); high mass ratio binaries where M_1 is massive ($> 10^7 {\rm M}_\odot$) and M_2 is not much more massive than the seed mass (**L**+**H**); the case where both BHs are massive, with masses above 10^7 M$_\odot$ (**H**+**H**). Since the populations of high-mass SMBHs in both simulation models reach similar masses (Fig. 6.3), the population of (**H**+**H**) binaries occupies the same region in both models. On the other hand, both the (**L**+**L**) and (**L**+**H**) populations are shifted in M_1 and M_2 in the SS-L050N0752 model compared to Ref-L100N1504.

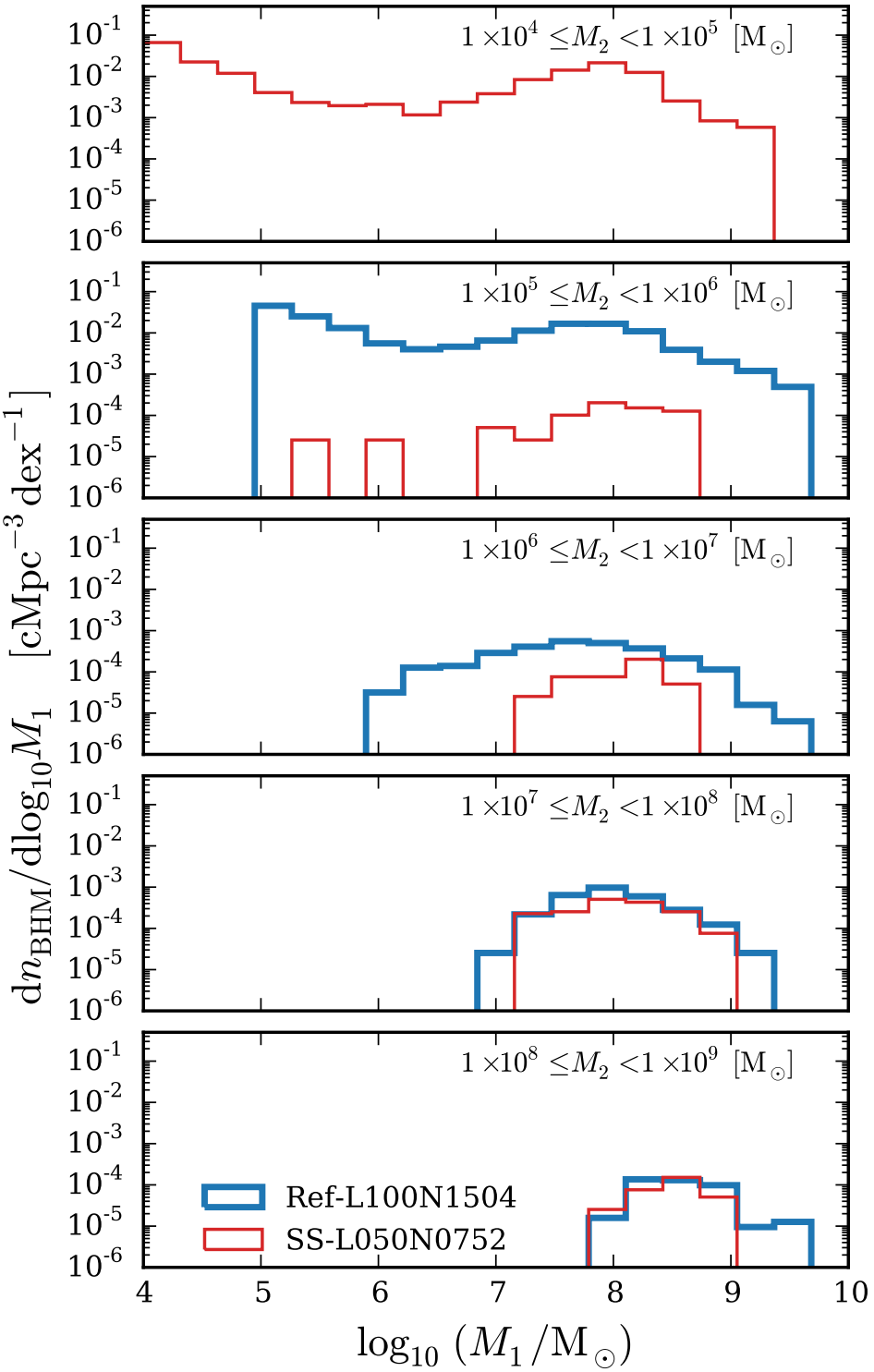

Fig. 6.5.: Co-moving number density of the more massive member of the BH binaries with mass M_1, for five non-contiguous ranges in the mass of the least massive member, M_2, as indicated in the legend (top to bottom). The population of SMBH binaries that involve a BH not much more massive than the seed mass ($< 10^6 \mathrm{M}_\odot$) are then shown in the top panel. Binaries where both BHs are massive ($> 10^7 \mathrm{M}_\odot$) are shown in the two bottom panels. The population (**H**+**H**), shown in the two bottom panels, is at least two orders of magnitude smaller than the (**L**+**L**) and (**L**+**H**) populations, shown in the top two panels.

6.4 Predicted gravitational wave event rate

In order to compute the expected GW signals from SMBH mergers in the simulations, we adopt the following strategy. We first calculate the frequency at the transition from the inspiral phase to the merger phase, $f_{\rm merger} = 0.018\, c^3/GM_{\rm total}$, for each merger event in EAGLE. We compute the minimum inspiral frequency $f_{\rm min} = 1 \times 10^{-3}\, c^3/GM_{\rm total}$ and an arbitrary final frequency $f_{\rm max} = 2 \times 10^{-1}\, c^3/GM_{\rm total}$. Assuming that both SMBHs in the binary have no spin, we use the Inspiral-Merger-Ringdown waveform model PhenomD (Khan et al., 2016) to compute the characteristic strain amplitude of the GWs from each binary, which depends only on the merging redshift (z) and the mass of each SMBH (M_1 and M_2). We compute the sensitivity curve of eLISA using the analytical approximation given in Eqs. (6.8) to (6.12). For this analysis we adopt the target frequency cut of the detector, $f_{\rm cut} = 3 \times 10^{-5}$ Hz. From all the computed GW signals, we filter the events that would be resolvable by the detector using Eq. (6.14) with a ratio of the signal to the sensitivity curve $k \geq 1$ (i.e. S/N $\gtrsim 5$). For all resolvable events we compute the observed duration $\tau_{\rm obs} = \tau_{\rm inspiral,obs} + \tau_{\rm merger,obs}$ using Eqs. (6.5) and (6.7) for the detected frequencies. Finally, from the number of resolvable sources we estimate the event rate of GW sources and the total number of expected observable events during the lifetime of the eLISA mission using Eqs. (6.15) and (6.16).

For SMBH binaries the S/N of the GW signals is accumulated in the last month of the inspiral phase (Sesana et al., 2011). Therefore, in this study we choose to only include sources that "merge" during the mission time, i.e., to construct the expected event rate we only consider events with $\tau_{\rm obs} \leq T_{\rm obs}$. In Fig. 6.6 we show the distribution of the observed duration for all the resolvable events. The performance of the detector improves as a function of the duration of mission and gaps in the data stream would affect the number of resolved events (e.g. Sesana et al., 2011). For this study we assume a fiducial eLISA mission continuous lifetime of $T_{\rm obs} = 3$yrs. We show in Figs. 6.7 and 6.8 the characteristic strain amplitude as a function of the observed merger frequency for all the GW events produced by SMBH coalescences in the EAGLE Ref-L100N1504 and SS-L050N0752 simulations respectively. To help visualise the mass range and redshift of BH coalescences that would be detected by eLISA, grey lines indicate the characteristic strain and observed merger frequency emitted by equal mass BH binaries ($M_1 = M_2$) coalescing at different redshifts z. The following characteristic features can be seen in the figures:

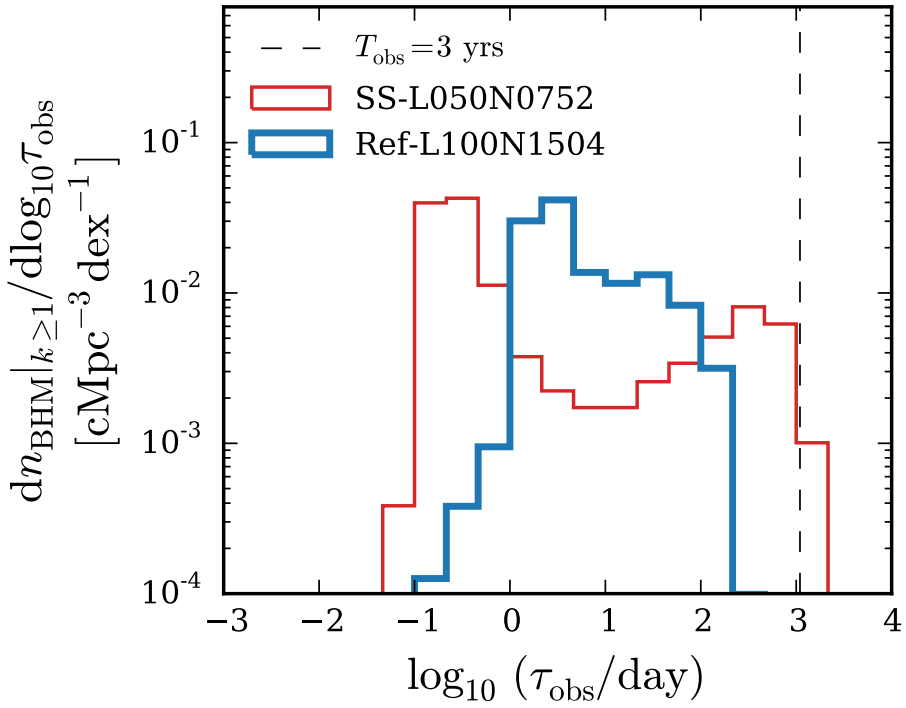

Fig. 6.6.: Distribution of the observed duration of the events that would be resolvable by the eLISA detector (i.e. the ratio of the GW signal to the detector's sensitivity curve $k \geq 1$). For this study, we assume an eLISA mission lifetime of $T_{\rm obs} = 3$ yrs (dashed vertical line). We only consider events with $\tau_{\rm obs} \leq T_{\rm obs}$ in the rest of the chapter.

1. For both models, the most densely populated region of events ($1\times10^{-3} \lesssim f_{\rm mer,obs}/[{\rm Hz}] \lesssim 1\times10^{-2}$ and $1\times10^{-19} \lesssim h_c \lesssim 1\times10^{-17}$ for Ref-L100N1504 and $1\times10^{-2} \lesssim f_{\rm mer,obs}/[{\rm Hz}] \lesssim 1\times10^{-1}$ and $1\times10^{-20} \lesssim h_c \lesssim 1\times10^{-18}$ for SS-L050N0752) corresponds to SMBH binaries where both BHs have masses not much greater that the seed mass (**L**+**L**). As illustrated in Fig. 6.2, we expect higher GW frequencies and smaller strain amplitudes from less massive BH mergers. Therefore, for the small seeds model the (**L**+**L**) population shifts to higher frequencies and lower amplitudes compared to the reference model. For both Ref-L100N1504 and SS-L050N0752 EAGLE models the (**L**+**L**) population of events occupies a region above the detection threshold of eLISA and hence will provide a high contribution to the data stream (as seen in Fig. 6.10).

2. The second most populated region of events ($1\times10^{-5} \lesssim f_{\rm mer,obs}/[{\rm Hz}] \lesssim 1\times10^{-4}$ and $1\times10^{-18} \lesssim h_c \lesssim 1\times10^{-16}$ for both simulations) corresponds to binaries from the (**L**+**H**) population. For both the Ref-L100N1504 and SS-

L050N0752 EAGLE models, there are significantly less events in the (**L**+**H**) population compared to the (**H**+**H**), with some falling outside the detection threshold of eLISA. Hence will not contribute significantly to the data stream.

3. Only few events from the (**H**+**H**) population occupy a region above the detection threshold of eLISA. However, there are significantly fewer events in the in this population of binaries compared to the (**L**+**L**) and (**L**+**H**) populations (at least two orders of magnitude fewer events, as seen in Fig. 6.5). Therefore, the binaries from the (**H**+**H**) population do not show up as a dense region in the plot.

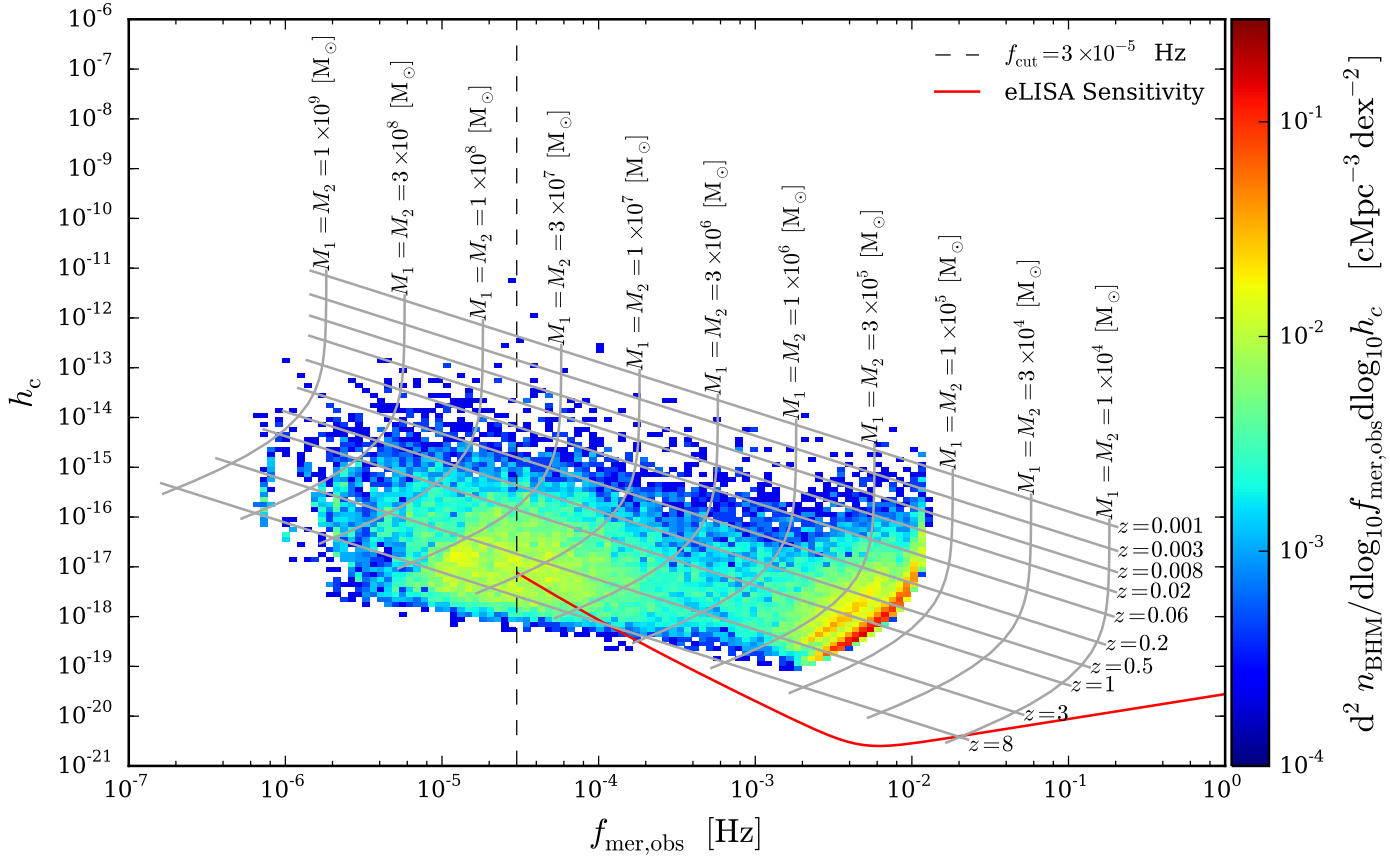

Fig. 6.7.: Characteristic strain amplitude h_c of the GW signals emitted by all SMBH coalescences in the EAGLE Ref-L100N1504 simulation as a function of the observed frequency at the transition between the inspiral phase and the merger phase of the SBMH coalescence process $f_{\rm mer,obs} = (0.018\, c^3/GM_{\rm total})/(1+z)$. Colour coding represents the co-moving number density of events per characteristic strain-observed merger frequency bin. Grey contour lines indicate the characteristic strain and observed merger frequency for equal mass BH binaries ($M_1 = M_2$) coalescing at different redshifts z. The sensitivity curve of eLISA calculated from the analytic approximation in Eq. (6.8) is shown in red. The black dashed line indicates the low-frequency cut-off of the sensitivity curve $f_{\rm cut} = 3 \times 10^{-5}$ Hz. GW signals above the sensitivity curve and to the right of the low-frequency cut-off can be resolved from the eLISA data stream.

Fig. 6.8.: As Fig. 6.7 but for the EAGLE SS-L050N0752 simulation.

The characteristic shift in amplitude and frequency of the detected GW signals that results from the different SMBH seed masses suggests that eLISA will be a powerful tool to discriminate between different SMBH seeding mechanisms. In Fig. 6.9 we show the number of detected SMBH coalescences observed per year at redshift $z = 0$ as a function of the frequency at the transition between the inspiral phase and the merger phase, $f_{\rm mer,obs}$. The figure shows a shift of a decade in frequency for the whole distribution between the simulation models. The amplitude of the peak of the distribution is, however, the same for both models. For lower frequencies (i.e. more massive mergers) the SS-L050N0752 model has fewer detected events (~0.3 dex) because these events have lower characteristic strain amplitude and therefore some fall below the detection threshold of the eLISA sensitivity curve.

For the signals detected by eLISA it will be possible to extract the physical parameters of the BH sources, such as their masses, luminosity distance, and sky locations, using a set of theoretical templates for the waveforms for each phase (i.e inspiral, merger, and ringdown phases) (Cutler & Flanagan, 1994; Flanagan & Hughes, 1998; Amaro-Seoane et al., 2013; Abbott et al., 2016). In Fig. 6.10 we have plotted the redshift distribution, the mass function of the more massive member of the binary, M_1, and the distribution of the mass ratio, M_1/M_2, of the number of detected SMBH coalescences per observed year at redshift $z = 0$ (left, central and right panels respectively). In this plot we have also included a variation of the Ref-L100N1504 simulation that include a delay to the SMBH merger timescales as detailed in Section 6.3.2.

From the first panel it is clear that SMBHs merging between redshift $z \sim 2$ and $z \sim 1$ will provide the greatest contribution to the event rate of GW signals in the EAGLE models. On the basis of the redshift distributions of detected signals it is thus not possible to discriminate between the SMBH seeding mechanisms implemented in our simulations. The M_1 mass function of the predicted event rate has a very pronounced peak at the SMBH seed mass $m_{\rm seed}$ ($10^5\,{\rm M}_\odot h^{-1}$ for the *'Ref-'* model and $10^4\,{\rm M}_\odot h^{-1}$ for the *'SS-'* model). Given the logarithmic scale of the plot, the galaxy formation model implemented in EAGLE predicts that GW signals will be dominated by the coalescence of BH seeds, which is also shown in the last panel of the figure, in which the mass ratio distribution peaks for equal mass SMBH coalescences for both models. This is a remarkable result, since it implies that the physical parameters of the GW sources recovered from the eLISA data stream will provide us with a profound insight into the nature of SMBHs and the initial mass distribution of seeds. We also find that adding a delay to the SMBH merger

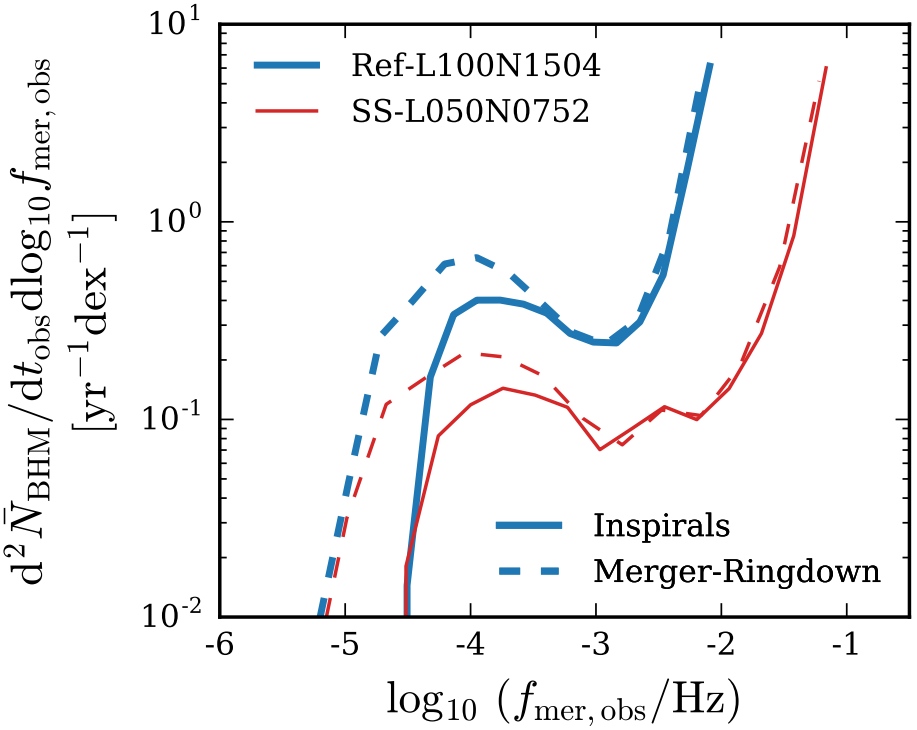

Fig. 6.9.: Number of detected SMBH coalescences per observed year as a function of the frequency at the transition between the inspiral phase and the merger phase $f_{\rm mer,obs}$. A shift of a decade in frequency of the whole distribution is observed for the SS-L050N0752 compared to the Ref-L100N1504 model. The amplitude of the peak of the distribution is the same for both models. For lower frequencies (i.e. more massive mergers), the SS-L050N0752 model has fewer detected events (by about 0.3 dex) because these events have lower characteristic strain amplitude, as expected for lower mass BHs, and therefore fall outside the detection threshold of the eLISA sensitivity curve.

timescales makes no significant difference in either the predicted event rate, nor to the mass function of the detected binaries. This is to be expected, since the galaxy formation model implemented in EAGLE predicts GW signals that will be dominated by the coalescence of BH seeds. These low mass SMBHs are hosted mainly by gas rich galaxies in which planet-like migration is predicted to lead to short coalescence time-scales (Colpi & Dotti, 2011; Mayer, 2013; Colpi, 2014).

We use Eq. (6.15) to calculate the event rate of GW signals resolved by the eLISA mission. The results are shown in Table 6.2. By propagation of error, the uncertainty on the expectation event rate due to the finite volume of the simulations is given by

$$\sigma = \sqrt{\sum_{z=0}^{z=\infty} \left(\frac{\sqrt{\bar{N}(z, k \geq 1)}}{\Delta z \Delta V_c} \frac{\Delta z}{\Delta t} \frac{\Delta V_c}{\Delta z} \frac{\Delta z}{(1+z)} \right)^2}. \tag{6.17}$$

The actual number of detections is drawn from a Poisson distribution that depends on the duration of the mission multiplied by the expectation rate given in the table. We find that for the estimated event rate of GWs is $\sim$ 2 events per year for the inspiral and the merger-ringdown phases (for both the Ref-L100N1504 with and without delays, and SS-L050N0752 simulations). We estimate that in a 3 year mission the eLISA detector should be able to resolve $\sim$ 6 mergers and $\sim$ 6 inspiral signals from SMBH mergers. Even with this low event rate the information carried by each gravitational waveform would provide us with a powerful tool to constrain the SMBH seed formation mechanisms.

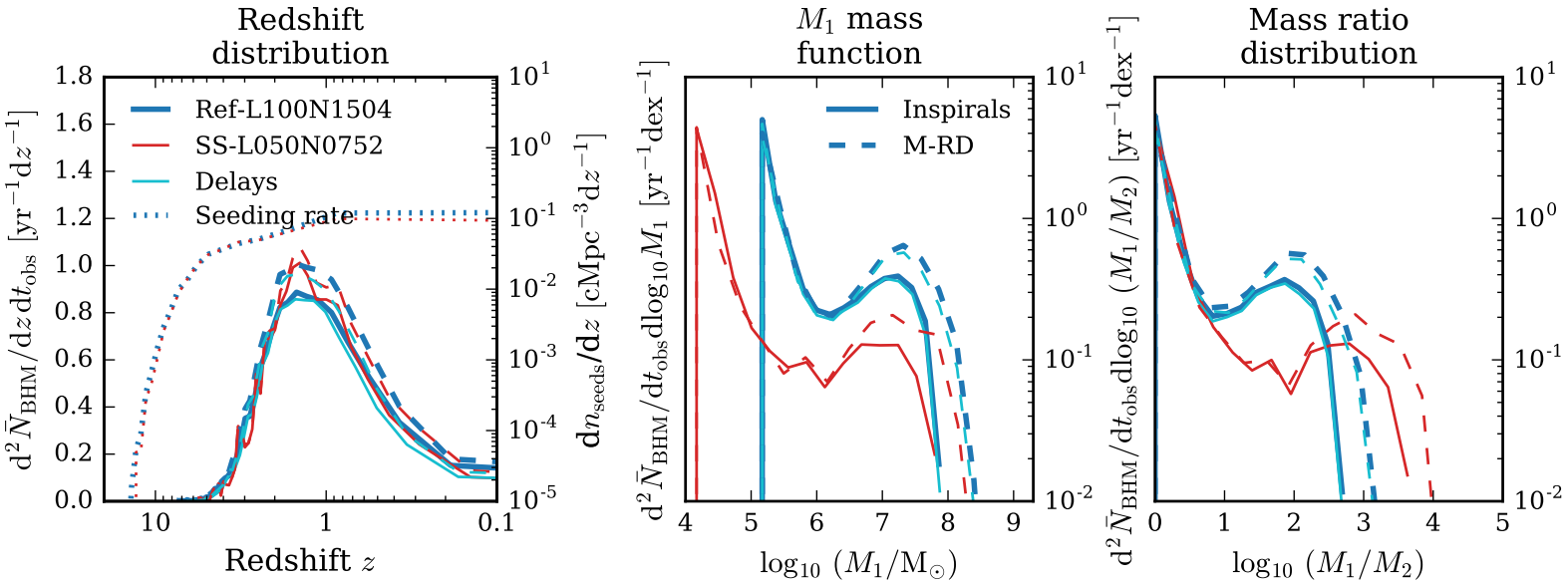

Fig. 6.10.: *LEFT PANEL:* Redshift distribution of the SMBH coalescences resolved by eLISA. The distribution peaks between redshift $z \sim 2$ and $z \sim 1$ for both the inspiral and the merger-ringdown phases for both EAGLE simulation. The differential redshift distribution of the SMBH seeding times are shown in dotted lines (right-hand axis). *MIDDLE PANEL:* Mass distribution of the more massive member of the binary, M_1, for the SMBH coalescences resolved by eLISA. For both models, the mass function peaks at $M_1 \sim m_{\rm seed}$ for both the inspiral and the merger-ringdown phases. *RIGHT PANEL:* Distribution of the mass ratio M_1/M_2 of the SMBH coalescences resolved by eLISA. The distribution peaks for equal mass SMBH binaries for both EAGLE simulation models. The model with added delay to the SMBH merger timescales has no significant difference in either the predicted event rate, nor in the mass function of the detected binaries.

Table 6.2.: Estimated event rates for the different simulation models. σ is the standard Poisson uncertainty on the expectation event rate due to the finite volume of the simulations.

Simulation	Inspiral Phase event rate [yr^{-1}]	σ_I [yr^{-1}]	Merger-Ringdown Phase event rate [yr^{-1}]	σ_{M-RD} [yr^{-1}]
Ref-L100N1504	2.02	0.01	2.36	0.02
Ref-L100N1504 + Delays	1.89	0.01	2.17	0.01
SS-L050N0752	2.02	0.04	2.16	0.04

6.5 Discussion and Conclusions

Using the EAGLE simulations, a state-of-the-art cosmological hydrodynamical simulation suite, we have computed the event rate of GW signals expected from SMBH mergers that should be resolved by a space-based GW detector such as the Evolved Laser Interferometer Space Antenna, eLISA.

The EAGLE simulations use modern smoothed particle hydrodynamics and physically motivated subgrid models to capture the unresolved physics. These simulations reproduce the observed galaxy population with unprecedented fidelity, providing a powerful tool to study galaxy formation and evolution.

A number of SMBH seed formation mechanisms have been proposed to explain the observed population of high-redshift quasars in our Universe. These mechanisms predict different initial mass functions of BHs seeds. These characteristic BH seed mass functions and the dynamical evolution that takes place during the merging process of SMBH binaries in the centres of colliding galaxies leave a unique imprint on the GW signals predicted by the models. Therefore, the information carried by the gravitational waveforms detected by a GW detector such as eLISA will provide us with a powerful tool to discriminate between different SMBH seeding models.

Since the processes involved in the SMBH seed formation models are not resolved by the simulations, we assume that seed BHs are produced sufficiently frequently that every halo above a certain threshold mass contains a central BH seed. In order to investigate the dependence on the assumed BH seed mass we used two simulation models using BH seeds that differ by an order of magnitude in mass. For the Ref-L100N1504 model, high-mass BH seeds ($m_{\rm seed} = 1.475 \times 10^5 {\rm M}_\odot$) were placed at the centre of every halo with total mass greater than $m_{\rm halo,th} = 1.475 \times 10^{10} {\rm M}_\odot$ that did not already contain a BH. For the SS-L050N0752 model, the BH seed mass used was $m_{\rm seed} = 1.475 \times 10^4 {\rm M}_\odot$. These BH seeds then grow by accreting gas and via mergers with other BHs. In the EAGLE models, BHs residing in low-mass haloes barely grow because star formation driven outflows are efficient and able to prevent cold gas accumulating around the BH (Bower et al. in preparation). As a result, three prominent populations of characteristic SMBH binaries build up in the simulations as a result of the halo mass-central BH mass relation in EAGLE, shown in Fig. 6.3. The groups are: SMBH binaries that involve two BHs not much more massive than the seed mass (**L**+**L**); high mass ratio binaries in which one BH is

massive ($> 10^7 M_\odot$) and the other is not much more massive than the seed mass (**L**+**H**); and the case where both BHs are massive, with masses between 10^7 and 10^8 $M_\odot$ (**H**+**H**). We also consider a variation of the Ref-L100N1504 reference model, where a prescription for the expected delays in the BH merger timescale has been included after their host galaxies merge. The added delays are based on the gas content in the nuclear region of the resulting galaxy after the merger.

We combine the merger rates of SMBHs in the simulations with the most recent phenomenological frequency-domain gravitational waveform model for non-precessing BH binaries described in Khan et al. (2016) (commonly referred to as "PhenomD"). We calculated that the merger rate of SMBHs is similar in the simulation models and will produce a low event rate of GW signals, nonetheless observable by a space-based interferometer such as eLISA. We find that the predicted event rate of GWs for the inspiral and merger-ringdown phases for both the *'Ref-'* and *'SS-'* models is ~ 2 events per year. Hence, in a 3 year mission the eLISA detector should be able to resolve ~ 6 mergers and ~ 6 inspiral signals from SMBH coalescences. Our analysis shows that these signals will be dominated by the coalescence of BH seeds (**L**+**L** population of binaries) merging between redshifts $z \sim 2$ and $z \sim 1$. Given the difference in the BH seed mass of the models, there is a characteristic shift of a decade in the observed frequency for the whole distribution of the GW signals (Fig. 6.9).

Compared to previous studies that propose that eLISA could distinguish between BH seed formation models based on the global properties of the merger distribution (i.e Sesana et al., 2007, 2011; Barausse, 2012), we find that eLISA could probe BH seeds down to low redshift because the GW signals from SMBH coalescences will be dominated by mergers of BHs that have not yet experienced significant growth (see Fig. 6.3, 6.10, and Bower et al. in preparation). Hence, different physical BH seeding mechanisms could be distinguished from the detected gravitational waveforms, allowing eLISA to provide us with profound insight into the origin of SMBHs and the initial mass distribution of SMBH seeds. We find that adding a delay to the SMBH merger timescales makes no significant difference in either the predicted event rate, nor to the mass function of the detected binaries (Fig. 6.10).

We find that EAGLE predicts GW signals that would be best detected by eLISA, but complementary observations of GW signals in different frequency windows will enable us to fully characterise the cosmic history of SMBHs (Crowder & Cornish, 2005; Sesana et al., 2008; Janssen et al., 2015; Moore et al., 2015). For instance,

pulsar timing arrays will be able to detect GWs in a lower frequency window (i.e., $f_{\rm obs} < 10^{-6}$[Hz] with $h_c > 10^{-17}$, Hellings & Downs 1983; Sesana et al. 2008; Kelley et al. 2017) than the SMBH mergers arising in our cosmological volume (Fig. 6.7). On the other hand, if the initial mass function of SMBH seeds extends to masses $< 10^4 {\rm M}_\odot$, intermediate frequency missions (i.e. $10^{-3} \lessapprox f_{\rm obs}/[{\rm Hz}] \lessapprox 10^{1}$ with $h_c > 10^{-25}$), like the proposed Advanced Laser Interferometer Antenna (ALIA, Bender et al. 2013), the Big Bang Observer (BBO, Harry et al. 2006), and the Decihertz Interferometer GW Observatory (DECIGO, Kawamura et al. 2006), will be suitable to detect the mergers of seeds and shed light on their initial mass function. It is also important to highlight that other GW sources, such as galactic white dwarf binaries, will also contribute to the eLISA data stream.

Since the EAGLE simulations reproduce a wide set of observational properties of the galaxy population we may expect the physics of the real Universe to be reasonably well captured by the phenomenological sub-grid models implemented in the simulations. Nevertheless, the predicted GW event rate is specific to the galaxy formation and evolution model implemented in these simulations and the sub-grid models for BH seeding and growth via accretion and mergers. In particular, in the EAGLE simulations BH seeds are placed into haloes of mass $m_{\rm halo,th} = 10^{10}\,{\rm M}_\odot$, which corresponds to a very small galaxy of stellar mass $m_* \sim 10^7 {\rm M}_\odot$. From observational constraints such galaxies are thought to be the smallest galaxies to host SMBHs at low redshift (Reines et al., 2013; Seth et al., 2014). In the simulation, the stellar mass of galaxies in which BHs are seeded depends little on redshift and the BH mass at birth is already 1% relative to the stellar mass. Some BH formation models suggest that BH seeds could form even more efficiently in still lower-mass galaxies at high redshift. In this case, SMBH mergers could be more common and therefore increase our predicted GW event rate. Our predicted rates are therefore conservative. Addressing this issue in more depth would require a simulation of considerably higher resolution (and yet comparable cosmological volume) coupled to a physical model of BH seed formation. Such a simulation is currently beyond the scope of cosmological simulation codes. Fortunately, since our models predict that eLISA should be very sensitive to the initial mass distribution of BH seeds, it will probe precisely these issues and directly complement theoretical developments. Further work using the EAGLE simulations, coupled to physical models of BH seed formation could be used to predict the GW signals from SMBH mergers that could be detected by future GW detectors.

7 Conclusions and Future Work

7.1 Summary of this thesis

In the standard model of cosmology, the energy density of the Universe is currently dominated by a form of dark energy that is consistent with a cosmological constant Λ, and cold dark matter, with only $\sim 5\%$ of the total cosmic energy density in the form of 'ordinary' baryonic matter. Measurements of the amplitude of the small temperature fluctuations in the cosmic microwave background (CMB) have allowed us to estimate the cosmological parameters with unprecedented fidelity (Planck Collaboration et al., 2016). The ΛCDM model has been tested thoroughly and it has been proven to successfully fit and predict a vast range of phenomena in the Universe, such as the large scale distribution of galaxies and the CMB itself. Despite its success, the nature of its two major components, the cosmological constant and the cold dark matter, are still unknown. Additionally, the cosmological constant is afflicted by the 'fine-tuning' and 'coincidence' problems. In order to shed light into these problems, this thesis is concerned with the study of the interplay between cosmology and galaxy formation. In particular, using advanced cosmological hydrodynamic simulations from the EAGLE suite (Schaye et al., 2015), and by developing fully analytic models of galaxy formation, we disentangle the role of cosmology from the role of astrophysics in the galaxy formation process.

In Chapter 3 we used a modified version of the EAGLE code to investigate the effect of the accelerated expansion of the Universe on the cosmic star formation rate. We compared a ΛCDM Universe to an Einstein-de Sitter model with $\Lambda = 0$. Contrary to previous studies (e.g. Springel & Hernquist, 2003), we find that the existence of the cosmological constant has little impact on the star formation history of the Universe. The star formation is suppressed only by $\approx 15\%$ at the present time, and we find that the properties of galaxies are almost indistinguishable in the two universes. By extrapolating fits to the evolution of the co-moving star formation rate density into the future, we show that, in our Universe, more than $\approx 88\%$ of the stars that will ever be produced, have already been formed by the present cosmic time. In the absence of dark energy, only $\approx 15\%$ more stellar mass would have been formed in the same time. The difference is small, bringing into question whether the

'coincidence problem' (the comparable energy densities of matter and dark energy) can be explained by an anthropic argument, i.e. the existence of dark energy (at its observed value) has negligible impact on the existence of observers to observe the cosmos. In comparison, the existence of supermassive black holes has a major impact on the Universe. In the absence of feedback from accreting black holes, the co-moving star formation rate density is enhanced by a factor of 2.5 at the present day.

One of the main outcomes of the work presented in this thesis is the introduction of a novel way to solve the Friedman equations, which allows us to expand the solution as a Taylor series. This is proven to be a very powerful tool in many ways: First, it clearly shows the effect of the cosmological constant in the expansion history of the Universe, which can be used as a pedagogical way to introduce the Friedmann equation and the accelerated expansion of the Universe. Second, it allows us to analytically approximate cosmological quantities, that would otherwise only be possible to solved numerically, e.g. the linear growth factor of density perturbations. This provides a simple direct connection of the accretion rate of dark matter haloes to the cosmological background.

Using this advantage, in Chapter 3 we develop a simple analytic model for the cosmic star formation rate that captures the suppression due to a cosmological constant. Using the analytic model, we can recognise that the existence of the peak in the star formation rate density results from the interaction of the star formation efficiency (set by the inter stellar medium physics) which limits the rate at which the galaxy can respond to convert in-falling material into stars, the relative abundance of efficiently star forming haloes (i.e. of masses $\approx 10^{12}\,\mathrm{M}_{\odot}$), and only at late times, the slowing growth rates of haloes due to the cosmological constant.

Chapter 4 presents the first rigorous test of the anthropic principle as an explanation of the observed value of the cosmological constant using the full machinery of galaxy formation theory developed in the EAGLE hydrodynamical simulations. We introduced a set of simulation with a wide range of Λ values, ranging from $\Lambda = 0$ to $\Lambda_0 \times 300$, where Λ_0 is the value of the cosmological constant in our Universe. We find that because the global star formation rate in our Universe peaks at $t = 3.5$ Gyr, before the onset of accelerating expansion, increases in Λ of even an order of magnitude have only a small effect on the star formation history and efficiency of the Universe. In universes with larger values of Λ, galaxies quickly become isolated from their cosmic surroundings, burning their finite matter supply and

forming stars at a decreasing rate. We use our results to predict the observed value of the cosmological constant, given a measure of the multiverse. We considered three simple but plausible models for where we would expect observers to be created. Testing the observer creation rate per constant mass between universes, we predicted a value of the cosmological constant that is $50 - 60$ times larger than the observed value. The probability of observing a value as small as our cosmological constant is $\sim 2\%$. We conclude that the impact of the cosmological constant on the formation of structure in the universe does not straightforwardly explain the small observed value of Λ. The anthropic argument for the value of Λ is not a particularly successful prediction.

In Chapter 5, using the solution of the Friedmann equation developed in Chapter 3, we introduce a fully analytic model of galaxy formation that connects the growth of dark matter haloes in a cosmological background, with the build up of stellar mass within these haloes. The model identifies the physical processes that drive the Galaxy-Halo co-evolution through cosmic time. The model restricts the role of baryonic astrophysics to setting the relation between galaxies and their halos. All astrophysical process enter into the model via an instantaneous star formation efficiency parameter which captures all the physical processes involved in the conversions of gas into stars, i.e. cooling, star formation law, feedback from star formation and accreting black holes, etc. We show that galaxy formation is revealed as a simple process where the instantaneous star formation efficiency within halos is only a function of their virial temperature. Despite its simplicity, the model reproduces self-consistently the shape and evolution of the cosmic star formation rate density, the specific star formation rate of galaxies, and the galaxy stellar mass function, both at the present time and at high redshift. By providing a set of analytic equations, the model can be easily "inverted" and allows for rapid experiments to be conducted, providing a great tool to explore the differential effects of baryonic physics, averaged over galaxy scales.

As we discussed in Chapters 3 and 5, supermassive black holes play a major role in the evolution of their host galaxies (e.g. Bower et al., 2006; Croton et al., 2006; Fabian, 2012; Kormendy & Ho, 2013; Heckman & Best, 2014). Hence, in Chapter 6, we estimate the expected event rate of gravitational wave signals from mergers of supermassive black holes that could be resolved by a future space-based interferometer, such as the Evolved Laser Interferometer Space Antenna (eLISA). This work is the first such estimates using a full set of cosmological hydrodynamical simulations. We demonstrate how these gravitational wave signals can provide profound insight

into the origin of supermassive black holes and the initial mass distribution of black hole seeds. We combine the merger rates of supermassive black holes in the EAGLE simulations with "PhenomD", a phenomenological frequency-domain gravitational waveform model (Khan et al., 2016). We predict a low event rate of ~ 2 detections per year by a gravitational wave detector such as eLISA. Nonetheless, our analysis shows that the signals will be dominated by the coalescence of black holes with masses similar to their initial seeds mass. Hence, we find that eLISA could probe black hole seeds down to low redshift because their gravitational wave signals will be dominated by mergers of binaries that have not yet experienced significant growth. This study is the first to predict that eLISA should be very sensitive to the initial mass distribution seeds, because in low mass galaxies, black holes exhibit very little growth (e.g. Bonoli et al., 2016; Bower et al., 2017; Bellovary et al., 2018).

7.2 Looking to the future

In this section, I explore some of the interesting ways in which the investigation in this thesis can be extended.

7.2.1 Using simulations to directly aid observational large-scale structure surveys

Despite the great success of the ΛCDM model, it is now being subjected to much more stringent tests than ever before. For instance, recent large-scale structure (LSS) measurements appear to be in tension with its predictions. The predicted level of LSS based on the standard model inferred from CMB measurements significantly exceeds what is inferred from actual cluster counts (Ade et al., 2014; Aghanim et al., 2016). Is this tension signalling that new physics is required? For example, a time-varying dark energy, or perhaps a modified theory of gravity? A contribution from massive neutrinos?. Cosmological hydrodynamical simulations offer a means to address this tension by including all the relevant baryonic effects that are key to understanding the present-day properties of the most massive systems in our Universe. Nonetheless, because of the large computational cost and complexity of the physics involved, traditionally, LSS studies have used the predictions from dark matter only simulations. Based on my experience with EAGLE, I intend to

develop a set of large-scale simulations specifically designed for LSS cosmology applications, with the effects of feedback realistically accounted for. With the upcoming surveys like the Dark Energy Survey Instrument (DESI), Euclid, and the Large Synoptic Survey Telescope (LSST), specifically designed for LSS cosmology, such simulations would be crucial to critically assess the evidence for physics beyond the standard model.

7.2.2 SMBH formation, growth and dynamics

Understanding the formation mechanisms of SMBHs, the nature of their growth, and how they affect their host galaxies are areas of exertive research. Nevertheless, given the limited spatial resolution in large scale cosmological simulations, physical processes involved in SMBH seeding, feedback, and dynamics are implemented via sub-grid prescriptions. Recent studies have improved the modelling SBMH in cosmological simulations (e.g. Tremmel et al., 2015). However, a thorough exploration of the full parameter space and more physically motivated models of SMBH formation and growth are needed for a more detailed analysis of the SMBH-galaxy co-evolution throughout cosmic time. Furthermore, connecting the seeding mechanisms and dynamics of SMBHs within galaxies is necessary to predict and inform future gravitational wave observations of merging SMBHs that could provide insight into their origin.

A new ambitious programme of simulations (EAGLE2) has been under development for the past two years, using refined feedback models, improved resolution and SMBH physical processes that I am helping to develop. There is a wealth of future projects that could be undertaken using these simulations. For example, the occupation probability of SMBHs on dwarf galaxies, and the dependance of the recycling of gas on the SMBH feedback parameters, and its effects on the specific star formation rate of galaxies.

7.2.3 Study the fundamental constants of nature

I am earnest to investigate how the different fundamental *constants of nature* affect galaxy formation and the seemingly *fine-tuning* of the Universe for life. Following up on Salcido et al. (2018) and Barnes et al. (2018), I intend to use hydrodynamical simulations to explore the effect of varying other cosmological parameters in galaxy

formation (for example, the fraction of baryons to dark matter). Investigating these fundamental constants is of much interest and provides a great opportunity to combine research on galaxy formation with multidisciplinary projects with scientists, philosophers, and public engagement.

7.3 Final remarks

It is an exciting time to be cosmologist. The continuous development of powerful and precise astronomical instrumentation is pushing the boundaries of the faintest galaxies that we can observe. Even more, the large number of imminent high precision observational surveys will probe our Universe on the largest cosmological scales. We have more information about the Cosmos than ever before.

This explosion of observational data will allow us to test our standard model of cosmology to the limit. Hopefully, this progress will reveal at last the nature of dark matter and dark energy, or possible extensions beyond the standard model that could have important implications for fundamental physics. However, this will only be possible if the data comes hand in hand with accurate and detailed theoretical predictions of galaxy formation in a cosmological context. On that note, cosmological hydrodynamical simulations provide a powerful tool to test our galaxy formation theories, as they are now capable of producing realistic universes. Furthermore, the time ahead looks even brighter; the future generation of software and hardware will allow us to build bigger and better simulations. This step however, will require a better understanding of the underlying physics and the adequacy of the subgrid models implemented.

This thesis, builds upon the work of many generations of scientists in our quest to answer some the most fundamental questions in science: How do galaxies form? How has the Universe become hospitable for life? What is the nature of the mysterious dark matter and dark energy? What is the ultimate fate of our Universe? This thesis explicitly tested the effect of the cosmological background on the formation of galaxies, and the ability of the Universe to produce life. In the longer term, the analytic model of galaxy formation presented in this work provides a powerful tool to understand the physics of galaxy formation, and can complement the more sophisticated techniques such as semi-analytic models and hydrodynamical simulations.

A

Derivation of the UNIVERSEAPP model

A.1 Cosmological expansion

Here we provide a brief summary of the analytic solution of the Friedmann equation developed in Salcido et al. (2018). Using a hat notation (ˆ) to denote quantities in our observable Universe, we set $\hat{a}_0 \equiv \hat{a}(t_0) = 1$, where $t_0 = 13.8$ Gyr is the present cosmic time. We adopt a normalisation such that the value of the expansion factor at an arbitrarily early time, t_1, is identical for every model, i.e. $a_1 \equiv a(t_1) = \hat{a}(t_1)$. We refer the reader to Salcido et al. (2018) for a rationale and full description of the normalisation and equations presented here.

Salcido et al. (2018) introduced a Taylor expansion solution of the Friedmann equation that provides a deep insight into the effect of the cosmological constant in the expansion factor,

$$a(t) \approx \left[\frac{3}{2}\frac{t}{t_m}\right]^{2/3}\left(1 + \frac{1}{4}\left(\frac{t}{t_\Lambda}\right)^2 + \frac{1}{80}\left(\frac{t}{t_\Lambda}\right)^4 + ...\right), \tag{A.1}$$

where the *matter timescale* is given by,

$$t_{\rm m} = \sqrt{\frac{3}{8\pi G\hat{\rho}_0}} = \frac{1}{\hat{H}_0\sqrt{\hat{\Omega}_{\rm m,0}}}, \tag{A.2}$$

and the *dark energy timescale* is given by,

$$t_\Lambda = \sqrt{\frac{3}{\Lambda c^2}} = \frac{1}{H_0\sqrt{\Omega_{\Lambda,0}}}. \tag{A.3}$$

A.2 The growth of density perturbations and the halo accretion rates

Dark matter structures are assumed to have grown from small initial density perturbations. Expressing the density, ρ, in terms of the density perturbation contrast against a density background,

$$\rho(\mathbf{x}, t) = \bar{\rho}(t)[1 + \delta(\mathbf{x}, t)], \tag{A.4}$$

the differential equation that governs the time dependence of the growth of linear perturbations in a pressureless fluid, such as e.g. dark matter, can be written as

$$\frac{\mathrm{d}^2\delta}{\mathrm{d}t^2} + 2\frac{\dot{a}}{a}\frac{\mathrm{d}\delta}{\mathrm{d}t} - 4\pi G\bar{\rho}\delta = 0. \tag{A.5}$$

The growing mode of Eq. (A.5) can be written as,

$$\delta(t) = D(t)\delta(t_0), \tag{A.6}$$

where $D(t)$ is the linear growth factor, which determines the normalisation of the linear matter power spectrum relative to the initial density perturbation power spectrum, and is computed by the integral

$$D(t) \propto \frac{\dot{a}}{a}\int_0^t \frac{\mathrm{d}t'}{\dot{a}^2(t')}. \tag{A.7}$$

Using the power-series approximation for $a(t)$ from Eq. (A.1), we can obtain an analytic solution of Eq. (A.7),

$$D(t) = \left[\frac{3}{2}\frac{t}{t_m}\right]^{2/3} \frac{2}{5}t_m^2 K_D \left(1 - 0.1591\left(\frac{t}{t_\Lambda}\right)^2 + 0.0366\left(\frac{t}{t_\Lambda}\right)^4\right), \tag{A.8}$$

where K_D is a normalisation constant. Requiring $\hat{D}(t_0) = 1$ gives $K_D = 4.70 \times 10^{-3}\,\mathrm{Gyr}^{-2}$.

The growth rates of linear perturbations do not directly predict the growth rates of haloes, however, we can directly connect the two through the approach developed

by Press & Schechter 1974. Correa et al. (2015) showed that the accretion rates of haloes can be written as (see also Neistein et al., 2006),

$$\frac{1}{M_h}\frac{\mathrm{d}M_h}{\mathrm{d}t} = \sqrt{\frac{2}{\pi}}\frac{(\delta_c/D)}{S(M_h)^{1/2}\left(q^\gamma - 1\right)^{1/2}}\frac{1}{D}\frac{\mathrm{d}D}{\mathrm{d}t}, \tag{A.9}$$

where M_h is the halo mass and $S(M_h)$ is the variance of the density field on the length scale corresponding the halo mass. δ_c is a parameter that represents a threshold in the linearly extrapolated density field for halo collapse. The parameters, q and γ, are related to the shape of the power-spectrum around the halo mass M_h. Approximating the scale dependence of the density field as a power-law around $10^{12}\,\mathrm{M}_\odot$ haloes as $S = S_0 M_h^{-\gamma}$, Correa et al. 2015 find $S_0 \approx 10^{4.2}, \gamma \approx 0.3$ and $q \approx 3.16$. These values depend only on the initial power spectrum (which we assume to be the same for all cosmological models) and do not depend on the cosmological parameters. This formulation thus neatly separates the contribution of the power-spectrum shape from the cosmological parameters.

Using the series approximation Eq. (A.1), the specific growth rate of halos can be written as,

$$\frac{1}{M_h}\frac{\mathrm{d}M_h}{\mathrm{d}t} = \frac{566.61}{\sqrt{S}\,t^{5/3}t_m^{4/3}}\left(1 - 0.3182\left(\frac{t}{t_\Lambda}\right)^2 + 0.0563\left(\frac{t}{t_\Lambda}\right)^4\right). \tag{A.10}$$

This explicitly shows how the presence of a cosmological constant modulates the halo growth rate. This differential equation can be solved by separation of variables to obtain the average mass history of dark matter halos,

$$\begin{aligned}\int_M^{M_0} M_h'^{\frac{-\gamma}{2}-1}\mathrm{d}M_h = \frac{566.61}{\sqrt{S_0}\,t_m^{4/3}} \times \\ \int_t^{t_0} t'^{-5/3}\left(1 - 0.3182\left(\frac{t'}{t_\Lambda}\right)^2 + 0.0563\left(\frac{t'}{t_\Lambda}\right)^4\right)\mathrm{d}t',\end{aligned} \tag{A.11}$$

where t_0, and M_0 are the present cosmic time and the mass of a halo today respectively. Integrating both sides and solving for $M(t)$ yields,

$$M_h(t) = \left[-\frac{424.958\gamma}{\sqrt{S_0}{t_m}^{4/3}} \left(t_0^{-2/3} \left(1 + 0.1590 \left(\frac{t_0}{t_\Lambda} \right)^2 - 0.0112 \left(\frac{t_0}{t_\Lambda} \right)^4 \right) \right. \right. \\ \left. \left. -t^{-2/3} \left(1 + 0.1590 \left(\frac{t}{t_\Lambda} \right)^2 - 0.0112 \left(\frac{t}{t_\Lambda} \right)^4 \right) \right) + M_0^{-\gamma/2} \right]^{-2/\gamma}. \tag{A.12}$$

Equation (A.12) provides an analytic expression for the of mass of a halo as a function of time.

A.3 The galaxy SFR

We now have all the necessary ingredients to calculate the stellar evolution of individual halos through cosmic time. Substituting Eq. (A.10) into Eq. (5.1), the stellar mass is given by the integral of,

$$\begin{aligned} \frac{\mathrm{d}M_*}{\mathrm{d}t} &= \epsilon_* \left[\frac{1}{M_h} \frac{\mathrm{d}M_h}{\mathrm{d}t} \right] M_h \\ &= \epsilon_* \frac{566.61}{\sqrt{S_0}\, t^{5/3} t_m^{4/3}} \left(1 - 0.3182 \left(\frac{t}{t_\Lambda} \right)^2 + 0.0563 \left(\frac{t}{t_\Lambda} \right)^4 \right) M_h^{\left(\frac{\gamma}{2}+1\right)}. \end{aligned} \tag{A.13}$$

where ϵ_* is given by either Eq. (5.3) or Eq. (5.4) and M_h by Eq. (A.12).

A.4 The cosmic SFR of the Universe

In order to calculate the cosmic SFR of the universe, we need to combine the specific halo mass accretion rate with an estimate of the halo abundance.

In the Press & Schechter analysis, the co-moving abundance of haloes of mass M_h at time t is given by (Press & Schechter, 1974),

$$\frac{dn(M_h, t)}{dM_h} = \frac{\hat{\rho}_0}{M_h^2} \frac{\delta_c \gamma}{\sqrt{2\pi} S^{1/2}} \frac{1}{D} \exp\left(-\frac{\delta_c^2}{2SD^2} \right) \tag{A.14}$$

where we have assumed that the density power spectrum is a power law with exponent γ and written the co-moving density of the Universe as $\hat{\rho}_0$ following our convention. Using the approximation we get,

$$\begin{aligned}\frac{dn(M_h,t)}{dM_h} = \frac{81.5919\hat{\rho}_0}{M_h^2\sqrt{S}t^{2/3}t_m^{4/3}}\left(1+0.1590\left(\frac{t}{t_\Lambda}\right)^2-0.0112\left(\frac{t}{t_\Lambda}\right)^4\right)\\ \times\exp\left[-\frac{232382}{S\,t^{4/3}t_m^{8/3}}\left(1+0.3182\left(\frac{t}{t_\Lambda}\right)^2+0.0028\left(\frac{t}{t_\Lambda}\right)^4\right)\right].\end{aligned} \tag{A.15}$$

The total cosmic SFR density is given by the integral of all star formation in all haloes,

$$\dot{\rho}_*(t) = \int \dot{M}_*(M_h)\frac{\mathrm{d}n(M_h,t)}{\mathrm{d}M_h}\mathrm{d}M_h = \int \epsilon_*(M_h)\dot{M}_h\frac{\mathrm{d}n(M_h,t)}{\mathrm{d}M_h}\mathrm{d}M_h \tag{A.16}$$

Using the halo growth rate from Eq. (A.10), the halo mass function fromEq. (A.15), together with the instantaneous star formation efficiency Eq. (5.3) or Eq. (5.4), the contribution to the cosmic SFR density from haloes of mass M_h (the integrand of Eq. (A.16)) is given by,

$$\begin{aligned}\frac{\mathrm{d}\dot{\rho}_*}{\mathrm{d}M_h} &= \epsilon_*\left[\frac{1}{M_h}\frac{\mathrm{d}M_h}{\mathrm{d}t}\right]M_h\frac{\mathrm{d}n(M_h,t)}{\mathrm{d}M_h}\\ &= \epsilon_*\frac{46230.9\hat{\rho}_0}{M_h S t^{7/3}t_m^{8/3}}\left(1-0.1590\left(\frac{t}{t_\Lambda}\right)^2-0.0056\left(\frac{t}{t_\Lambda}\right)^4\right)\\ &\times\exp\left[-\frac{232382}{S\,t^{4/3}t_m^{8/3}}\left(1+0.3182\left(\frac{t}{t_\Lambda}\right)^2+0.0028\left(\frac{t}{t_\Lambda}\right)^4\right)\right].\end{aligned} \tag{A.17}$$

GWs - Parameter variations

B

In this section we test our predictions against variations of the different parameters and assumptions used in our calculations. The parameters that we vary are:

- Dimensionless spin parameters (χ_i)
  - $\chi_i = 0$ for merging BHs with no spin
  - $\chi_i = 1$ for maximally spinning coalescing BHs aligned with the orbital angular momentum of the binary
- Simulated volume
  - Ref-L100N1504 with volume $(100\,\mathrm{cMpc})^3$
  - Ref-L050N0752 with volume $(50\,\mathrm{cMpc})^3$
  - Ref-L025N0376 with volume $(25\,\mathrm{cMpc})^3$
- Resolution
  - Reference model *'Ref'* (with baryonic particle mass $\mathrm{M_{gas}} = 1.81 \times 10^6\,\mathrm{M_\odot}$, dark matter particle mass $\mathrm{M_{gas}} = 9.70 \times 10^6\,\mathrm{M_\odot}$, co-moving gravitational softening $\epsilon_{\mathrm{com}} = 2.66\,\mathrm{ckpc}$, and maximum proper gravitational softening $\epsilon_{\mathrm{prop}} = 0.70\,\mathrm{ckpc}$)
  - High-resolution recalibrated model *'Recal'* (with baryonic particle mass $\mathrm{M_{gas}} = 2.26 \times 10^5\,\mathrm{M_\odot}$, dark matter particle mass $\mathrm{M_{gas}} = 1.21 \times 10^6\,\mathrm{M_\odot}$, co-moving gravitational softening $\epsilon_{\mathrm{com}} = 1.33\,\mathrm{ckpc}$, and maximum proper gravitational softening $\epsilon_{\mathrm{prop}} = 0.35\,\mathrm{ckpc}$).

We show in Fig. B.01 the redshift distribution of the eLISA SMBH coalescence detections for both the inspiral and merger-ringdown phases. The event rates for non spinning and maximally spinning BHS ($\chi_i = 0$ and $\chi_i = 1$) are shown in the right

panel. We obtain consistent results for the different EAGLE simulation models used in this study, where for both the inspiral and merger-ringdown phases the redshift distribution of the event rate peaks between redshift $z \approx 2$ and $z \approx 1$. There is a slight increase in the event rate when $\chi_i = 1$, which is not significant and the predicted event rate is consistent with ~ 2.

In Fig. B.02 we show the mass function of the more massive member of the binary, M_1, for the SMBH coalescences resolved by eLISA. For the merger-ringdown phase non spinning and maximally spinning BHS ($\chi_i = 0$ and$\chi_i = 1$) are shown in the right panel. For both the inspiral and merger-ringdown phases the mass function has a very pronounced peak at $M_1 \sim m_{\rm seed}$. Given the logarithmic scale of the plot, the galaxy formation model implemented in EAGLE predicts that GW signals will be dominated by the coalescence of BH seeds (also shown in Fig. B.03, in which the mass distribution of the mass ratio M_1/M_2 of the predicted event rate is dominated by equal mass SMBH coalescences).

Our event rate predictions are robust to variations of simulated volume, resolution, and parameters used to calculate the GW detections of the eLISA detector such as the dimensionless spin parameters χ_1. We summarise in Table B.01 the predicted event rates for both the inspiral and merger-ringdown phases for all the different parameter variations, simulated volumes and resolutions. Overall, the predicted event rates of GW signals resolved by the eLISA detector are ~ 2 events per year for all the reference models, whereas the high-resolution recalibrated model Recal-L025N0752 yields ~ 3 events per year. This does not represent a significant change in the predicted event rate.

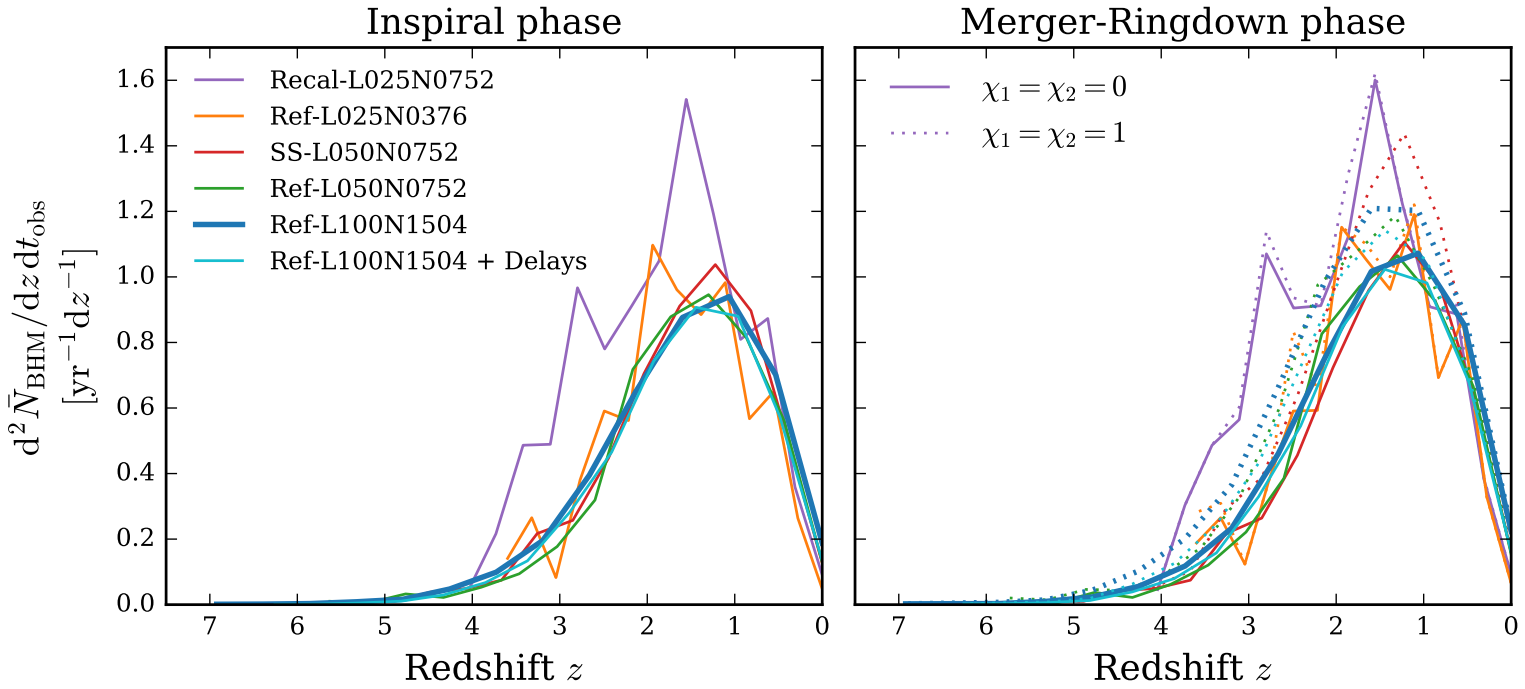

Fig. B.01.: Number of SMBH coalescences resolved by eLISA per observed year, per unit redshift. *LEFT PANEL:* inspiral phase. *RIGHT PANEL:* merger-ringdown phase. Solid lines were calculated using dimensionless spin parameters $\chi_i = 0$. For the dotted lines $\chi_i = 1$. The distribution peaks between redshift $z \sim 2$ and $z \sim 1$ for both the inspiral and the merger-ringdown phases.

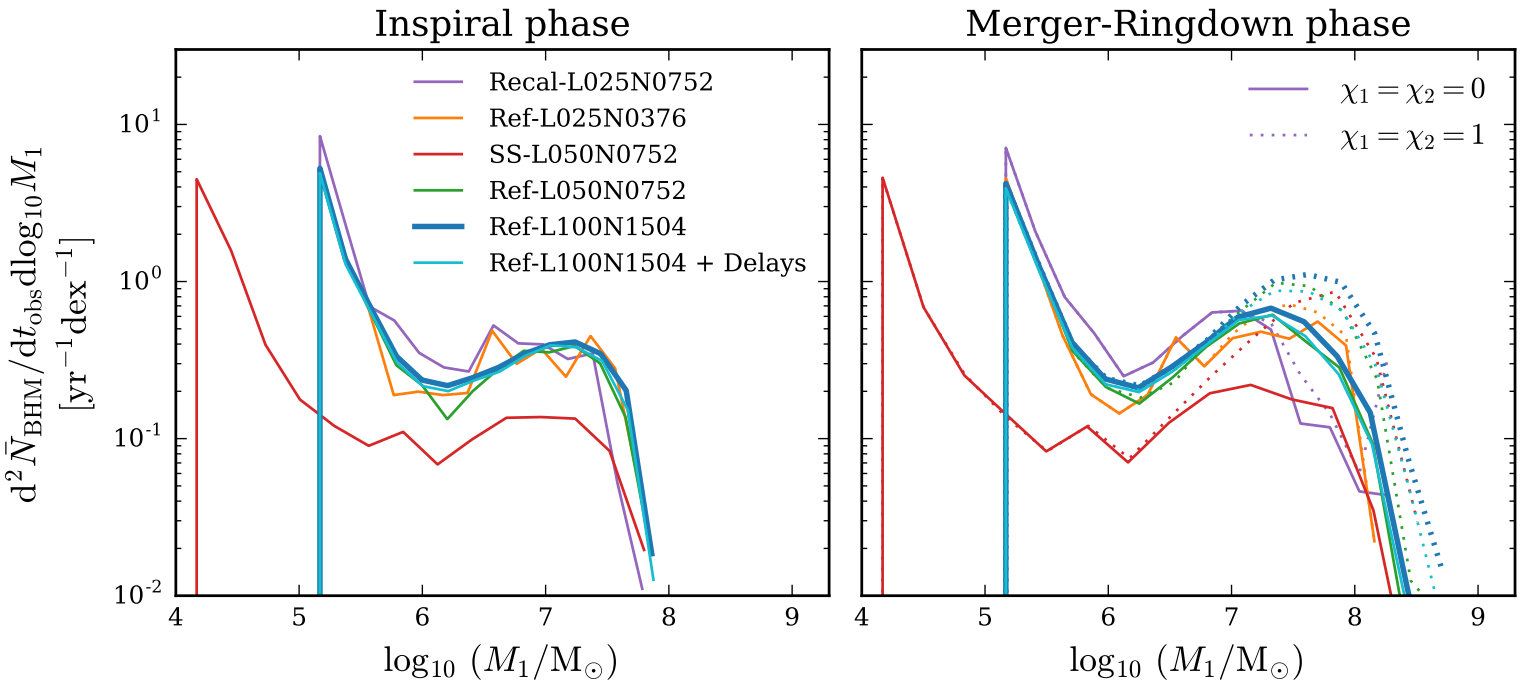

Fig. B.02.: Distribution of mass of the more massive member of the binary, M_1, of the SMBH coalescences resolved by eLISA. *LEFT PANEL:* inspiral phase. *RIGHT PANEL:* merger-ringdown phase. Solid lines were calculated using dimensionless spin parameters $\chi_i = 0$. For dotted lines $\chi_i = 1$. The distribution peaks at $M_1 \sim m_{\mathrm{seed}}$ for both the inspiral and the merger-ringdown phases.

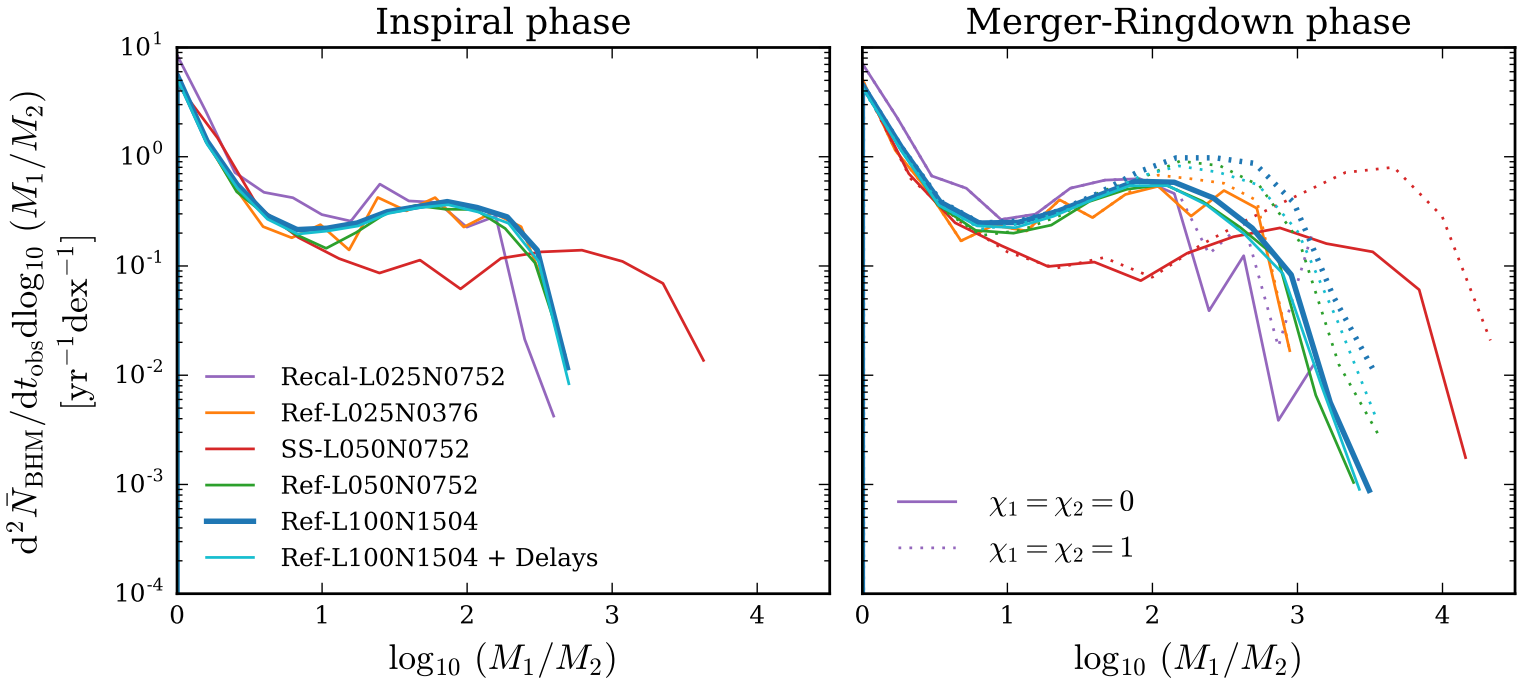

Fig. B.03.: Distribution of the mass ratio, M_1/M_2, of the SMBH coalescences resolved by eLISA. *LEFT PANEL:* inspiral phase. *RIGHT PANEL:* merger-ringdown phase. Solid lines were calculated using dimensionless spin parameters $\chi_i = 0$. For dotted lines $\chi_i = 1$. The distribution peaks at equal mass SMBH binaries for both the inspiral and the merger-ringdown phase.

Table B.01.: Estimated event rates for the different simulation models. σ is the standard Poisson uncertainty on the expectation event rate due to the finite volume of the simulations.

$f_{\rm cut}$ [Hz]	χ_i	Simulation	Inspiral Phase event rate [$\rm yr^{-1}$]	$\sigma_{\rm I}$ [$\rm yr^{-1}$]	Merger-Ringdown Phase event rate [$\rm yr^{-1}$]	$\sigma_{\rm M-RD}$ [$\rm yr^{-1}$]
3×10^{-5}	0	Ref-L100N1504	2.02	0.01	2.36	0.02
		Ref-L100N1504 + Delays	1.89	0.01	2.17	0.01
		SS-L050N0752	2.02	0.04	2.16	0.04
		Ref-L050N0752	1.93	0.04	2.21	0.04
		Ref-L025N0376	1.99	0.11	2.24	0.11
		Recal-L025N0752	2.91	0.14	3.12	0.15
	1	Ref-L100N1504	2.02	0.01	2.91	0.02
		Ref-L100N1504 + Delays	1.89	0.01	2.55	0.02
		SS-L050N0752	2.02	0.04	2.75	0.05
		Ref-L050N0752	1.93	0.04	2.64	0.05
		Ref-L025N0376	1.99	0.11	2.39	0.12
		Recal-L025N0752	2.91	0.14	3.24	0.15

Bibliography

Abbott B. P., et al., 2016, Physical Review Letters, 116, 061102

Adams F. C., 2008, J. Cosmology Astropart. Phys., 8, 010

Adams F. C., Alexander S., Grohs E., Mersini-Houghton L., 2017, J. Cosmology Astropart. Phys., 3, 021

Ade P. a. R., et al., 2014, Astronomy and Astrophysics, 571, A20

Agarwal B., Dalla Vecchia C., Johnson J. L., Khochfar S., Paardekooper J.-P., 2014, MNRAS, 443, 648

Aghanim N., et al., 2016, Astronomy and Astrophysics, 594, A22

Aguirre A., Gratton S., Johnson M. C., 2007, Phys. Rev. D, 75, 123501

Alexander D. M., Hickox R. C., 2012, New Astron. Rev., 56, 93

Alvarez M. A., Wise J. H., Abel T., 2009, ApJ, 701, L133

Amaro-Seoane P., et al., 2012, Classical and Quantum Gravity, 29, 124016

Amaro-Seoane P., et al., 2013, GW Notes, Vol. 6, 6, 4

Angulo R. E., Springel V., White S. D. M., Jenkins A., Baugh C. M., Frenk C. S., 2012, MNRAS, 426, 2046

Antonini F., Barausse E., Silk J., 2015, ApJ, 812, 72

Babcock H. W., 1939, Lick Observatory Bulletin, 19, 41

Bagla J. S., 2002, Journal of Astrophysics and Astronomy, 23, 185

Bahé Y. M., et al., 2016, MNRAS, 456, 1115

Baldry I. K., et al., 2012, MNRAS, 421, 621

Banks T., 1985, Nuclear Physics B, 249, 332

Barausse E., 2012, MNRAS, 423, 2533

Barnes L. A., 2012, Publ. Astron. Soc. Australia, 29, 529

Barnes L. A., 2017, preprint, (arXiv:1704.01680)

Barnes L., Francis M. J., Lewis G. F., Linder E. V., 2005, Publ. Astron. Soc. Australia, 22, 315

Barnes L. A., Francis M. J., James J. B., Lewis G. F., 2006, MNRAS, 373, 382

Barnes L. A., et al., 2018, MNRAS, 477, 3727

Barrow J. D., Tipler F. J., 1986, The anthropic cosmological principle

Begelman M. C., Blandford R. D., Rees M. J., 1980, Nature, 287, 307

Begelman M. C., Rossi E. M., Armitage P. J., 2008, MNRAS, 387, 1649

Behroozi P. S., Wechsler R. H., Conroy C., 2013a, ApJ, 762, L31

Behroozi P. S., Wechsler R. H., Conroy C., 2013b, ApJ, 770, 57

Behroozi P., Wechsler R., Hearin A., Conroy C., 2018, preprint, (arXiv:1806.07893)

Bellovary J., Cleary C., Munshi F., Tremmel M., Christensen C., Brooks A., Quinn T., 2018, preprint, (arXiv:1806.00471)

Bender P. L., Begelman M. C., Gair J. R., 2013, Classical and Quantum Gravity, 30, 165017

Benson A. J., 2012, New Astron., 17, 175

Benson A. J., Bower R. G., Frenk C. S., Lacey C. G., Baugh C. M., Cole S., 2003, ApJ, 599, 38

Berger M. J., Colella P., 1989, Journal of Computational Physics, 82, 64

Berlind A. A., Weinberg D. H., 2002, ApJ, 575, 587

Bode P., Ostriker J. P., Xu G., 2000, The Astrophysical Journal Supplement Series, 128, 561

Bond J. R., Cole S., Efstathiou G., Kaiser N., 1991, ApJ, 379, 440

Bonoli S., Mayer L., Kazantzidis S., Madau P., Bellovary J., Governato F., 2016, MNRAS, 459, 2603

Booth C. M., Schaye J., 2009, MNRAS, 398, 53

Bose S., Deason A. J., Frenk C. S., 2018, ApJ, 863, 123

Bouché N., et al., 2010, ApJ, 718, 1001

Bousso R., 2006, Physical Review Letters, 97, 191302

Bousso R., Leichenauer S., 2009, Phys. Rev. D, 79, 063506

Bousso R., Leichenauer S., 2010, Phys. Rev. D, 81, 063524

Bousso R., Susskind L., 2012, Phys. Rev. D, 85, 045007

Bousso R., Freivogel B., Yang I.-S., 2006, Phys. Rev. D, 74, 103516

Bousso R., Harnik R., Kribs G. D., Perez G., 2007, Phys. Rev. D, 76, 043513

Bousso R., Freivogel B., Yang I.-S., 2009, Phys. Rev. D, 79, 063513

Bouwens R. J., et al., 2012, ApJ, 754, 83

Bower R. G., 1991, MNRAS, 248, 332

Bower R. G., Benson A. J., Malbon R., Helly J. C., Frenk C. S., Baugh C. M., Cole S., Lacey C. G., 2006, MNRAS, 370, 645

Bower R. G., McLeish T. C. B., Tanner B. K., Smithson H. E., Panti C., Lewis N., Gasper G. E. M., 2014, Proc. R. Soc. A, 470, 20140025

Bower R. G., Schaye J., Frenk C. S., Theuns T., Schaller M., Crain R. A., McAlpine S., 2017, MNRAS, 465, 32

Brainerd T. G., Specian M. A., 2003, ApJ, 593, L7

Buchhave L. A., Latham D. W., 2015, ApJ, 808, 187

Burgarella D., et al., 2013, A&A, 554, A70

Carr B. J., Rees M. J., 1979, Nature, 278, 605

Carroll S. M., 2001, Living Reviews in Relativity, 4, 1

Carter B., 1974, in Longair M. S., ed., IAU Symposium Vol. 63, Confrontation of Cosmological Theories with Observational Data. pp 291–298

Carter B., 1983, Philosophical Transactions of the Royal Society of London Series A, 310, 347

Chabrier G., 2003, PASP, 115, 763

Chimento L. P., Jakubi A. S., Pavón D., Zimdahl W., 2003, Phys. Rev. D, 67, 083513

Clark P. C., Glover S. C. O., Smith R. J., Greif T. H., Klessen R. S., Bromm V., 2011, Science, 331, 1040

Cole S., Aragon-Salamanca A., Frenk C. S., Navarro J. F., Zepf S. E., 1994, MNRAS, 271, 781

Cole S., et al., 2005, Monthly Notices of the Royal Astronomical Society, 362, 505

Colpi M., 2014, Space Sci. Rev., 183, 189

Colpi M., Dotti M., 2011, Advanced Science Letters, 4, 181

Cooray A., Sheth R., 2002, Phys. Rep., 372, 1

Correa C. A., Wyithe J. S. B., Schaye J., Duffy A. R., 2015, MNRAS, 450, 1514

Couchman H. M. P., Rees M. J., 1986, MNRAS, 221, 53

Cowley W. I., et al., 2018, ApJ, 853, 69

Crain R. A., et al., 2009, MNRAS, 399, 1773

Crain R. A., et al., 2015, MNRAS, 450, 1937

Creasey P., Theuns T., Bower R. G., 2013, Monthly Notices of the Royal Astronomical Society, 429, 1922

Creasey P., Theuns T., Bower R. G., 2015, Monthly Notices of the Royal Astronomical Society, 446, 2125

Croton D. J., 2013, Publications of the Astronomical Society of Australia, 30

Croton D. J., et al., 2006, MNRAS, 365, 11

Crowder J., Cornish N. J., 2005, Phys. Rev. D, 72, 083005

Cucciati O., et al., 2012, A&A, 539, A31

Cullen L., Dehnen W., 2010, MNRAS, 408, 669

Cutler C., Flanagan É. E., 1994, Phys. Rev. D, 49, 2658

Dalla Vecchia C., Schaye J., 2012, MNRAS, 426, 140

Davé R., Finlator K., Oppenheimer B. D., 2012, MNRAS, 421, 98

Davé R., Thompson R., Hopkins P. F., 2016, MNRAS, 462, 3265

Davies P. C. W., 1983, Progress in Particle and Nuclear Physics, 10, 1

Davies P. C. W., Unwin S. D., 1981, Proceedings of the Royal Society of London Series A, 377, 147

Davis M., Efstathiou G., Frenk C. S., White S. D. M., 1985, ApJ, 292, 371

Dekel A., Silk J., 1986, ApJ, 303, 39

Devecchi B., Volonteri M., 2009, ApJ, 694, 302

Devecchi B., Volonteri M., Rossi E. M., Colpi M., Portegies Zwart S., 2012, MNRAS, 421, 1465

Di Matteo T., Springel V., Hernquist L., 2005, Nature, 433, 604

Di Matteo T., Colberg J., Springel V., Hernquist L., Sijacki D., 2008, ApJ, 676, 33

Diemer B., More S., Kravtsov A. V., 2013, ApJ, 766, 25

Dodelson S., Kaplinghat M., Stewart E., 2000, Physical Review Letters, 85, 5276

Dolag K., Borgani S., Murante G., Springel V., 2009, MNRAS, 399, 497

Doroshkevich A. G., Zel'dovich Y. B., Novikov I. D., 1967, Soviet Astronomy, 11, 233

Driver S. P., et al., 2018, MNRAS, 475, 2891

Dubois Y., Peirani S., Pichon C., Devriendt J., Gavazzi R., Welker C., Volonteri M., 2016, MNRAS, 463, 3948

Durier F., Dalla Vecchia C., 2012, MNRAS, 419, 465

Efstathiou G., 1992, MNRAS, 256, 43P

Efstathiou G., 1995, MNRAS, 274, L73

Einstein A., 1916, Annalen der Physik, 354, 769

Eisenstein D. J., et al., 2005, The Astrophysical Journal, 633, 560

Ellis G., Silk J., 2014, Nature, 516, 321

Ellis G. F. R., Stoeger W. R., 2009, General Relativity and Gravitation, 41, 1475

Enoki M., Inoue K. T., Nagashima M., Sugiyama N., 2004, ApJ, 615, 19

Escala A., Larson R. B., Coppi P. S., Mardones D., 2005, ApJ, 630, 152

Fabian A. C., 1994, ARA&A, 32, 277

Fabian A. C., 2012, ARA&A, 50, 455

Fan X., 2006, New Astron. Rev., 50, 665

Fanidakis N., Baugh C. M., Benson A. J., Bower R. G., Cole S., Done C., Frenk C. S., 2011, MNRAS, 410, 53

Ferrarese L., Merritt D., 2000, ApJ, 539, L9

Finlator K., Davé R., 2008, MNRAS, 385, 2181

Fischer D. A., Valenti J., 2005, ApJ, 622, 1102

Fitts A., et al., 2017, MNRAS, 471, 3547

Flanagan E. E., Hughes S. A., 1998, Phys. Rev. D, 57, 4535

Fosalba P., Crocce M., Gaztañaga E., Castander F. J., 2015, MNRAS, 448, 2987

Freivogel B., 2011, Classical and Quantum Gravity, 28, 204007

Freivogel B., Kleban M., Rodríguez Martínez M., Susskind L., 2006, Journal of High Energy Physics, 3, 039

Frenk C. S., White S. D. M., Davis M., Efstathiou G., 1988, The Astrophysical Journal, 327, 507

Friedmann A., 1922, Zeitschrift fur Physik, 10, 377

Fukugita M., Hogan C. J., Peebles P. J. E., 1998, ApJ, 503, 518

Furlong M., et al., 2015, MNRAS, 450, 4486

Furlong M., et al., 2017, MNRAS, 465, 722

Gair J. R., Vallisneri M., Larson S. L., Baker J. G., 2013, Living Reviews in Relativity, 16, 7

Garriga J., Vilenkin A., 2000, Phys. Rev. D, 61, 083502

Garriga J., Vilenkin A., 2001, Phys. Rev. D, 64, 043511

Garriga J., Vilenkin A., 2013, J. Cosmology Astropart. Phys., 5, 037

Garriga J., Livio M., Vilenkin A., 2000, Phys. Rev. D, 61, 023503

Garriga J., Schwartz-Perlov D., Vilenkin A., Winitzki S., 2006, J. Cosmology Astropart. Phys., 1, 017

Gebhardt K., et al., 2000, ApJ, 539, L13

Gibbons G. W., Turok N., 2008, Phys. Rev. D, 77, 063516

Gilbank D. G., Baldry I. K., Balogh M. L., Glazebrook K., Bower R. G., 2010, MNRAS, 405, 2594

Gingold R. A., Monaghan J. J., 1977, Monthly Notices of the Royal Astronomical Society, 181, 375

Gonzalez G., 1997, MNRAS, 285, 403

Greif T. H., Springel V., White S. D. M., Glover S. C. O., Clark P. C., Smith R. J., Klessen R. S., Bromm V., 2011, ApJ, 737, 75

Gültekin K., et al., 2009, ApJ, 698, 198

Guth A. H., 2007, Journal of Physics A Mathematical General, 40, 6811

Haardt F., Madau P., 2001, in Neumann D. M., Tran J. T. V., eds, Clusters of Galaxies and the High Redshift Universe Observed in X-rays.

Haas M. R., Schaye J., Booth C. M., Dalla Vecchia C., Springel V., Theuns T., Wiersma R. P. C., 2013, MNRAS, 435, 2931

Habouzit M., Volonteri M., Dubois Y., 2017, MNRAS, 468, 3935

Haehnelt M. G., 1994, MNRAS, 269, 199

Hannam M., 2014, General Relativity and Gravitation, 46, 1767

Harrison C. M., 2017, Nature Astronomy, 1, 0165

Harry G. M., Fritschel P., Shaddock D. A., Folkner W., Phinney E. S., 2006, Classical and Quantum Gravity, 23, 4887

Heath D. J., 1977, Monthly Notices of the Royal Astronomical Society, 179, 351

Heckman T. M., Best P. N., 2014, Annual Review of Astronomy and Astrophysics, 52, 589

Hellings R. W., Downs G. S., 1983, ApJ, 265, L39

Henriques B. M. B., White S. D. M., Thomas P. A., Angulo R., Guo Q., Lemson G., Springel V., Overzier R., 2015, MNRAS, 451, 2663

Hoekstra H., Yee H. K. C., Gladders M. D., 2004, ApJ, 606, 67

Hoffman L., Loeb A., 2007, MNRAS, 377, 957

Hogan C. J., 2000, Reviews of Modern Physics, 72, 1149

Hopkins P. F., 2013, MNRAS, 428, 2840

Hopkins P. F., Quataert E., Murray N., 2011, Monthly Notices of the Royal Astronomical Society, 417, 950

Hopkins P. F., Kereš D., Oñorbe J., Faucher-Giguère C.-A., Quataert E., Murray N., Bullock J. S., 2014, MNRAS, 445, 581

Hubble E. P., 1925, The Astrophysical Journal, 62

Hubble E., 1929, Proceedings of the National Academy of Science, 15, 168

Hudson M. J., et al., 2015, MNRAS, 447, 298

Huterer D., et al., 2015, Astroparticle Physics, 63, 23

Ilbert O., et al., 2013, A&A, 556, A55

Inayoshi K., Haiman Z., Ostriker J. P., 2016, MNRAS, 459, 3738

Janssen G., et al., 2015, Advancing Astrophysics with the Square Kilometre Array (AASKA14), p. 37

Jenkins A., 2010, MNRAS, 403, 1859

Jenkins A., et al., 1998, ApJ, 499, 20

Johnson J. L., Greif T. H., Bromm V., 2008, MNRAS, 388, 26

Karim A., et al., 2011, ApJ, 730, 61

Katz H., Sijacki D., Haehnelt M. G., 2015, MNRAS, 451, 2352

Kauffmann G., Haehnelt M., 2000, MNRAS, 311, 576

Kawamura S., et al., 2006, Classical and Quantum Gravity, 23, S125

Kelley L. Z., Blecha L., Hernquist L., 2017, MNRAS, 464, 3131

Kennicutt Jr. R. C., 1998, ApJ, 498, 541

Khan S., Husa S., Hannam M., Ohme F., Pürrer M., Forteza X. J., Bohé A., 2016, Phys. Rev. D, 93, 044007

King A., 2003, ApJ, 596, L27

Klein A., et al., 2016, Phys. Rev. D, 93, 024003

Klypin A. A., Trujillo-Gomez S., Primack J., 2011, ApJ, 740, 102

Knobe J., Olum K. D., Vilenkin A., 2003, preprint, (arXiv:physics/0302071)

Komatsu E., et al., 2011, The Astrophysical Journal Supplement Series, 192, 18

Kormendy J., Ho L. C., 2013, ARA&A, 51, 511

Koushiappas S. M., Zentner A. R., 2006, ApJ, 639, 7

Koushiappas S. M., Bullock J. S., Dekel A., 2004, MNRAS, 354, 292

Lacey C., Cole S., 1993, MNRAS, 262, 627

Lacey C. G., et al., 2016, MNRAS, 462, 3854

Lagos C. d. P., et al., 2015, MNRAS, 452, 3815

Le Brun A. M. C., McCarthy I. G., Schaye J., Ponman T. J., 2014, MNRAS, 441, 1270

Lemaître G., 1927, Annales de la Société Scientifique de Bruxelles, 47, 49

Lewis A., Challinor A., Lasenby A., 2000, ApJ, 538, 473

Lewis G. F., Barnes L. A., Schmidt F. b. B., 2016, A Fortunate Universe

Li C., White S. D. M., 2009, MNRAS, 398, 2177

Linde A. D., 1984, Reports on Progress in Physics, 47, 925

Linde A., 1987, in , Three Hundred Years of Gravitation. pp 604–630, http://adsabs.harvard.edu/abs/1987thyg.book..604L

Linde A., 2017, Reports on Progress in Physics, 80, 022001

Lineweaver C. H., Egan C. A., 2007, ApJ, 671, 853

Loeb A., Barkana R., 2001, Annual Review of Astronomy and Astrophysics, 39, 19

Loeb A., Rasio F. A., 1994, ApJ, 432, 52

Loeb A., Batista R. A., Sloan D., 2016, J. Cosmology Astropart. Phys., 8, 040

Lucy L. B., 1977, The Astronomical Journal, 82, 1013

Lupi A., Colpi M., Devecchi B., Galanti G., Volonteri M., 2014, MNRAS, 442, 3616

Lupi A., Haardt F., Dotti M., Fiacconi D., Mayer L., Madau P., 2016, MNRAS, 456, 2993

Madau P., Dickinson M., 2014, ARA&A, 52, 415

Madau P., Rees M. J., 2001, ApJ, 551, L27

Magorrian J., et al., 1998, AJ, 115, 2285

Martel H., Shapiro P. R., Weinberg S., 1998, ApJ, 492, 29

Mayer L., 2013, Classical and Quantum Gravity, 30, 244008

Mayer L., Kazantzidis S., Madau P., Colpi M., Quinn T., Wadsley J., 2007, Science, 316, 1874

McAlpine S., et al., 2016, Astronomy and Computing, 15, 72

McAlpine S., Bower R. G., Rosario D. J., Crain R. A., Schaye J., Theuns T., 2018, preprint, (arXiv:1805.08293)

Meißner U.-G., 2014, preprint, (arXiv:1409.2959)

Micic M., Holley-Bockelmann K., Sigurdsson S., Abel T., 2007, MNRAS, 380, 1533

Misner C. W., Thorne K. S., Wheeler J. A., 1973, Gravitation

Mo H., van den Bosch F., White S., 2010, Galaxy Formation and Evolution. Galaxy Formation and Evolution, Cambridge University Press

Moore C. J., Cole R. H., Berry C. P. L., 2015, Classical and Quantum Gravity, 32, 015014

Moster B. P., Somerville R. S., Maulbetsch C., Bosch F. C. v. d., Macciò A. V., Naab T., Oser L., 2010, ApJ, 710, 903

Moster B. P., Naab T., White S. D. M., 2013, MNRAS, 428, 3121

Moster B. P., Naab T., White S. D. M., 2018, MNRAS, 477, 1822

Moustakas J., et al., 2013, ApJ, 767, 50

Mutch S. J., Croton D. J., Poole G. B., 2013, MNRAS, 435, 2445

Muzzin A., et al., 2013, ApJ, 777, 18

Naab T., Ostriker J. P., 2017, ARA&A, 55, 59

Neistein E., van den Bosch F. C., Dekel A., 2006, MNRAS, 372, 933

Neyman J., Scott E. L., 1952, ApJ, 116, 144

Noeske K. G., et al., 2007, ApJ, 660, L47

Norberg P., Frenk C. S., Cole S., 2008, MNRAS, 383, 646

Ohme F., 2012, Classical and Quantum Gravity, 29, 124002

Omukai K., 2001, ApJ, 546, 635

Oort J. H., 1932, Bulletin of the Astronomical Institutes of the Netherlands, 6, 249

Oppenheimer B. D., Davé R., 2008, MNRAS, 387, 577

Oppenheimer B. D., Davé R., Kereš D., Fardal M., Katz N., Kollmeier J. A., Weinberg D. H., 2010, MNRAS, 406, 2325

Page D. N., 2008, J. Cosmology Astropart. Phys., 10, 025

Page D. N., 2017, preprint

Peacock J. A., 2007, MNRAS, 379, 1067

Peebles P. J. E., 1980, The large-scale structure of the universe

Penzias A. A., Wilson R. W., 1965, The Astrophysical Journal, 142, 419

Penzo C., Macciò A. V., Casarini L., Stinson G. S., Wadsley J., 2014, MNRAS, 442, 176

Penzo C., Macciò A. V., Baldi M., Casarini L., Oñorbe J., Dutton A. A., 2016, MNRAS, 461, 2490

Perlmutter S., et al., 1999, ApJ, 517, 565

Peterson J. R., Fabian A. C., 2006, Phys. Rep., 427, 1

Pillepich A., et al., 2018, MNRAS, 473, 4077

Piran T., Jimenez R., Cuesta A. J., Simpson F., Verde L., 2016, Physical Review Letters, 116

Planck Collaboration et al., 2014, A&A, 571, A16

Planck Collaboration et al., 2016, A&A, 594, A13

Portinari L., Chiosi C., Bressan A., 1998, A&A, 334, 505

Press W. H., Schechter P., 1974, ApJ, 187, 425

Price D. J., 2008, Journal of Computational Physics, 227, 10040

Puchwein E., Baldi M., Springel V., 2013, MNRAS, 436, 348

Qu Y., et al., 2017, MNRAS, 464, 1659

Quinlan G. D., 1996, New Astron., 1, 35

Rahmati A., Schaye J., Bower R. G., Crain R. A., Furlong M., Schaller M., Theuns T., 2015, MNRAS, 452, 2034

Rahmati A., Schaye J., Crain R. A., Oppenheimer B. D., Schaller M., Theuns T., 2016, MNRAS, 459, 310

Rees M. J., 1986, MNRAS, 218, 25P

Regan J. A., Haehnelt M. G., 2009, MNRAS, 396, 343

Regan J. A., Johansson P. H., Wise J. H., 2016, MNRAS, 459, 3377

Reines A. E., Greene J. E., Geha M., 2013, ApJ, 775, 116

Riess A. G., et al., 1998, AJ, 116, 1009

Robertson B. E., et al., 2013, ApJ, 768, 71

Rodríguez-Puebla A., Primack J. R., Behroozi P., Faber S. M., 2016, MNRAS, 455, 2592

Rosas-Guevara Y. M., et al., 2015, MNRAS, 454, 1038

Rosas-Guevara Y., Bower R. G., Schaye J., McAlpine S., Dalla Vecchia C., Frenk C. S., Schaller M., Theuns T., 2016, MNRAS, 462, 190

Rubin V. C., Ford Jr. W. K., 1970, The Astrophysical Journal, 159, 379

Sakharov A. D., 1984, Zhurnal Eksperimentalnoi i Teoreticheskoi Fiziki, 87, 375

Salcido J., Bower R. G., Theuns T., McAlpine S., Schaller M., Crain R. A., Schaye J., Regan J., 2016, MNRAS, 463, 870

Salcido J., et al., 2018, MNRAS, 477, 3744

Sawala T., Frenk C. S., Crain R. A., Jenkins A., Schaye J., Theuns T., Zavala J., 2013, MNRAS, 431, 1366

Sawala T., et al., 2016, MNRAS, 456, 85

Schaller M., et al., 2015a, MNRAS, 451, 1247

Schaller M., Dalla Vecchia C., Schaye J., Bower R. G., Theuns T., Crain R. A., Furlong M., McCarthy I. G., 2015c, MNRAS, 454, 2277

Schaller M., Dalla Vecchia C., Schaye J., Bower R. G., Theuns T., Crain R. A., Furlong M., McCarthy I. G., 2015b, MNRAS, 454, 2277

Schaye J., 2004, ApJ, 609, 667

Schaye J., Dalla Vecchia C., 2008, MNRAS, 383, 1210

Schaye J., et al., 2010, MNRAS, 402, 1536

Schaye J., et al., 2015, MNRAS, 446, 521

Schellekens A. N., 2013, Reviews of Modern Physics, 85, 1491

Segers M. C., Crain R. A., Schaye J., Bower R. G., Furlong M., Schaller M., Theuns T., 2016, MNRAS, 456, 1235

Sesana A., Volonteri M., Haardt F., 2007, MNRAS, 377, 1711

Sesana A., Vecchio A., Colacino C. N., 2008, MNRAS, 390, 192

Sesana A., Vecchio A., Volonteri M., 2009, MNRAS, 394, 2255

Sesana A., Gair J., Berti E., Volonteri M., 2011, Phys. Rev. D, 83, 044036

Seth A., Agüeros M., Lee D., Basu-Zych A., 2008, ApJ, 678, 116

Seth A. C., et al., 2014, Nature, 513, 398

Shapiro S. L., Teukolsky S. A., 1983, Black holes, white dwarfs, and neutron stars: The physics of compact objects

Shapley H., Curtis H. D., 1921, Bulletin of the National Research Council, Vol. 2, Part 3, No. 11, p. 171-217, 2, 171

Smoot G. F., et al., 1992, The Astrophysical Journal Letters, 396, L1

Somerville R. S., Davé R., 2015, ARA&A, 53, 51

Somerville R. S., Hopkins P. F., Cox T. J., Robertson B. E., Hernquist L., 2008, MNRAS, 391, 481

Song M., et al., 2016, ApJ, 825, 5

Springel V., 2005, MNRAS, 364, 1105

Springel V., Hernquist L., 2003, Monthly Notices of the Royal Astronomical Society, 339, 312

Springel V., White S. D. M., Tormen G., Kauffmann G., 2001, MNRAS, 328, 726

Springel V., Di Matteo T., Hernquist L., 2005a, MNRAS, 361, 776

Springel V., et al., 2005b, Nature, 435, 629

Springel V., Frenk C. S., White S. D. M., 2006, Nature, 440, 1137

Sudoh T., Totani T., Makiya R., Nagashima M., 2017, MNRAS, 464, 1563

Sugimura K., Omukai K., Inoue A. K., 2014, MNRAS, 445, 544

Susskind L., Thorlacius L., Uglum J., 1993, Phys. Rev. D, 48, 3743

Tacchella S., Trenti M., Carollo C. M., 2013, ApJ, 768, L37

Tacchella S., Bose S., Conroy C., Eisenstein D. J., Johnson B. D., 2018, preprint

Tamburello V., Capelo P. R., Mayer L., Bellovary J. M., Wadsley J. W., 2017, MNRAS, 464, 2952

Tegmark M., Aguirre A., Rees M. J., Wilczek F., 2006, Phys. Rev. D, 73, 023505

Tinto M., 1988, American Journal of Physics, 56, 1066

Tomczak A. R., et al., 2014, ApJ, 783, 85

Trayford J. W., et al., 2015, MNRAS, 452, 2879

Trayford J. W., Theuns T., Bower R. G., Crain R. A., Lagos C. d. P., Schaller M., Schaye J., 2016, MNRAS,

Tremmel M., Governato F., Volonteri M., Quinn T. R., 2015, MNRAS, 451, 1868

Trujillo-Gomez S., Klypin A., Primack J., Romanowsky A. J., 2011, ApJ, 742, 16

Tyson J. A., Valdes F., Wenk R. A., 1990, The Astrophysical Journal Letters, 349, L1

Vilenkin A., 1995, Phys. Rev. D, 52, 3365

Vilenkin A., 2007a, Journal of High Energy Physics, 1, 092

Vilenkin A., 2007b, Journal of Physics A Mathematical General, 40, 6777

Vilenkin A., Winitzki S., 1997, Phys. Rev. D, 55, 548

Volonteri M., 2010, A&ARv, 18, 279

Volonteri M., Bellovary J., 2011, in von Berlepsch R., ed., Reviews in Modern Astronomy Vol. 23, Reviews in Modern Astronomy. p. 189, doi:10.1002/9783527644384.ch11

Volonteri M., Bellovary J., 2012, Reports on Progress in Physics, 75, 124901

Volonteri M., Haardt F., Madau P., 2003, ApJ, 582, 559

Volonteri M., Silk J., Dubus G., 2015, ApJ, 804, 148

Volonteri M., Habouzit M., Pacucci F., Tremmel M., 2016,] 10.1017/S1743921315010005, 319, 72

Wang J., Fischer D. A., 2015, AJ, 149, 14

Wechsler R. H., Tinker J. L., 2018, preprint

Weinberg S., 1987, Physical Review Letters, 59, 2607

Weinberg S., 1989, Reviews of Modern Physics, 61, 1

Weinberg S., 2000, preprint

Wendland H., 1995, Advances in Computational Mathematics, 4, 389

Wetzel A. R., Nagai D., 2015, ApJ, 808, 40

White S. D. M., Frenk C. S., 1991, ApJ, 379, 52

White S. D. M., Rees M. J., 1978, MNRAS, 183, 341

Wiersma R. P. C., Schaye J., Smith B. D., 2009a, MNRAS, 393, 99

Wiersma R. P. C., Schaye J., Theuns T., Dalla Vecchia C., Tornatore L., 2009b, MNRAS, 399, 574

Wise J. H., Turk M. J., Abel T., 2008, ApJ, 682, 745

Wright T., 1750, An original theory or new hypothesis of the universe

Wyithe J. S. B., Loeb A., 2003, ApJ, 590, 691

Zaritsky D., Smith R., Frenk C., White S. D. M., 1993, ApJ, 405, 464

Zlatev I., Steinhardt P. J., 1999, Physics Letters B, 459, 570

Zlatev I., Wang L., Steinhardt P. J., 1999, Physical Review Letters, 82, 896

Zwicky F., 1933, Helvetica Physica Acta, 6, 110

de Simone A., Guth A. H., Linde A., Noorbala M., Salem M. P., Vilenkin A., 2010, Phys. Rev. D, 82, 063520

van de Voort F., 2017, in Fox A., Davé R., eds, Astrophysics and Space Science Library Vol. 430, Gas Accretion onto Galaxies. p. 301, doi:10.1007/978-3-319-52512-9_13

van de Voort F., Schaye J., Booth C. M., Dalla Vecchia C., 2011, MNRAS, 415, 2782

van den Bosch F. C., Norberg P., Mo H. J., Yang X., 2004, MNRAS, 352, 1302

van den Bosch F. C., Ogiya G., Hahn O., Burkert A., 2018, MNRAS, 474, 3043